

Durham E-Theses

The evolution of galaxies and AGN from deep x-ray and optical surveys

Mumbrú, Marc Vallbé

How to cite:

Mumbrú, Marc Vallbé (2004) *The evolution of galaxies and AGN from deep x-ray and optical surveys*, Durham theses, Durham University. Available at Durham E-Theses Online:
<http://etheses.dur.ac.uk/2968/>

Use policy

The full-text may be used and/or reproduced, and given to third parties in any format or medium, without prior permission or charge, for personal research or study, educational, or not-for-profit purposes provided that:

- a full bibliographic reference is made to the original source
- a [link](#) is made to the metadata record in Durham E-Theses
- the full-text is not changed in any way

The full-text must not be sold in any format or medium without the formal permission of the copyright holders.

Please consult the [full Durham E-Theses policy](#) for further details.

The Evolution of Galaxies and AGN from Deep X-ray and Optical Surveys

by Marc Vallbé Mumburú

Abstract

Two complementary new surveys of the X-ray background (XRB), the WHDF and the 10×10 ks, are presented. 140 serendipitous X-ray hard and soft sources ($S_{2-10 \text{ keV}} \gtrsim 3 \cdot 10^{-15}$; $S_{0.5-2 \text{ keV}} \gtrsim 4 \cdot 10^{-16} \text{ erg cm}^{-2} \text{ s}^{-1}$) have been identified and characterised by conducting concurrent optical and X-ray observations.

A principal aim of this work has been to establish whether X-ray luminous narrow-emission line galaxies (NELGs) are the sources that are the major contributors to the hard XRB, along with finding an explanation for their emission mechanisms. We build a case for a hidden AGN as the most likely explanation for such emission and, while NELGs are indeed found to be major contributors to the hard XRB, they are so as the nearby representatives of a major class of obscured AGN, most of which are too faint for probing with current spectroscopic facilities and appear either as “normal” galaxies or as blank fields in optical observations. In particular, we find no evidence of significant contribution from starbursts to the XRB intensity.

We also explore the high-redshift population of luminous absorbed AGN and report on the discovery of a type II QSO candidate at $z = 2.12$. But the number of such sources observed is found to be significantly below the predictions from obscured AGN models of the XRB and, inspired by the discovery of several broad-line quasars amongst the hardest sources in the WHDF and also in other surveys, we suggest that X-ray luminous absorbed AGN show optical broad lines more often than not. This affects the relationship between gas and dust in AGN and has direct consequences for the basic unification schemes for AGN.

In a parallel program, not only to study how the stellar content of the present universe was assembled over time but also to understand the photometric properties of the galaxies that host an AGN, we perform detailed analysis of the evolutionary properties of early-type galaxies. We find that a significant fraction of colour-selected elliptical and lenticular galaxies in the direction of the WHDF show colours that are too blue to be consistent with the predictions of a simple monolithic collapse at high-redshift and passive evolution thereafter. Their large scatter in photometric observables seem to imply divergent histories and indicate that the early-type populations are rather heterogeneous. In particular, significant low-redshift star formation is deduced from the large scatter in their colour-magnitude relation and from the presence of [O II] $\lambda 3727$ emission lines.

THE EVOLUTION OF GALAXIES AND AGN FROM DEEP X-RAY AND OPTICAL SURVEYS

by Marc Vallbé Mumbrú

A dissertation submitted to the University of Durham
in accordance with the regulations for admittance to
the Degree of Doctor of Philosophy.

**A copyright of this thesis rests
with the author. No quotation
from it should be published
without his prior written consent
and information derived from it
should be acknowledged.**

Department of Physics
University of Durham

2004



20 APR 2005

Contents

1	Introduction	1
1.1	Evolution of Galaxies and AGN	1
1.1.1	Active Galactic Nuclei	2
1.2	X-ray Astronomy	7
1.3	The X-ray Background	10
1.3.1	Spectral Properties	11
1.3.2	Isotropy	11
1.3.3	Source Content	12
1.4	The Durham X-ray Surveys	14
1.4.1	Motivation	14
1.4.2	The WHDF & 10×10 ks Chandra Surveys	17
1.5	Summary	21
2	X-ray Data	23
2.1	The Chandra X-ray Observatory	24
2.1.1	Focusing X-rays	24
2.1.2	The ACIS Instrument	27
2.2	Data Reduction	30
2.2.1	Source Detection	30
2.2.2	Flux Estimation	36
2.2.3	Catalogues of Chandra Sources	37
2.3	Temporal Properties	49
2.3.1	Long time-scale variability	49
2.3.2	Short time-scale variability	50
2.4	Number Counts	50
2.4.1	Methodology	50
2.4.2	Results	54
2.4.3	Contribution to the hard xrb	60
2.5	Spectral Properties	61
2.6	Summary	63
3	Optical follow-up of Chandra sources	64
3.1	Wide Field Imager	65
3.1.1	WFI Data and Reduction Analysis	65
3.1.2	Registration and Mosaicking	72
3.1.3	Object Detection and Classification	72
3.1.4	Photometric Calibration	76
3.2	Wide Field Camera	83
3.2.1	WFC Data and Reduction Analysis	83
3.2.2	Astrometry	85

3.3	WHDF Imaging	85
3.4	LDSS2 Spectroscopy	90
3.4.1	LDSS2 Data and Reduction Analysis	93
3.4.2	LDSS2 Extraction and Calibration Analysis	95
3.5	WYFFOS	103
3.6	Public Databases and Surveys	103
3.6.1	NED	104
3.6.2	2dF Surveys	106
3.6.3	Sloan Digital Sky Survey	108
3.7	Summary	112
4	The Nature of the XRB	113
4.1	Source Content	113
4.1.1	Source Classification	114
4.1.2	Emission Mechanisms	117
4.2	AGN Host Galaxy Properties	124
4.2.1	Optically Blank Population	130
4.3	Population Synthesis Models	133
4.3.1	Obscured AGN	133
4.3.2	Hard QSOs	134
4.3.3	Type II QSOs	136
4.3.4	Redshift Distribution	141
4.4	Minor Contributors	145
4.4.1	Stellar Contamination	145
4.4.2	Extremely Red Objects	145
4.4.3	Ultraluminous Compact X-ray Sources	146
4.5	Summary	149
5	Evolution of Early-type Galaxies	151
5.1	Evolutionary Models	151
5.2	Colour-Magnitude	157
5.3	Summary & Discussion	161
6	Summary and Conclusions	162
6.1	X-ray Data	162
6.2	Optical Follow-up of Chandra Sources	163
6.3	The Nature of the XRB	164
6.4	Evolution of Early-type Galaxies	166
6.5	Future Prospects	167
A	Spectro-photometric albums	170
	References	195

List of Figures

1.1	Schematic diagram of the unification scenario of AGN	4
1.2	Discovery of the x-ray background	8
1.3	The cosmic energy density spectrum	10
1.4	The XRB intensity spectrum	12
1.5	Absorption at x-ray energies for different absorbing columns	16
1.6	XRB population synthesis models	17
1.7	The optical $7' \times 7'$ <i>Herschel Deep Field</i>	20
2.1	Wolter I grazing incidence imaging system	25
2.2	Chandra: High Resolution Mirror Assembly	25
2.3	Simulated PSFs as a function of off-axis angles	26
2.4	Observed and simulated 85% encircled energy diameters	26
2.5	Schematic of the ACIS focal plane	27
2.6	Chandra effective areas as a function of energy	28
2.7	Chandra image of the <i>Herschel Deep Field</i>	29
2.8	Light curve plot of the WHDF background	32
2.9	Density of sources versus off-axis angle	34
2.10	Exposure map in the hard band	36
2.11	Long time-scale variability	49
2.12	Short time-scale variability	51
2.13	Cumulative distribution of sky area available at survey flux limit	53
2.14	Cumulative source number counts	55
2.15	Cumulative number counts, WHDF	57
2.16	Differential number counts, WHDF	59
2.17	Contribution to the hard XRB	60
2.18	Hardness ratios	62
3.1	WFI focal plane layout	67
3.2	WFI dark frame	68
3.3	WFI flat field image	70
3.4	Optical GSGP4 WFI image	73
3.5	Stellarity index vs. g magnitude	75
3.6	Offsets between Chandra and WFI positions	76
3.7	Standard star calibration plots	77
3.8	Photometric check: WFI vs. 2QZ	79
3.9	B -band differential number counts in GSGP4	80
3.10	WFC mosaic camera	83
3.11	Schematic of the WFC focal plane	84
3.12	The optical $16' \times 16'$ <i>Herschel Deep Field</i>	86
3.13	Finding chart for LDSS2 targeted sources in field GSGP4	91

3.14	LDSS2 slit masks (September 2002)	92
3.15	LDSS2 flatfield image	95
3.16	LDSS2 mask on GSGP4	96
3.17	LDSS2 spectra of X-ray sources (WHDF, 2001)	97
3.18	LDSS2 spectra of X-ray sources (WHDF, 2002)	98
3.19	LDSS2 spectra of X-ray sources (WHDF, GSGP4, 2002)	99
3.20	LDSS2 spectra of X-ray sources (GSGP4, 2002)	100
3.21	LDSS2 spectra of red-selected galaxies (WHDF, 2002; 1)	101
3.22	LDSS2 spectra of red-selected galaxies (WHDF, 2002; 2)	102
3.23	Offsets between NED and Chandra positions	104
3.24	Offsets between 2QZ and Chandra positions	106
3.25	Offsets between SDSS and Chandra positions	108
4.1	R band magnitude vs. X-ray flux	118
4.2	$\log f_X/f_{\text{opt}}$ vs. f_X , R , HR	120
4.3	$B - R$ vs. $R - I$ in the WHDF	121
4.4	$g - r$ vs. $r - i$ in the GSGP4	122
4.5	$g' - r'$ vs. $r' - i'$ in the F864	123
4.6	$g - r$ colours vs. z and r , GSGP4	125
4.7	$r - i$ colours vs. z and r , GSGP4	126
4.8	Hardness ratio vs. colours and z , WHDF	128
4.9	Hardness ratio vs. colours and z , GSGP4	129
4.10	Number counts for different populations	131
4.11	Fluxes vs. hardness and band ratios for optically blank sources	132
4.12	Hardness ratio with optical identification	134
4.13	Optical spectra of the hardest BLAGN and NLXGS	135
4.14	Optical spectrum of a heavily obscured high- z AGN in F864	137
4.15	IR spectrum of a heavily obscured high- z AGN in F864	137
4.16	Optical spectrum of a type II QSO candidate	139
4.17	Optical images of a type II QSO candidate	139
4.18	Redshift distribution of X-ray sources	143
4.19	Optical images of a ERO	146
4.20	Optical image of a ULX	147
4.21	Optical spectrum of a ULX	148
5.1	Colour-colour diagram of the red field early-type galaxies	153
5.2	$B - R$ colour index vs. redshift for field E and S0 galaxies	155
5.3	$R - I$ colour index vs. redshift for field E and S0 galaxies	156
5.4	Colour-colour diagrams for early-type galaxies in the WHDF	157
5.5	Colour-magnitude diagram for field E and S0 galaxies	158
5.6	$B - R$ colour-magnitude diagram vs. redshift for E and S0 galaxies	159
5.7	$R - I$ colour-magnitude diagram vs. redshift for E and S0 galaxies	160

List of Tables

1.1	Photometric summary of the surveyed fields	19
2.1	Journal of the Chandra observations	31
2.2	Summary of Chandra detections	35
2.3	Chandra sources in the F864 field	38
2.3	... continued	39
2.4	Chandra sources in the GSGP4 field	40
2.4	... continued	41
2.4	... continued	42
2.4	... continued	43
2.4	... continued	44
2.5	Chandra sources in the WHDF field	45
2.5	... continued	46
2.5	... continued	47
2.5	... continued	48
3.1	Resources employed in each field	66
3.2	Log of WFI observations in GSGP4 and photometric limits	66
3.3	Coefficients from Landolt Calibration	77
3.4	WFI counterparts to Chandra sources in GSGP4	81
3.4	... continued	82
3.5	Log of WFC observations in F864	84
3.6	Photometric limits of the WHDF	86
3.7	Optical counterparts to Chandra sources in the WHDF	87
3.7	... continued	88
3.7	... continued	89
3.8	Log of LDSS2 observations in GSGP4 and WHDF	94
3.9	LDSS2 break-down of Chandra sources	94
3.10	WYFFOS spectroscopy in F864	103
3.11	NED counterparts to Chandra sources in F864	105
3.12	2QZ counterparts to Chandra sources in GSGP4	107
3.13	SDSS counterparts to Chandra sources in F864	109
3.13	... continued	110
3.13	... continued	111
4.1	Spectroscopic classification of sources.	116

Declaration

The work described in this thesis was undertaken between 2000 and 2004 whilst the author was a research student under the supervision of Prof. Tom Shanks in the Department of Physics at the University of Durham. This work has not been submitted for any other degree at the University of Durham or at any other University.

This document is copyleft © 2004 by Marc Vallbé Mumbrú under the terms of the GNU Free Documentation License. Permission is granted to copy, distribute and/or modify this document under its terms. The author has asserted his right to be identified as the author of this work.

Acknowledgements

The work carried out in this thesis would not have been possible without the guidance of my supervisor, Tom Shanks. With his enthusiastic approach to science and vast knowledge of extragalactic astronomy, he has introduced me to many different aspects of the subject. I am particularly grateful for the opportunities I have been given to go observing; there is always something wonderful about being in a remote place, eyes raised to the sky.

Ioannis Georgantopoulos deserves special mention for teaching me pretty much all I know about x-ray data analysis and, generally, for leading the way. Efharistó pára polí. I would also like to thank Phil Outram for his practical advice on all sort of matters; Dave Gilbank for his endless patience with my mosaic data and introducing me to `IDL` and `Python`; Chris Done for answering all kinds of x-ray related questions; and Katherine Gunn for setting the wheels into motion. Nigel Metcalfe and Peter Draper are credited for ensuring the magnitudes of the galaxies in the catalogues fall somewhere between 15–25 and, jointly with Alan Lotts and David Stockdale, for removing the frustration from the computing experience in the department.

In the people with whom I have shared offices and corridors I found excellent mates: Adam; Bill; Chris; Dajana; Nick; Peder; Steve. Very warm thanks go to Phil and Antonio for their hospitality; to Peter for his numerous attempts to delay completion of this thesis by treating me to Star Trek DVDs, pigs, sheep, hedgehogs and comets; and most importantly to José for continuously taking care of me over the past two years.

I acknowledge La Caixa, the British Council and the Department of Physics for financial patronage.

Lastly, the biggest thanks are for my family. Pare, Mare i Arnau, sense el vostre amor i suport en tot moment no estaria escrivint aquestes ratlles. Una abraçada. Above all I thank Núria for her love. Un petó.

*Come with me now, Pilgrim of the stars,
For our time is upon us and our eyes
shall see the far country
and the shining cities of Infinity.*

Burnham's Celestial Handbook (1978)

CHAPTER I

Introduction

*Twinkle, twinkle, quasi-star,
Biggest puzzle from afar.
How unlike the other ones,
Brighter than a trillion Suns.
Twinkle, twinkle, quasi-star,
How I wonder what you are!*

George Gamow

1.1 Evolution of Galaxies & Active Galactic Nuclei

The ways galaxies form and evolve play an important role in any cosmological model and have always enjoyed the attention of astronomers. The currently favoured model of structure formation, the *hierarchical theory*, considers the adiabatic growth of initial density fluctuations that have the same entropy as the surrounding medium, at any given time. Small fragments of denser regions, with masses $\sim 10^5 M_{\odot}$, collapse and, while a few remain isolated to become dwarf galaxies, most subsequently merge with neighbours to build up galaxies of normal mass (10^9 to $10^{11} M_{\odot}$). The hierarchical clustering continues and galaxies are attracted together to form clusters of galaxies; the clusters then form superclusters. This *bottom-up* scenario is consistent with cold dark matter.

The details of how these processes occur are, however, still highly uncertain. It now seems clear that the most dramatic effects of galaxy evolution are linked to interactions with the environment (neighbour galaxies and the hot intracluster medium) and to supermassive black holes (SMBH; $M_{\bullet} \sim 10^8 M_{\odot}$) resident in the centre of bulges which often manifest as active galactic nuclei (AGN). The present work explores how galaxies and AGN interrelate.



1.1.1 Active Galactic Nuclei

Galaxies that emit unusually large amounts of energy —well in excess of the thermonuclear output from their stars— from a very compact central source are known as active galaxies or, alternatively, active galactic nuclei or AGN. Since the mid-Twentieth Century, several types of AGN have been found, each displaying a variety of properties that led astronomers to classify them first as separate phenomena. Carl Seyfert discovered in 1943 the first such kind and the most common AGN in the local universe: a type of spiral galaxy with extremely bright nonthermal emission in its nucleus; W. W. Morgan (1958) originally identified another type of powerful galactic nucleus, known as N galaxy, with luminosities intermediate between Seyfert galaxies and quasars; quasi-stellar objects (contracted to quasars or to its acronym QSOs), found in 1963 as the optical counterparts to powerful radio sources in the 3C catalogue (Schmidt 1963), are unresolved objects that emit more energy than several supergiant galaxies and show conspicuous ionization lines in their spectra; BL Lacs, named after BL Lacertae which was found to be a most peculiar counterpart to a radio source in 1968, resemble quasars but lack both emission and absorption lines, and display extremely compact and severe variability as well as polarised light; radio galaxies are another form of active galaxy that have a radio output in the range $10^{35} - 10^{38}$ Watts and are always located in elliptical galaxies, many of which are the central dominant member of a cluster.

Although stellar collision in dense galactic nuclei was first considered as a means to explain the galactic nucleus phenomenon (e.g. Spitzer & Saslaw 1966), observations of the motions of stars and gas in nearby galaxies such as M87 or NGC4151, the high powers involved and reports of acute variability on very short time-scales (\sim hours; e.g. figure 2.12), strongly suggest that emission from AGN is driven by accretion onto a supermassive black hole at the centre of galaxies. Gas from the interstellar medium, from the tidal disruption of stars near the black hole or from flows of intergalactic gas on to the central galaxy of a cluster as the gas cools, would release gravitational potential energy as it spirals onto the nucleus forming first an optically thick accretion disc as a result of conservation of angular momentum. This is in agreement with the nonthermal continuum emission observed at all wavelengths.

Continuum emission of AGN exhibits almost equal power per decade of frequency in nearly all wavebands studied and a set of dips and bumps consistently recur from one AGN to the other. These features include *a*) an x-ray continuum well represented by a power-law produced in a hot optically-thin plasma in a corona surrounding the disc; *b*) the “big blue bump”, thermal emission extending over the ultraviolet (UV) resulting from the heating of the accretion disc by the dissipation of gravitational energy; *c*) the “near infrared inflection”, a dip between $1-1.5 \mu\text{m}$, practically the only continuum feature with a well defined frequency (Neugebauer et al. 1987); *d*) the “infrared bump”, a broad feature longward of the $1 \mu\text{m}$ inflec-

tion resulting from high energy light absorbed by the obscuring material around the AGN and being thermally re-radiated in the infrared (see Edelson et al. 1987 for an alternative non-thermal explanation); and e) the “submillimetre break”, an abrupt decrease in emission and the strongest feature in normal quasar continua. In a minority of cases, highly relativistic bipolar outflows of energetic particles lead to extended radio emission.

The fact that the spectra of AGN are extraordinarily similar over a range of $\sim 10^{11}$ in frequency despite their luminosities may differ by a factor of $\sim 10^7$, suggests that the physical processes involved in their emission mechanisms are fundamentally the same.

Line Diagnosis

The broad collection of AGN species is further unravelled by similarities shared between different kinds of AGN and by subdivisions. One of the most striking features of most AGN is the presence in the optical of high ionization emission lines superimposed on the nonthermal spectrum from the central source, indicating the presence of strong ionizing radiation. These are commonly used to divide AGN into two categories: type I AGN have both broad emission lines ($\text{FWHM} \gtrsim 1000 \text{ km s}^{-1}$) and narrow emission lines ($\text{FWHM} \lesssim 1000 \text{ km s}^{-1}$), while type II AGN have narrow lines only (e.g. Osterbrock 1989). For instance, a quasar is usually defined as a compact object with broad lines ($\text{Ly}\alpha$, $\text{C IV } \lambda 1550$, $\text{C III } \lambda 1909$, $\text{Mg II } \lambda 2800$, etc.) and very bright (absolute magnitude $M_B \lesssim -23$ in the optical or a luminosity $L_X \gtrsim 10^{44} \text{ erg s}^{-1}$ in x-rays). At lower luminosities (Schmidt & Green 1983 adopt $M_B \gtrsim -21.5 + 5 \log h_0$)¹, Seyfert type I active galaxies (Sy 1) have narrow ($[\text{O II}] \lambda 3727$, $[\text{O III}] \lambda 5007$, etc) and broad emission lines, while Seyfert type II galaxies (Sy 2) lack broad lines.

Astronomers usually interpret the line width as a velocity dispersion due to Doppler broadening; hence, different widths correspond to emission from material orbiting at different (speeds and therefore) distances from the nucleus.² Broad lines are emitted from dense regions moving faster and closer to the core which are known as broad-line regions (BLRs). They may be dense inflowing clouds or perhaps transient structures lifted from the surface of the accretion disc by powerful magnetic reconnecting events, moving at speeds (inferred from the line broadening) in excess of 10^4 km s^{-1} . Variability studies in the line emission show that the BLRs are typically a few light-months across. The central black hole irradiates the gases to produce low-ionization emission lines (such as the Balmer series of hydrogen). At larger radii of ten to a thousand light-years from the central ionization source, the narrow line regions (NLRs) contain gas clouds that move at more moderate velocities of a few hundred km s^{-1} and radiate strongly in forbidden lines of ionized metals as well as hydrogen (see for instance Peterson 1997). In both cases, clouds of material are excited by the strong electromagnetic fields and de-excite

¹ $h_0 \equiv H_0/100$, where $H_0 = R^{-1}(dR/dt)$ is the Hubble constant (and R the cosmic scale factor).

²Even the narrow emission lines are too broad to be interpreted as due to pure thermal motion.

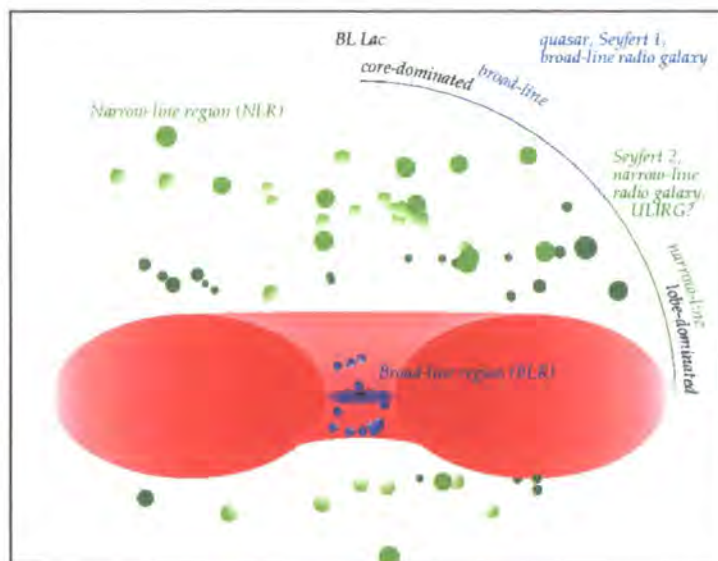


Figure 1.1: Schematic diagram of the unification scenario of active galactic nuclei showing the geometric interrelations between broad and narrow-line regions, obscuring molecular material (taken as a torus for convenience) and photo-ionized scattering medium. Depending on our line of sight to the object, the AGN will appear as a Seyfert I, II, BL Lac, quasar, *etc.* Various observational arguments strongly suggest that the energy output of AGN is derived from the gravitational potential of a supermassive black hole which has an accretion disc of gases spiralling onto it. Figure courtesy of C. Simpson.

emitting line radiation. This can provide useful information on the physical conditions prevailing in the clouds. The presence of forbidden transitions, for instance, which in terrestrial conditions de-excite collisionally before they had time to radiate, places upper limits on the density of NLRs so that collisional effects are insignificant ($n_{\text{NLR}} \lesssim 10^5\text{--}10^6 \text{ cm}^{-3}$ depending on the transitions seen; $n_{\text{BLR}} \gtrsim 10^9\text{--}10^{10} \text{ cm}^{-3}$). Furthermore, as the irradiation by large quantities of x-rays and UV light creates very highly ionized species which are only found in extreme environments ("coronal" lines; *e.g.* [Si VI]), AGN are a privileged laboratory for atomic physics diagnosis.

Unified Model

Despite the idiosyncrasies inherent in each type, closer examination shows that many of the differences amongst AGN may be due to different inclinations of the source to the line of sight, their fuelling rate or evolutionary stage and that there is probably a continuous transition between the BLRs and the NLRs (*e.g.* Dopita 1997). Amongst the Seyfert population, for instance, it is found that the narrow line properties of Sy 1 and Sy 2 are very similar. Thus, the discovery of broad emission lines (from scattered flux into our line of sight) in the polarised spectra of a number of Seyfert II galaxies provided the basis for a unified model for AGN in which the principal discriminating parameter is the inclination of an obscuring

screen of molecular gas and dust around the AGN with respect to our line of sight (e.g. Antonucci 1993; cf. also Rowan-Robinson 1977 and Lawrence & Elvis 1982). This screen may be in the form of a patchy dust covering, an axisymmetric structure or a 4π steradian shell of varying thickness; it is usually assumed toroidal for convenience based on observations of NGC 1068 and other Sy 2 in linear polarised light (Antonucci & Miller 1985). Hence, it is proposed that in type II objects the BLRS, lying close to the core, are hidden by obscuring matter in the line of sight (AGN seen edge-on); in type I objects, on the other hand, the emission from the BLRS is seen within the opening angle of the obscuring material (*i.e.*, face on). In both cases, the NLRS, further out, are external to this obscuration and can always be seen. Figure 1.1 on the preceding page shows a schematic plot of this model.

Further support for unification scenarios is provided by infrared observations which reveal broad emission lines from hydrogen recombination such as Pa α and Br γ in moderate column density Sy 2 spectra (Blanco et al. 1990; Hines 1991)³ and also from x-ray observations which reveal characteristic absorption features associated with a large column of obscuring material along the line of sight (Mulchaey et al. 1993; Awaki et al. 1991). Of fundamental relevance to our work, the AGN unification paradigm is the basis for the most successful cosmological x-ray background (XRB) population synthesis models (Madau et al. 1994; Comastri et al. 1995; Gunn 1999; Gilli et al. 2001; cf. § 1.4.1, 4.3).

Evolution

The subject of the evolution of the active galactic nucleus population began in the late 1960s with Schmidt's seminal work (Schmidt 1968, 1970). He developed and applied the luminosity-volume test (V/V_m) for analysing the space distribution of samples of radio and optically selected quasars and showed that there was a strong evolution in the space densities of both kinds of AGN towards higher redshift, increasing by a factor > 100 between $z \simeq 0$ and $z \simeq 2$. The reasons of the decline from $z \simeq 2$ are not yet understood.

The x-ray luminosity function, $\phi_X(L_X)$, for example, giving the space density of QSOs as a function of their luminosity, can be parameterised into two power laws intersecting at a 'break luminosity', L_X^* , according to Boyle et al. (1994). At zero redshift the $\phi_X(L_X, z=0)$ can be described by:

$$\phi_X(L_X, z=0) = \begin{cases} \phi_X^* L_{X44}^{-\gamma_1} & L_X < L_X^*(z=0) \\ \phi_X^* L_{X44}^{-\gamma_2} L_{X44}^{*(\gamma_2-\gamma_1)} & L_X > L_X^*(z=0) \end{cases}$$

where ϕ_X^* is the normalization of the $\phi_X(L_X)$ measured in units of $\text{Mpc}^{-3}/(10^{44} \text{ ergs}^{-1})$ and L_{X44} is the 0.3–3.5 keV x-ray luminosity in units of $10^{44} \text{ ergs}^{-1}$; γ_1 and γ_2 represent the low and high luminosity slopes of the x-ray luminosity function

³The extinction by dust is wavelength-dependent. Due to their size of ~ 100 nm, dust grains scatter and obscure ultraviolet and optical light while leave relatively unaffected near infrared photons.

respectively. Assuming that the number density of AGN does not evolve, but they undergo pure luminosity evolution (PLE) alone which becomes stationary at a maximum redshift, z_{cut} , the luminosity function can be parametrized by the evolution of the characteristic "knee", L_X^* , such that:

$$L_X^*(z) = \begin{cases} L_X^*(0)(1+z)^k & z \leq z_{cut} \\ L_X^*(z_{cut}) & z > z_{cut} \end{cases}$$

Adopting the values of Model G in Boyle et al. of $\gamma_1 = 1.53$, $\gamma_2 = 3.38$, $L_X^*(0) = 10^{43.70}$, $k = 3.03$, $z_{cut} = 1.89$ and $\phi_X^* = 0.79 \times 10^{-6} \text{Mpc}^{-3}/(10^{44} \text{ergs}^{-1})$ for a cosmology with $q_0 = 0.0$ and $H_0 = 50 \text{ kms}^{-1} \text{Mpc}^{-1}$, the best fit of a PLE model would indicate that either a) short lived quasars are being produced at the same rate at all redshifts but with progressively lower luminosities at lower z , or b) quasars are long lived phenomena and have been dimming systematically since $z \sim 2$.

Observational findings that most bulges in the local universe contain a massive black hole (Magorrian et al. 1998) seem to refute the latter hypothesis since, in that case, only a fraction of galaxies would contain SMBHs. It therefore appears that almost every galaxy could have undergone an AGN phase at some point. Based on this empirical finding, Kormendy & Gebhardt (2001) suggest that SMBHs are mostly a bulge phenomena and were formed at the same time as the bulge component of galaxies; AGN would then trace the distribution of bulges in the Universe.

Another most interesting clue to understand the galaxy-AGN connection arises from the striking similarity between the evolution with redshift of the space density of bright AGN and the star formation history of the Universe. This strongly suggests that AGN and star formation are related phenomena, but the details of the actual links are again not known. It could be that AGN are fuelled by the same cold gas in the discs of galaxies that drives their star formation rate (SFR), in which case AGN would be less numerous in dense cluster regions, analogous to the SFR-density relation (e.g. Gómez et al. 2003; Dressler et al. 1985; Bower & Balogh 2004). Others (Gunn 1979; Shlosman et al. 1990) have proposed instead that galaxy-galaxy collisions fuel the AGN activity by driving gas into the cores of the galaxies. This would also enhance the star formation and possibly leave distorted morphologies in the AGN host galaxies.

As we see, despite being fundamental to comprehend the circumstances of galaxies at different epochs, the AGN phenomenon continues to elude understanding. To constrain models of galaxy formation and evolution, formation and growth of the black hole and behaviour of accretion processes and rates (which govern luminosities and spectral energy distributions) with cosmic time, it is important to determine any systematic correlations between the several properties of galaxies and AGN: a) photometry (luminosity function, space density); b) morphology (shape, concentration, structure); c) redshift; d) star formation rate; e) spectroscopy (line

spectra); f) colourimetry (spectral energy distributions); g) environment; *etc.*

Valuable progress has been attained in recent years and some of these issues have been now partially addressed. Spectral variability analyses have placed limits on the masses of nuclear black holes (Nikolajuk et al. 2004); clustering analyses, on their active life-times (Martini & Weinberg 2001). Deep imaging of host galaxies and studies of galaxy/AGN clustering environments are also increasing our knowledge of the relations between them. These advances have been possible with the availability of large homogeneous optical surveys (such as the 2QZ or SDSS) and, crucially, with the advent of large and accurate x-ray observatories with imaging and spectroscopic capabilities comparable to optical telescopes. This is especially important since, whilst studies based on optical properties of galaxies systematically miss a large fraction of AGN (those obscured by dust), which complicates evolution studies, most of the active galaxy forms are more readily identified from x-ray observations. This is also reflected on the fact that, with current technologies, the sky density of x-ray selected AGN is considerably larger than that of optically selected objects (by a factor of ~ 10 ; Alexander et al. 2003).

1.2 X-ray Astronomy

Invariably linked to the presence of hot gas and high energy particles, x-rays are emitted in a broad range of physical conditions in the Universe, being particularly conspicuous around violent explosions and strong electromagnetic & gravitational fields. Numerous objects characterised by processes at these high energies have been discovered and studied in this light over the last forty years: neutron stars, hot plasmas, active galactic nuclei, supernovae & their remnants, galaxy clusters, black hole candidates, stellar coronae, *etc.* In some cases, such as the physics of black hole neighbourhoods, of neutron stars and of hot intergalactic gas, most exploration is essentially undertaken from x-ray observations.

X-ray astronomy started about half a century after some of the most important physical x-ray studies were completed, such as x-ray diffraction by Laue and Bragg, x-ray scattering by Barkla or x-ray spectroscopy of atoms by Siegbahn, all of which took place in the 1910–1925 period. The basic reason for this slow start being the effective absorption by the Earth's atmosphere of x-rays from the Universe, astronomers had to wait until aeronautics was mature enough as to send rockets at considerable altitude (~ 35 km for 30 keV photons, ~ 80 km for 3 keV photons). The first such rockets detected x-rays from the Sun (Friedman et al. 1951) and subsequent research was concentrated towards solar studies. In one of these studies, while trying to detect fluorescent x-rays from the lunar surface generated by solar x-rays, Giacconi et al. (1962) discovered the first extrasolar x-ray source, Scorpius X-1, and a homogeneous extended background which seemed to be of extragalactic origin, thus effectively opening the field of x-ray astronomy (figure 1.2 on the next page). The discovery of entirely new and unexpected types

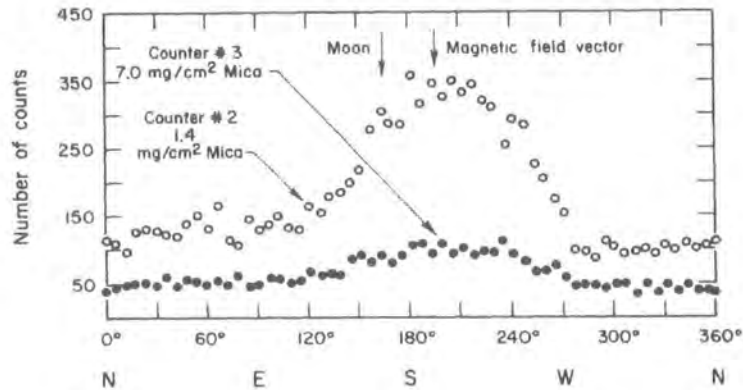


Figure 1.2: Recorded counts from two Geiger counters of the payload of the Aerobee rocket used by Giacconi et al. (1962). The results imply the presence of an x-ray source different from the Moon and of a cosmic background radiation.

of sources, such as Scorpius X-1, emitting thousands of times more energy in x-rays than in the visible light, and the Crab nebula, outputting 10^{10} more energy in x-rays than the Sun, stimulated a strong interest in it.

The development of new types of detector and superior mirror technology, coupled with advances in astronautics, lead the progress in the field. To increase the few minutes of observing time admitted by x-ray rocket missions and the spectral sensitivity range of balloon experiments (only useful for energies above ~ 20 keV, where many sources are weak), Uhuru⁴, the first orbiting x-ray observatory, was launched from Italy's San Marco station in Kenya on 12th December 1970, coinciding with the independence day of this country. The Uhuru payload weighted less than 60 kg and had two sets of proportional counters with a collecting area of as much as 840 cm^2 . For over two years it scanned the sky and produced the first all-sky catalogue of x-ray sources, containing a few hundred of them, reaching intensities of about $1/1000$ of that of the Crab nebula. A large number of x-ray binary stars with compact components was discovered in the galactic plane, together with supernova remnants and other diffuse structures. Outside the galactic plane, most of the sources were AGN and clusters of galaxies (Gursky et al. 1972). This is the picture that, roughly, still describes the present knowledge of the x-ray Universe.

Uhuru and other primaeval x-ray satellites (Ariel-V, HEAO-1, Ginga⁵, etc.) featured no optical systems: directional information was difficult to obtain and the opening angle of these primitive x-ray telescopes was defined by a simple mechanical collimating mask to limit the field-of-view (FOV) covered by the detectors (in most cases gas-filled proportional counters), which yielded low angular resolutions. The implementation of proper focusing x-ray optics capabilities were developed for the first time for the HEAO-2 (renamed to Einstein after successfully

⁴Meaning *freedom* in Swahili.

⁵Meaning *Milky Way* in Japanese.

launched) for soft x-rays (< 4.5 keV), and proved a crucial step in order to image the x-ray sky. Einstein's 2'' High Resolution Imager and sensitive spectrometers made possible to map extended objects such as supernova remnants and intracluster gas in galaxy clusters in detail, and produced large catalogues of x-ray sources that were subsequently employed to conduct detailed astrophysical studies. Amongst other highlights, it demonstrated that quasars emit x-rays and that distant such sources contribute strongly to the diffuse background (Giacconi et al. 1979).

The Röntgen Observatory Satellite, known as ROSAT (Truemper 1990), provided the first high resolution images of the soft 0.1–2.4 keV x-ray sky. It increased our knowledge by conducting first an all-sky survey (this yielded the, so far, largest catalogue of x-ray sources, exceeding 50000) and, for almost a decade, targeted observations of a full range of astronomical objects, from solar system neighbours such as comets or the Moon, to distant QSOs. Launched in 1993, ASCA, the Advanced Satellite for Cosmology and Astrophysics (Tanaka et al. 1994), opened the doors to 2–10 keV imaging and to the CCDs with two Solid-state Imaging Spectrometers (Burke & Daniels 1991) with sensitivities of $\sim 10^{-14} \text{ erg cm}^{-2} \text{ s}^{-1}$ (Einstein carried the first semi-conductor detector—a forerunner to today's CCDs—the Solid State Spectrometer). It enabled spectroscopic observations of faint x-ray sources with unprecedented sensitivity and medium resolution imaging in the hard x-ray band. BeppoSAX, launched in April 1996 (Boella et al. 1997), offered a wide spectral coverage, from 0.1 to 200 keV, as well as imaging capabilities below 10 keV. It allowed for thorough studies in harder bands than those available with ROSAT.

Golden Era of X-ray Astronomy

The launch of Chandra and XMM-Newton observatories in July and December of 1999 respectively, almost forty years after the detection of the first extragalactic x-rays, has seen x-ray astronomy reach full maturity. Chandra's superb subarcsecond spatial resolution and XMM's unprecedented throughput have made a reality the promise of large x-ray telescopes with high spectral and spatial resolutions.

Chandra (previously known as the Advanced X-ray Astrophysics Facility, AXAF), has an imaging capability in 0.4–8 keV x-rays comparable to that currently possible with ground-based optical telescopes. The X-ray Multi-Mirror Mission, XMM, which has three x-ray telescope modules, each containing 58 nested concentric mirrors, provides unprecedented collecting area for high resolution spectroscopy of faint sources, combined with good spatial resolution ($\sim 3''$) from 0.1–12 keV over a 30' diameter field-of-view. These two observatories have played a fundamental role in our work. Chandra in particular, provided the first observations and the sources that it detected constitute the skeleton around which this thesis is built. XMM has been used in the XMM-Newton/2dF Survey, a complementary study in the same regions, reaching shallower flux limits and wider in areal coverage (Georgakakis et al. 2004).

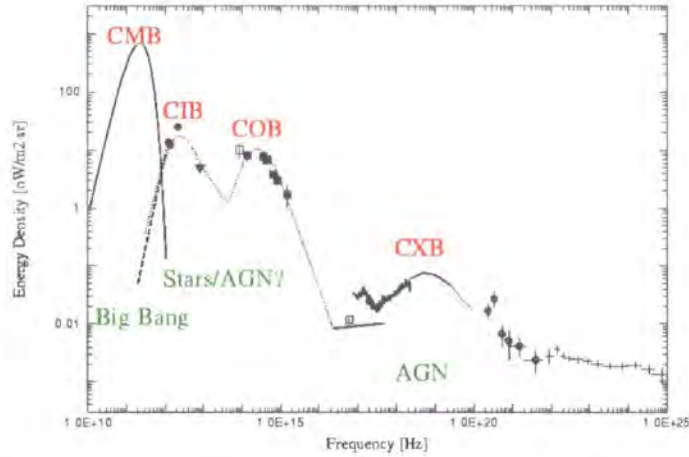


Figure 1.3: The cosmic energy density spectrum, from the radio band to γ -rays in a ν/ν representation, where a horizontal line represents equal energy per decade of frequency. The extragalactic background radiation gives a fossil record of all radiation processes in the Universe, integrated over cosmic time. The distinct components correspond to the cosmic microwave background (CMB), the cosmic far infrared background (CIB), the cosmic optical/ultraviolet background (COB) and the cosmic x-ray background (CXB). The CXB is energetically not the strongest (the CMB clearly dominates the energetic budget of the Universe) but it is nevertheless interesting since it is where active black holes in galactic nuclei radiate. So much so, that x-rays are the most efficient domain to detect QSO and AGN, with 10 times the optical sky density. Note that the CXB extends over four decades of wavelength, which should be borne in mind whenever considering models for the CXB based on data from only a small part of its spectrum. From Hasinger (2000).

1.3 The X-ray Background

The first diffuse cosmic background ever reported (Giacconi et al. 1962; figure 1.2), the x-ray background (XRB) dominates the sky energy density from ~ 100 eV to gamma-rays above 1 MeV (see figure 1.3).

The origin of its different components is a matter which is still being explored; it is not yet clear whether they originate in separate classes of objects or in separate physical mechanisms. x-ray background population synthesis models have been successfully used to account for the XRB intensity in the range of 1–100 keV in terms of a population of obscured AGN (Madau et al. 1994; Comastri et al. 1995; Gunn 1999). Recent deep Chandra and XMM-Newton observations have resolved $\sim 85\%$ of the 0.5–10 keV background into individual sources and the large numbers of AGN amongst them favours these models (e.g. Hornschemeier et al. 2000; Giacconi et al. 2001; the present work, § 4.3). Nevertheless, over half of its frequency range in logarithmic space remains unexplained.

Over the following few pages we review its major characteristics.

1.3.1 Spectral Properties

Galactic emission, possibly emerging from a hot local bubble ($T \sim 10^6$ K; McCammon & Sanders 1990), accounts for most of the background below ~ 0.5 keV. At these energies, extragalactic contributions are minimised by interstellar absorption, which prevents a large fraction of any cosmological contribution from being observed. This is in stark contrast with the XRB above 0.5 keV, which is mainly of extragalactic origin, and hence the $\lesssim 0.5$ keV XRB will be left aside in the remainder of this thesis.

The spectral band from 0.5 to 3 keV has been thoroughly studied with the first generation of imaging x-ray telescopes. Deep ROSAT surveys resolved $\sim 70\%$ of it into discrete sources, most of them QSOs at redshifts $z \gtrsim 1$ (Hasinger et al. 1998; Boyle et al. 1994). These are primarily steep spectrum sources, which are responsible for a soft excess in this band as compared with the 3–15 keV range (Garmire & Nousek 1980; Wu et al. 1991; Shanks et al. 1991). This makes the 0.5–3 keV spectrum well approximated by a power-law with energy spectral index 0.8 ± 0.2 .

The HEAO-1 A2 and A4 experiments measured the 3 keV to 6 MeV band. Marshall et al. (1980) find that the 3–45 keV range is excellently fit by a ~ 40 keV thermal Bremsstrahlung model. Gruber (1992) analytically fits the 3–60 keV measurements with

$$I(\epsilon) = 7.877\epsilon^{-0.29} e^{\frac{-\epsilon}{41.13 \text{ keV}}} \text{ keV s}^{-1} \text{ sr}^{-1} \text{ cm}^{-2} \text{ keV}^{-1}$$

and the 60 keV to 6 MeV with a double power law:

$$I(\epsilon) = 1652\epsilon^{-2.0} + 1.754\epsilon^{-0.70} \text{ keV s}^{-1} \text{ sr}^{-1} \text{ cm}^{-2} \text{ keV}^{-1}.$$

Below ~ 100 keV the uncertainties in these fits amount to 2%. Over the 3–15 keV band in particular, which is roughly where Chandra and XMM operate, an excellent fit is also provided by a power law $I(\epsilon) \propto \epsilon^{-\alpha}$ with energy spectral index $\alpha = 0.4$ (Gendreau et al. 1995; Chen et al. 1997). Figure 1.4 on the next page shows the intensity spectrum of the XRB.

In terms of energy density, most of it is contained between 20 and 40 keV, as can be seen from figure 1.3. The 0.5–10 keV Chandra band contains $\sim 25\%$ of the total energy of the XRB (with the 0.5–2 keV range contributing just a few percent).

1.3.2 Isotropy

Above 3 keV, the XRB is isotropic to within a few percent on large scales, once the Galaxy and a weak large-scale anisotropy are removed (Warwick et al. 1980; Iwan et al. 1982; Schwartz & Gursky 1974). The latter contamination, significantly weaker than the former, is consistent with the Compton-Getting effect due to the motion of the Milky Way with respect to the cosmic microwave background (CMB)

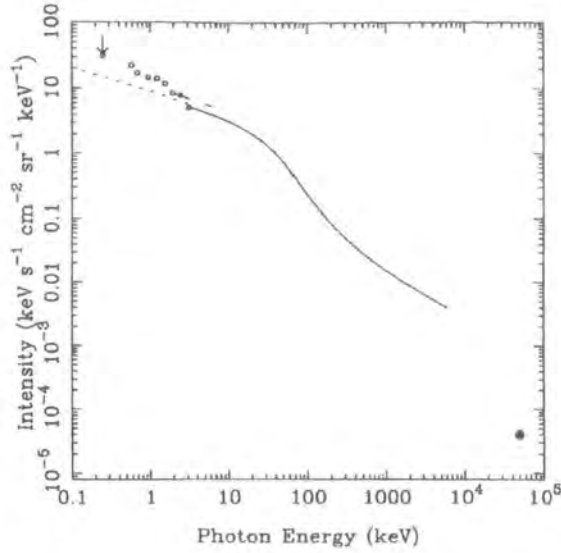


Figure 1.4: The XRB intensity spectrum I_ϵ , from Fabian & Barcons (1992). In the 2–10 keV range, the XRB measurements can be fit by a power law of the form $P(\epsilon) \equiv \frac{N}{\epsilon} = A\epsilon^{-\Gamma}$, where $P(\epsilon)$ is the photon intensity, ϵ is the energy and the photon index has a value of $\Gamma = 1.4$.

as measured from the CMB dipole (Shafer 1983). The inferred direction in the 2–10 keV band for the XRB dipole is $l = 280^\circ$, $b = 30^\circ$, with velocity $475 \pm 165 \text{ km s}^{-1}$, roughly consistent with the CMB dipole. The isotropy and the dipole radiation field observed on the largest scales are strongly suggestive of a distant extragalactic origin of the $\gtrsim 3$ keV XRB. The extragalactic nature has been confirmed, not only by the wealth of extragalactic sources detected as contributors, but also by the observation by Barber et al. (1996) that the nearby spiral galaxy NGC55 casts a shadow on the soft x-ray background. The isotropy is also suggestive that, at large scales ($\gtrsim 100$ Mpc), the Universe is isotropic.

On small angular scales, such as those available with Chandra and XMM small fields of view, large scale structure studies are difficult due to counting statistics uncertainties and from the small distances probed perpendicular to the line of sight (Chandra’s ACIS-I $16' \times 16'$ correspond roughly to an area $4 \times 4 \text{ Mpc}^2$ at $z = 1$). Nevertheless, intrinsic sky fluctuations attributable to the lumpiness of the x-ray sources can always be found (“cosmic variance”); the auto-correlation function of the XRB on those scales is dominated, then, by the spread of the clustering of QSOs, galaxies and clusters of galaxies.

1.3.3 Source Content

The extragalactic source content of the x-ray background has been a major unsettled issue of x-ray astronomy for four decades now. The facts that it has a spectrum that fits remarkably well a 40 keV Bremsstrahlung radiation over the

range 3–45 keV (Marshall et al. 1980) stimulated the controversy over whether the XRB had its origin in a thermal free-free emission from an optically thin intergalactic plasma (Cowsik & Kobetich 1972; Field & Perrenod 1977; Hoyle 1963) or if it was instead the result of the integrated emission from individual faint sources emitting over cosmic times.

In the beginning of the 1990s the debate settled in favour of the discrete source origin of the XRB due to the FIRAS instrument aboard COBE not detecting a predicted strong Compton distortion of the spectrum of the cosmic microwave background, were diffuse thermal emission to be responsible for a substantial fraction of the XRB (Mather et al. 1990; Barcons et al. 1991; Wright et al. 1994). At about the same time, Shanks et al. (1991), in consonance with previous Einstein surveys (Giacconi et al. 1979; Griffiths et al. 1983; Maccacaro et al. 1988), reported from a ROSAT study that a major percentage of the intensity of the soft 0.1–2 keV XRB was due to unobscured quasars. By the end of the decade about 60–80% of the XRB intensity in the 0.5–2 keV band had been resolved, to a limiting flux of $\sim 10^{-15} \text{ erg cm}^{-2} \text{ s}^{-1}$, into discrete sources, most of them broad-line AGN at $z > 1$ (Hasinger et al. 1998; Schmidt et al. 1998; Boyle et al. 1994). Given that the steep spectra of QSOs produce an excess intensity in the soft band and contribute little to the flatter 3–300 keV XRB, the lack of observed flat-spectrum sources (*e.g.* type II AGN, starburst galaxies, *etc.*) left the question of what is the main component of the XRB still unanswered.

At harder energies, first results that resolved $\sim 30\%$ of the XRB_{2–10 keV} into faint discrete sources were obtained at flux levels of a few $10^{-14} \text{ erg cm}^{-2} \text{ s}^{-1}$ with ASCA (Inoue et al. 1996; Georgantopoulos et al. 1997; Ueda et al. 1999) and BeppoSAX (Cagnoni et al. 1998; Fiore et al. 1999). However, we have had to wait for the Chandra and XMM-Newton satellites to resolve the bulk of the hard XRB. In recent months, different teams (*e.g.* Mushotzky et al. 2000 in the SSA13; Hornschemeier et al. 2000 and Alexander et al. 2003 in the Hubble Deep Field North; Campana et al. 2001 in the Chandra Deep Field South) have published the results of their respective surveys and resolve $\sim 80\%$ of the hard XRB into point sources. The vast majority have been identified with obscured AGN. However, given the source fluctuations in the small Chandra field of view and the optical faintness of the sample, which complicates optical spectroscopic follow-up (50% have $i \gtrsim 23.5$), more surveys are mandatory to investigate issues as the origin of the x-ray emission in the whole sample, the host properties of the AGN found, *etc.*, so that we can finally obtain a self-consistent picture of the evolution of the sources over a wide range of x-ray fluxes. It is in this spirit that we undertook the Durham x-ray surveys.

[It is worth noting that clusters of galaxies cannot contribute significantly to the cosmological XRB. Their luminosity functions and their negative evolution with redshift (meaning that most luminous clusters are most numerous at the present epoch; Edge et al. 1990) are well quantified and an integration of their contribution to the 0.5–2 and 2–10 XRBs gives a result of ~ 10 and 3%, respectively (*e.g.* Fabian & Barcons 1992).]

1.4 The Durham X-ray Surveys

1.4.1 Motivation

The discovery that quasars emit x-rays and that distant such sources contribute strongly to the diffuse XRB (Giacconi et al. 1979) initially suggested that they could explain the whole XRB at 2 keV (Zamorani et al. 1981; Marshall et al. 1983). Although these results proved an overestimate, they promoted QSOs as the best candidates to explain the XRB.

Using optical multifibre spectroscopy and ROSAT observations centred on the ultraviolet excess (UVX) fields of Boyle et al. (1990), Shanks et al. (1991) pursued optimised identification of optical counterparts to many XRB sources. Their study revealed that over 50% of resolved x-ray sources corresponded to QSOs which, as a result, were responsible for $\sim 30\%$ of the XRB at 1 keV. Further observations led to an accurate determination of their x-ray luminosity function and evolution (Boyle et al. 1994) which, in turn, permitted extrapolation of the Shanks et al. result to faint fluxes and high redshifts. That suggested a maximum contribution of 50% of the XRB at 1 keV, unless the luminosity function steepened at the faint end. Georgantopoulos et al. (1996) assessed the number count behaviour of the QSO population and found that their $\log N$ vs. $\log S$ relationship undergoes an abrupt break at $\sim 10^{-14} \text{ erg cm}^{-2} \text{ s}^{-1}$, turning over to a power-law slope of $\gamma = 1.1 \pm 0.5$ at fainter limits from an Euclidean slope at the brightest fluxes.

Given that the contribution of the broad-line AGN population appeared to drop at faint fluxes and that they can contribute no more than $\sim 50\%$ of the total XRB, the emergence of a new x-ray source population seemed required (see Georgantopoulos et al. 1996 and 1993 for further QSO clustering constraints).

Spectral Paradox of the XRB

Apart from the constraints from luminosity function, number counts and clustering analyses, there has always been a major problem with the QSO population being a large contributor to the XRB, which stems from their spectral shape. Typical unobscured QSOs have steep spectra with $\Gamma \simeq 2$ (Turner & Pounds 1989) while the XRB spectrum below 15 keV is a good fit to a power-law slope of $\Gamma \simeq 1.4$ (Gendreau et al. 1995; Chen et al. 1997; see figure 1.4 for the intensity spectrum of the XRB).⁶ This “spectral paradox” (de Zotti et al. 1982) makes it more difficult to explain the XRB as more of it is understood in terms of QSOs since it becomes increasingly imperative to find new sources with flat enough spectra as to compensate the steepness introduced by QSOs.

Thus, it was soon understood that ordinary QSOs cannot comprise the whole XRB and that the new population had to have flat spectra at high 2–10 keV energies and

⁶ Γ is the photon index and relates the photon intensity and the energy of the photons as described in the caption of figure 1.4.

also at lower 0.5–2 keV energies but at faint fluxes ($S \lesssim 4 \cdot 10^{-15} \text{ erg cm}^{-2} \text{ s}^{-1}$). Solid evidence of this new population was found with ASCA when it was realised that 2–10 keV source number counts doubled ROSAT counts in the soft band (e.g. Georgantopoulos et al. 1998; see figure 2.14); a major fraction of these hard sources was identified with galaxies with optical narrow emission lines.

Narrow Emission-Line Galaxies

The earliest proof that optically faint galaxies could be important contributors to the XRB came from the studies of Jahoda et al. (1991) and Roche et al. (1995). Einstein observations revealed that most spiral galaxies have their x-ray emission linearly related to their blue band luminosity (e.g. Fabbiano et al. 1992), and these authors cross-correlated galaxy catalogues with deep ROSAT x-ray observations. Roche et al. found that $B < 21$ galaxies contribute to $\sim 5\%$ of the XRB. A more significant result was obtained cross-correlating fainter galaxies with deep ROSAT images of the unresolved XRB, which implied that red and blue $B < 23$ galaxies were responsible, with similar amplitude, for $\sim 23\%$ of the unresolved XRB at 1 keV (Almaini et al. 1997).

The discovery from deep ROSAT and ASCA observations of a new population of x-ray luminous narrow emission-line galaxies (NELGs) triggered a significant advance in our understanding of the nature of the origin of the hard and faint x-ray background (e.g. Griffiths et al. 1996; Romero-Colmenero et al. 1996; Hasinger 1996; Georgantopoulos et al. 1996). These NELGs seemed to belong to the high luminosity end of the “normal” galaxy distribution and are characterized by x-ray luminosities typically 50 times brighter than normal field galaxies, as well as a convenient hard x-ray spectrum, needed to solve the spectral paradox. However, several questions such as which are the dominant mechanisms for their x-ray emission or their host galaxy properties were ill-constrained and had to wait for the new generation observatories Chandra and XMM to be thoroughly addressed.

As for the dominant x-ray emission mechanism, it has been proposed that they could be evolved starburst galaxies in which x-ray emission comes from massive x-ray binaries (Griffiths & Padovani 1990). Indeed, it is known that galaxies undergoing bursts of star-forming activity show higher x-ray to optical flux ratios than normal galaxies (Fabbiano et al. 1984) and David et al. (1992) have suggested a two-component model in which x-ray emission in starbursts comes both from long-lived low mass x-ray binaries (as in more passive spiral galaxies) and also from short-lived high mass binaries and supernovae. It is the emission from the latter, which they find directly proportional to $60 \mu\text{m}$ far infrared emission, that traces the star formation rate. However, x-ray NELGs are more x-luminous than any known starburst galaxy, which in turn also fail to provide hard enough spectra to match the residual XRB. In particular, massive x-ray binary stars, although they have a similar spectral slope to the XRB, display a turnover at around 20 keV (White et al. 1983) which will shift to even lower energies for high redshift objects

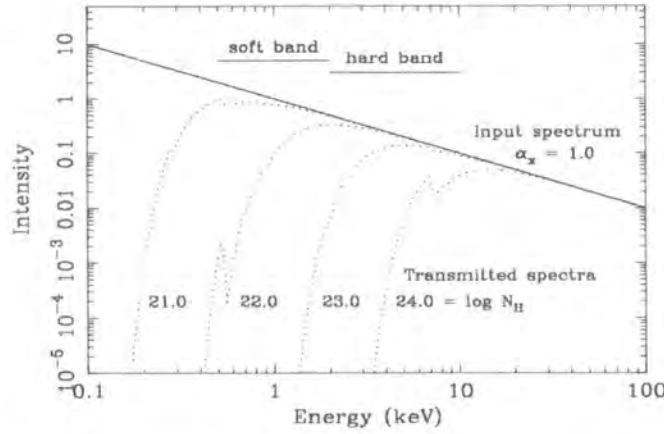


Figure 1.5: Absorption at x-ray energies for column densities of $N_H = 10^{21}$, 10^{22} , 10^{23} and 10^{24} cm^2 , derived using XSPEC. The incident spectrum is a power-law, $I \propto \nu^{-\alpha_x}$, with spectral index $\alpha_x = 1$. From Gunn (1999).

and are thus incapable to account for the residual XRB which must come from a much broader range of redshifts. At least two further observational arguments seem to argue against the starburst origin of most of the x-ray emission in these galaxies: first, Iwasawa et al. (1997) showed that infrared fluxes of these NELGs are generally too low for the x-ray emission to be entirely due to starforming activity; second, emission-line ratios allowed Boyle et al. (1995) to identify the brightest ROSAT NELGs as a mixture of starburst and Seyfert II galaxies.

Another popular explanation is that these galaxies contain a hidden AGN. In unified schemes for AGN (Antonucci 1993), x-ray emission can be absorbed and/or scattered. Photo-electric absorption flattens the intrinsic AGN x-ray spectrum by removing the lower energy photons, which has the overall effect of hardening the observed spectrum (figure 1.5). Such models have been successfully employed to explain the spectrum of the entire 2–100 keV XRB and it is found that at least $\sim 80\%$ of its intensity can be explained in terms of obscured and unobscured objects, with hiding by column densities in the range $10^{21} \lesssim N_H \lesssim 10^{25} \text{ cm}^{-2}$ affecting ~ 5 times more sources than $N_H \lesssim 10^{21} \text{ cm}^{-2}$ unobscured AGN (Madau et al. 1994; Comastri et al. 1995; Gunn 1999; see figure 1.6 on the next page).

Starbursts and AGN need not be independent phenomena. In fact, there is a wealth of observations which indicate that in some cases they are closely related. Amongst the most significant, the similitude between the star formation history of the Universe (Madau et al. 1996) and the luminosity evolution of bright AGN (Boyle et al. 1994) or the discovery of obscured AGN surrounded by starburst regions (Iwasawa et al. 1997; Boyle et al. 1995). This makes it plausible that their x-ray emission results from various degrees of importance of the two phenomena combined together. The relative contribution of each one of them in such hybrid model is, however, undetermined.

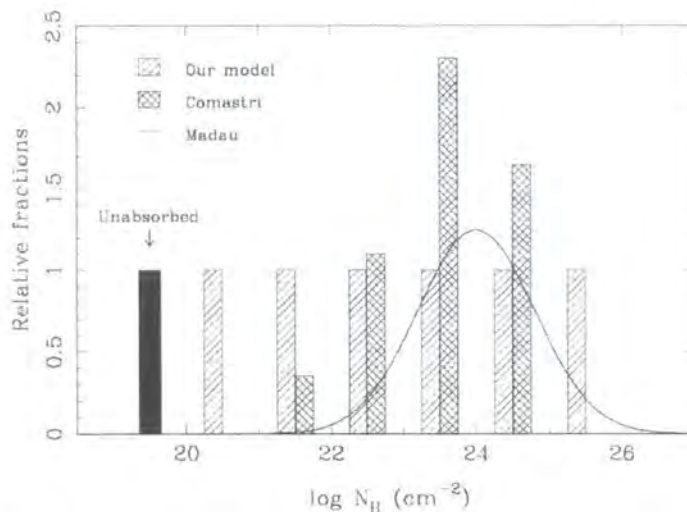


Figure 1.6: Comparison of different distributions of column densities in AGN populations used by various authors. Each is scaled to the same amount of unobscured objects (shown here at $N_H = 10^{19.5} \text{ cm}^{-2}$) and overlaid as a solid box. Gunn (1999)’s model of a flat distribution of columns is shown as hatched regions; the Comastri et al. (1995) model is shown as cross-hatched regions; these two models are shown slightly offset from one another for clarity. The Madau et al. (1994) model is shown as the solid line describing a Gaussian distribution. From Gunn (1999).

The present thesis has, as its major starting point, the aim to establish if x-ray luminous NELGs are the sources that are the major contributors to the hard XRB, along with finding an explanation for their dominant x-ray emission mechanisms. We build a case for a hidden AGN as the most likely explanation for such emission and, while NELG galaxies are indeed found to be major contributors to the hard XRB, they are so as the nearby representatives of a major class of obscured AGN, most of which is too faint for probing with current spectroscopic facilities and appear either as “normal” galaxies or as blank fields in optical observations (§ 4.1 and 4.2). In particular, we find no evidence of significant contribution from starbursts to the XRB intensity.

1.4.2 The WHDF & 10×10 ks Chandra Surveys

For this work we have been observing and identifying serendipitous x-ray hard and soft sources found in three fields with Chandra as a means to study the origin of the hard XRB, the nature of x-ray emitting galaxies and x-ray faint sources in general.

Surveys above 2 keV have been undertaken by previous x-ray missions, but sensitivity and spatial resolution limits have always restricted their completeness. Uhuru (Forman et al. 1978), Ariel V (McHardy et al. 1981), HEAO-1 (Piccinotti et al. 1982) and Ginga (Kondo et al. 1992) boarded collimator-type detectors instead of

imaging instruments and source confusion is significant with such technologies. Their sensitivity limits ($\sim 10^{-11} \text{ erg cm}^{-2} \text{ s}^{-1}$ in the canonical 2–10 keV band) allowed to detect sources that account for $\sim 3\%$ of the hard XRB. And most being identified with bright unobscured AGN, which had a spectral slope much steeper than that of the XRB and hence could not contribute to the bulk of the hard XRB. Better results already indicating the emergence of a faint, hard, x-ray population were obtained with ASCA and BeppoSAX, which resolved $\sim 30\%$ of the $\text{XRB}_{2-10 \text{ keV}}$ into discrete sources at flux levels of a few $10^{-14} \text{ erg cm}^{-2} \text{ s}^{-1}$ (Inoue et al. 1996; Ueda et al. 1999; Georgantopoulos et al. 1997; Cagnoni et al. 1998; Fiore et al. 1999). However, the sources contributing the bulk of the 2–8 keV XRB were not found prior to the launch of Chandra and XMM-Newton.

GSGP4 & F864 Fields

Chandra targeted the GSGP4 and F864 extragalactic fields to build upon older studies of shallower and wider areas in the Deep ROSAT Survey (Shanks et al. 1991). Since QSOs were deemed very important x-ray emitters, the original ROSAT observations of these two fields were centred on two ultraviolet excess (UVX) QSO fields of Boyle et al. (1990) and Boyle et al. (1991), respectively. This enabled a prompt identification of QSOs as optical counterparts to many x-ray sources. Further spectroscopic follow-up revealed that QSOs account for 30–50% of the XRB at 1 keV (Boyle et al. 1994). ASCA observations in the 2–8 keV band in these fields showed the existence of a population of hard sources emerging at faint fluxes (Georgantopoulos et al. 1997).

In November–December 2000 we undertook a wide solid angle, intermediately deep, x-ray survey of the GSGP4 and F864 fields. Chandra instrument ACIS-S was employed to follow seven subregions in GSGP4 and an extra three in F864 for ~ 10 ks each (hence the name “ 10×10 ks” by which these surveys will be collectively called in this thesis; see table 2.1 for the journal of the observations). The ten pointings cover an effective solid angle of just over a square degree and reach a sensitivity depth of $3 \cdot 10^{-15} \text{ erg cm}^{-2} \text{ s}^{-1}$ in the 0.5–2 keV soft band and of $1 \cdot 10^{-14} \text{ erg cm}^{-2} \text{ s}^{-1}$ in the 2–10 keV hard band. However, due to degrading effects off the aiming point (see § 2.1.2), we decided to make use of the full data in the S3 chip only, complementing it with individual conspicuous sources in neighbouring chips. This action reduces the actual survey area in our analyses to $\sim 0.2 \text{ deg}^2$.

These exposures represent a compromise between studying a faint population highly relevant to the hard XRB and, by surveying a large area, minimising the cosmic variance due to the discrete nature of the XRB and to Chandra’s tiny field of view (which produced about 40% spread in the normalisations of different fields; cf. § 2.4.2 and Cowie et al. 2002). Indeed, the 2–10 keV source counts turn over around $10^{-14} \text{ erg cm}^{-2} \text{ s}^{-1}$ and therefore source numbers are maximised per unit exposure time in short, 5–20 ks, exposures like our own. This survey in the hard band is therefore designed to fill a gap at intermediate fluxes between deeper

Field	U (u)	B (b)	R (r)	I (i)	Z (z)	H	K
WHDF central	27	28.2	26.5	25.5	-	23	20
WHDF extended	-	26	26	24	23	-	-
F864	(22)	26.3 (22.2)	25.7 (22.2)	(21.3)	(20.5)	-	-
GSGP4	-	25	24.5	23.5	-	-	-

Table 1.1: Summary of the photometric limits of the surveyed fields.

and narrower Chandra and XMM observations and shallower BeppoSAX and ASCA surveys.

As well as the availability of several x-ray observations with previous observatories which allow for comparisons and variability studies (see § 2.3.1, for instance), the 10×10 ks survey has the advantage of high quality follow-up optical spectroscopic and photometric observations. Apart from our own campaigns, the GSGP4 and F864 fields overlap with the two largest observational programs ever undertaken in optical wavelengths: the Sloan Digital Sky Survey (SDSS,⁷ York et al. 2000) and the 2dF Galaxy and Quasar redshift surveys (2dFGRS,⁸ Colless et al. 2001; and 2QZ,⁹ Croom et al. 2001, respectively), which provide an unprecedented spectroscopic and photometric database which we exploit to full advantage. The SDSS is a major imaging and spectroscopic ongoing effort to provide 10^6 spectra and cover 10^5 deg^2 of the sky in the five u , g , r , i , z bands down to $g \sim 23$ magnitude, thus providing a uniform and homogeneous multi-colour catalogue (Fukugita et al. 1996; Stoughton et al. 2002). The 2dF redshift surveys, completed in July 2003, are two integrated major spectroscopic efforts that exploited the capabilities of the 2dF multi-fibre spectrograph on the 3.9 m Anglo-Australian Telescope (AAT) to obtain spectra for a quarter million objects over an area of approximately fifteen hundred square degrees. Table 1.1 summarises the photometric coverage in our surveys; for the full relevant details regarding follow-up observations the reader is referred to chapter 3.

WHDF

To complement the 10×10 ks surveys and probe deeper into fainter fluxes, where most of the XRB is produced, we conducted in December 2000 a single moderately deep 75 ks observation of the *William Herschel Deep Field* (WHDF) with Chandra's ACIS-I detector. The observation reaches fluxes of $4 \cdot 10^{-16} \text{ erg cm}^{-2} \text{ s}^{-1}$ in the soft 0.5–2 keV band, $3 \cdot 10^{-15} \text{ erg cm}^{-2} \text{ s}^{-1}$ in the hard 2–8 keV band and $1 \cdot 10^{-15} \text{ erg cm}^{-2} \text{ s}^{-1}$ in the total 0.5–8 keV band, and resolves over $\sim 70\%$ of the hard XRB (§ 2.4.3).

A few ultradeep observations, such as the 2 mega-second CDF-N survey, have essentially resolved the XRB in the 2–8 keV band down to $1.4 \times 10^{-16} \text{ erg cm}^{-2} \text{ s}^{-1}$

⁷<http://www.sdss.org>

⁸<http://msowww.anu.edu.au/2dFGRS/>

⁹<http://www.2dfquasar.org>



Figure 1.7: Central $7' \times 7'$ Herschel Deep Field true colour image, formed by mapping U , B and R images into blue, green and red respectively. Photometry reaches $B_{3\sigma} = 28.2$ at its deepest.

(Alexander et al. 2003). These studies provide an excellent chance to find the greatest numbers of sources that contribute, at any rate, to the xrb. However, given that the cumulative counts quickly flatten at fluxes fainter than $\sim 10^{-14} \text{ erg cm}^{-2} \text{ s}^{-1}$ it is the 70–300 ks x-ray surveys like this one in the WHDF that are finding most of the hard x-ray sources that contribute to the bulk of the background. The study of these sources will constrain the nature of most of the sources of the xrb at these energies.

The WHDF is particularly well-suited for these analyses. It is a high galactic latitude field, which maximises extragalactic detections, and its location in the constellation of *Pisces* in the celestial equator makes it a feasible target from observatories in both hemispheres. It has been the subject of an extensive observing campaign from optical to infrared wavelengths, reaching depths of $U \sim 27$, $B \sim 28$, $R \sim I \sim 26$, $H \sim 22.5$ and $K \sim 20$ over 50 arcmin^2 (Metcalf et al. 2001; McCracken et al. 2000). To match the ACIS-I exposure, it has recently been extended to a $16 \times 16 \text{ arcmin}^2$ area in the B ($\lesssim 26$), R ($\lesssim 26$), I ($\lesssim 24$) and Z ($\lesssim 23$) bands (table 1.1).

1.5 Summary

A fundamental goal of observational cosmology is to elucidate the relationships between galaxies and AGN, of utmost relevance for large scale structure formation. These are most evident in the black hole–galactic bulge relationships ($M_{\text{bulge}} : M_{\bullet} : \sigma_{\star}$) in the local universe reported by Magorrian et al. (1998) and further studied by Ferrarese & Merritt (2000), and also in the similar AGN space density and star formation histories of the Universe.

While studies based on optical properties of galaxies miss a large fraction of AGN, better datasets can be obtained from x-ray surveys. Hard x-rays are able to penetrate the thick nebulae and, on the grounds that AGN contain massive black holes in the centres of galaxies which are powered by accretion processes and are surrounded by dense clouds of gas and dust, observations in these wavelengths reach highly obscured AGN which are otherwise absent in optical images.

We have undertaken two x-ray surveys amounting to 175 ks of Chandra observation in the WHDF, GSGP4 and F864, three high latitude extragalactic fields with sufficiently low Galactic neutral hydrogen column densities as to maximise visibility of extragalactic sources and minimise contamination by Galactic stars and hot gas above ~ 0.3 keV. These observations, complemented with a strong optical follow-up program, aim at providing new constraints on our understanding of galaxy and AGN evolution by investigating the sources that contribute most to the x-ray background. The origin of the XRB, particularly at hard energies, has been an active subject of research for over 40 years and, despite that Chandra and XMM-Newton have resolved most of it into individual sources, their nature remains largely a mystery. This is in good measure a result of the difficulty to pursue optical spectroscopic follow-up for about half of the samples, where obscuration renders the objects very faint. Nevertheless, it is hard to overstate the importance of the (> 2 keV) XRB as a probe of black hole evolution.

Observationally, it seems now well established that the cosmic background at x-ray regimes is largely due to accretion onto SMBH integrated over cosmic times and that it therefore accounts for the integrated x-ray emission from all objects and processes in the Universe since it was about a billion years old ($0 \lesssim z \lesssim 10$). At soft energies it is dominated by AGN, most of which are type I Seyferts and QSOs. At hard energies, a population of flat-spectrum sources at faint fluxes are responsible for a major fraction of the background. Although several type II AGN have been identified amongst this population and they seem to be the dominant contributors, the relative importance of the contribution from star formation is still ill-constrained. Dilucidating this question is important from several fronts. For one thing it would provide new handles on our understanding of the links between AGN and star formation. More immediately, though, it would help clarify the fraction of obscured (be it for weak emission lines or obscured by dust in the optical or absorption by gas in the x-rays) to unobscured AGN in the Universe at

different epochs. This is a crucial question risen from XRB population synthesis models which needs to be confronted and, clearly, the most advantageous tools we have are surveys of the x-ray background.

This thesis presents work which is largely motivated by all of these issues. It is organised as follows. Chapter 2 describes the x-ray data and their analysis, including the generation of the catalogues, source number count, spectral and introductory variability studies (§ 2.2.3, 2.4, 2.5 and 2.3, respectively). Chapter 3 is concerned with the optical follow-up: imaging and spectroscopic data acquisition and reduction. In chapter 4 we combine the data and results from the two preceding chapters to classify the sources into different categories and discuss the origin of their x-ray emission (§ 4.1), the properties of x-ray galaxies (§ 4.2), the XRB population synthesis models (§ 4.3), *etc.* This chapter is complemented with a study of the evolutionary properties of early-type galaxies (§ 5). Finally, in chapter 6 we summarise the main conclusions of this work.

CHAPTER II

X-ray Data

... and all that jazz.

X-ray astronomy bade farewell to the last millennium in full swing. The launch in 1999 of two excellent x-ray facilities, Chandra and XMM-Newton, has brought what many astronomers already call the *golden age* of x-rays. They have provided an unsuspected wealth of high quality data and, complementary as they are, truly revolutionised the field.

We have undertaken with Chandra two x-ray surveys of the cosmic x-ray background in three different extragalactic regions of the sky, to investigate the nature of the hard and soft sources that are serendipitously detected at faint fluxes. Ten observations of 10 ks each have been conducted in fields GSGP4, in the south galactic pole, and F864, in the north galactic cap. A further single 75 ks observation has been undertaken on the *Herschel Deep Field*, on the celestial equator. In total, 140 sources down to hard band fluxes of $3 \cdot 10^{-15} \text{ erg cm}^{-2} \text{ s}^{-1}$ ($S/N \geq 3$) have been detected in the combined datasets.

The present chapter is concerned with this data. We start reviewing the main characteristics of the instrumentation involved (§ 2.1). Then, section 2.2 describes the procedures related to the reduction of the data, the detection of sources and it also presents the catalogues of the main x-ray properties for the samples. In section 2.3 we give a brief account of variability issues of the x-ray sources detected. We proceed in section 2.4 with a discussion of the source number counts *versus* flux relation in some of its most notable forms: we calculate the available area of the survey as a function of flux in order to compute the cumulative and differential source counts, which are compared to other surveys. In this section we also show that the sources in the WHDF account for $\gtrsim 70\%$ of the hard XRB, with the major uncertainty coming from the dispersion on its normalisation. Finally, we close this chapter with a review of the x-ray spectral properties of the detected sources, confirming the solution of the “spectral paradox” of the XRB and noting the existence of a bright hard population which contributes appreciably to the background (§ 2.5).

CHAPTER II

X-ray Data

... and all that jazz.

X-ray astronomy bade farewell to the last millennium in full swing. The launch in 1999 of two excellent x-ray facilities, Chandra and XMM-Newton, has brought what many astronomers already call the *golden age* of x-rays. They have provided an unsuspected wealth of high quality data and, complementary as they are, truly revolutionised the field.

We have undertaken with Chandra two x-ray surveys of the cosmic x-ray background in three different extragalactic regions of the sky, to investigate the nature of the hard and soft sources that are serendipitously detected at faint fluxes. Ten observations of 10 ks each have been conducted in fields GSGP4, in the south galactic pole, and F864, in the north galactic cap. A further single 75 ks observation has been undertaken on the *Herschel Deep Field*, on the celestial equator. In total, 140 sources down to hard band fluxes of $3 \cdot 10^{-15} \text{ erg cm}^{-2} \text{ s}^{-1}$ ($S/N \geq 3$) have been detected in the combined datasets.

The present chapter is concerned with this data. We start reviewing the main characteristics of the instrumentation involved (§ 2.1). Then, section 2.2 describes the procedures related to the reduction of the data, the detection of sources and it also presents the catalogues of the main x-ray properties for the samples. In section 2.3 we give a brief account of variability issues of the x-ray sources detected. We proceed in section 2.4 with a discussion of the source number counts *versus* flux relation in some of its most notable forms: we calculate the available area of the survey as a function of flux in order to compute the cumulative and differential source counts, which are compared to other surveys. In this section we also show that the sources in the WHDF account for $\gtrsim 70\%$ of the hard XRB, with the major uncertainty coming from the dispersion on its normalisation. Finally, we close this chapter with a review of the x-ray spectral properties of the detected sources, confirming the solution of the “spectral paradox” of the XRB and noting the existence of a bright hard population which contributes appreciably to the background (§ 2.5).

2.1 The Chandra X-ray Observatory

After considerable delay and major restructuring, the Chandra x-ray Observatory (CXO; Weisskopf et al. 2000 and 1996) was finally launched by NASA on July 23, 1999, into a highly elliptical orbit. As the satellite spends about 80% of the time above the van Allen radiation belts, this allows for reasonably high observing efficiency; its orbiting period of ~ 64 hours means that continued observations of up to ~ 175 ks are possible.

Of interest to us, Chandra's principal scientific elements are the High Resolution Mirror Assembly (HRMA) and the on-axis scientific instruments. These will be reviewed and contextualised in the following pages.

2.1.1 Focusing X-rays

The construction of imaging x-ray optics is a difficult problem which was pioneered in the middle of the last century at the construction of x-ray microscopes by H. A. Kirkpatrick, A. V. Baez and H. Wolter. The weak refraction, with a refraction index slightly smaller than 1, suggests optical systems where total reflection is achieved by approaching incidence at grazing angles (Compton 1923). To overcome the astigmatism inherent in any single mirror system (Jentsch 1929), Wolter showed in 1952 that an image over an extended field of view can be formed by glancing reflections off a combination of a paraboloid and either a hyperboloid or an ellipsoid coaxial and confocal mirrors. The simplest of these design, known as Wolter type I and shown in figure 2.1, allows for several nested mirrors so that the effective area of the telescope is increased many-fold. For this reason it is a favourite design of astronomical x-ray telescopes and is also featured in Chandra.

The High Resolution Mirror Assembly (HRMA) consists of a nested set of four concentric thin-walled, iridium-coated, mirror pairs reflecting 0.1–10 keV x-rays into one of the four focal plane detectors, ACIS-I/S or HRC-I/S (figure 2.2; van Speybroeck et al. 1997). Their diameters range from 1.23 to 0.6 m, have a focal length of 10 m and an unobscured clear aperture of 1145 cm². This yields effective areas of ~ 800 cm² at ~ 0.25 keV, ~ 400 cm² at around 5 keV and ~ 100 cm² at 8 keV. The images it produces have a half-power diameter of the point-spread function (PSF) of $< 0.5''$, which is well matched by the detectors' pixel size and resolution. This means that Chandra is capable of subarcsecond angular resolutions, an increase of an order of magnitude over any previous x-ray telescope. It therefore provides an excellent opportunity for high angular and spectral resolution of x-ray sources. Nevertheless, the PSF quickly broadens, and the encircled energy fraction decreases, as the off-axis angle increases due to mirror aberrations (see figures 2.3 and 2.4). Furthermore, the performance also degrades at higher energies because of larger x-ray scattering; figure 2.6 on page 28 shows the effective area available as a function of the energy of incident photons for the Chandra instruments.

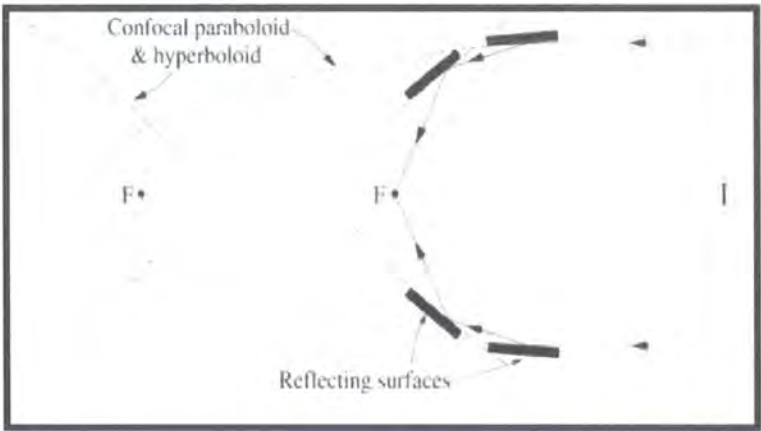


Figure 2.1: Wolter I imaging system, consisting of a paraboloid-hyperboloid pair. This is an aplanatic system of grazing incidence mirrors free of spherical and coma aberrations. The HRMA aboard Chandra features this design, which lends itself to nesting several mirrors inside one another to increase the effective area of the telescope.

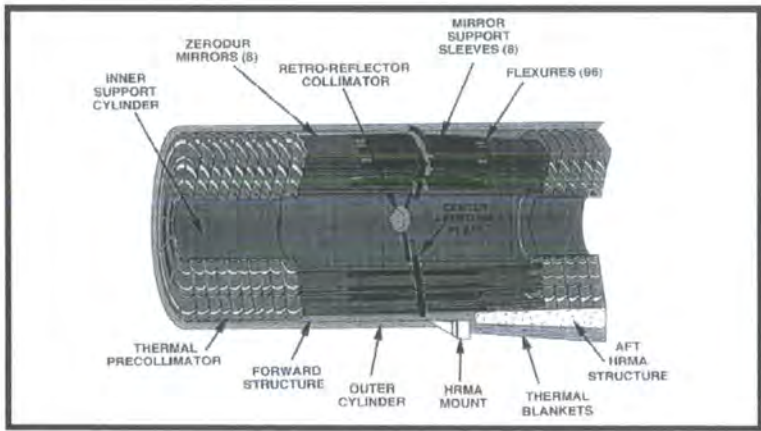


Figure 2.2: High Resolution Mirror Assembly (HRMA) aboard Chandra. Four concentric mirror pairs are nested in a typical Wolter type I design. The mirror outer diameters are 1.23, 0.99, 0.87 and 0.65 m and it has an unobscured clear aperture of 1145 cm² and focal lengths of 10 m.

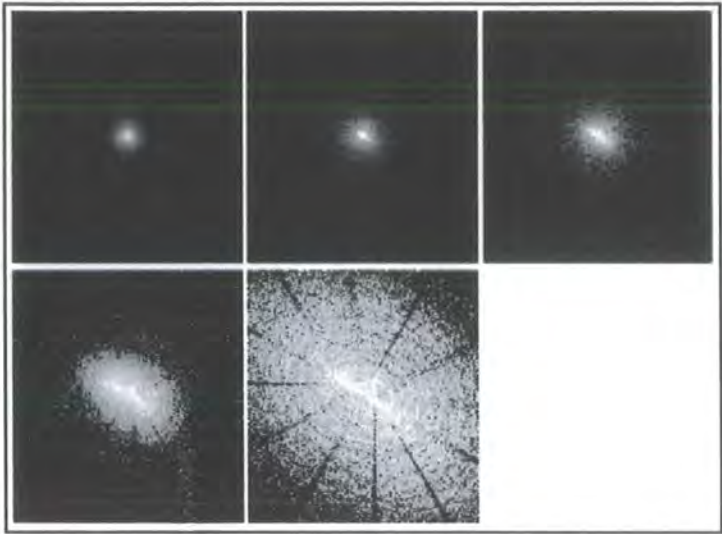


Figure 2.3: Simulated PSFs for the HRC-I instrument at 1.497 keV as a function of off-axis angles; clockwise from the top left, off-axis angles: 0, 1.5', 3', 12' and 6'. FOV $\sim 0.5^\circ$. The point-spread function of the Chandra telescope depends on the spectral energy distribution of the source and location in the telescope field of view. Because of the Wolter type I design, the image quality is best in a small area centred about the optical axis. The on-axis PSF has a circular symmetry and the best resolution is achieved for photon energies around 0.277 keV, where the PSF can be approximated by a single Gaussian with 85% of the energy within less than 1". At lower or higher energies and at larger off-axis angles the resolution degrades. See also figure 2.4 which shows the 85% encircled energy diameter as a function of off-axis angle and energy. (From the *CXO Detect Manual*.)

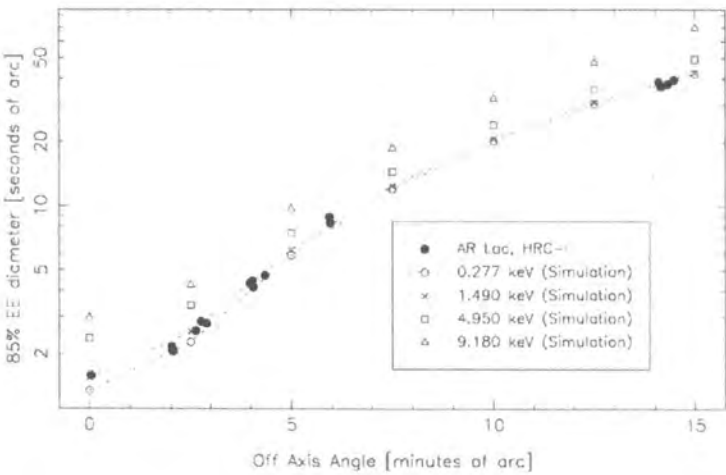


Figure 2.4: Observed and simulated 85% encircled energy diameters from Jerius et al. (2000).

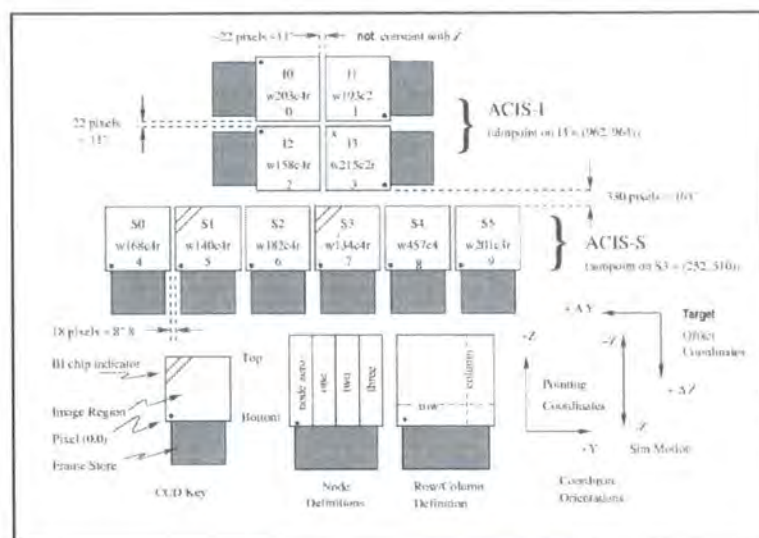


Figure 2.5: Schematic drawing of the ACIS focal plane. The nominal aimpoints are marked with a '+' on S3 and 'x' on I3. S1 & S3 are BI chips; the rest, FI. The view is along the optical axis, from the source towards the detectors. From the "Chandra proposers' observatory guide".

2.1.2 The ACIS Instrument

The four focal plane science instruments are the High Resolution Camera S & I (HRC-S/I) and the AXAF CCD Imaging Spectrometer S & I (ACIS-S/I).¹ Our data were taken with the ACIS detectors and hence only these are reviewed.

CCDs have become the *de facto* standard detectors in astronomy. In the field of x-rays, they have spatial resolution comparable to microchannel plates and better energy resolution than gas proportional counters. ACIS (Garmire et al. 2003) consists of 10 planar 1024×1024 pixel CCDs tilted tangential to the focal plane; pixel size is $24 \mu\text{m}$, corresponding to a pixel scale of $0.492''$. Six of the chips are arranged in a 1×6 array ($8.3' \times 50.6'$) and are used either for imaging or as a grating read-out; collectively, they form the ACIS-S detector. The second and fourth element of the array are back-illuminated (BI), whereas the rest are front-illuminated (FI).² ACIS-I consists of an array of 2×2 FI chips ($16.9' \times 16.9'$), used for imaging. At any one time, any combination of up to 6 chips can be active. The on-axis image quality is $\sim 0.5''$ FWHM, increasing to $\sim 3''$ at $\sim 4'$ off-axis. Their disposition on the focal plane is shown in figure 2.5.

¹ S and I stand for 'spectrograph' and 'imager' respectively. As for 'ACIS', different versions specify that the first 'A' stands just for 'Advanced'.

²Back-illuminated devices (gate structures opposing the incident beam) have better response to lower-energy photons than front-illuminated chips (gate structures facing beam). Below 0.3 keV the quantum efficiency (including the optical blocking filters) of the front illuminated chips drops off steeply. A steep rise of the background due to charged particles is also observed.

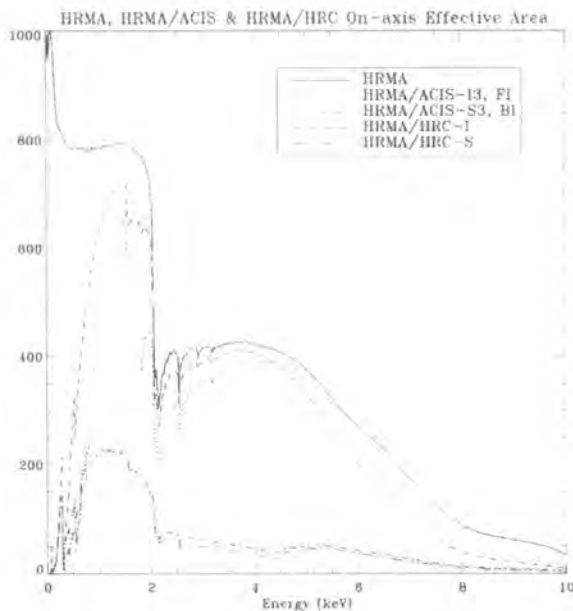


Figure 2.6: Predicted effective areas of the HRMA, HRMA/ACIS and HRMA/HRC as a function of energy. The structure near 2 keV is due to the iridium M-edge. The HRMA/ACIS effective areas are the products of the HRMA effective area and the quantum GSGP4 efficiency of ACIS-I-3 (front illuminated) or ACIS-S-3 (back-illuminated) chips. For the FI chip, the on-axis effective areas (integrated over the PSF to $> 99\%$ encircled energy) are 110 cm^2 at 0.5 keV, 600 cm^2 at 1.5 keV and 40 cm^2 at 8 keV. Vignetting at $10'$ from the aimpoint reduces the effective area by a factor of ~ 0.2 . From the “Chandra proposers’ observatory guide”.

Energy Resolution

ACIS is designed to provide high resolution spectral and temporal photon-counting images of x-ray objects. Originally, The FI CCDs approached the theoretical limit for the energy resolution at almost all energies (results ranging from 60 eV FWHM at 1 keV to 150 eV at 8 keV), while the BI CCDs exhibited poorer resolution. However, during the first stages of the mission, a strong low energy proton flux in the radiation (the belts contain protons of about $\sim 100 \text{ keV}$ at intensities of $\sim 10^8 \text{ protons cm}^2 \text{ sec}^{-1}$) harmed the FI chips by increasing their charge transfer inefficiency. The BI CCDs, placed upside-down, have enough extra bulk silicon protecting their gate structures to stop a few hundred keV protons and suffered no deterioration.

At the time of the observations we were unsure of the outreach of the damage and, for caution, decided to use the ACIS-S configuration, with aimpoint on BI S3, for the $10 \times 10 \text{ ks}$ exposures. The WHDF was observed in the ACIS-I mode, more appropriate for imaging, and can be seen in figure 2.7.

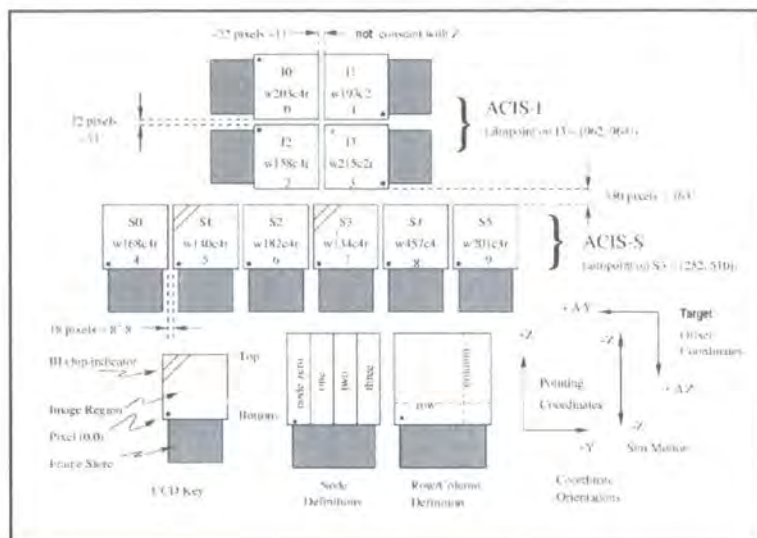


Figure 2.5: Schematic drawing of the ACIS focal plane. The nominal aimpoints are marked with a '+' on S3 and 'x' on I3. S1 & S3 are BI chips; the rest, FI. The view is along the optical axis, from the source towards the detectors. From the "Chandra proposers' observatory guide".

2.1.2 The ACIS Instrument

The four focal plane science instruments are the High Resolution Camera S & I (HRC-S/I) and the AXAF CCD Imaging Spectrometer S & I (ACIS-S/I).¹ Our data were taken with the ACIS detectors and hence only these are reviewed.

CCDs have become the *de facto* standard detectors in astronomy. In the field of x-rays, they have spatial resolution comparable to microchannel plates and better energy resolution than gas proportional counters. ACIS (Garmire et al. 2003) consists of 10 planar 1024×1024 pixel CCDs tilted tangential to the focal plane; pixel size is $24 \mu\text{m}$, corresponding to a pixel scale of $0.492''$. Six of the chips are arranged in a 1×6 array ($8.3' \times 50.6'$) and are used either for imaging or as a grating read-out; collectively, they form the ACIS-S detector. The second and fourth element of the array are back-illuminated (BI), whereas the rest are front-illuminated (FI).² ACIS-I consists of an array of 2×2 FI chips ($16.9' \times 16.9'$), used for imaging. At any one time, any combination of up to 6 chips can be active. The on-axis image quality is $\sim 0.5''$ FWHM, increasing to $\sim 3''$ at $\sim 4'$ off-axis. Their disposition on the focal plane is shown in figure 2.5.

¹S and I stand for 'spectrograph' and 'imager' respectively. As for 'ACIS', different versions specify that the first 'A' stands just for 'Advanced'.

²Back-illuminated devices (gate structures opposing the incident beam) have better response to lower-energy photons than front-illuminated chips (gate structures facing beam). Below 0.3 keV the quantum efficiency (including the optical blocking filters) of the front illuminated chips drops off steeply. A steep rise of the background due to charged particles is also observed.

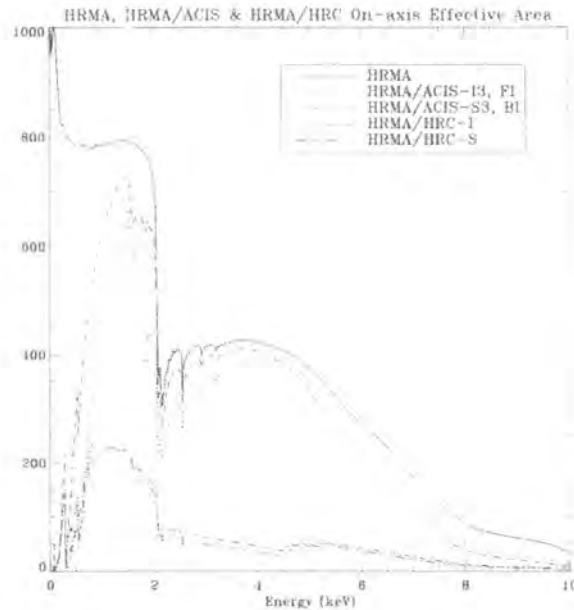


Figure 2.6: Predicted effective areas of the HRMA, HRMA/ACIS and HRMA/HRC as a function of energy. The structure near 2 keV is due to the iridium M-edge. The HRMA/ACIS effective areas are the products of the HRMA effective area and the quantum GSGP4 efficiency of ACIS-I-3 (front illuminated) or ACIS-S-3 (back-illuminated) chips. For the FI chip, the on-axis effective areas (integrated over the PSF to $> 99\%$ encircled energy) are 110 cm^2 at 0.5 keV, 600 cm^2 at 1.5 keV and 40 cm^2 at 8 keV. Vignetting at $10'$ from the aimpoint reduces the effective area by a factor of ~ 0.2 . From the “Chandra proposers’ observatory guide”.

Energy Resolution

ACIS is designed to provide high resolution spectral and temporal photon-counting images of x-ray objects. Originally, The FI CCDs approached the theoretical limit for the energy resolution at almost all energies (results ranging from 60 eV FWHM at 1 keV to 150 eV at 8 keV), while the BI CCDs exhibited poorer resolution. However, during the first stages of the mission, a strong low energy proton flux in the radiation (the belts contain protons of about $\sim 100 \text{ keV}$ at intensities of $\sim 10^8 \text{ protons cm}^2 \text{ sec}^{-1}$) harmed the FI chips by increasing their charge transfer inefficiency. The BI CCDs, placed upside-down, have enough extra bulk silicon protecting their gate structures to stop a few hundred keV protons and suffered no deterioration.

At the time of the observations we were unsure of the outreach of the damage and, for caution, decided to use the ACIS-S configuration, with aimpoint on BI S3, for the $10 \times 10 \text{ ks}$ exposures. The WHDF was observed in the ACIS-I mode, more appropriate for imaging, and can be seen in figure 2.7.

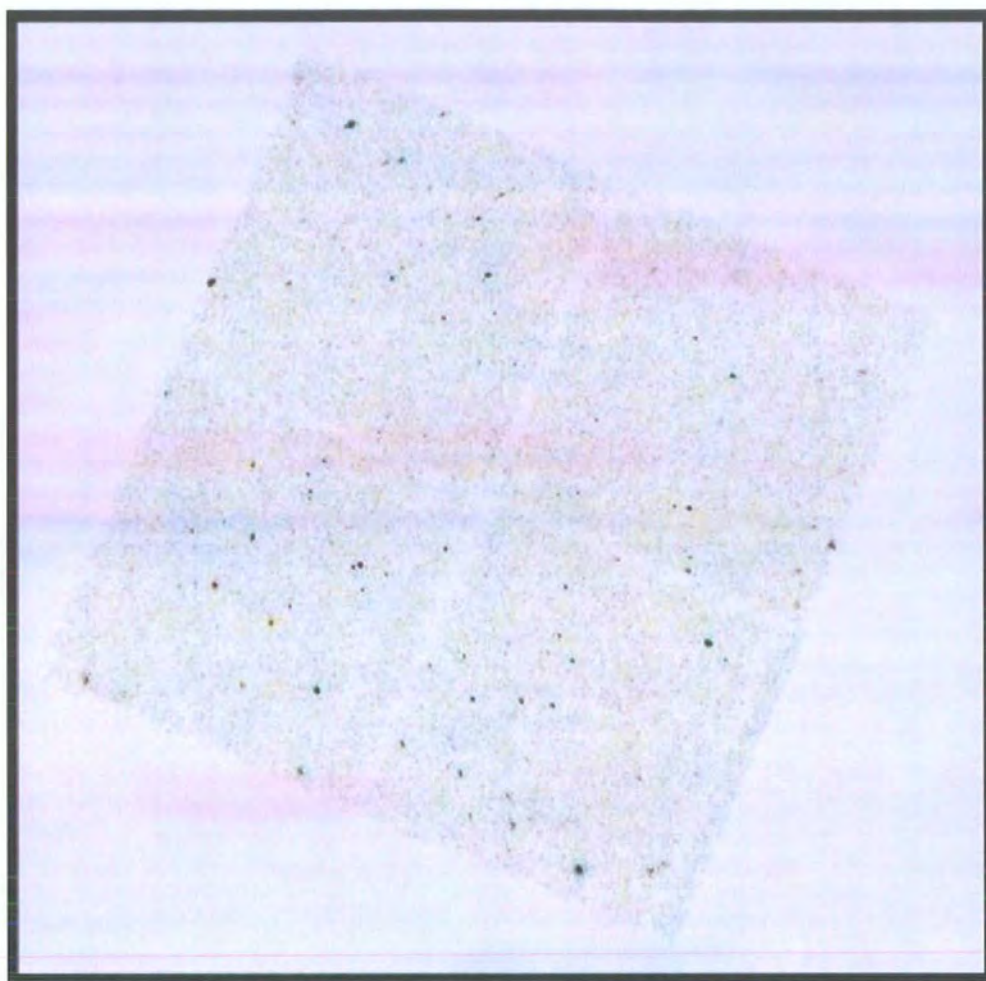


Figure 2.7: Inverted true-colour image of 75 ks with Chandra on the WHDF ($\alpha = 00^h 22^m 33.3^s$, $+00^\circ 20' 55.0''$, J2000), taken in January 2001. Soft sources appear cyan, while hard sources are yellow. Note the population of magenta and yellow objects showing up in this image.

2.2 Data Reduction

Between November of 2000 and January of 2001, Chandra imaged the WHDF, GSGP4 and F864 fields for a total of 175 ks with the ACIS instrument. A log of the observations is found in table 2.1 on the following page. On all occasions, ACIS was operated using six active chips to increase the chances of serendipitous science. Issues like saturating telemetry were highly improbable due to the nature of our surveys which aimed at extragalactic blank fields. The data delivered from ACIS undergoes some local processing onboard which, apart from removing bias (the amount of charge in a pixel not exposed to any x-ray induced signal), identifies the position and amplitude of any events according to a number of criteria depending on the precise operating mode. An x-ray event always requires a local maximum in the charge distribution above the defined threshold; then they are graded according to the position and amount of charge collected in a limited region containing and surrounding the pixels; and finally passed into the telemetry stream. We operated the ACIS-I instrument in very faint mode (VFAINT; at -120° C on the focal plane). This format provides the event position in the focal plane where it took place, time of occurrence, its amplitude and the pixel values in a 5×5 island about the pixel responsible for the event (although events are still graded by the contents of the central 3×3 cell). ACIS-S was operated in FAINT mode (as for the contents of the surrounding pixels, just the 3×3 island is provided). In our analysis, only events with standard ASCA grades 0, 2, 3, 4 and 6 were included while bad columns, hot pixels and columns at the limits of the readout nodes, where event select does not work properly, were discarded.

During the observations the spacecraft was dithered in a Lissajous figure, spanning $16''$ peak to peak. This serves the purposes of exposing the gaps in-between chips and of smoothing out pixel-to-pixel gain variations. The dither is removed during high-level ground processing of the data.

The data were reduced and analysed using standard methods and the Chandra *Interactive Analysis of Observations* (CIAO) software, version 2.0 provided by the Chandra x-ray Centre (CXC).³

2.2.1 Source Detection

Apart from undetected contributors to the XRB, background of x-ray detectors for astronomy can be broadly divided in two components: diffuse sky background (hard cosmic ray induced events) and instrument background. Chandra has a very low and uniform instrumental background and at our exposures we are always signal limited. Furthermore, the background count rate, except during periods of solar flaring activity, is rather stable. The problem from flares is particularly acute for the BI chips, where high-background periods affect the observations 5–10% of

³<http://asc.harvard.edu/ciao/>

Table 2.1: Journal of the Chandra observations. All were undertaken between November 2000 and January 2001.

Obs. ID ^a	Target	RA ^b	DEC ^b	N_H ^c	Exposition ^d	Obs. mode	Bckgrnd (S) ^e	Bckgrnd (H) ^e	Bckgrnd (T) ^e
900069	GSGP4X:048	00 ^h 57 ^m 17.1 ^s	-27° 22' 03.0''	1.8	11843	ACIS-S/FAINT	.0044	.0067	.010
900070	GSGP4X:057	00 ^h 57 ^m 26.0 ^s	-27° 43' 38.0''	1.8	8963	ACIS-S/FAINT	.030	.058	.086
900071	GSGP4X:069	00 ^h 57 ^m 36.7 ^s	-27° 33' 05.0''	1.8	9245	ACIS-S/FAINT	.039	.073	.11
900072	GSGP4X:082	00 ^h 57 ^m 49.7 ^s	-27° 23' 06.0''	1.8	8960	ACIS-S/FAINT	.0069	.011	.019
900073	GSGP4X:091	00 ^h 58 ^m 01.3 ^s	-27° 53' 11.0''	1.8	9456	ACIS-S/FAINT	.0024	.0034	.0057
900074	GSGP4X:109	00 ^h 58 ^m 24.4 ^s	-27° 29' 23.0''	1.8	11920	ACIS-S/FAINT	.0017	.0021	.0041
900075	GSGP4X:114	00 ^h 58 ^m 36.4 ^s	-27° 48' 49.0''	1.8	12138	ACIS-S/FAINT	.0043	.0026	.0071
900076	RXJ13434+0001	13 ^h 43 ^m 29.2 ^s	+00° 01' 33.0''	2.6	9952	ACIS-S/FAINT	.0024	.0048	.0048
900077	F864X:052	13 ^h 44 ^m 07.3 ^s	-00° 28' 33.0''	2.6	9574	ACIS-S/FAINT	.0018	.0043	.0043
900078	F864X:012	13 ^h 44 ^m 25.1 ^s	-00° 01' 07.0''	2.6	9760	ACIS-S/FAINT	.0020	.0046	.0046
900079	WHDF	00 ^h 22 ^m 33.3 ^s	+00° 20' 55.0''	2.7	71221	ACIS-I/VFAINT	0.082	0.153	-

^aChandra observation identifier^bNominal pointing; J2000.^cHydrogen column density in units of 10^{20} cm^{-2} .^dIntegration time, in seconds^eBackground estimates (in counts pixel⁻¹) in the soft (S), hard (H) and total (T) x-ray bands.

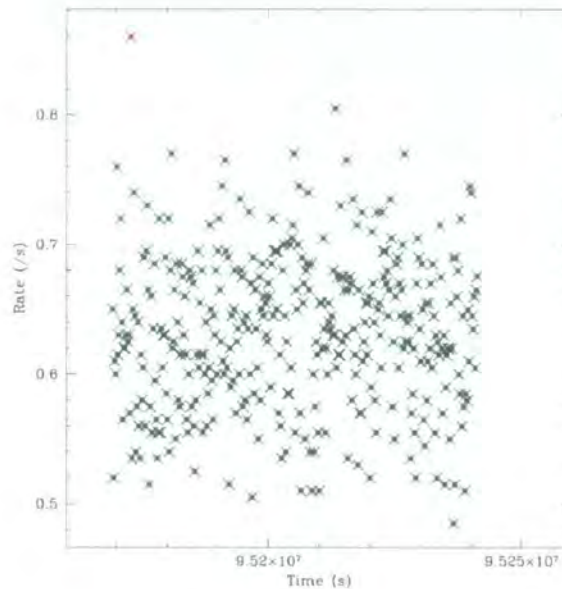


Figure 2.8: Light curve plot of the background regions in the WHDF, using 200-second time bins and the total 0.5–8 keV band. No significant high-background periods (with count rates 3.5σ higher than the average) are found during the 75 ks exposure. More stringent conditions for the removal of high background times were not deemed necessary considering the low level of the quiescent background.

the time. Their effect on FI chips is less severe. The flares can be identified by examining light curves of source-free regions of the data. We produced lightcurve plots such as that shown in figure 2.8 for the WHDF, using M. Markevitch’s `LC_CLEAN` tool. We find for example that the average residual cosmic background rate in the 2–8 keV band in the direction of the WHDF is $\sim 10 \text{ counts s}^{-1}$ over the entire ACIS-I detector.

Celldetect

ACIS’ low background generally makes detecting sources an easy task. There are various techniques for source selection, including sliding cells, wavelet-based algorithms and the optimal matched filter method. The sliding cell method is the best known for x-ray images; it was developed for the Einstein observatory and was heavily employed with ROSAT. This is a fast and robust method optimised for the detection of faint isolated unresolved sources in which the cell jumps by one third of its size and candidate regions are flagged whenever the net counts exceed the desired enhancements over the background. Wavelet-based algorithms are better suited to separate closely spaced point sources while the optimal match filter algorithm excels at the detection of faint low surface brightness features.

Since neither crowded fields nor extended sources are an issue in any of our exposures, we decided on the use of the `CELLDETECT` sliding cell algorithm (Calderwood et al. 2001) to detect our sources. It has two variants according to how the backgrounds are computed: “local detect” estimates the background from a frame around the detect cell whereas “map detect” requires a background map. As figures 2.3 and 2.4 show, the PSF varies strongly with the off-axis angle and also with photon energy. Therefore, different detect cell sizes are appropriate for different spatial regions and for different energies. `CELLDETECT` compensates for this by increasing the size of the cell with off-axis distance. The user specifies the reference energy band and the desired encircled energy to be encompassed in the detect cell, and `CELLDETECT`, with a knowledge of the instrument, calculates the radius at which the PSF reached the given encircled energy. Harnden et al. (1984) indicate that the optimum cell size is approximately 3.6 times the sigma of the PSF; for a Gaussian PSF that corresponds to the encircled energy setting of 0.80 and that is the value we used.

Given a signal-to-noise threshold ratio, SNR_{thr} , `CELLDETECT` outputs the detection cells in which the condition $\text{SNR} \geq \text{SNR}_{\text{thr}}$ is fulfilled. In the case where the background is estimated from the background frame, SNR is given by equation 2.1:

$$\text{SNR} = \frac{S}{\sigma_S} = \frac{C(b^2 - d^2)d^{-2} - Q}{\sqrt{\sigma_C^2(b^2 - d^2)^2d^{-4} + \sigma_Q^2}}. \quad (2.1)$$

S is the expected total source counts in the square detection cell of size d ; C is the total counts in the detect cell; Q is the total counts in the surrounding background frame, which is a $b \times b$ box.⁴ Overall we have found that a frame surrounding the cell to estimate the background locally has a good efficiency at finding sources that are not too distant ($\lesssim 7'$) from the aim point. At larger distances, extended false detections in the vicinity of significant exposure variations (such as those due to detector edges) become a problem when used with a low SNR threshold and visual re-inspection is required to filter out spurious sources.

We generated three energy-dependent images in the soft 0.3–2 keV, hard 2–8 keV and total 0.3–8 keV bands binned every two pixels in both directions and sources were extracted independently for each image. We followed Brandt et al. (2000) and used the 2–8 keV hard band to minimise instrumental backgrounds and thus maximise the signal-to-noise ratio. As explained below in § 2.2.2, at a later stage we used a convenient flux conversion factor and converted to the standard hard 2–10 keV ASCA band in order to allow comparisons with results from the literature. Running `CELLDETECT` in different fashions (with and without a constant background, with various fixed and variable detection cells, ...) did not result in any appreciable differences in the outputs.

⁴Cf. equation 2.5 and Harnden et al. (1984).

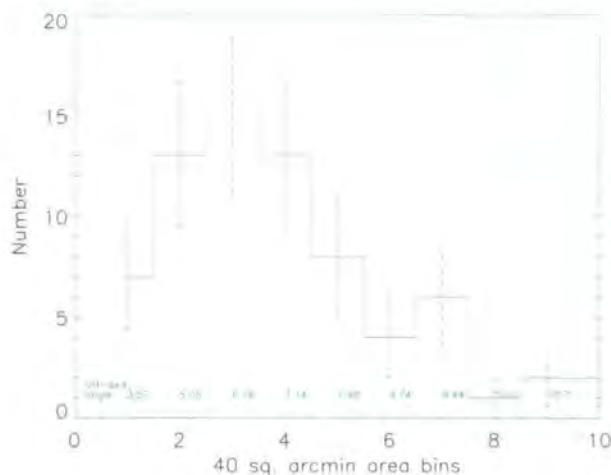


Figure 2.9: Number of sources in the WHDF detected in annuli bins centred about ACIS-I aimpoint. All the bins have the same area ($\sim 40'$); errors are \sqrt{n} . The off-axis distance that corresponds to each annulus' outer diameter can be read in the bottom of the figure. Apart from a dip close to the *crux* formed by the chip gaps, the source density is consistent with being constant out to a radius of $\sim 7'$, and then shows a gradual decrease.

Detections

Sources were detected to a SNR limit of 2. Table 2.2 on the following page lists a breakdown of source detections in the different energy bands. Above a SNR of 3, almost 150 sources were detected in at least one band, 40 of which were detected in the hard 2–8 keV band and 99 in the soft 0.3–2 keV band. Note that, amongst the hard sources, over 75% are detected as well in the soft band with a high significance ($\text{SNR} \geq 3$). If the hard population is representative of highly obscured AGN, this indicates that, even in type II AGN, significant soft emission can still be produced (by means of scattering, partial covering of the central radiation, *etc*; see Turner et al. 1997, for instance). It could as well be that the hard population is found at very high redshifts ($z \gtrsim 2$), in which case hard emission would be shifted into the soft band. Optical spectroscopy for these sources can clarify the situation and in chapter 4 we will argue that most of these sources are indeed obscured AGN at $z \lesssim 1.5$. This proportion drops from almost 80 to just 40% if the least significant detections are also considered; therefore, sources detected in the $2.5 \geq S/N \geq 2$ significance band should be regarded with some caution, specially if they are also detected with a lot of counts, indicative then of large detection cells far off-axis. As for the soft sources, only between $1/3$ and $1/2$ are detected in the hard band. Despite the fact that this effect can be partially attributed to Chandra's improved sensitivity in the soft band, it already anticipates that a large fraction of the soft x-ray background in these surveys will be caused by unobscured type I AGN.

SNR	Field	Any	Spurs.	Total	Hard	≥ 3	≥ 2.5	≥ 2	Soft	≥ 3	≥ 2.5	≥ 2
≥ 5	WHDF	32	0	32	10	9	9	10	20	17	18	18
	GSGP4	19	0	19	0	0	0	0	14	3	7	8
	F864	11	0	11	0	0	0	0	11	4	5	7
≥ 4	WHDF	42	1	41	15	14	14	15	32	20	24	25
	GSGP4	31	1	31	0	0	0	0	23	3	7	10
	F864	14	1	14	1	1	1	1	12	4	5	7
≥ 3	WHDF	69	5	66	31	23	26	27	49	22	28	31
	GSGP4	51	3	50	5	4	5	5	32	4	8	12
	F864	20	3	20	4	4	4	4	18	4	5	7
≥ 2.5	WHDF	102	25	91	47	28	32	33	59	25	32	35
	GSGP4	66	15	65	13	8	9	9	44	5	9	13
	F864	26	5	26	5	5	5	5	22	4	5	7
≥ 2	WHDF	170	100	143	77	32	36	37	80	26	33	36
	GSGP4	122	75	113	25	12	13	13	67	5	9	13
	F864	41	25	41	8	7	7	7	28	4	5	7

Table 2.2: Summary of Chandra x-ray detections above a signal-to-noise ratio of 2 tabulated for each observed field. The numerals are the number of sources detected above the S/N ratio specified on the left-most column. **Any**, **Total**, **Hard** and **Soft** headline the energy band of the detections: *any* band (sources with a given S/N in at least one band); 0.3–8 keV *total* band; 2–8 keV *hard* band; 0.3–2 keV *soft* band. Scriptsize numbers to the right of the **Hard** and **Soft** columns are to be understood as the quantity of *hard* and *soft* sources which have a counterpart in the *soft* and *hard* bands, respectively, detected with a significance as specified in the corresponding column header. Note in particular that many of the hard sources have a very bright soft counterpart. The fourth column, in scriptsize, presents estimates of the number of spurious sources amongst the numbers of the third column based on false detection rates in `CELLDETECT` run on sets of simulated Chandra data that contained only a background-like component.

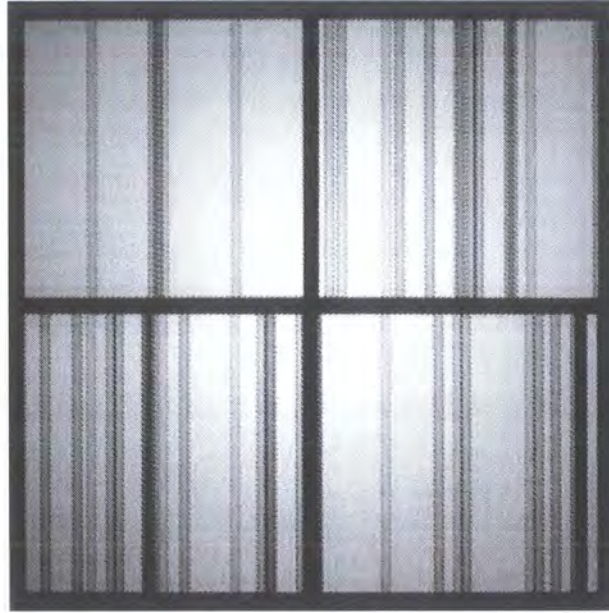


Figure 2.10: Exposure map in the hard band for the WHDF observation, showing spatial differences in exposure over the detector.

Figure 2.9 on page 34 shows the number of detected sources in equiareal annuli centred on the aimpoint of the 75 ks ACIS-I observation of the WHDF. The source density is seen to decline at radii $\gtrsim 7'$.

2.2.2 Flux Estimation

Simulations have shown that simple aperture photometry is very accurate across the ACIS-I detector. Event counts at the position of every detection were found using the CIAO `get_counts` script for the soft and hard bands and the apertures provided by `CELLEDETECT`; background estimates were measured from a collection of source-free background regions and subtracted from the total counts. To account for variations in effective exposure across the image in the forms of energy-dependent vignetting and detector efficiency gradients, we produced monochromatic soft (at 1 keV) and hard (at 3 keV) exposure maps with the tools `mkinstmap` and `mkexpmap` (figure 2.10). These were used to weight the exposure time of each source. Dividing the net counts over the effective exposure time provided a count flux for every source.

Energy fluxes were computed from count rates separately for the bright ($S/N \geq 3$) and faint ($S/N < 3$) populations in our sample. Sources with a power-law spectrum with $\Gamma = 1.2$ and $\Gamma = 0.54$, taken from the mean photon index of the sources in each of the two samples, and the corresponding Galactic absorption for the field, were assumed respectively. That yielded, for the bright sample, unabsorbed flux conversion factors of $(4.63 \pm 0.1) \times 10^{-12} \text{ erg cm}^{-2} \text{ s}^{-1}$ in the 0.5–2 keV band for 1 counts $^{-1}$

in the 0.3–2 keV band and of $(3.08 \pm 0.3) \times 10^{-11} \text{ erg cm}^{-2} \text{ s}^{-1}$ in the 2–10 keV band for 1 counts^{-1} in the 2–8 keV band, where the quoted uncertainties are for photon indices in the range $1.0 \leq \Gamma \leq 1.5$. For the faint sample conversion factors of 4.60×10^{-12} and $4.03 \times 10^{-11} \text{ erg cm}^{-2} \text{ s}^{-1}$ were obtained.

The choice of spectrum for converting count rates to energy fluxes is an important issue for which a simple solution does not exist. As such, different authors have taken different approaches. Brandt et al. (2001), for instance, converted using the Γ value determined from the ratio of the hard-to-soft band counts for every single source. Giacconi et al. (2001) and Campana et al. (2001) used $\Gamma = 1.4$, corresponding to the slope of the XRB, whereas Mushotzky et al. (2000) and Cowie et al. (2002) have used $\Gamma = 1.2$ based on the argument that on average the spectra of these sources must be slightly flatter than that of the XRB. None of these procedures is fully adequate given that the spectra for individual sources may be not as simple as a single power-law. We have chosen to convert count rates to energy fluxes using a single $\Gamma = 1.2$ that matches the average spectrum of our sample. This method shares *a posteriori* the philosophy that, on average, sources should be harder than the XRB but is optimised for our particular sample and should give the best average conversion and, therefore, the best estimate of the contribution of the sources in our sample to the XRB. The fact that our value has also been used by different authors on different assumptions reassures about its reasonability.

2.2.3 Catalogues of Chandra Sources

We have compiled catalogues of the sources detected with Chandra and their main x-ray properties. Although for completion the lists include sources detected with low significance, we have restricted our main analyses to those detections at $S/N \geq 3$. MARX⁵ simulations of Chandra data containing only a background-like component have shown that in an ACIS-I field with our exposure we should expect about one false detection per observation at this threshold (e.g. $\sim 10^{-6}$ for one 1024×1024 chip). We have also restricted the acquisition of sources to angular separations $< 10'$ from the aimpoint. Data collected far from the aimpoint will be out of focus; moreover, at larger off-axis angles, vignetting reduces the effective area by a factor > 0.2 (cf. figures 2.3, 2.4 and 2.9).

Altogether a total of 140 sources have been detected with $S/N \geq 3$ in at least one of the three bands, 136 in the full (0.3–8 keV) band, 40 in the hard (2–8 keV) band (of which 9 were not detected in the soft band) and 99 in the soft (0.3–2 keV) band (69 of which were not detected in the hard band). The WHDF (10 × 10 ks) survey faint flux limits are 4×10^{-16} (3×10^{-15}) and $3 \times 10^{-15} \text{ erg cm}^{-2} \text{ s}^{-1}$ (1×10^{-14}) in the soft and hard band respectively. The brightest source has a flux of 1×10^{-13} (soft) and $2 \times 10^{-13} \text{ erg cm}^{-2} \text{ s}^{-1}$ (hard).

⁵<http://space.mit.edu/ASC/MARX/>

Table 2.3: Chandra sources detected in the F864 field with $S/N \geq 2$.

Chandra ID	CXOF864	RA (J2000)	Dec	SNR ^a	HR	Flux ($\times 10^{-15}$ erg cm $^{-2}$ s $^{-1}$)		
						(0.5–10 keV)	(0.5–2 keV)	(2–10 keV)
F864CH001	J134334.3+000105	13 ^h 43 ^m 34.252 ^s	+00° 01' 05.2''	2.0	-0.56 ± 0.28	9 ± 4	3 ± 1.1	5 ± 3
F864CH002	J134332.0+000303	13 ^h 43 ^m 32.014 ^s	+00° 03' 03.1''	7.4	-0.56 ± 0.10	51 ± 8	23 ± 3	34 ± 8
F864CH003	J134329.2+000133	13 ^h 43 ^m 29.227 ^s	+00° 01' 32.9''	10.5	-0.61 ± 0.06	108 ± 12	51 ± 4	63 ± 11
F864CH004	J134327.8+000009	13 ^h 43 ^m 27.843 ^s	+00° 00' 08.5''	2.9	-0.85 ± 0.15	14 ± 5	5.1 ± 1.5	3 ± 3
F864CH005	J134322.0+000010	13 ^h 43 ^m 22.013 ^s	+00° 00' 10.2''	6.3	-0.65 ± 0.11	38 ± 7	19 ± 3	20 ± 6
F864CH006	J134329.6-000141	13 ^h 43 ^m 29.583 ^s	-00° 01' 41.1''	2.3	-0.45 ± 0.27	11 ± 5	3.4 ± 1.2	8 ± 4
F864CH007	J134327.3-000139	13 ^h 43 ^m 27.297 ^s	-00° 01' 38.7''	5.6	-0.71 ± 0.11	29 ± 6	15 ± 2	13 ± 5
F864CH008	J134325.7-000123	13 ^h 43 ^m 25.657 ^s	-00° 01' 23.2''	2.0	-0.78 ± 0.21	9 ± 4	3.3 ± 1.2	3 ± 3
F864CH009	J134332.7-000204	13 ^h 43 ^m 32.677 ^s	-00° 02' 03.5''	11.3	-0.77 ± 0.05	106 ± 11	55 ± 5	37 ± 8
F864CH010	J134413.0-002721	13 ^h 44 ^m 13.022 ^s	-00° 27' 20.9''	2.0	-0.67 ± 0.30	06 ± 3	2.1 ± 0.9	3 ± 3
F864CH011	J134409.6-002831	13 ^h 44 ^m 09.628 ^s	-00° 28' 30.7''	5.9	-0.70 ± 0.10	34 ± 6	17 ± 3	15 ± 5
F864CH012	J134415.6-002925	13 ^h 44 ^m 15.557 ^s	-00° 29' 24.5''	3.2	-0.65 ± 0.19	12 ± 4	5.9 ± 1.6	6 ± 3
F864CH013	J134414.1-002950	13 ^h 44 ^m 14.084 ^s	-00° 29' 50.4''	8.3	-0.81 ± 0.07	54 ± 7	29 ± 3	15 ± 5
F864CH014	J134412.9-003006	13 ^h 44 ^m 12.887 ^s	-00° 30' 05.9''	6.5	-0.50 ± 0.12	37 ± 7	16 ± 3	28 ± 7
F864CH015	J134409.1-003039	13 ^h 44 ^m 09.122 ^s	-00° 30' 38.5''	2.3	-0.33 ± 0.31	09 ± 4	2.5 ± 1.0	8 ± 4
F864CH016	J134424.0-002847	13 ^h 44 ^m 23.987 ^s	-00° 28' 46.7''	3.3	-0.73 ± 0.18	11 ± 3	5.5 ± 1.5	4 ± 3
F864CH017	J134418.8-003043	13 ^h 44 ^m 18.812 ^s	-00° 30' 42.5''	3.6	-0.71 ± 0.15	15 ± 4	8 ± 2	6 ± 3
F864CH018	J134413.8-003122	13 ^h 44 ^m 13.810 ^s	-00° 31' 21.5''	2.0	-0.11 ± 0.33	09 ± 4	2.1 ± 0.9	10 ± 5
F864CH019	J134356.3-002540	13 ^h 43 ^m 56.265 ^s	-00° 25' 39.9''	2.6	-0.69 ± 0.20	13 ± 4	4.7 ± 1.4	5 ± 3
F864CH020	J134420.1-003111	13 ^h 44 ^m 20.087 ^s	-00° 31' 11.1''	9.7	-0.70 ± 0.07	81 ± 10	40 ± 4	37 ± 8
F864CH021	J134355.5-003148	13 ^h 43 ^m 55.540 ^s	-00° 31' 47.7''	2.3	-0.67 ± 0.22	12 ± 4	4.2 ± 1.4	5 ± 3
F864CH022	J134351.1-003049	13 ^h 43 ^m 51.145 ^s	-00° 30' 48.8''	2.0	-0.80 ± 0.19	10 ± 4	3.8 ± 1.3	3 ± 3

(continues...)

Table 2.3: Chandra sources detected in the F864 field with $S/N \geq 2$ (continued).

Chandra ID	CXOF864	RA	Dec	SNR ^a	HR	Flux ($\times 10^{-15}$ erg cm $^{-2}$ s $^{-1}$)		
						(0.5–10 keV)	(0.5–2 keV)	(2–10 keV)
		(J2000)						
F864CH023	J134356.6–003231	13 ^h 43 ^m 56.620 ^s	–00° 32′ 31.2″	2.1	–0.50 ± 0.25	12 ± 4	3.8 ± 1.3	8 ± 4
F864CH024	J134353.8–003240	13 ^h 43 ^m 53.811 ^s	–00° 32′ 40.1″	2.5	–0.16 ± 0.23	20 ± 6	4.7 ± 1.4	21 ± 7
F864CH025	J134347.1–003114	13 ^h 43 ^m 47.091 ^s	–00° 31′ 14.1″	2.1	–0.20 ± 0.25	15 ± 5	3.8 ± 1.3	15 ± 6
F864CH026	J134346.3–003225	13 ^h 43 ^m 46.333 ^s	–00° 32′ 24.5″	3.2	–0.50 ± 0.18	17 ± 4	7.6 ± 1.8	13 ± 5
F864CH027	J134426.0–000056	13 ^h 44 ^m 25.972 ^s	–00° 00′ 56.2″	4.2	–0.50 ± 0.16	20 ± 5	8.7 ± 1.9	15 ± 5
F864CH028	J134432.4–000048	13 ^h 44 ^m 32.435 ^s	–00° 00′ 47.9″	2.7	+0.00 ± 0.32	10 ± 4	2.1 ± 0.9	13 ± 5
F864CH029	J134425.1+000124	13 ^h 44 ^m 25.067 ^s	+00° 01′ 23.5″	2.4	–0.82 ± 0.17	11 ± 4	4.2 ± 1.3	3 ± 3
F864CH030	J134438.3–000051	13 ^h 44 ^m 38.339 ^s	–00° 00′ 51.1″	4.5	–0.57 ± 0.16	20 ± 5	9.1 ± 1.9	13 ± 5
F864CH031	J134433.3–000350	13 ^h 44 ^m 33.307 ^s	–00° 03′ 50.2″	2.8	+0.23 ± 0.27	13 ± 5	2.1 ± 0.9	21 ± 7
F864CH032	J134420.8–000459	13 ^h 44 ^m 20.815 ^s	–00° 04′ 59.3″	3.1	–0.41 ± 0.22	12 ± 4	5 ± 1.4	11 ± 4
F864CH033	J134417.4–000442	13 ^h 44 ^m 17.435 ^s	–00° 04′ 41.8″	2.7	–0.71 ± 0.19	14 ± 4	5 ± 1.5	5 ± 3
F864CH034	J134420.3–000524	13 ^h 44 ^m 20.277 ^s	–00° 05′ 24.2″	4.1	–0.62 ± 0.16	18 ± 4	8.7 ± 1.9	11 ± 4
F864CH035	J134435.4–000532	13 ^h 44 ^m 35.413 ^s	–00° 05′ 32.0″	2.2	–0.17 ± 0.29	12 ± 4	2.9 ± 1.1	13 ± 5
F864CH036	J134433.6–000537	13 ^h 44 ^m 33.574 ^s	–00° 05′ 37.4″	5.5	–0.90 ± 0.07	30 ± 5	16.5 ± 2.6	4 ± 3
F864CH037	J134431.7–000546	13 ^h 44 ^m 31.655 ^s	–00° 05′ 46.2″	2.3	–0.38 ± 0.26	13 ± 5	3.7 ± 1.2	10 ± 5
F864CH038	J134429.2–000553	13 ^h 44 ^m 29.209 ^s	–00° 05′ 53.1″	3.7	–0.74 ± 0.14	16 ± 4	8.3 ± 1.9	6 ± 3
F864CH039	J134408.1–000310	13 ^h 44 ^m 8.0640 ^s	–00° 03′ 09.8″	2.2	–0.67 ± 0.22	12 ± 4	4.2 ± 1.3	5 ± 3
F864CH040	J134424.6–000618	13 ^h 44 ^m 24.587 ^s	–00° 06′ 17.5″	7.3	–0.80 ± 0.07	50 ± 7	26.4 ± 3	15 ± 5
F864CH041	J134405.4–000339	13 ^h 44 ^m 05.431 ^s	–00° 03′ 39.3″	2.0	–0.14 ± 0.26	14 ± 5	3.3 ± 1.2	15 ± 6

^aMost significant signal from the 3 bands as computed by CELLDETECT.

Table 2.4: Chandra sources detected in the GSGP4 field with $S/N \geq 2$.

Chandra ID	CXOGSGP4	RA	Dec	SNR ^a	HR	Flux ($\times 10^{-15}$ erg cm ⁻² s ⁻¹)		
						(0.5–10 keV)	(0.5–2 keV)	(2–10 keV)
		(J2000)						
GSGP4CH001	J005716.8–272129	00 ^h 57 ^m 16.843 ^s	–27° 21′ 28.6″	5.3	–0.60 ± 0.12	35.6 ± 7.1	12.3 ± 2.1	19 ± 6
GSGP4CH002	J005719.8–272036	00 ^h 57 ^m 19.793 ^s	–27° 20′ 35.9″	2.1	–0.75 ± 0.23	12.2 ± 5.5	2.4 ± 0.9	3 ± 3
GSGP4CH003	J005717.9–271830	00 ^h 57 ^m 17.921 ^s	–27° 18′ 30.2″	7.3	–0.79 ± 0.08	53.0 ± 8.2	20.5 ± 2.6	14 ± 5
GSGP4CH004	J005714.9–271852	00 ^h 57 ^m 14.938 ^s	–27° 18′ 52.2″	4.8	–0.70 ± 0.13	26.1 ± 5.9	9.6 ± 1.8	10 ± 5
GSGP4CH005	J005701.0–272336	00 ^h 57 ^m 01.026 ^s	–27° 23′ 35.7″	2.2	–0.09 ± 0.30	16.8 ± 7.2	2.1 ± 0.8	14 ± 6
GSGP4CH006	J005659.4–272251	00 ^h 56 ^m 59.413 ^s	–27° 22′ 51.4″	3.0	–0.11 ± 0.23	14.2 ± 4.7	3.4 ± 1.1	17 ± 6
GSGP4CH007	J005715.3–271735	00 ^h 57 ^m 15.278 ^s	–27° 17′ 34.6″	2.9	–0.58 ± 0.19	29.1 ± 9.0	5.2 ± 1.4	12 ± 6
GSGP4CH008	J005710.7–271653	00 ^h 57 ^m 10.738 ^s	–27° 16′ 53.1″	2.0	–0.39 ± 0.19	35.2 ± 10.1	5.5 ± 1.4	20 ± 8
GSGP4CH013	J005723.5–274556	00 ^h 57 ^m 23.476 ^s	–27° 45′ 55.8″	3.2	–0.80 ± 0.13	20.9 ± 6.0	8.1 ± 1.9	5 ± 4
GSGP4CH014	J005720.6–274454	00 ^h 57 ^m 20.587 ^s	–27° 44′ 53.7″	2.6	–0.25 ± 0.24	32.4 ± 11.3	4.6 ± 1.5	23 ± 9
GSGP4CH015	J005717.4–274237	00 ^h 57 ^m 17.418 ^s	–27° 42′ 36.9″	4.6	–0.47 ± 0.15	35.5 ± 8.4	11.3 ± 2.3	25 ± 8
GSGP4CH025	J005743.7–273300	00 ^h 57 ^m 43.748 ^s	–27° 33′ 00.2″	2.1	–0.33 ± 0.27	23.5 ± 9.4	3.5 ± 1.2	15 ± 7
GSGP4CH026	J005736.8–273305	00 ^h 57 ^m 36.795 ^s	–27° 33′ 05.2″	5.6	0.13 ± 0.16	40.7 ± 9.2	7.7 ± 1.9	60 ± 13
GSGP4CH027	J005742.9–273057	00 ^h 57 ^m 42.873 ^s	–27° 30′ 56.6″	2.2	–0.23 ± 0.27	25.5 ± 10.0	3.5 ± 1.2	19 ± 8
GSGP4CH028	J005741.9–273158	00 ^h 57 ^m 41.905 ^s	–27° 31′ 58.0″	2.1	0.26 ± 0.22	37.3 ± 12.0	3.1 ± 1.2	44 ± 13
GSGP4CH029	J005740.0–273129	00 ^h 57 ^m 40.000 ^s	–27° 31′ 28.6″	2.5	0.11 ± 0.23	35.3 ± 11.8	3.5 ± 1.2	37 ± 12
GSGP4CH030	J005741.0–273111	00 ^h 57 ^m 40.971 ^s	–27° 31′ 11.0″	2.1	0.65 ± 0.19	33.3 ± 10.8	1.3 ± 0.8	52 ± 14
GSGP4CH031	J005733.4–273131	00 ^h 57 ^m 33.435 ^s	–27° 31′ 30.6″	2.1	–0.60 ± 0.21	29.4 ± 10.2	5.3 ± 1.6	11 ± 6
GSGP4CH032	J005732.5–273145	00 ^h 57 ^m 32.515 ^s	–27° 31′ 44.8″	2.1	0.33 ± 0.22	35.3 ± 11.6	2.7 ± 1.1	44 ± 13
GSGP4CH033	J005731.3–273310	00 ^h 57 ^m 31.336 ^s	–27° 33′ 09.8″	2.2	0.06 ± 0.24	33.3 ± 11.4	3.5 ± 1.2	33 ± 11
GSGP4CH034	J005730.9–273203	00 ^h 57 ^m 30.901 ^s	–27° 32′ 03.2″	7.0	–0.61 ± 0.11	56.7 ± 10.1	19.7 ± 2.9	29 ± 9
GSGP4CH035	J005736.9–273024	00 ^h 57 ^m 36.872 ^s	–27° 30′ 24.0″	2.6	0.41 ± 0.15	72.6 ± 16.5	4.9 ± 1.5	96 ± 19

(continues. . .)

Table 2.4: Chandra sources detected in the GSGP4 field with $S/N \geq 2$ (continued).

Chandra ID	CXOGSGP4	RA	Dec	SNR ^a	HR	Flux ($\times 10^{-15} \text{ erg cm}^{-2} \text{ s}^{-1}$)		
		(J2000)				(0.5–10 keV)	(0.5–2 keV)	(2–10 keV)
GSGP4CH036	J005729.3–273043	00 ^h 57 ^m 29.291 ^s	−27° 30′ 43.4″	5.0	−0.42 ± 0.13	52.7 ± 10.1	16.2 ± 2.7	40 ± 10
GSGP4CH037	J005728.8–273136	00 ^h 57 ^m 28.783 ^s	−27° 31′ 35.9″	2.3	0.09 ± 0.17	64.7 ± 15.9	6.7 ± 1.7	67 ± 16
GSGP4CH038	J005726.6–273158	00 ^h 57 ^m 26.637 ^s	−27° 31′ 58.1″	2.3	0.27 ± 0.17	64.7 ± 15.7	5.3 ± 1.6	78 ± 17
GSGP4CH039	J005725.1–273202	00 ^h 57 ^m 25.077 ^s	−27° 32′ 02.0″	2.3	0.07 ± 0.18	58.8 ± 15.1	6.2 ± 1.6	59 ± 15
GSGP4CH040	J005724.5–273201	00 ^h 57 ^m 24.524 ^s	−27° 32′ 01.3″	9.3	−0.69 ± 0.07	112.4 ± 14.0	41.2 ± 4.2	45 ± 11
GSGP4CH041	J005732.8–273007	00 ^h 57 ^m 32.815 ^s	−27° 30′ 06.5″	7.8	−0.41 ± 0.09	103.3 ± 14.2	31.5 ± 3.7	80 ± 15
GSGP4CH043	J005745.1–272923	00 ^h 57 ^m 45.122 ^s	−27° 29′ 23.0″	2.4	−0.53 ± 0.15	58.8 ± 14.5	10.2 ± 2.1	26 ± 10
GSGP4CH045	J005726.4–273041	00 ^h 57 ^m 26.441 ^s	−27° 30′ 40.6″	2.3	0.22 ± 0.14	96.1 ± 19.2	8.4 ± 2.0	111 ± 20
GSGP4CH046	J005725.7–273113	00 ^h 57 ^m 25.711 ^s	−27° 31′ 12.5″	2.0	0.44 ± 0.12	105.9 ± 19.8	6.7 ± 1.7	144 ± 23
GSGP4CH047	J005725.1–273140	00 ^h 57 ^m 25.092 ^s	−27° 31′ 39.9″	2.0	0.20 ± 0.16	78.4 ± 17.5	7.1 ± 1.8	89 ± 18
GSGP4CH048	J005722.3–273151	00 ^h 57 ^m 22.332 ^s	−27° 31′ 51.4″	2.4	0.42 ± 0.12	107.9 ± 20.0	7.1 ± 1.8	144 ± 23
GSGP4CH049	J005726.8–273015	00 ^h 57 ^m 26.835 ^s	−27° 30′ 15.4″	2.4	0.30 ± 0.11	162.8 ± 24.9	12.9 ± 2.4	200 ± 27
GSGP4CH050	J005725.2–273030	00 ^h 57 ^m 25.201 ^s	−27° 30′ 29.8″	2.1	0.42 ± 0.11	143.2 ± 23.1	9.3 ± 2.0	192 ± 27
GSGP4CH051	J005723.1–273042	00 ^h 57 ^m 23.110 ^s	−27° 30′ 42.0″	2.2	0.36 ± 0.11	153.0 ± 24.1	11.1 ± 2.2	196 ± 27
GSGP4CH052	J005722.0–273126	00 ^h 57 ^m 22.000 ^s	−27° 31′ 26.0″	4.2	0.23 ± 0.11	79.0 ± 12.6	13.1 ± 2.4	127 ± 18
GSGP4CH053	J005734.9–272829	00 ^h 57 ^m 34.914 ^s	−27° 28′ 28.5″	3.1	−0.11 ± 0.12	65.8 ± 11.5	15.8 ± 2.6	77 ± 14
GSGP4CH054	J005725.8–272943	00 ^h 57 ^m 25.778 ^s	−27° 29′ 42.5″	2.4	0.32 ± 0.09	223.6 ± 29.2	17.3 ± 2.8	278 ± 32
GSGP4CH055	J005722.5–272955	00 ^h 57 ^m 22.474 ^s	−27° 29′ 55.1″	2.4	0.41 ± 0.09	186.3 ± 26.5	12.4 ± 2.4	248 ± 30
GSGP4CH056	J005718.3–273105	00 ^h 57 ^m 18.255 ^s	−27° 31′ 05.4″	2.4	0.23 ± 0.09	223.6 ± 29.4	19.5 ± 2.9	259 ± 31
GSGP4CH058	J005717.1–273330	00 ^h 57 ^m 17.094 ^s	−27° 33′ 29.8″	3.0	0.13 ± 0.11	77.0 ± 12.5	14.5 ± 2.5	114 ± 17
GSGP4CH059	J005716.5–273233	00 ^h 57 ^m 16.521 ^s	−27° 32′ 32.7″	4.4	−0.04 ± 0.09	115.5 ± 15.3	25.8 ± 3.4	146 ± 20
GSGP4CH068	J005755.4–272402	00 ^h 57 ^m 55.392 ^s	−27° 24′ 02.2″	2.6	−0.67 ± 0.22	24.3 ± 9.3	4.6 ± 1.5	8 ± 5

(continues. . .)

Table 2.4: Chandra sources detected in the GSGP4 field with $S/N \geq 2$ (continued).

Chandra ID	CXOGSGP4	RA	Dec	SNR ^a	HR	Flux ($\times 10^{-15} \text{ erg cm}^{-2} \text{ s}^{-1}$)		
		(J2000)				(0.5–10 keV)	(0.5–2 keV)	(2–10 keV)
GSGP4CH069	J005749.3–272324	00 ^h 57 ^m 49.336 ^s	−27° 23′ 23.8″	3.1	−0.67 ± 0.30	6.3 ± 3.3	2.3 ± 1.0	3 ± 3
GSGP4CH070	J005749.1–272237	00 ^h 57 ^m 49.066 ^s	−27° 22′ 36.6″	2.6	−0.43 ± 0.24	28.3 ± 10.5	4.6 ± 1.5	15 ± 8
GSGP4CH071	J005801.4–272231	00 ^h 58 ^m 01.406 ^s	−27° 22′ 31.3″	2.5	−0.83 ± 0.16	24.3 ± 8.7	5.0 ± 1.5	4 ± 4
GSGP4CH072	J005760.0–272127	00 ^h 57 ^m 59.970 ^s	−27° 21′ 26.9″	13.0	−0.95 ± 0.02	210.1 ± 16.9	88.6 ± 6.3	14 ± 6
GSGP4CH073	J005758.5–272309	00 ^h 57 ^m 58.465 ^s	−27° 23′ 08.6″	2.2	−0.11 ± 0.33	18.2 ± 8.5	2.3 ± 1.0	15 ± 8
GSGP4CH074	J005745.7–272430	00 ^h 57 ^m 45.661 ^s	−27° 24′ 29.7″	3.0	−0.43 ± 0.24	14.6 ± 5.4	4.5 ± 1.4	11 ± 5
GSGP4CH075	J005803.5–272136	00 ^h 58 ^m 03.457 ^s	−27° 21′ 35.9″	7.5	−0.68 ± 0.09	72.1 ± 11.4	26.2 ± 3.4	30 ± 9
GSGP4CH076	J005755.4–271957	00 ^h 57 ^m 55.442 ^s	−27° 19′ 56.8″	2.7	−0.65 ± 0.19	34.4 ± 11.1	6.4 ± 1.7	11 ± 6
GSGP4CH077	J005745.9–272009	00 ^h 57 ^m 45.869 ^s	−27° 20′ 08.8″	4.3	−0.47 ± 0.16	31.4 ± 7.8	9.9 ± 2.1	22 ± 8
GSGP4CH078	J005734.0–272311	00 ^h 57 ^m 33.973 ^s	−27° 23′ 11.4″	4.5	−0.35 ± 0.16	35.5 ± 8.5	10.4 ± 2.2	30 ± 9
GSGP4CH079	J005803.6–275300	00 ^h 58 ^m 03.573 ^s	−27° 53′ 00.1″	2.3	−0.80 ± 0.19	19.2 ± 7.7	3.9 ± 1.3	4 ± 4
GSGP4CH080	J005801.7–275317	00 ^h 58 ^m 01.707 ^s	−27° 53′ 16.5″	8.2	−0.59 ± 0.09	87.1 ± 12.5	30.0 ± 3.6	47 ± 11
GSGP4CH081	J005749.9–275241	00 ^h 57 ^m 49.949 ^s	−27° 52′ 41.1″	3.3	−0.68 ± 0.17	18.8 ± 5.6	6.9 ± 1.7	8 ± 4
GSGP4CH082	J005747.5–275412	00 ^h 57 ^m 47.478 ^s	−27° 54′ 11.8″	7.3	−0.48 ± 0.11	61.4 ± 10.7	19.7 ± 2.9	41 ± 10
GSGP4CH083	J005805.8–275004	00 ^h 58 ^m 05.789 ^s	−27° 50′ 04.4″	7.6	−0.69 ± 0.09	70.3 ± 11.0	25.7 ± 3.3	29 ± 9
GSGP4CH084	J005814.7–275002	00 ^h 58 ^m 14.689 ^s	−27° 50′ 02.2″	2.1	−0.64 ± 0.23	21.1 ± 8.4	3.9 ± 1.3	7 ± 5
GSGP4CH085	J005742.3–275031	00 ^h 57 ^m 42.315 ^s	−27° 50′ 31.4″	4.2	−0.66 ± 0.14	28.7 ± 7.0	10.3 ± 2.1	13 ± 6
GSGP4CH086	J005807.3–274740	00 ^h 58 ^m 07.305 ^s	−27° 47′ 40.0″	2.2	−0.05 ± 0.23	36.4 ± 11.9	4.3 ± 1.4	33 ± 11
GSGP4CH087	J005759.9–274733	00 ^h 57 ^m 59.910 ^s	−27° 47′ 32.6″	7.4	−0.76 ± 0.08	74.3 ± 11.0	28.3 ± 3.5	23 ± 8
GSGP4CH088	J005749.6–274816	00 ^h 57 ^m 49.566 ^s	−27° 48′ 15.7″	2.5	0.50 ± 0.18	46.0 ± 12.8	2.6 ± 1.0	65 ± 15
GSGP4CH089	J005808.9–274617	00 ^h 58 ^m 08.932 ^s	−27° 46′ 16.5″	2.6	−0.80 ± 0.13	38.3 ± 10.9	7.8 ± 1.8	7 ± 5
GSGP4CH090	J005828.5–273033	00 ^h 58 ^m 28.476 ^s	−27° 30′ 33.4″	4.3	−0.56 ± 0.16	21.2 ± 5.5	7.1 ± 1.6	12 ± 5

(continues. . .)

Table 2.4: Chandra sources detected in the GSGP4 field with $S/N \geq 2$ (continued).

Chandra ID	CXOGSGP4	RA	Dec	SNR ^a	HR	Flux ($\times 10^{-15} \text{ erg cm}^{-2} \text{ s}^{-1}$)		
		(J2000)				(0.5–10 keV)	(0.5–2 keV)	(2–10 keV)
GSGP4CH091	J005826.2–272925	00 ^h 58 ^m 26.155 ^s	−27° 29′ 25.4″	2.6	−0.08 ± 0.28	19.8 ± 7.8	2.4 ± 0.9	17 ± 7
GSGP4CH092	J005825.4–273234	00 ^h 58 ^m 25.368 ^s	−27° 32′ 34.0″	2.1	−0.50 ± 0.31	12.2 ± 5.9	2.1 ± 0.8	6 ± 4
GSGP4CH093	J005819.9–272856	00 ^h 58 ^m 19.939 ^s	−27° 28′ 55.6″	4.7	−0.86 ± 0.09	22.8 ± 5.2	9.2 ± 1.8	4 ± 3
GSGP4CH094	J005818.8–272936	00 ^h 58 ^m 18.808 ^s	−27° 29′ 35.9″	3.0	−0.29 ± 0.26	11.0 ± 4.1	3.1 ± 1.0	10 ± 5
GSGP4CH095	J005818.2–272848	00 ^h 58 ^m 18.160 ^s	−27° 28′ 47.8″	4.0	−0.53 ± 0.21	13.4 ± 4.4	4.4 ± 1.2	8 ± 4
GSGP4CH096	J005834.9–272713	00 ^h 58 ^m 34.915 ^s	−27° 27′ 13.4″	4.8	−0.43 ± 0.17	22.0 ± 5.7	6.8 ± 1.5	16 ± 6
GSGP4CH097	J005815.3–272809	00 ^h 58 ^m 15.256 ^s	−27° 28′ 08.6″	2.8	−0.69 ± 0.20	19.8 ± 7.1	3.8 ± 1.1	6 ± 4
GSGP4CH098	J005839.0–272712	00 ^h 58 ^m 38.966 ^s	−27° 27′ 11.5″	2.8	−0.08 ± 0.28	19.8 ± 7.8	2.4 ± 0.9	17 ± 7
GSGP4CH099	J005812.0–272804	00 ^h 58 ^m 12.021 ^s	−27° 28′ 04.4″	2.2	−0.60 ± 0.25	15.2 ± 6.4	2.8 ± 1.0	6 ± 4
GSGP4CH100	J005825.2–272529	00 ^h 58 ^m 25.222 ^s	−27° 25′ 28.7″	2.4	−0.64 ± 0.23	16.7 ± 6.7	3.1 ± 1.0	6 ± 4
GSGP4CH101	J005811.4–272636	00 ^h 58 ^m 11.431 ^s	−27° 26′ 35.5″	6.5	−0.86 ± 0.07	44.8 ± 7.3	18.0 ± 2.5	8 ± 4
GSGP4CH102	J005807.1–272851	00 ^h 58 ^m 07.058 ^s	−27° 28′ 51.1″	3.0	−0.29 ± 0.23	13.4 ± 4.6	3.7 ± 1.1	12 ± 5
GSGP4CH103	J005826.4–272437	00 ^h 58 ^m 26.430 ^s	−27° 24′ 37.0″	3.2	0.37 ± 0.21	14.9 ± 4.8	2.0 ± 0.8	27 ± 7
GSGP4CH104	J005814.0–272550	00 ^h 58 ^m 14.000 ^s	−27° 25′ 49.5″	6.3	−0.48 ± 0.12	42.4 ± 7.9	13.6 ± 2.1	29 ± 8
GSGP4CH105	J005807.3–272713	00 ^h 58 ^m 07.270 ^s	−27° 27′ 13.4″	2.2	−0.09 ± 0.30	16.7 ± 7.1	2.1 ± 0.8	14 ± 6
GSGP4CH106	J005812.8–272510	00 ^h 58 ^m 12.767 ^s	−27° 25′ 09.8″	2.5	−0.60 ± 0.21	22.8 ± 7.9	4.1 ± 1.2	9 ± 5
GSGP4CH107	J005804.7–272624	00 ^h 58 ^m 04.710 ^s	−27° 26′ 24.1″	2.4	−0.57 ± 0.22	21.3 ± 7.6	3.8 ± 1.1	9 ± 5
GSGP4CH108	J005800.8–272741	00 ^h 58 ^m 00.813 ^s	−27° 27′ 40.7″	5.0	−0.71 ± 0.11	32.2 ± 6.6	11.9 ± 2.0	12 ± 5
GSGP4CH109	J005818.7–272356	00 ^h 58 ^m 18.679 ^s	−27° 23′ 56.3″	3.5	−0.52 ± 0.17	19.6 ± 5.3	6.5 ± 1.5	12 ± 5
GSGP4CH110	J005817.4–272337	00 ^h 58 ^m 17.377 ^s	−27° 23′ 37.2″	2.3	−0.57 ± 0.22	21.3 ± 7.6	3.8 ± 1.1	9 ± 5
GSGP4CH111	J005758.4–272736	00 ^h 57 ^m 58.404 ^s	−27° 27′ 36.1″	2.1	−0.13 ± 0.21	35.0 ± 10.3	4.5 ± 1.2	29 ± 9
GSGP4CH112	J005836.2–275017	00 ^h 58 ^m 36.168 ^s	−27° 50′ 16.8″	5.5	−0.57 ± 0.14	28.5 ± 6.3	9.7 ± 1.8	16 ± 6

(continues. . .)

Table 2.4: Chandra sources detected in the GSGP4 field with $S/N \geq 2$ (continued).

Chandra ID	CXOGSGP4	RA	Dec	SNR ^a	HR	Flux ($\times 10^{-15}$ erg cm ⁻² s ⁻¹)		
		(J2000)				(0.5–10 keV)	(0.5–2 keV)	(2–10 keV)
<i>GSGP4CH113</i>	J005835.4–274841	00 ^h 58 ^m 35.380 ^s	−27° 48′ 40.9″	6.4	−0.76 ± 0.09	37.8 ± 6.9	14.3 ± 2.2	12 ± 5
<i>GSGP4CH114</i>	J005844.3–274856	00 ^h 58 ^m 44.325 ^s	−27° 48′ 55.6″	2.7	−0.23 ± 0.27	19.4 ± 7.6	2.7 ± 0.9	14 ± 6
<i>GSGP4CH115</i>	J005839.0–274716	00 ^h 58 ^m 39.031 ^s	−27° 47′ 15.6″	2.1	−0.56 ± 0.28	13.4 ± 6.1	2.4 ± 0.9	6 ± 4
<i>GSGP4CH116</i>	J005838.6–274717	00 ^h 58 ^m 38.577 ^s	−27° 47′ 16.8″	2.6	−0.20 ± 0.44	7.5 ± 4.6	1.0 ± 0.6	6 ± 4
<i>GSGP4CH117</i>	J005851.8–274757	00 ^h 58 ^m 51.849 ^s	−27° 47′ 57.3″	3.2	0.25 ± 0.24	12.3 ± 4.3	2.0 ± 0.8	20 ± 6
<i>GSGP4CH118</i>	J005828.0–275157	00 ^h 58 ^m 27.989 ^s	−27° 51′ 57.1″	7.6	−0.77 ± 0.08	54.0 ± 8.3	20.7 ± 2.6	16 ± 6
<i>GSGP4CH119</i>	J005828.0–275126	00 ^h 58 ^m 27.989 ^s	−27° 51′ 25.6″	4.6	−1.00 ± 0.00	23.9 ± 4.3	10.3 ± 1.9	0 ± 0
<i>GSGP4CH120</i>	J005820.7–274757	00 ^h 58 ^m 20.652 ^s	−27° 47′ 57.2″	2.7	−0.69 ± 0.20	19.4 ± 7.0	3.7 ± 1.1	6 ± 4
<i>GSGP4CH121</i>	J005822.1–274541	00 ^h 58 ^m 22.145 ^s	−27° 45′ 40.9″	3.3	−0.36 ± 0.20	17.0 ± 5.0	5.0 ± 1.3	14 ± 5
<i>GSGP4CH123</i>	J005814.1–274841	00 ^h 58 ^m 14.139 ^s	−27° 48′ 40.5″	2.1	−0.08 ± 0.28	19.4 ± 7.6	2.4 ± 0.9	17 ± 7
<i>GSGP4CH125</i>	J005833.8–274360	00 ^h 58 ^m 33.774 ^s	−27° 43′ 59.8″	2.1	−1.00 ± 0.00	14.9 ± 4.8	3.4 ± 1.1	0 ± 0

^aMost significant signal from the 3 bands as computed by `CELLDETECT`.

Table 2.5: Chandra sources detected in the WHDF field with $S/N \geq 3$.

Chandra ID	CXOWHDF	RA ^a	Dec ^a	Θ^b	Counts	SNR ^c	HR	Flux ($\times 10^{-15}$ erg cm ⁻² s ⁻¹)		
		(J2000)						(0.5–10 keV)	(0.5–2 keV)	(2–10 keV)
WHDFCH001	J002235.2+002035	00 ^h 22 ^m 35.175 ^s	00° 20′ 34.6″	0.5′	9.4	3.0	-0.18 ± 0.19	14.0 ± 4.0	2.4 ± 0.6	11 ± 3
WHDFCH004	J002238.0+002139	00 ^h 22 ^m 38.029 ^s	00° 21′ 38.6″	1.3′	3.8	1.9	-0.49 ± 0.22	2.6 ± 0.9	0.8 ± 0.2	2 ± 1
WHDFCH005	J002236.0+001850	00 ^h 22 ^m 35.963 ^s	00° 18′ 50.0″	2.1′	78.7	8.8	-0.60 ± 0.04	56.0 ± 4.0	21.1 ± 1.0	35 ± 4
WHDFCH007	J002224.8+002011	00 ^h 22 ^m 24.821 ^s	00° 20′ 10.9″	2.2′	26.6	4.9	0.81 ± 0.10	11.6 ± 2.0	0.2 ± 0.1	12 ± 2
WHDFCH008	J002222.9+002013	00 ^h 22 ^m 22.884 ^s	00° 20′ 13.2″	2.6′	6.8	2.6	-0.19 ± 0.23	3.6 ± 1.1	0.7 ± 0.2	3 ± 1
WHDFCH010	J002229.1+002325	00 ^h 22 ^m 29.053 ^s	00° 23′ 25.1″	2.7′	2.5	1.4	-0.68 ± 0.18	2.1 ± 0.7	0.9 ± 0.2	1 ± 1
WHDFCH012	J002249.7+002042	00 ^h 22 ^m 49.660 ^s	00° 20′ 41.8″	4.0′	5.2	2.1	-0.53 ± 0.17	3.8 ± 1.1	1.3 ± 0.3	3 ± 1
WHDFCH014	J002249.4+002016	00 ^h 22 ^m 49.414 ^s	00° 20′ 15.9″	4.0′	10.1	3.1	-0.54 ± 0.12	7.1 ± 1.5	2.4 ± 0.4	5 ± 1
WHDFCH015	J002248.0+002101	00 ^h 22 ^m 48.004 ^s	00° 21′ 01.0″	3.6′	15.1	3.8	-0.33 ± 0.13	9.2 ± 1.8	2.1 ± 0.4	7 ± 2
WHDFCH016	J002245.2+001823	00 ^h 22 ^m 45.164 ^s	00° 18′ 22.6″	3.9′	22.4	4.7	-0.43 ± 0.10	14.3 ± 2.2	3.9 ± 0.5	10 ± 2
WHDFCH017	J002244.5+001826	00 ^h 22 ^m 44.468 ^s	00° 18′ 25.6″	3.7′	458.0	21.3	-0.54 ± 0.01	322.0 ± 10.0	109.0 ± 2.8	212 ± 10
WHDFCH019	J002244.3+001749	00 ^h 22 ^m 44.281 ^s	00° 17′ 48.5″	4.1′	9.1	2.9	-0.21 ± 0.20	5.2 ± 1.4	1.0 ± 0.3	4 ± 1
WHDFCH020	J002236.1+002434	00 ^h 22 ^m 36.142 ^s	00° 24′ 33.8″	3.7′	15.3	3.8	-0.55 ± 0.10	10.8 ± 1.8	3.7 ± 0.5	7 ± 2
WHDFCH021	J002231.1+002441	00 ^h 22 ^m 31.059 ^s	00° 24′ 41.2″	3.8′	8.1	2.7	-0.36 ± 0.18	5.0 ± 1.3	1.2 ± 0.3	4 ± 1
WHDFCH023	J002224.1+001753	00 ^h 22 ^m 24.109 ^s	00° 17′ 52.7″	3.8′	8.4	2.8	-0.28 ± 0.19	4.8 ± 1.3	1.0 ± 0.3	4 ± 1
WHDFCH024	J002218.9+001833	00 ^h 22 ^m 18.945 ^s	00° 18′ 33.1″	4.2′	5.5	2.2	-0.31 ± 0.23	5.4 ± 1.8	1.2 ± 0.4	4 ± 2
WHDFCH028	J002234.2+001609	00 ^h 22 ^m 34.187 ^s	00° 16′ 08.6″	4.7′	10.1	2.9	-0.32 ± 0.17	6.1 ± 1.5	1.4 ± 0.3	5 ± 1
WHDFCH030	J002224.7+001640	00 ^h 22 ^m 24.699 ^s	00° 16′ 39.6″	4.7′	11.3	3.1	-0.27 ± 0.17	6.7 ± 1.5	1.4 ± 0.3	5 ± 2
WHDFCH034	J002237.6+001555	00 ^h 22 ^m 37.648 ^s	00° 15′ 55.4″	5.1′	1.7	0.7	-0.72 ± 0.19	2.1 ± 0.9	0.9 ± 0.3	1 ± 1
WHDFCH036	J002231.7+002539	00 ^h 22 ^m 31.734 ^s	00° 25′ 38.8″	4.7′	90.2	9.3	-0.48 ± 0.04	63.0 ± 5.0	18.8 ± 1.0	44 ± 5
WHDFCH038	J002223.4+001602	00 ^h 22 ^m 23.442 ^s	00° 16′ 02.4″	5.4′	7.8	2.5	-0.66 ± 0.10	6.3 ± 1.3	2.7 ± 0.4	4 ± 1
WHDFCH042	J002213.2+001953	00 ^h 22 ^m 13.249 ^s	00° 19′ 53.4″	5.1′	4.3	1.6	-0.58 ± 0.17	3.5 ± 1.1	1.3 ± 0.3	2 ± 1

(continues...)

Table 2.5: Chandra sources detected in the WHDF field with $S/N \geq 3$ (continued).

Chandra ID	CXOWHDF	RA ^a	Dec ^a	Θ^b	Counts	SNR ^c	HR	Flux ($\times 10^{-15} \text{ erg cm}^{-2} \text{ s}^{-1}$)		
		(J2000)						(0.5–10 keV)	(0.5–2 keV)	(2–10 keV)
WHDFCH043	J002255.2+001907	00 ^h 22 ^m 55.172 ^s	00° 19′ 06.7″	5.7′	0.0	0.0	-0.20 ± 0.09	0.0 ± 0.0	0.0 ± 0.0	0 ± 0
WHDFCH044	J002255.1+002056	00 ^h 22 ^m 55.092 ^s	00° 20′ 55.7″	5.4′	48.0	6.8	0.60 ± 0.10	27.0 ± 4.0	1.0 ± 0.3	26 ± 4
WHDFCH045	J002251.5+001725	00 ^h 22 ^m 51.450 ^s	00° 17′ 24.5″	5.7′	12.5	3.1	-0.04 ± 0.19	6.9 ± 1.6	1.0 ± 0.3	6 ± 2
WHDFCH048	J002241.3+002533	00 ^h 22 ^m 41.297 ^s	00° 25′ 33.3″	5.0′	29.1	5.2	-0.43 ± 0.08	21.5 ± 3.0	5.9 ± 0.7	16 ± 3
WHDFCH049	J002240.3+002549	00 ^h 22 ^m 40.278 ^s	00° 25′ 48.6″	5.1′	19.1	4.0	0.49 ± 0.17	10.0 ± 2.0	0.5 ± 0.2	10 ± 2
WHDFCH052	J002233.3+001505	00 ^h 22 ^m 33.339 ^s	00° 15′ 04.8″	5.8′	17.2	3.8	-0.50 ± 0.10	12.0 ± 2.0	3.8 ± 0.5	8 ± 2
WHDFCH055	J002211.9+001950	00 ^h 22 ^m 11.862 ^s	00° 19′ 50.4″	5.4′	36.0	5.8	-0.22 ± 0.10	22.0 ± 3.0	4.2 ± 0.5	18 ± 3
WHDFCH058	J002255.1+001907	00 ^h 22 ^m 55.139 ^s	00° 19′ 07.4″	5.7′	43.0	6.3	-0.20 ± 0.09	25.0 ± 3.0	4.6 ± 0.6	20 ± 3
WHDFCH060	J002228.5+001502	00 ^h 22 ^m 28.453 ^s	00° 15′ 01.9″	6.0′	32.0	5.4	-0.32 ± 0.09	19.0 ± 3.0	4.4 ± 0.6	15 ± 3
WHDFCH061	J002225.4+001456	00 ^h 22 ^m 25.402 ^s	00° 14′ 55.5″	6.3′	25.7	4.7	-0.10 ± 0.13	15.0 ± 2.5	2.3 ± 0.4	12 ± 2
WHDFCH066	J002212.0+001817	00 ^h 22 ^m 11.953 ^s	00° 18′ 17.1″	5.9′	12.8	3.0	-0.46 ± 0.12	8.5 ± 1.7	2.5 ± 0.4	6 ± 2
WHDFCH067	J002211.8+001836	00 ^h 22 ^m 11.801 ^s	00° 18′ 36.1″	5.8′	5.9	1.8	-0.39 ± 0.20	3.7 ± 1.1	1.0 ± 0.2	3 ± 1
WHDFCH069	J002210.7+002238	00 ^h 22 ^m 10.728 ^s	00° 22′ 37.5″	5.8′	14.1	2.9	0.64 ± 0.18	6.8 ± 1.7	0.2 ± 0.1	7 ± 2
WHDFCH071	J002253.3+001660	00 ^h 22 ^m 53.293 ^s	00° 16′ 59.6″	6.3′	116.0	10.6	0.69 ± 0.06	61.0 ± 6.0	1.6 ± 0.3	59 ± 5
WHDFCH076	J002232.7+002702	00 ^h 22 ^m 32.679 ^s	00° 27′ 02.2″	6.1′	19.8	4.1	-0.31 ± 0.12	12.3 ± 2.2	2.7 ± 0.4	10 ± 2
WHDFCH080	J002208.8+002159	00 ^h 22 ^m 08.772 ^s	00° 21′ 59.3″	6.2′	4.0	0.9	-0.60 ± 0.17	3.4 ± 1.1	1.3 ± 0.3	2 ± 1
WHDFCH083	J002258.9+001755	00 ^h 22 ^m 58.865 ^s	00° 17′ 54.8″	7.0′	55.3	7.0	0.05 ± 0.09	31.0 ± 4.0	3.6 ± 0.5	27 ± 4
WHDFCH088	J002251.6+002526	00 ^h 22 ^m 51.555 ^s	00° 25′ 25.9″	6.4′	27.4	4.5	0.40 ± 0.14	14.1 ± 2.5	0.8 ± 0.2	13 ± 3
WHDFCH090	J002248.8+001519	00 ^h 22 ^m 48.795 ^s	00° 15′ 18.7″	6.8′	73.2	8.2	-0.40 ± 0.05	48.0 ± 4.0	12.6 ± 0.9	36 ± 4
WHDFCH091	J002240.2+001357	00 ^h 22 ^m 40.232 ^s	00° 13′ 57.2″	7.1′	24.9	4.2	-0.06 ± 0.13	14.1 ± 2.4	2.1 ± 0.4	12 ± 2
WHDFCH094	J002235.7+002706	00 ^h 22 ^m 35.654 ^s	00° 27′ 06.4″	6.2′	21.3	3.9	0.54 ± 0.18	10.7 ± 2.2	0.5 ± 0.2	10 ± 2
WHDFCH099	J002211.2+002404	00 ^h 22 ^m 11.187 ^s	00° 24′ 04.1″	6.3′	16.9	3.6	0.10 ± 0.17	8.8 ± 1.9	1.0 ± 0.2	8 ± 2

(continues. . .)

Table 2.5: Chandra sources detected in the WHDF field with $S/N \geq 3$ (continued).

Chandra ID	CXOWHDF	RA ^a	Dec ^a	Θ^b	Counts	SNR ^c	HR	Flux ($\times 10^{-15}$ erg cm $^{-2}$ s $^{-1}$)		
		(J2000)						(0.5–10 keV)	(0.5–2 keV)	(2–10 keV)
WHDFCH104	J002239.4+002734	00 ^h 22 ^m 39.373 ^s	00° 27′ 33.9″	6.8′	0.3	0.1	-0.64 ± 0.55	0.3 ± 0.3	0.1 ± 0.1	0 ± 0
WHDFCH105	J002230.6+002735	00 ^h 22 ^m 30.572 ^s	00° 27′ 35.4″	6.7′	22.5	3.6	0.15 ± 0.15	12.1 ± 2.3	1.2 ± 0.3	11 ± 2
WHDFCH109	J002209.9+001629	00 ^h 22 ^m 09.917 ^s	00° 16′ 28.9″	7.3′	82.2	8.7	-0.55 ± 0.04	67.0 ± 5.0	22.9 ± 1.4	44 ± 5
WHDFCH110	J002207.4+002308	00 ^h 22 ^m 07.433 ^s	00° 23′ 07.7″	6.8′	29.9	5.1	-0.42 ± 0.08	22.0 ± 3.0	6.0 ± 0.7	16 ± 3
WHDFCH113	J002301.2+001918	00 ^h 23 ^m 01.247 ^s	00° 19′ 18.0″	7.1′	8.5	1.8	-0.43 ± 0.16	6.0 ± 1.5	1.7 ± 0.4	4 ± 1
WHDFCH116	J002237.5+002747	00 ^h 22 ^m 37.520 ^s	00° 27′ 46.9″	6.9′	6.3	1.2	-0.27 ± 0.23	4.5 ± 1.4	0.9 ± 0.3	4 ± 1
WHDFCH120	J002234.5+001312	00 ^h 22 ^m 34.489 ^s	00° 13′ 11.7″	7.7′	5.9	1.2	-0.73 ± 0.09	6.0 ± 1.3	3.0 ± 0.5	3 ± 1
WHDFCH127	J002256.2+001526	00 ^h 22 ^m 56.207 ^s	00° 15′ 26.0″	7.9′	13.6	2.1	0.01 ± 0.19	8.3 ± 1.9	1.1 ± 0.3	7 ± 2
WHDFCH131	J002229.8+001241	00 ^h 22 ^m 29.847 ^s	00° 12′ 41.2″	8.2′	7.2	1.0	-0.58 ± 0.13	5.6 ± 1.3	2.0 ± 0.4	4 ± 1
WHDFCH136	J002303.6+002242	00 ^h 23 ^m 03.603 ^s	00° 22′ 42.3″	7.7′	15.6	2.8	-0.19 ± 0.16	12.0 ± 2.5	2.2 ± 0.5	10 ± 2
WHDFCH138	J002259.1+002528	00 ^h 22 ^m 59.139 ^s	00° 25′ 27.8″	7.8′	84.3	8.7	-0.33 ± 0.05	78.0 ± 7.0	18.2 ± 1.4	60 ± 6
WHDFCH139	J002240.2+002833	00 ^h 22 ^m 40.242 ^s	00° 28′ 32.5″	7.8′	9.3	1.2	-0.62 ± 0.10	7.5 ± 1.5	3.0 ± 0.5	5 ± 1
WHDFCH141	J002250.4+001317	00 ^h 22 ^m 50.369 ^s	00° 13′ 17.0″	8.7′	24.1	3.1	-0.28 ± 0.11	15.5 ± 2.5	3.3 ± 0.5	12 ± 2
WHDFCH143	J002241.9+002830	00 ^h 22 ^m 41.929 ^s	00° 28′ 29.9″	7.8′	7.5	0.8	-0.44 ± 0.17	5.1 ± 1.3	1.4 ± 0.3	4 ± 1
WHDFCH145	J002229.5+001200	00 ^h 22 ^m 29.515 ^s	00° 12′ 00.2″	8.9′	18.1	2.1	-0.49 ± 0.10	13.9 ± 2.3	4.3 ± 0.6	10 ± 2
WHDFCH146	J002227.4+001209	00 ^h 22 ^m 27.424 ^s	00° 12′ 08.8″	8.8′	16.8	1.7	-0.08 ± 0.16	10.0 ± 2.0	1.5 ± 0.3	9 ± 2
WHDFCH151	J002200.9+001818	00 ^h 22 ^m 00.946 ^s	00° 18′ 17.5″	8.5′	10.6	1.3	-0.34 ± 0.16	6.8 ± 1.6	1.6 ± 0.3	5 ± 2
WHDFCH153	J002224.1+001156	00 ^h 22 ^m 24.072 ^s	00° 11′ 56.4″	9.2′	0.0	0.0	-1.00 ± 0.00	2.4 ± 0.4	2.4 ± 0.4	0 ± 0
WHDFCH154	J002201.2+001721	00 ^h 22 ^m 01.173 ^s	00° 17′ 21.3″	8.7′	15.5	1.7	-0.06 ± 0.17	9.2 ± 2.0	1.4 ± 0.3	8 ± 2
WHDFCH159	J002245.4+002922	00 ^h 22 ^m 45.370 ^s	00° 29′ 21.8″	8.9′	54.6	5.9	-0.51 ± 0.05	41.0 ± 4.0	13.0 ± 1.0	28 ± 4
WHDFCH160	J002236.5+002937	00 ^h 22 ^m 36.486 ^s	00° 29′ 36.8″	8.7′	8.5	1.0	-0.46 ± 0.15	7.5 ± 1.8	2.2 ± 0.4	5 ± 2
WHDFCH161	J002157.7+001857	00 ^h 21 ^m 57.654 ^s	00° 18′ 56.6″	9.1′	27.7	3.8	-0.28 ± 0.10	23.0 ± 4.0	5.0 ± 0.6	19 ± 4

(continues. . .)

Table 2.5: Chandra sources detected in the WHDF field with $S/N \geq 3$ (continued).

Chandra ID	CXOWHDF	RA ^a	Dec ^a	Θ^b	Counts	SNR ^c	HR	Flux ($\times 10^{-15} \text{ erg cm}^{-2} \text{ s}^{-1}$)		
		(J2000)						(0.5–10 keV)	(0.5–2 keV)	(2–10 keV)
WHDFCH162	J002222.6+001050	00 ^h 22 ^m 22.645 ^s	00° 10′ 49.6″	10.4′	70.1	5.4	-0.46 ± 0.05	51.0 ± 4.0	14.8 ± 1.1	36 ± 4
WHDFCH163	J002154.1+002309	00 ^h 21 ^m 54.101 ^s	00° 23′ 08.7″	10.0′	10.7	0.5	-0.46 ± 0.13	7.7 ± 1.7	2.3 ± 0.4	6 ± 2
WHDFCH164	J002308.1+001511	00 ^h 23 ^m 08.067 ^s	00° 15′ 11.3″	10.4′	16.0	1.1	-0.40 ± 0.12	12.2 ± 2.3	3.2 ± 0.5	9 ± 2
WHDFCH165	J002311.4+001533	00 ^h 23 ^m 11.441 ^s	00° 15′ 33.1″	10.9′	30.4	2.2	-0.15 ± 0.11	20.0 ± 3.0	3.3 ± 0.5	16 ± 3
WHDFCH166	J002214.8+001057	00 ^h 22 ^m 14.829 ^s	00° 10′ 56.7″	10.9′	31.7	1.8	-0.40 ± 0.08	27.0 ± 4.0	7.1 ± 0.8	20 ± 3

^aComparison of the ACIS-I data with optical astrometry revealed an aspect offset that caused coordinates to be shifted by $RA_d = 0.42$ and $DEC_d = -1.34''$; due corrections have been applied.

^bOff-axis distance from the aimpoint in arcminutes.

^cSignal-to-noise ratio in the hard 2–8 keV band as computed by MVM. Note that all sources listed have $S/N \geq 3$ in at least one band.

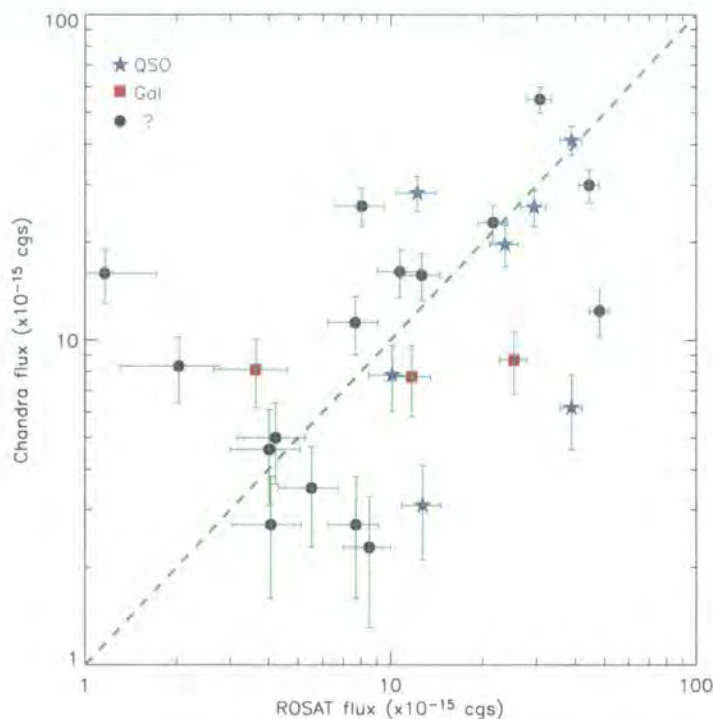


Figure 2.11: Chandra *vs.* ROSAT 0.5–2 keV fluxes for the same sources. Blue stars are QSOs and red squares are galaxies, while black dots lack spectroscopic identification.

2.3 Temporal Properties

Active galactic nuclei are known to be highly variable on all sort of time scales and over a wide range of frequencies. The study of their variability is an advantageous tool to assess the relationships between different emission spectral features and to determine intrinsic physical properties, such as its nuclear black hole size and mass. Without going into much detail, we have made simple comparisons to assess the temporal properties of our x-ray sample over two very different periods of time: a decade and a day.

2.3.1 Long Time-Scale Variability

The GSGP4 and F864 fields were actively surveyed with ROSAT in the 1990's. We have produced figure 2.11 to compare the fluxes derived from Chandra *versus* those previously found with ROSAT. This information is plotted for all Chandra sources which have a 4σ ROSAT counterpart within $15''$; it is therefore not complete in that it misses bright Chandra sources which remained undetected with ROSAT and *vice-versa*. Spectral information, if available, is also given. The plot shows that, regardless of type, at most $\sim 50\%$ of the sources seem to be constant flux-emitters

at decade time-scales. This fraction could in principle increase by a small amount due to confusion and blending of sources by ROSAT, but the number of sources detected with only one mission argues more strongly in the opposite direction and it is likely to lower the given upper limit.

2.3.2 Short Time-Scale Variability

We have taken advantage of the 20 hours of continuous Chandra observation of the WHDF to perform time series analysis of the photon flux for 20 of the brightest sources in search for \sim day-scale variability. We have found that $\sim 20\%$ of the sample show signs of acute flux changes at these scales. Figure 2.12 on the following page shows the examples.

2.4 Number Counts

The number-flux relation in any of its forms is the most fundamental measure which directly describes the contribution of individual sources to the XRB. In this section we compute the differential source counts, $n(S)$, and the cumulative number counts, $N(> S)$, for the soft and hard bands. We also calculate the source contribution of the WHDF survey towards the hard x-ray background.

2.4.1 Methodology

The differential counts, $n(S)$, are the sum of the reciprocal areas available for detecting a source in the flux interval, $\Omega(S)$, divided by the width of the flux interval, ΔS :

$$\begin{aligned} n(S) &\equiv \frac{dN(> S)}{dS} \\ &= \sum \frac{(1/A_i)}{\Delta S} \end{aligned} \quad (2.2)$$

It follows that the cumulative source counts, $N(> S)$, are the sum of the inverse areas of the sources that are brighter than flux S .

The sky area over which a source may be observed depends on the flux limit at each pixel in the image, which in turn is a function of the PSF and the effective exposure at every pixel.

In order to find the sky coverage available to a given flux limit S_{lim} at signal to noise ratios larger than a given threshold, $S/N \geq \zeta$, we proceed as follows. First we consider a source with a flux S_{lim} that falls on pixel i, j ; the S/N at which such a source would be detected in a fixed-size cell centred at pixel i, j is computed and its value assigned to pixel i, j . Then all pixels for which $S/N \geq \zeta$ are counted and this is converted to sky area with the knowledge of the pixel scale.

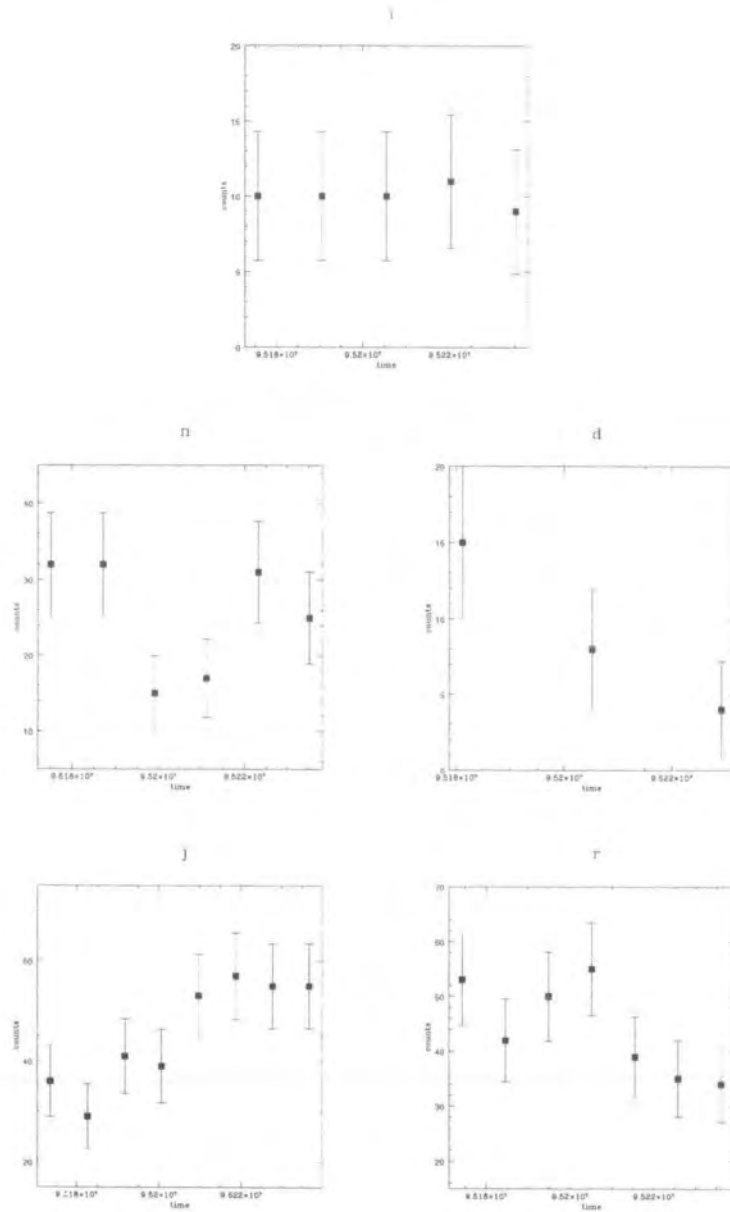


Figure 2.12: X-ray variability (counts *versus* time) in some bright sources of the WHDF. Source *i* is an example of a constant source, while the other four sources show signs of variability on short time-scales.

Using the same notation as in equation (2.1), the number of net counts, C , within a detection cell relates to the energy flux, S , via the formula

$$C = S \times \tau \times \kappa \quad (2.3)$$

where κ is the count-rate to energy-flux conversion factor and is constant, and τ is the effective exposure, which is accounted for with exposure maps (§ 2.2.2). However, the counts that fall in the detection cell depend on the fraction of energy that is spread within the cell, which is given by the integral of the point spread function over the cell, α . Therefore the counts within the detection cell for a source with flux S_{lim} can be found solving the equation

$$C_{\text{lim}}^{i,j} = S_{\text{lim}} \times \tau^{i,j} \times \kappa \times \alpha^{i,j} + B \quad (2.4)$$

where B is the expected background counts in the detection cell.

For each instrument configuration (ACIS-I & ACIS-S), HRMA PSF morphologies across the image were extracted from the Chandra 2d_PSF library files⁶, included in the CIAO software distribution (Jerius et al. 2000). Given that the off-axis angle of the source is within the library field of view, monochromatic PSF model images in library files No. 1 (F1) were used. The PSF models were calculated for defocus=0 position and a single energy of 1.4967 keV for the soft band and for an energy of 4.51 keV for the hard band.

The counts $C^{i,j}$ are used together with background estimations from table 2.1 to calculate the S/N at pixel i, j :⁷

$$\text{SNR}^{i,j} = \frac{C_{\text{lim}}^{i,j} - B}{\sqrt{\sigma_C^2 + \sigma_B^2}} = \frac{S_{\text{lim}} \times \tau^{i,j} \times \kappa \times \alpha^{i,j}}{\sqrt{\sigma_C^2 + \sigma_B^2}}. \quad (2.5)$$

Thus “flux limit maps” of the Chandra image are constructed for a range of fluxes and the sky area available at a given flux limit is found by summing all the pixels with S/N values larger than this limit, $S/N \geq \zeta$. Figure 2.13 on the next page displays the sky area available at the flux limit of the WHDF survey, for which we have set $\zeta = 3$. It tells us that the survey reaches 3σ flux limits of $4 \cdot 10^{-16}$, 10^{-15} and $3 \cdot 10^{-15} \text{ erg cm}^{-2} \text{ s}^{-1}$ in the soft, total and hard energy bands, respectively. For the 10×10 ks survey, a similar analysis shows that the flux limits are $3 \cdot 10^{-15}$ and $10^{-14} \text{ erg cm}^{-2} \text{ s}^{-1}$ in the soft and hard bands, respectively.

⁶<http://asc.harvard.edu/cal/Hrma/hrma/psf>

⁷Note that B and σ_B are calculated from a set of background regions and therefore their values are independent of $C^{i,j}$.

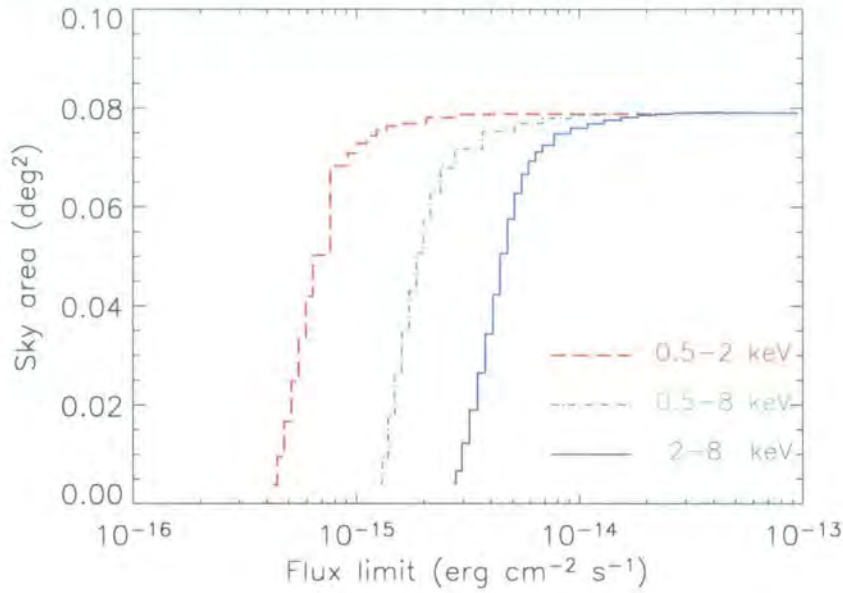


Figure 2.13: Cumulative distribution of sky area available at WHDF survey flux limit (3σ).

Incompleteness & Bias

The $\log N$ vs. $\log S$ parameters derived in the following subsection could be subject to some biases: *a)* source confusion, *b)* contamination by fake sources, *c)* inefficiency of source detection, *d)* Eddington bias.

Source confusion is not an issue because the sky density of sources detected and Chandra’s superb spatial resolution does not allow for it (according to Alexander et al. 2003 source confusion is not an issue even at 2 Ms exposures). On the other hand, detection of spurious sources is a more likely contaminant, particularly at large off-axis distances. However, we have selected sources found at S/N where this effect is very small; also it has been further reduced by careful visual selection of sources at large radii from the aimpoint.

Eddington (1913) noted that the flux distribution of the detected sources suffers from a bias resulting from the fact that faint sources can be detected only if superposed on positive background fluctuations and therefore their fluxes are systematically overestimated. We have not undertaken Monte Carlo simulations to assess its effect on our data, but instead have scaled the results from other teams. In the 1 Ms surveys this bias starts affecting the data at a level of 20 and 30 counts in the soft and hard bands respectively. Assuming that most noise is due to unresolved residual XRB that scales linearly with exposure, our background levels in the WHDF are $\sim 7.5\%$ of the 1 Ms exposures. At our survey limit of 3σ , sources typically have 10–12 counts, and hence Eddington bias is bound to be a minor effect. Further support for this is found in surveys of similar characteristics as the ones here presented. For instance, Eddington bias is found to over-estimate the cumu-

lative number counts by about 1% in the ACIS-I 75 ks exposures of the ELAIS fields (Manners et al. 2003). Also Cowie et al. (2002) measured the effects of incompleteness and bias for a sample of sources including observations of the Hawaii Survey fields SSA13 and SSA22, similar to the WHDF in observational details, and concluded that the number counts of sources with fluxes above a few times $10^{-15} \text{ erg cm}^{-2} \text{ s}^{-1}$ were exempt of any of these issues. Finally, Yang et al. (2003) confirm that above flux thresholds of 10 (soft) and 12 (hard) counts per exposures from $40 \lesssim \tau \lesssim 70$ ks, the detection is complete and the derived fluxes consistent with the input values in Monte Carlo simulations and, in particular, Eddington bias is small and can be safely ignored.

2.4.2 Results

We determine the source counts from 3×10^{-15} to $10^{-13} \text{ erg cm}^{-2} \text{ s}^{-1}$ in the 2–10 keV band and from 4×10^{-16} to also $10^{-13} \text{ erg cm}^{-2} \text{ s}^{-1}$ in the 0.5–2 keV soft band. This yields about two decades in logarithmic flux for the study of the $\log N$ vs. $\log S$ dependence.

Cumulative Number Counts

For each source we compute its S_N in the relevant band according to equation (2.5) and find the corresponding available area, A_i , for the flux of the source that corresponds to the given S_N . We then compute the cumulative number counts as

$$N(S) = \sum \frac{1}{A_i}. \quad (2.6)$$

Figure 2.14 on the following page shows the cumulative number counts for the WHDF and the 10×10 ks survey, in the soft and hard energy bands. We immediately note the excellent overlap of the two hard number count curves. Indeed, in all the common range, from $-14.5 \lesssim \log S_X(\text{cgs}) \lesssim -13$, they are almost indistinguishable. The agreement in the soft band is not as good and there seems to be a shortage of sources in the WHDF in the range $-14. \lesssim \log S_X(\text{cgs}) \lesssim -13.9$. The spread in the normalisation in this region is considerable, of $\sim 50\%$, much larger than what would be expected from only Poisson statistics in the fields. However this comes as no surprise since the area observed in our fields is small and the spread can easily accommodated as cosmic variance. In fact, Cowie et al. (2002) report a similar spread ($\sim 40\%$) in the normalisations of the counts in the SSA13, CDF-N, CDF-S and *Lockman Hole* fields, although in the hard band. As we say, modern x-ray detectors suffer from smallness of FOV and hence deep surveys are limited in sky coverage; as a result, a large number of surveys are mandatory to obtain self-consistent and accurate estimates of the evolution of the sources over a wide range of fluxes.

Also in figure 2.14, an early prediction of the Chandra number counts based solely on ROSAT data (using Boyle et al. 1994 x-ray luminosity function, model

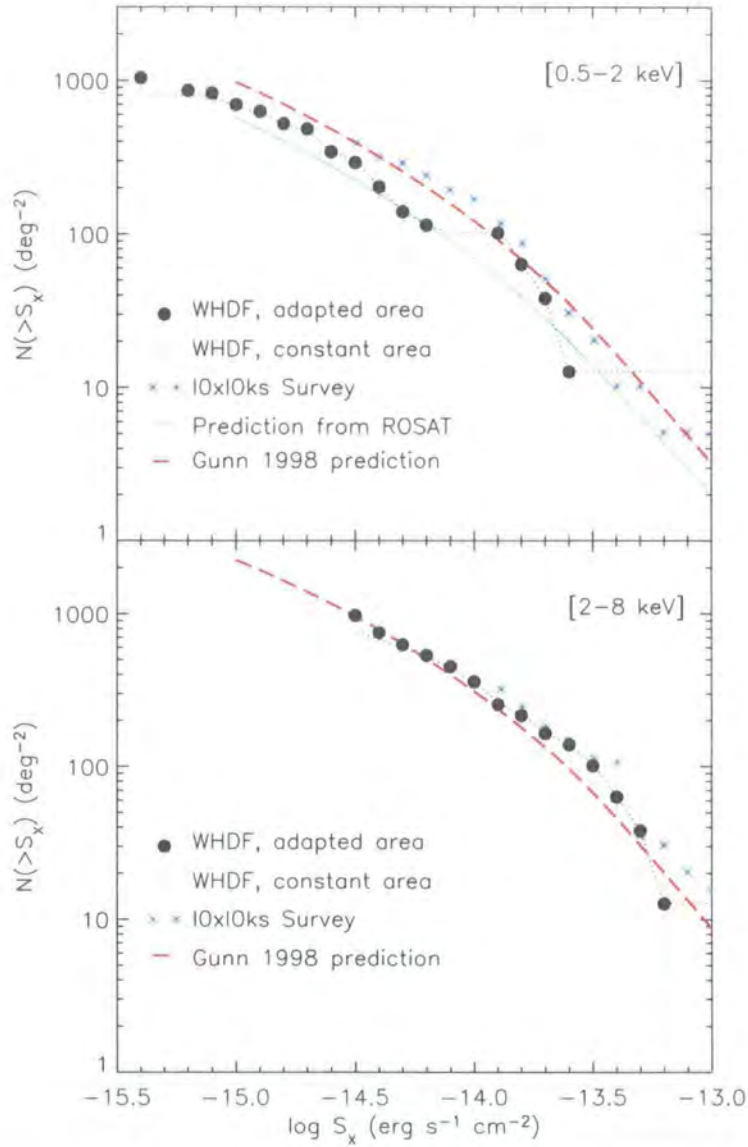


Figure 2.14: Cumulative source number counts per square degree for sources detected in the soft (top) and hard (bottom) band images, in the WHDF and 10×10 ks surveys. The dotted line following the same distribution as the WHDF black dots are the number counts if the area of the survey is taken as constant as opposed to being a function of flux; we note that diverging effects are only observed at the faintest limits. Plotted as a thin green line in the soft band, an early prediction from ROSAT data is seen to underpredict the counts. On the other hand, the predictions from Gunn (1999) fit the data in both bands very well (red thick dashed line).

POW0.0 and extrapolating to faint fluxes) is also plotted in the soft band. Although its shape is in overall agreement with the Chandra $\log N$ vs. $\log S$, it seems to systematically underpredict the observed number counts. A likely explanation is the emergence of a new population of sources at fainter limits which are intrinsically harder. These sources would output a sizeable fraction of their output at soft energies, but the fact that the sensitivity of x-ray detectors and their PSF depend on the spectral shape of the sources would explain why the ROSAT models, based on an instrument with peak-sensitivity at softer energies than Chandra even though they cover a common energy band (~ 1 keV vs. ~ 1.5 keV in the 0.5–2 keV band, respectively), underpredict the number counts. Hence they would be more easily detected with Chandra. Support for this hardening being the result from the absorption of the softest x-ray photons comes from straight comparison of the hard and soft counts. We see that the hard $\log N$ vs. $\log S$ is marginally steeper than the soft one (see equations 2.7 and 2.8), which means that the ratio of hard to soft sources increases towards fainter fluxes, consistent with the explanation of absorption, which will act to harden and dim the x-ray flux observed.

On the same plot we compare the observed number counts with the predictions of Gunn (1999) (using Model G of Boyle et al. 1994). These are based on an AGN population synthesis model of a flat distribution of column densities in logarithmic space (figure 1.6). We see that the agreement in the hard band is good, although the counts below $\log S_X(\text{cgs}) \lesssim -13.7$ seem to be systematically slightly underpredicted. It is difficult to judge due to the large error bars of the data points at bright fluxes, but it could be a sign that the prediction is overall marginally steeper than the observed curve. In the soft band the agreement is equally plausible once we take into account the shortage of sources detected in the WHDF in the flux range $-14.3 \lesssim \log S_X(\text{cgs}) \lesssim -13.9$.

Finally, we note that the correction for the available surface being dependent on flux is only appreciable at the faintest limits and the divergence is more acute in the hard band (the WHDF number counts with a constant area equal to the size of the ACIS-I FOV are shown as a dotted line labelled as “WHDF constant area”).

We fit the slope of the $\log N$ vs. $\log S$ for each band with a power-law using a weighted least-squares method and compare it with results published in the literature. In figure 2.15 we plot the cumulative source counts per square degree for the soft and hard bands in the WHDF (filled circles) with 1σ uncertainty bars (incorporating Poisson number statistics but not accounting for flux estimation uncertainties nor for the available area of the survey at the flux limit of our survey). Also shown are the results from Mushotzky et al. (2000) on the SSA13 field (red filled area), Giacconi et al. (2001) on the *Chandra Deep Field-South* (CDF-S; blue filled area) and Brandt et al. (2001) on the *Chandra Deep Field-North* (CDF-N; stripped area) obtained from their quoted best-fitting power-laws and uncertainties. The best power-law fit to our data is shown in the figure as a thick yellow

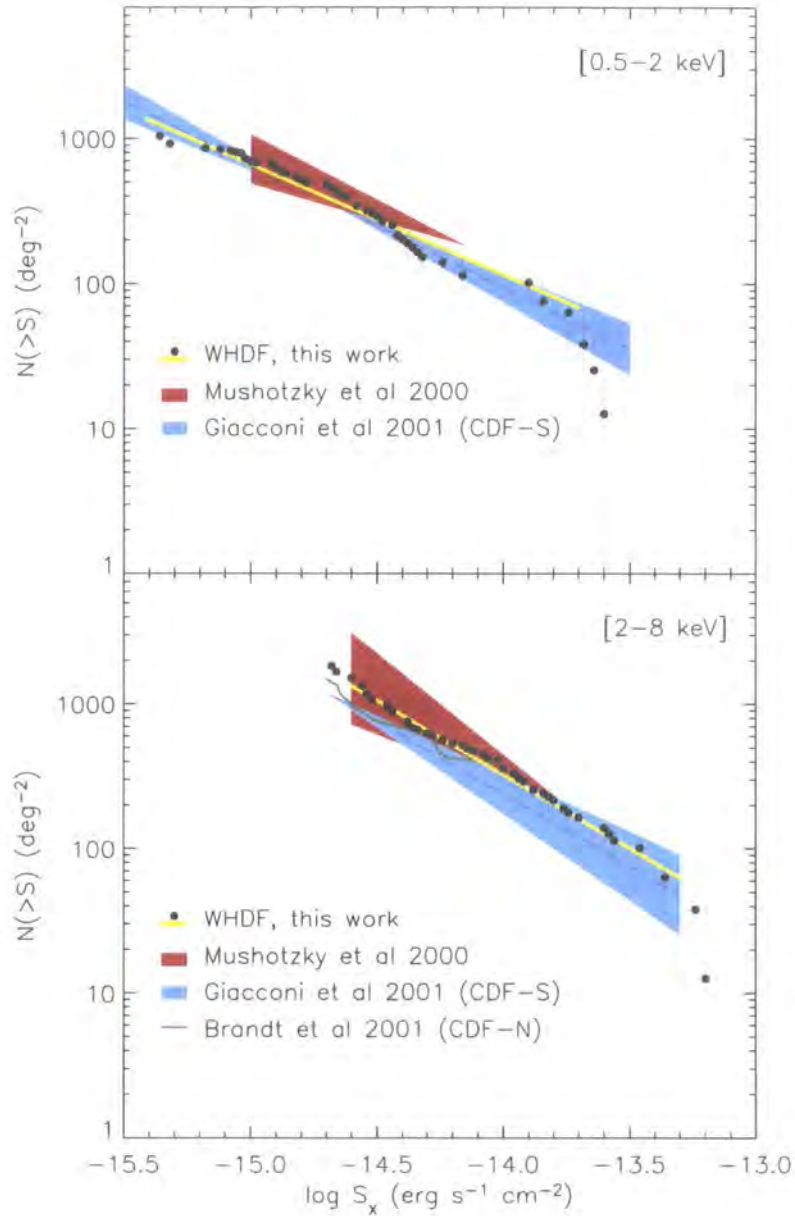


Figure 2.15: Cumulative source number counts per square degree for sources detected in the soft (top) and hard (bottom) band images of the WHDF. Filled circles (with 1σ uncertainty bars) are data points and the yellow strip shows the best-fitting power law. The data is compared with the source counts on SSA13 of Mushotzky et al. 2000 (red shading), on CDFs of Giacconi et al. 2001 (blue shading) and on CDFN of Brandt et al. 2001 (green line).

line and for the soft band has a shape of:

$$\log N = (-8.6 \pm 0.4) - (0.76 \pm 0.03) \log S \quad (2.7)$$

while for the hard band it can be represented by:

$$\log N = (-11.8 \pm 0.5) - (1.02 \pm 0.04) \log S \quad (2.8)$$

Equation (2.7) gives a fit almost identical to that found in the CDF-S by Giacconi et al. in the flux range where both surveys overlap and confirm earlier results with ROSAT of a slope of 0.8 ± 0.2 . Above $3 \times 10^{-15} \text{ erg cm}^{-2} \text{ s}^{-1}$ our data also agree well with Mushotzky et al. but, below that flux, the WHDF suffers a depletion of sources around $\log S_{0.5-2 \text{ keV}} \simeq 14$ (cgs) and the agreement is not good. In the hard band, the fit given by equation (2.8) is in perfect agreement with the results of Mushotzky et al. and clearly confirm a break in the slope compared to the quasi-Euclidean behaviour at brighter fluxes (e.g. Cagnoni et al. 1998).

Differential Number Counts

Differential number counts have many advantages radioastronomers are well acquainted with. The two most notable are in the statistical independence of the data points and in the ease with which breaks and shape changes might be seen (Jauncey 1975). We have plotted in figure 2.16 the differential source counts per square degree per unit flux as filled circles with 1σ uncertainty bars (as for the cumulative counts, including only Poisson uncertainties on the counts). We have normalised to a unit flux of $10^{-15} \text{ erg cm}^{-2} \text{ s}^{-1}$ and multiplied the differential $n(S)$ function by $S^{2.5}$ since in this representation an Euclidean $n(S)$ yields a horizontal line. A weighted least-square fitting with a single power-law has been attempted in the soft and in the hard bands. In the former the best fit is given by:

$$\log n(S) = (-22.7 \pm 1.5) - (1.7 \pm 0.1) \log S \quad (2.9)$$

over the flux range $(0.6-32) \times 10^{-15} \text{ erg cm}^{-2} \text{ s}^{-1}$. For the 2–8 keV band over the flux range $(2-80) \times 10^{-15} \text{ erg cm}^{-2} \text{ s}^{-1}$ the best fit is:

$$\log n(S) = (-25.7 \pm 0.4) - (1.94 \pm 0.03) \log S \quad (2.10)$$

As can be seen in figure 2.16 these fits are very similar to that of the ELAIS Deep x-ray Survey (Manners et al. 2003). They are also in very good agreement with the results from the CHAMP survey of Kim et al. (2004). In the soft band, however, the fit by a single power-law is not as satisfactory as in the hard band. Cowie et al. (2002) fit a broken power-law to the combined counts of the CDF-S, CDF-N, SSA13

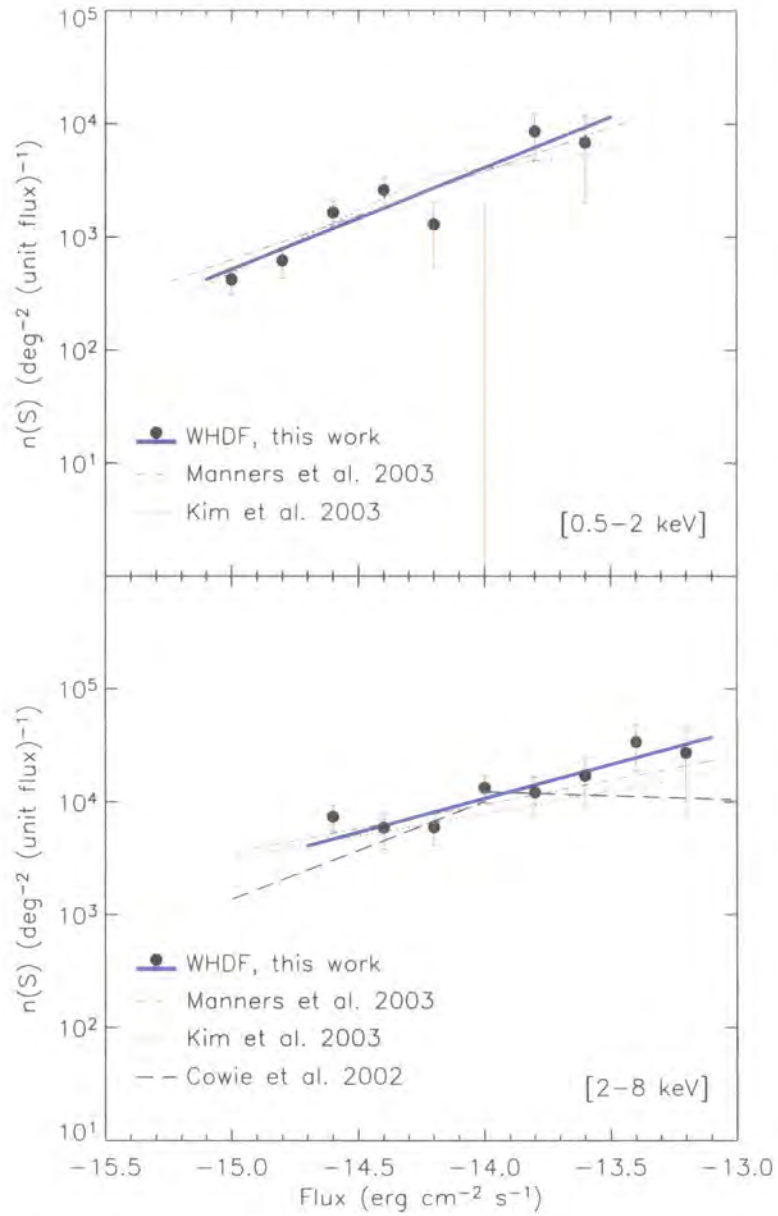


Figure 2.16: Differential source number counts per square degree and unit flux normalised by $S^{2.5}$ at a flux of $10^{-15} \text{ erg cm}^{-2} \text{ s}^{-1}$ for sources detected in the soft (top) and hard (bottom) band images of the WHDF. $n(S)$ has units of number per square degree per $10^{-15} \text{ erg cm}^{-2} \text{ s}^{-1}$.

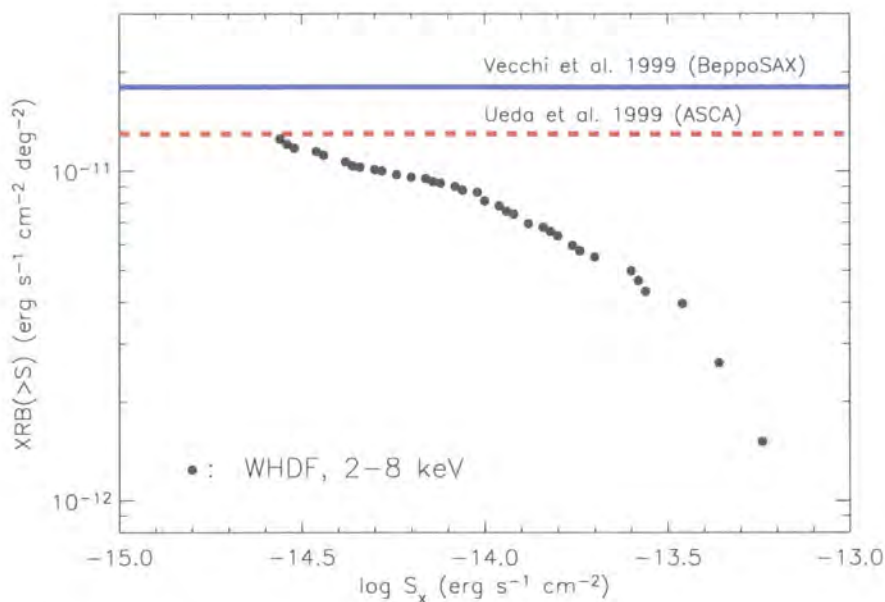


Figure 2.17: Contribution to the hard x-ray background. We plot the integrated hard band flux for sources fainter than $10^{-13} \text{ erg cm}^{-2} \text{ s}^{-1}$ in the WHDF and compare it to the normalisations from BeppoSAX and ASCA.

& SSA22 Chandra fields in the 2–8 keV band and their results agree comfortably within the error limits of our data.

2.4.3 Resolved Fraction of the Hard X-ray Background

Our fitted $N(>S)$ gives an integrated contribution of $1.25 \times 10^{-11} \text{ erg cm}^{-2} \text{ s}^{-1} \text{ deg}^2$ for fluxes $2.75 \lesssim S \text{ (cgs)}/10^{-15} \lesssim 100$ in the hard band. The actual resolved fraction of the XRB depends on the absolute intensity of the XRB emission, which different studies esteem different by $\sim 30\%$. When the contributions above $10^{-13} \text{ erg cm}^{-2} \text{ s}^{-1}$ from Giommi et al. (2000), della Ceca et al. (2001) and Ueda et al. (1999) are subtracted, Vecchi et al. (1999) and Ishisaki et al. (1999) measure residual values of 1.8 and $1.3 \times 10^{-11} \text{ erg cm}^{-2} \text{ s}^{-1} \text{ deg}^2$, respectively for the hard XRB. Taking the latter value, the contribution of resolved sources in the WHDF accounts for virtually the whole 2–8 XRB. On the other hand, it makes up to $\sim 70\%$ of the hard XRB if we take the BeppoSAX measurements. In this case, given that the peak contribution arises near the break at $1.4 \times 10^{-14} \text{ erg cm}^{-2} \text{ s}^{-1}$, while at the faint end counts converge slower than logarithmically and therefore faint sources provide a small contribution to the XRB, it seems that there would still be room for a new class of source or even a small contribution from diffuse emission.⁸

⁸*cf.* e.g. Fukugita et al. (1998); Phillips et al. (2001) in regard to the problem of the missing baryons in the local universe compared to the expectations from Big Bang nucleosynthesis arguments and observed light-element ratios, which could be in warm/hot diffuse intergalactic structures.

2.5 Spectral Properties

A hardness ratio defined as $HR = (S_H - S_S)/(S_H + S_S)$, with S_H and S_S being the count fluxes in the hard and soft band respectively, was computed to study the x-ray spectral properties of the detected sources. A plot of hardness ratio versus x-ray fluxes for each of the detected sources can be found in figure 2.18. Assuming that each source can be described by a single power-law, $P(E) \propto E^{-\Gamma}$ with P being the photon intensity (units of $\text{photons cm}^2 \text{s}^{-1} \text{keV}^{-1} \text{sr}^{-1}$), E the photon energy and Γ the photon index, the ratios of the counts in the soft band to those in the hard band can be used to compute the photon indices of individual sources. For reference we have overplotted in figure 2.18 the hardness ratios corresponding to photon indices of $\Gamma = 2.2$ (adequate for the mean QSO spectrum), $\Gamma = 1.4$ (which approximately describes the XRB spectrum from 3 to 15 keV; e.g. Marshall et al. 1980; Gendreau et al. 1995; Vecchi et al. 1999) and of $\Gamma = -1$.

Confirming the trend found with ROSAT (Hasinger et al. 1993; Almaini et al. 1996) we note a progressive hardening of the soft population as fluxes get fainter; the average spectrum for our sources in this band yields a photon index $\Gamma = 1.6 \pm 0.1$, flatter than the ROSAT-canonical of $\Gamma = 1.8$. This works into solving the spectral paradox. A hardening at fainter fluxes is not observed in the hard band. We worry that this result could be partially ascribed to selection effects favouring the detection of sources with intrinsically softer spectra at a given flux limit. However, it can easily accommodate within the framework of absorbed faint sources. Figure 1.5 shows how different energies are affected by different amounts of absorption and, while column densities of $n_H \sim 10^{22} \text{ cm}^2$ already seriously dim the soft 0.5–2 keV band, it takes columns well in excess of $n_H \sim 10^{23} \text{ cm}^2$ to dim the 2–10 keV range to a similar degree. Hence high hardness ratios caused by absorption will more likely imply faint fluxes in the soft band than in hard band. A similar conclusion is reached by detailed x-ray colour-colour analyses, such as those performed in the ChAMP survey by Kim et al. (e.g. 2004). These scientists find that the hardening occurs in the soft colour but not in the hard colour, suggesting that the cause for this is mainly absorption rather than intrinsic spectral hardening.

We also note that there is a large range of hardness ratios in the sample at all fluxes. At the faint end there is a smooth transition between soft and hard sources, but at brighter levels we observe a clear bimodality with a major group of soft bright sources with $HR \sim -0.7$ and a smaller group of hard bright sources with $HR \sim 0.3$; this bimodality is confirmed in both WHDF and 10×10 ks surveys. Therefore, there seems to be a relatively bright and hard ($\Gamma \simeq -0.1$) population of sources which make an appreciable contribution to the XRB. We will inspect with more detail this hard and bright population in section 4.3.

A final observation from the hardness ratio vs. fluxes plot is that in the F864 field the fraction of hard sources is much smaller than in the other two fields.

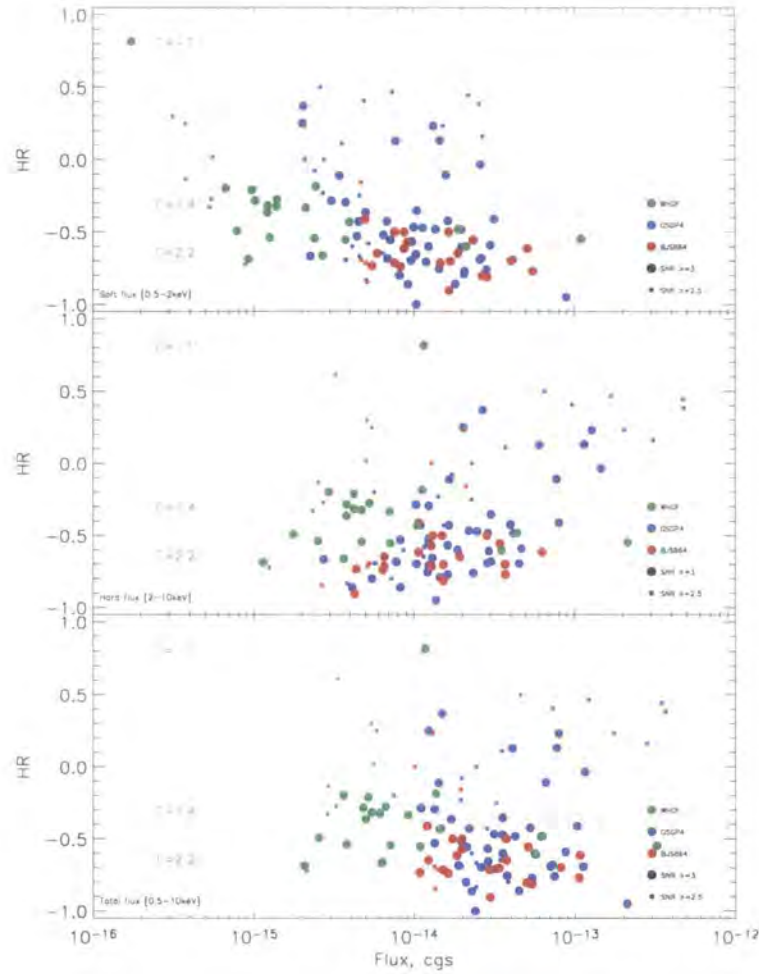


Figure 2.18: Hardness ratio versus fluxes in the soft (top), hard (middle) and total (bottom) bands. Green, blue and red colours represent sources in the WHDF, GSGP4 and F864 fields, respectively. We have included detections in the range $2.5 \leq S/N \leq 3$ as well, marked with small circles. For reference we have included some photon indices calculated assuming no intrinsic absorption. Note the progressive hardening towards fainter fluxes in the soft band and the presence of a population of very hard and bright sources and also that in the F864 field the sources are generally soft.

2.6 Summary

This chapter has been concerned with the x-ray data of the WHDF and 10×10 ks surveys of the cosmic XRB. We have reviewed the characteristics of the instrumentation involved in the data acquisition and the processes of data reduction and construction of catalogues of x-ray sources. In these catalogues there are 140 sources detected with $S/N \geq 3$ in at least one band. A very high proportion of hard (2–10 keV) sources (over 75%) are also detected with high significance in the soft band (0.5–2 keV). If the hard band population is representative of highly obscured AGN at low-to-intermediate redshifts ($z \lesssim 1.5$), this indicates that in type II AGN significant soft emission can still be produced. In the soft band, only $\sim 40\%$ of the sources are significant emitters in the hard band, which argues in favour of a large fraction of the XRB at soft energies resulting from unobscured AGN. We have assessed the basic temporal properties and showed that at most half of the x-ray sources seem to be constant flux-emitters over time-scales of a decade; at time-scales of a day, we find that acute flux changes might affect 10–20% of the brightest x-ray sources. We have then derived the source number counts down to fluxes of $4 \cdot 10^{-16}$ ($3 \cdot 10^{-15}$) and $3 \cdot 10^{-15}$ ($1 \cdot 10^{-14}$) $\text{erg cm}^{-2} \text{s}^{-1}$ in the soft and hard bands of the WHDF (10×10 ks) survey, and fitted their slopes with a power-law using a weighted least-squares method. We find a spread in the normalisations of the counts of $\sim 50\%$ in the two surveys, which we attribute to cosmic variance. Our fitted $\log N$ vs. $\log S$ in the WHDF are consistent with most other results in the literature, once cosmic variance is accounted for; in the soft band the fit is almost identical to that in the CDF-S while, in the hard band, excellent agreement is obtained with the results in the SSA13 survey. This results in an integrated contribution of $1.25 \times 10^{-11} \text{ erg cm}^{-2} \text{s}^{-1} \text{ deg}^2$ for fluxes $2.75 \lesssim S_{\text{(cgs)}/10^{-15}} \lesssim 100$ in the hard band. Finally, we have described the x-ray spectral properties of the sample. The sources are found to harden with soft flux but not with hard flux, as expected if their flat spectra are due to absorption of soft x-ray photons. We have also identified, from both surveys, a major group of hard bright sources with $HR \sim 0.3$ which seem to contribute appreciably to the XRB.

CHAPTER III

Optical follow-up of Chandra sources

The only uniform ccd is a dead one.

Mackay (1986)

This chapter reports on the imaging and spectroscopic efforts undertaken to identify in the more familiar optical and near-infrared domains the Chandra sources described in chapter 2. We describe herein the acquisition and reduction of data processes and present a description of the datasets employed.

Understanding the multiwavelength properties of x-ray sources is of utmost importance since it allows us to link by comparison our knowledge in different electromagnetic domains into a bigger synthetic picture. With Chandra's sub-arcsecond spatial resolution and such a long tradition in optical astronomy, correlating our Chandra sources with their optical/near-infrared counterparts is an unavoidable starting point to characterise and understand the populations that contribute to the XRB.

In order to maximise the number of sources for which information is available in the optical and in other wavelength regimes, we have undertaken a double program by searching in public catalogues (datamining) and by obtaining our own data (observational). The latter is convenient for it is tailored to fit our particular project, while the former is a cheap and suitable way to reach beyond our data, particularly for the more conspicuous sources. Compared to datamining, pursuing one's own optical surveys excels in the imaging and photometric aspects, while for the more expensive spectroscopic follow-up, we have found both approaches to data-gathering to be of similar efficiency.

In terms of datamining, for all fields we have searched the NASA *Extragalactic Database*. For the GSGP4 field we have also crosscorrelated our Chandra sources with the 2dFGRS (Colless et al. 2001) and the 2QZ (Croom et al. 2001) surveys,

while for fields WHDF and F864, data from the SDSS has proven useful, particularly for multi-colour photometry. In addition, we have pursued a) for field F864, deep optical imaging with INT/WFC and optical spectroscopy with WHT/ WYFFOS & AAT/2dF; b) for field GSGP4, optical imaging with AAT/WFI and optical spectroscopy with Magellan-1/LDSS2; c) in field WHDF, very deep optical and near-infrared imaging with WHT/ Prime Focus Camera, Calar Alto's Ω Prime, UKIRT & CTIO; and optical spectroscopy from Magellan-1/LDSS2 & Gemini-N/GMOS. An inventory of instruments and datasets used in each field is given in table 3.1 on the next page.

Sections 3.1–3.3 are concerned with the optical imaging (WFI on the GSGP4, WFC on the F864, the Herschel Deep Field, respectively); sections 3.4 & 3.5, with the optical spectroscopy (LDSS2 on the WHDF and GSGP4, WYFFOS on F864). Lastly, section 3.6 deals with the public data employed (NED, 2dF, SDSS).

3.1 Wide Field Imager

The Wide Field Imager (WFI) camera is a wide-field CCD imaging mosaic used at the f/3.3 prime focus of the 3.9 m Anglo-Australian Telescope (AAT; at the Coonabarabran observatory of Siding Springs).¹ It provides a focal plane detector system of 8192×8192 pixels made up of a 4×2 array of 2048×4096 15 micron pixel thinned, back-illuminated, CCDs cooled to ~ 170 K. In this format it yields a pixel scale near the field centre of $0.2295'' \text{ pixel}^{-1}$. Figure 3.1 on page 67 displays the distribution of the CCDs in the focal plane.

On 27th–28th December 2000 we employed WFI to target the GSGP4 field for a total of two hours equally split amongst the g (#90), r (#91) and i (#92) WFI Sloan filters into 4×600 s exposures each. Previous imaging and photometry in this region existed from UKST/APM/SuperCOSMOS but at much shallower (by ~ 4 mag) regimes. With our WFI data we cover an area of roughly $33' \times 33'$ centred on $\alpha = 00^h 57^m 57^s$, $\delta = -27^\circ 35' 19''$ (J2000) to a limiting depth of $g \sim 25.3$, $r \sim 25.0$, $i \sim 23.7$ magnitude (table 3.2).

3.1.1 WFI Data and Reduction Analysis

Prior to obtaining good photometry we reduced the data to remove any signatures from the instrument. The end result of the reduction process can be seen in figure 3.4 on page 73, which shows the mosaicked field in the i band.

The data reduction was carried out with a custom-written pipeline using mostly standard routines from the IRAF², Starlink³ and WCS-TOOLS⁴ (Mink 1997) suites. The same pipeline with minor adjustments had been employed successfully for the

¹<http://www.aao.gov.au>

²<http://iraf.noao.edu> (IRAF is distributed by the National Optical Astronomy Observatory which is operated by AURA Inc. under contract with the NSF).

³<http://www.starlink.rl.ac.uk>

⁴<http://tdc-www.harvard.edu/software/wcstools/index.html>

Table 3.1: Resources employed in each field.

Field	X-ray		Optical	
	Imaging	Spectroscopy	Imaging	Spectroscopy
WHDF	Chandra	–	WHDF/PFC, Ω Prime, UKIRT, CTIO.	LDSS2, GMOS.
GSGP4	Chandra	XMM	AAT/WFI.	LDSS2, 2dF.
F864	Chandra	XMM	INT/WFC, SDSS.	WYFFOS.

Table 3.2: Journal of the observations of the GSGP4 field with WFI on 27th–28th December 2000, including the photometric limits achieved.

RA ^a	DEC ^a	Band	Exposure ^b	Magnitude ^c	Area ^d	FWHM ^e
00 ^h 57 ^m 57 ^s	–27° 35′ 19″	<i>g</i> (#90)	40	25.3	0.30	2.0
00 ^h 57 ^m 57 ^s	–27° 35′ 19″	<i>r</i> (#91)	40	25.0	0.30	1.85
00 ^h 57 ^m 57 ^s	–27° 35′ 19″	<i>i</i> (#92)	40	23.7	0.30	1.40

^aNominal pointing, J2000.
^bIntegration time, in minutes
^c3 σ limit
^dCoverage, in square degrees
^eSeeing: full width at half maximum, in arcsec

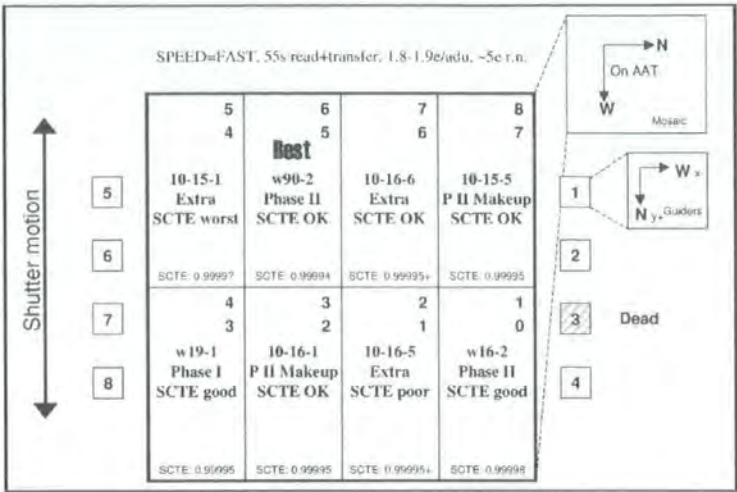


Figure 3.1: WFI focal plane layout.

reduction of WFC imaging in the F864 field (*cf.* § 3.2). WFI outputs pixel data in the form of multi-extension FITS (MEF) format files. After a failed attempt to use IRAF's MSCRED (with WFC data it would not deal successfully with linearity corrections and others), we found more convenient to convert the MEF files to plain FITS format. IRAF's imcopy did the job of splitting the mosaic images into single-chip images.

Debiasing

Instrumental signatures need to be removed in reverse order from which they were introduced and therefore the first step in reduction analysis is debiasing.

During the digitization process, A/D convertors can only measure a positive incoming signal but, in the presence of random readout noise and at low light levels, the true input signal can be negative. To prevent truncation of the negative signals, the signal is *biased* by adding a pedestal level before it passes through the A/D. This bias needs to be removed in order to maintain correct count ratios between different sources.

CCD detectors generate an underscan/overscan region by reading out the amplifier before/after all the charge from the pixel array has already been clocked, which can be used to monitor and correct this DC offset and RMS noise of the electrons. In the WFI chips the bias levels were not stabilised but fluctuated by several units (ADU) and therefore overscan subtraction was essential (with the added benefit that it also removed any fixed pattern noise). We debiased by fitting a scalar value for each CCD in each image individually from the overscan regions and then subtracting it from each column in the frame. This still left an appreciable fixed-pattern low-level structure from column-to-column variation in the composition of the bias level, which did not seem to vary neither with time nor with telescope point-

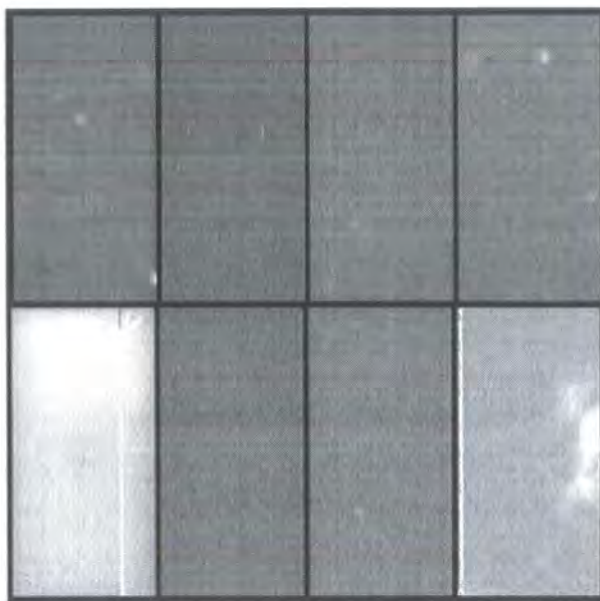


Figure 3.2: Image for a 1800 s dark frame taken with the guide CCD turned off, after zero subtraction, trimming and overscan subtraction. CCD4, with the worst dark current, shows considerable structure on large scales, as does CCD1 (note a bright region on its right edge). Chips 1,2,5,7 and 8 all show globular-cluster-like structure (“warm blobs”), where dark currents are elevated by 5–50 ADU per pixel over several hundred pixels. We had to subtract the thermal current from our science frames.

ing. We corrected this bias structure by subtracting a master zero frame, obtained by averaging (with minmax rejection) eighteen frames with zero integration times taken at the beginning and end of the night. At this point, images were trimmed to the final active CCD area.

Linearity Correction

The mosaic chips show significant nonlinearity effects over their full dynamic range, where the quantum efficiency is a function of the count level. This has an effect on photometric measurements, which could diverge for the same object in different frames to significant levels (a few tenths of magnitude). We corrected for nonlinearity by applying the WFI-website recommended third-order polynomials to the observed counts, bringing residual errors to a negligible degree ($< 0.2\%$).

Dark Current

WFI is operated in rather warm conditions and thermal excitation effects were apparent in our dark frames after removal of the overscan and bias levels (figure 3.2). The most prominent structures caused by dark current were on chips one and four, but some globular-cluster-like features could be seen in most chips.

A simple treatment demands three or more dark frames (long integrations with the shutter closed, of exposure times matched to those of the observations) in order to median-stack them to get rid of cosmic rays. Unfortunately we only obtained one dark during the observations and therefore had to pursue a slightly more involved path to get the dark frame free from cosmic rays. The aim being to locate those in the dark frame, we used `sExtractor` to construct an image of detected objects in the dark frame with the local background subtracted (an object *check* image). That *check* image indeed detected all the cosmic rays but unfortunately some of the globular-cluster-like structures were also included as objects. In this respect it would have been convenient that `sExtractor` had an option to limit the maximum number of pixels an object can have. But it did not, so to get rid of those in the *check* image we used the characteristic that the counts of the thermal noise are of the order of ~ 50 , much lower than those for cosmic rays, to substitute with IRAF's `imreplace` all values lower than κ , with $35 \leq \kappa \leq 75$ according to each particular structure, in those regions where dark current was detected as an object. We then subtracted with `imarith` the background-subtracted object *check* image from the linearly- and `badpixel-` (with `fixpix`) corrected dark frame. Finally, inspection of the resultant images showed that the dark-current patterns were still there but not a single cosmic ray was present (all values were < 100).

Subtraction of the dark frame (properly scaled to time exposures) corrected for the thermal current.

Flat Fielding

The quantum efficiency (QE) over an entire chip is never uniform. Local pixel-to-pixel variations are usually of a few percent in QE. Larger-scale spatial variations can be more important, particularly on thinned CCDs, where the thinning process is usually non-homogeneous. To calibrate for these sensitivity variations, along with likely illumination and filter throughput differences across the camera, images are flat fielded. Given their multiplicative nature, correction requires dividing the data by a flat-field.

Flat-fields are frames exposed to a uniform source of illumination, such that any response variations will be flagged. Three evening and three morning twilight flats (*i.e.*, short exposures of regions of sky devoid of stars taken in the beginning and end of each night) were taken with each filter and combined into a master flat-field. On passing, it is worth noting that the twilight sky has a different background spectrum than that which is observed in the dark night sky, which means that the illumination correction derived from twilight flats is likely to leave a non-uniform background of dark sky in observation frames. Obtaining a flatfield by combining the data itself after filtering out the astronomical objects would have the correct underlying illumination spectrum and so would produce the correct sensitivity for the detector. Unfortunately, the low quantity of data available from each night and also the presence of fringing in the r - and i -band images (see § 3.1.1) advised

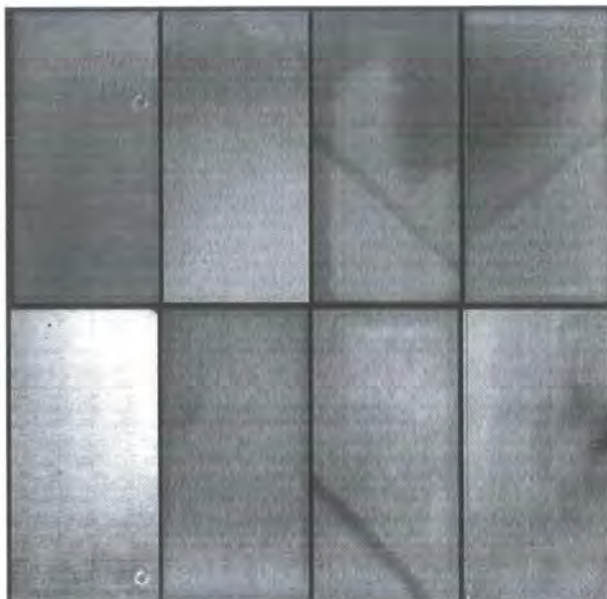


Figure 3.3: Example flat-field image for filter g , showing non-uniform response across the detector.

against taking this route. This fringing dominates the night sky spectrum in the science observations, but its contribution in the twilight sky flats is smaller because, at bright twilight, continuum emission dominates over line emission. Dome flats, where lamps illuminating the dome are used as a uniform background, were also regarded as unsatisfactory on the grounds that their spectrum did not reflect that of the night sky. Therefore a master flatfield frame in all g , r and i bands was created, comprising a median-combination of all available g , r and i twilight images for each night, rejecting deviant pixels using the `avsigclip` routine after scaling each of the individual frames by the inverse of the mode to obtain a less biased average given that some pixels are rejected. Figure 3.3 shows the master flat-field for the g filter.

Given that response may have changed through the night, the stability of the flats over that period (and hence the accuracy of the master flat-fields) was assessed by comparing the corresponding master flats from dusk to dawn, dividing one frame by the other (properly scaled) and studying the deviation from unity of the resultant image. In this way, flats were found to be highly uniform all across the frame and consistent with each other to better than 3%.

Data in each band were then flatfielded by dividing each science frame by the corresponding normalised flat obtained from dividing the flat by the average value before flat-field division, in order to roughly preserve the correct counts in the objects.

Sky frames flattened by the above procedure still displayed some illumination gradients (of the order of $\sim 5\%$) across the chips. To correct for this defect we cre-

ated an **illumination correction**. We imcombined all field images of the same effective exposure (already flatfielded) with a median operation, scaling & weighting by the mode and applying a cosmic ray rejection algorithm, to obtain new sky-flats (*raw sky-flats*). To remove any signal from objects not completely removed in the medianing of images, we constructed an object *check* image with `sextractor`. These *check* images were subtracted from the *raw sky-flats*. As commented above, the resulting images suffered from severe fringing in the *r* and *i* bands (*fringed sky flats*). The fringes were removed by convolving the sky flats with a Gaussian blur filter ($\sigma = 25$). An additional convolution, this time with a boxcar filter, proved advantageous to further smooth the images into the final sky-flats for the *r* and *i* images, where fringing was more severe. To obtain completely flat and uniform (constant throughput) chips, we first scaled the background level of every chip to that of chip number 6, which is allegedly the better-behaved chip, and then divided all field frames by the sky-flats, in the same way we flatfielded before.

Defringing

The night sky is mostly a continuum spectrum at optical regimes, but at longer wavelengths significant structure arises due to emission lines from molecules in the atmosphere, predominantly OH-radicals. The fringing effect is caused by the interference of multiple reflections between the two surfaces of the CCD when the wavelength of the incident light is an integer multiple of the distance between the two surfaces of the CCD (*cf.* Goudfrooij et al. 1998). On thinned CCDs such as WFI (which, as a result, achieve overall higher quantum efficiencies and respond better to blue wavelengths), the thickness of the detector is of the same order as the wavelength of these emission lines which, as a result, are amplified via interference in the chip. The fringes are additive and, although their intensity varies through the night, we found that their pattern remained stable in the course of the observing run (confirming that the relative strengths of the emission lines in the illumination spectrum remained constant). The amplitude variations were of the order of $\sim 5\%$ in the *i* filter, but the effects were already notorious with the *r* filter.

Fringe removal was achieved by subtracting a fringe image made from a combination of flat-fields. In particular, the same *fringed sky-flats* described above were scaled to the background of the data frame to defringe, which was subtracted from the scaled fringed flat. This scaling of the amplitude of the fringe mask to the amplitude of the fringes in each data frame before subtraction is important because emission line intensities vary on short time scales (\sim minutes) and so the level of fringing in each image can be significantly different from observation to observation. The resultant image was that of the fringes alone, at the adequate intensity for each frame to defringe. This image was then subtracted from the data frame

resulting in a defringed image. This procedure can be written as:

$$DData[i] = FData[i] - \left[FFlat \times \frac{\text{mode}(FData[i])}{\text{mode}(FFlat)} - \text{mode}(FData[i]) \right], \quad (3.1)$$

where $DData[i]$ is the defringed data frame labelled i ; $FData[i]$ is the fringed data frame (after illumination correction) labelled i , which we want to defringe; $FFlat$ is the fringed sky-flat as obtained from the medianing of sky images and subtraction of an object check image. Following equation (3.1) the fringing was reduced to less than 1% of sky. Measurements of the effective gain (computed as $\Gamma_{\text{eff}} = \frac{\mu}{\sigma^2}$, with μ being the mean and σ the standard deviation in the histogram of counts; random readout noise being negligible at < 5 rms) in sample regions across the chips showed that the S/N did not change appreciably and, since these fringe levels are of the order of the residual non-linearity, better defringing was not attempted since it would not improve the photometry.

3.1.2 Registration and Mosaicking

Image registration and mosaicking was performed with the help of a routine developed by David Gilbank based on the *Starlink* software CCDPACK. One image of each target was taken as the reference and the relative offsets to the others calculated using the tasks FINDOBJ, FINDOFF and FINDREG to find common objects amongst frames and calculate the offsets to sub-pixel accuracy. The images were then geometrically transformed with subpixel shifts and bilinear interpolation to conserve flux using TRANNDF and, lastly combined using a 3- σ clipped mean within the MAKEMOS task.

Astrometry

The WCSTOOLS package (Mink 1997) was employed to perform astrometry against the USNO-A2.0 astrometric catalogue (Monet 1998) and to calculate the World Coordinate System (WCS) of the images. Internal accuracy was found to be better than 0.3 arcsec over all the detector area.

3.1.3 Object Detection and Classification

The automated detection and photometry of objects in the registered and mosaicked images was performed with `sExtractor 2.2.2` (Bertin & Arnouts 1996),⁵ a fast and robust package that handles well large fits files like our data. It generally works by fitting and subtracting the background and determining whether pixels belong to that background or to objects; splitting non-background areas into separate objects; determining the properties of each object; and outputting them into a catalogue. However it is also highly configurable by the user.

⁵Source EXtractor. <http://terapix.iap.fr/>

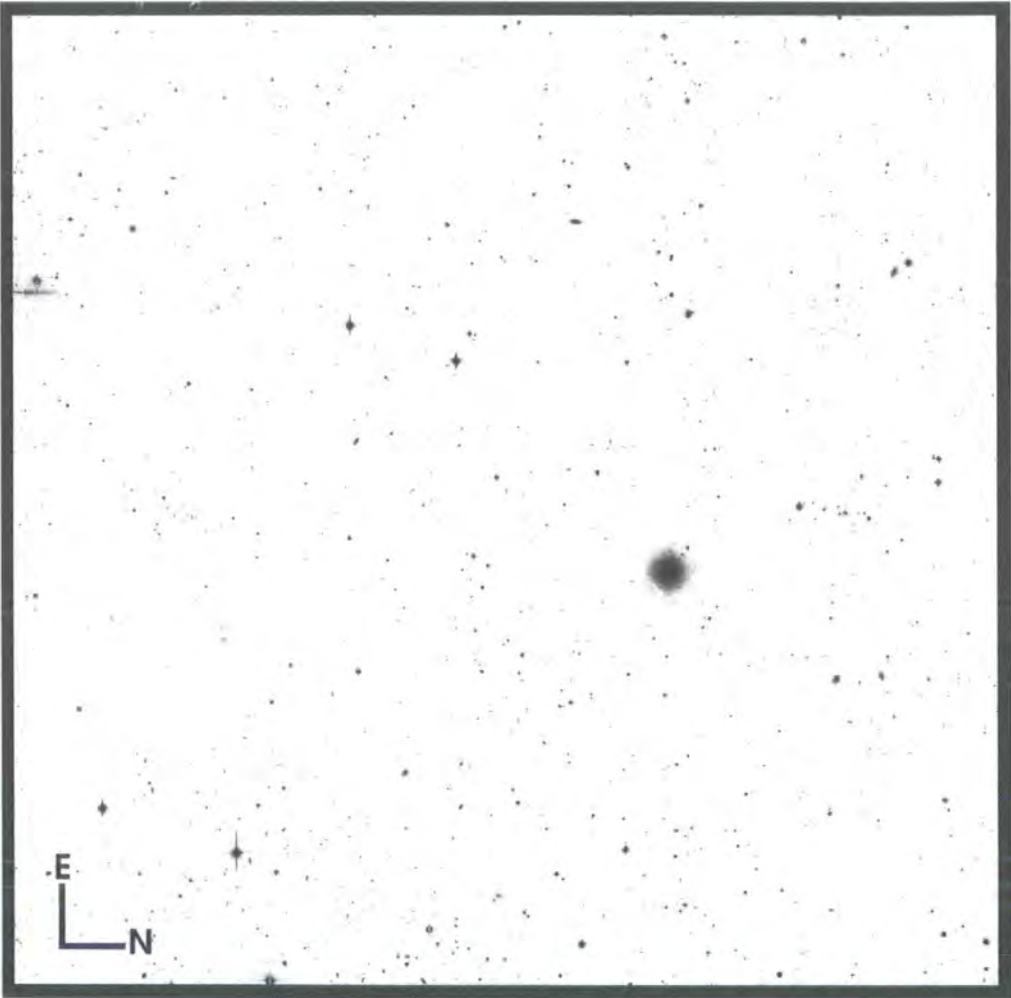


Figure 3.4: Final reduced mosaic of the GSGP4 field (centred on $\alpha = 00^h 57^m 57^s$, $\delta = -27^\circ 35' 19''$, J2000). This represents a 40-minute exposure with the *i* WFI filter, reaching a limiting depth of $i \sim 23.7$ magnitude. The field size is $33' \times 33'$; east is up and north to the right. Acquired with the AAT on the 27th–28th December 2000.

All source detection was undertaken in a single image, while the photometry was performed applying the apertures and positions found in that detection image to the different passband data. Since colour properties of the Chandra counterparts were fundamental, this procedure proved very convenient because the photometry is done on the same objects with the same apertures for each filter. It also alleviated the task of matching catalogues from different filters (with possible images from different filters undetected in a certain passband or deblended into multiple images).

Source Detection

To build the detection image we built a χ^2 -image, where each pixel value corresponds to the probability that the given pixel flux comes from the sky background or from a source. This method, pioneered by Szalay et al. (1999), optimises the available colour information into a composite image of the g , r and i passbands, provided that the images are sky-noise limited (i.e., instrumental sources of pixel noise are irrelevant compared to the photon noise of the sky background). Since we wanted to correlate these sources with Chandra detections and were not concerned about having a lot of spurious sources in the optical catalogues (they would just not be used), we tagged the pixels likely to be sky by clipping the probability image at a low detection threshold, well below the “optimal Bayes threshold” (Fukunaga 1990). The process then continued using this binary mask to create contiguous regions and deblending them into separate objects.

`SEXTRACTOR` provided a good framework to perform these operations. It was run in dual image mode, with 10 adjacent pixels as the minimum detection area and with `BACK_TYPE=MANUAL & BACK_VALUE=0.0, 0.0` so that `SEXTRACTOR` did not fit and subtract any background before applying a detection threshold. This step is important because our χ^2 -image is a positive definite quantity and subtracting a background would affect the detection threshold.

Two convolution filters were applied before the detection of pixels above the threshold and two catalogs were generated. Filtering the data essentially smooths the image and so removes the capriciousness of the position of pixel boundaries, which increases the S/N for faint, extended objects. We chose two different filters to increase the number of detections. The main catalogue was obtained by filtering with a top-hat kernel and a secondary catalogue was obtained with a mexican-hat convolution, which is useful in very crowded star fields and in the vicinity of nebulosities. The second catalogue contained a few deblended objects which appeared as single detections in the main catalogue. A master list was created after updating the main catalogue with the deblended sources found with the mexican-hat filter.

An attempt to find extra Chandra counterparts was made operating `SEXTRACTOR` in `ASSOC` mode, where Chandra sources' positions were fed into `SEXTRACTOR` with a search radius ($2''$) and priority given to the nearest association. No extra sources were obtained for which any reliable magnitude or colour information could be derived.

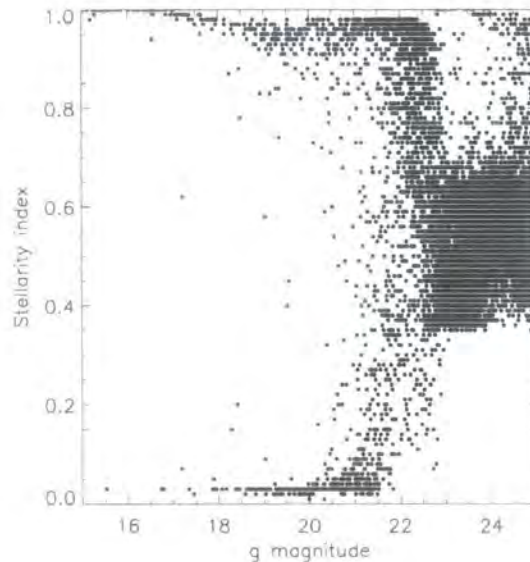


Figure 3.5: Stellarity index, `CLASS_STAR`, against g magnitude. At magnitudes fainter than $g \simeq 22.5$ the index breaks down and becomes unreliable.

Source Classification

`sextractor`'s stellarity index, `CLASS_STAR`, is produced through a neural network which requires knowledge of the seeing conditions of the observations in order to distinguish between extended and point-like sources. Accurate estimations of the seeing are also necessary in aperture photometry, to match with precision the point spread functions of the different filters and ensure that the same physical sample regions are accounted for in galaxies when colours are measured.

To estimate the seeing we ran `sextractor` with an initial value of the seeing taken from the image `FITS` headers and with a detection threshold of 8σ and `CLASS_STAR`=0.99 to detect only the brightest stars. We excluded saturated stars and cosmic rays by setting a minimum number of pixels per detection of `DETECT_MINAREA`=25 and high and low cuts to the total counts. We then fitted Gaussian profiles to the detections and the mean full width at half maximum (FWHM) was taken. In this way we obtained a seeing of $2''$, $1.85''$ and $1.40''$ for the g , r and i images respectively.

Figure 3.5 plots the stellarity index, `CLASS_STAR`, against the g magnitude. We see that the index is unreliable for magnitudes fainter than $g \simeq 22.5$.

Positional Accuracy of Counterparts

Chandra sources were correlated with WFI detections in search for optical counterparts to x-ray objects. Sources were matched if their centroids in the x-ray and optical regimes were closer than $2''$. A total of 67 objects fulfilled this requirement. Their positional offsets are presented in figure 3.6. The mean offsets are found to be $0.29''$ and $0.09''$ in right ascension and declination respectively.

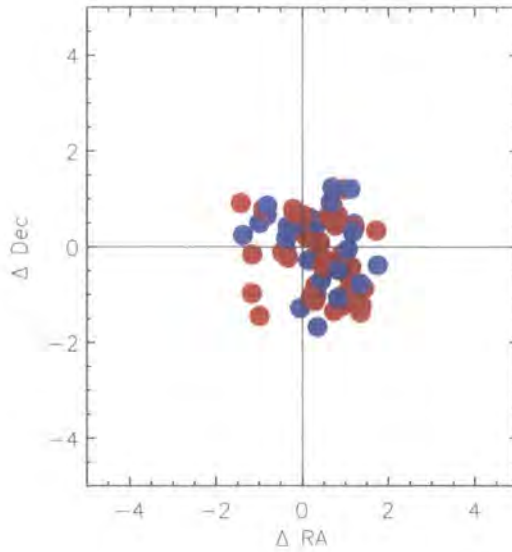


Figure 3.6: Offsets between Chandra and WFI positions for the same sixty-seven objects from table 3.4, in arcsecond units.

3.1.4 Photometric Calibration

Colours & Transformations

The magnitudes we measure for all objects are in the ‘natural’ CCD bands (which agree with standard *BRI* for sources with zero colour); this system is referred, in the remainder of this thesis, simply as *gri*. Using WFI observations of Landolt (1992) standard fields, we provide solutions to colour equations measured each night for transforming between our internal (‘instrumental’ magnitude plus zero point) and the Johnson-Cousins photometric systems:

$$-g_{\text{instr}} + B_{\text{Landolt}} = a^i (B - R)_{\text{Landolt}} + b^i \quad (3.2)$$

$$-r_{\text{instr}} + R_{\text{Landolt}} = a^j (B - R)_{\text{Landolt}} + b^j \quad (3.3)$$

$$-r_{\text{instr}} + R_{\text{Landolt}} = a^k (R - I)_{\text{Landolt}} + b^k \quad (3.4)$$

$$-i_{\text{instr}} + I_{\text{Landolt}} = a^l (R - I)_{\text{Landolt}} + b^l \quad (3.5)$$

where \bar{a} are the colour terms and \bar{b} the zero points of the photometry.

Six calibration stars were altogether detected with WFI, but given that WFI’s field of view is larger than Landolt’s Selected Areas, they fell on chips five, six and seven only. The transformation equations calculated using these chips can be safely extrapolated to the rest because our flat fielding has uniformised them to the point where all chips have the same mode value. Hence, no difference in zero point

Band	Zero point (<i>b</i>)	Colour term (<i>a</i>)
<i>g</i> (<i>i</i>)	26.123 ± 0.012	$+0.314 \pm 0.009$
<i>r</i> (<i>j</i>)	25.929 ± 0.012	-0.057 ± 0.009
<i>r</i> (<i>k</i>)	25.925 ± 0.012	-0.159 ± 0.026
<i>i</i> (<i>l</i>)	25.549 ± 0.004	-0.165 ± 0.009

Table 3.3: Coefficients from Landolt Calibration. The letters in parentheses next to the band name represent the superindices in equations 3.2 –3.5.

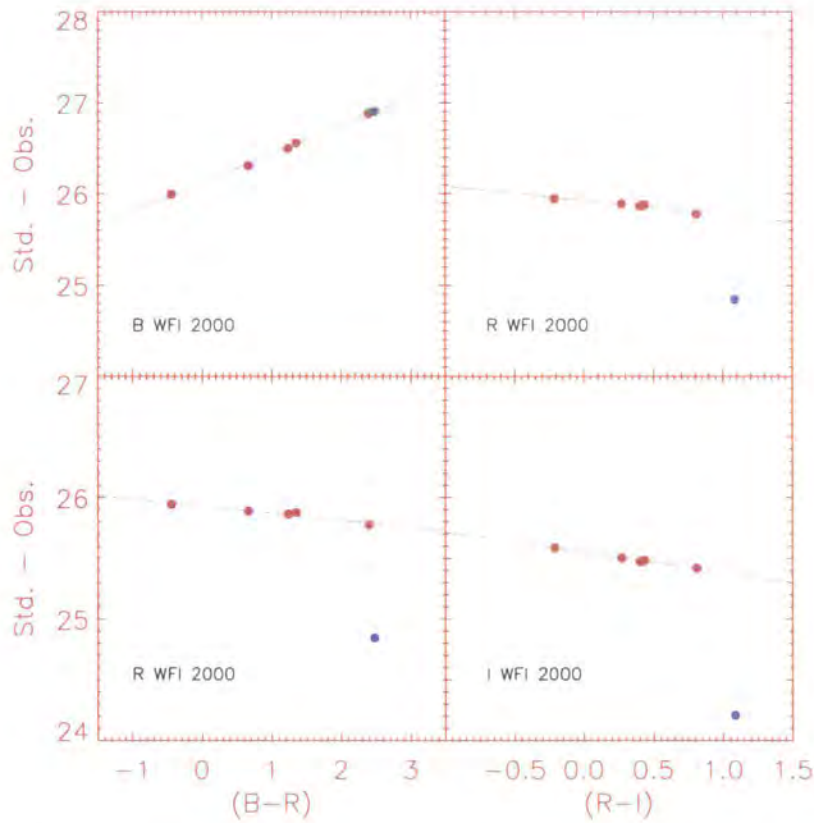


Figure 3.7: Standard star calibration plots (catalogue colour vs. catalogue minus instrumental magnitude) for the GSGP4 *g*, *r* and *i* bands. The lines indicate the adopted colour equations (the fits exclude the blue points).

between chips should exist and with this method we calibrate all chips to the same system. The best-fit solutions were used to calculate the zero-points and the colour terms; the results are shown in table 3.3 on the page before, while figure 3.7, on the same page, shows the data on which these are drawn. In three calibration plots, the standard star T Phe G (marked as a blue dot in the plots) is clearly off the mean line, and has not been considered for the fits. Unfortunately our observations did not comprise a range of observations for different airmasses and therefore we could not derive the extinction terms. Since no log of such information could be found for Siding Springs, we arbitrarily used the average extinction coefficients for La Palma as obtained with the Carlsberg Meridian Telescope.⁶ These are 0.19 for g' , 0.09 for r' and 0.05 for i' . Assuming a difference of 10% between the adopted and the true extinction values and given that our observations took place at zenithal distances of $27^\circ \leq ZD \leq 46^\circ$ that would introduce a photometric error of < 0.01 magnitude, which is of the same order as the uncertainty in the zero points in the three bands (see table 3.3).

For the photometry we chose an aperture diameter of $2.5 \times \text{FWHM}$, as opposed to the same aperture Landolt used ($14''$), and then applied an empirically derived aperture correction to the flux measured, based on a curve of growth analysis. Although this correction is only proper for point-like sources with atmospheric and instrumental broadening (PSF), it is as well a good first-order correction for galaxies. In any case, this correction is small, $\sim 2\%$. In favour of adopting this aperture: i) Lilly, Cowie & Gardner (1991) found a similar value to be optimal for the measurement of faint galaxy colours; ii) it fits better the sizes of our (faint) objects; iii) and is also sensible as a match to fibre sizes, as we were looking ahead to fibre-spectroscopy follow-up.

The stability of the photometric zero-points through the night was tested from the different science exposures and found to be consistent to $\sim 3\%$.

Kron Magnitudes

To derive colours, we convolved the r and i images with a Gaussian blur to the worst seeing (in the g band) and then used the same photochromes to find the magnitudes in all objects. We adopted `SEXTRACTOR MAG_AUTO` magnitudes which are an approximation to a total magnitude based on a flexible elliptical aperture and have low uncertainties and systematic errors at faint magnitudes. From the object's second-order moments of the light distributions the ellipticity and position angle (widths for a bivariate Gaussian) are computed; then, an ellipse, some constant times these widths, is used as an aperture (*cf.* Kron 1980). For unsaturated sources, the systematic errors of `MAG_AUTO` magnitudes are significantly lower than the 1σ uncertainties. These in turn decrease from 0.3 magnitudes at the 50% completeness limit to 0.1 magnitudes at 2 magnitudes brighter than the

⁶<http://www.ast.cam.ac.uk/~dwe/SRF/camc.html>

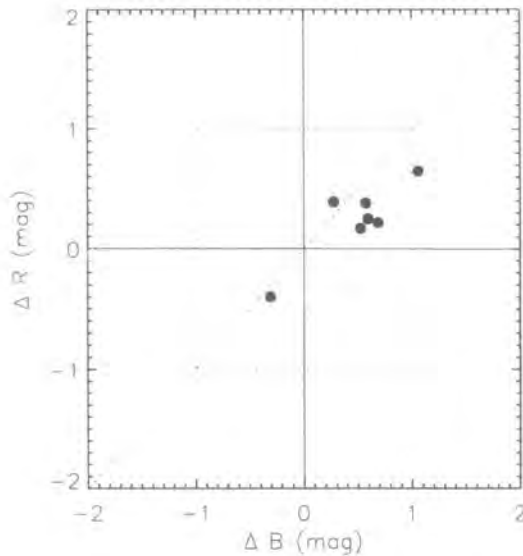


Figure 3.8: Photometric comparison between WFI and 2QZ B and R magnitudes for the same bright quasars. Variability is thought to be the main cause of the discrepancies, in which case the QSO class would not be an adequate benchmark to test our photometry.

completeness limit. Moreover, it has been shown that `MAG_AUTO` contain a constant fraction of the flux from the object independently of its brightness (Bertin & Arnouts 1996 and references therein). The comparison with $5''$ circular aperture photometry yielded a mean systematic offset of < 0.05 magnitudes. Given other uncertainties and that our main objective were colours, we neglected this correction and for all further studies we used total Kron magnitudes as given by the `MAG_AUTO` parameter.

Photometric Checks

To test the accuracy of our photometry, we have produced figure 3.8, which shows the differences in B and R magnitudes for the same bright quasars as detected by WFI and the 2QZ survey (see tables 3.4 and 3.12). We see that, on average, WFI magnitudes are $\langle \Delta B \rangle \simeq 0.49$, $\langle \Delta R \rangle \simeq 0.24$ magnitude fainter. Although the sample comprises only 7 objects, the differences are large enough as to make the discrepancy significant. This could be a sign that a) the WFI photometry of bright point-like sources is not accurate; b) the WFI photometry of quasars is sufficiently deep as to be contaminated by the glare of the host galaxies; or that c) QSOs are variable sources.

The third case seems to be the most influential as the AGN class is known to be highly variable on all timescales. For instance, our LDSS2 observations yielded several high quality spectra for optical counterparts to X-ray sources which we a

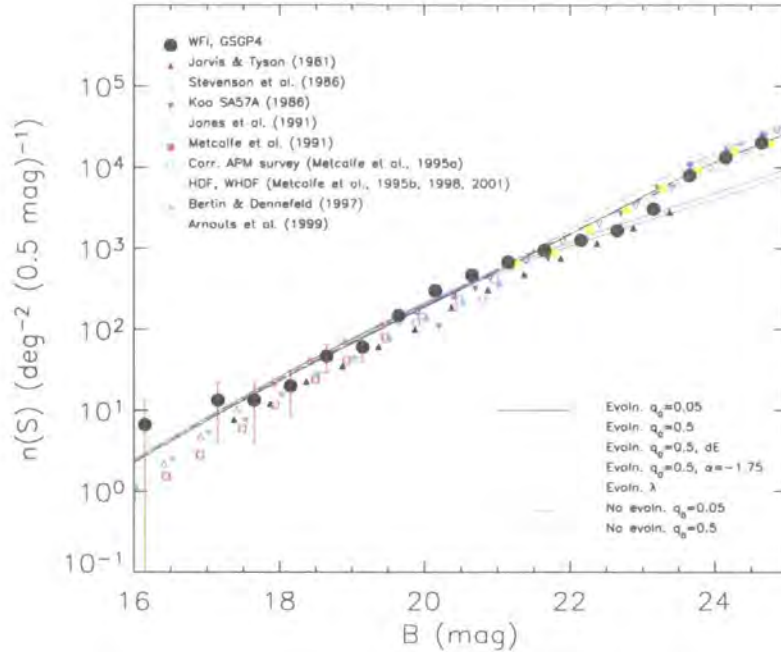


Figure 3.9: B -band differential number counts compilation. The big black dots are the data points from the galaxies in the GSGP4 field (converted to the standard passband using the colour equations provided in the text). The models shown are discussed in Metcalfe et al. (2001).

priori deemed, on basis of preexisting photometry, too faint to be detected with the given exposure times (and *vice versa*; see § 3.4). From this we concluded that large optical variability exists in our samples; this variability could plausibly be reflected in figure 3.8. The second case, when QSO magnitudes are contaminated by light from host galaxies, seems to occur in one object (GSGP4CH083), which `sExtractor` on WFI frames detects as an extended source (`CLASS_STAR`=0.03).

That the WFI photometry of bright point-like sources is not accurate seems unlikely on views of figure 3.9. It shows the differential number counts of galaxies in the GSGP4 field and compares them with various results published in the literature (Arnouts et al. 1999; Bertin & Dennefeld 1997; Jarvis & Tyson 1981; Jones et al. 1991; Koo 1986; Metcalfe et al. 2001, 1998, 1995a,b, 1991; Stevenson et al. 1986) and with the evolutionary models of Metcalfe et al. (2001). Over a span of almost 10 magnitudes, we find that our number counts agree very well with the results from other teams and with the models which allow for some evolution. This plot tests the magnitudes of the fainter extended population but we can not find any reason why the photometry for bright point-like sources should be less accurate. The favourable comparison of our $n(B)$ with the rest of the results reassures us of the reasonability of our photometry.

Table 3.4 presents the catalogue of crosscorrelated Chandra–WFI sources in the GSGP4 field.

Table 3.4: WFI counterparts to Chandra sources in GSGP4.

Chandra ID	RA ^a	DEC ^a	Separation ^b	<i>g</i>	<i>r</i>	<i>i</i>	SI ^c
GSGP4CH_001	14.320066	-27.357971	0.4	22.49	21.81	20.48	0.42
GSGP4CH_002	14.332558	-27.343382	0.4	26.13	25.94	24.08	0.43
GSGP4CH_005	14.254095	-27.393167	0.7	24.44	23.67	22.82	0.43
GSGP4CH_011	14.352496	-27.725599	0.3	27.33	24.94	22.39	0.53
GSGP4CH_012	14.384881	-27.705395	1.3	24.56	23.55	22.47	0.66
GSGP4CH_014	14.335690	-27.747965	1.1	25.39	23.96	22.78	0.42
GSGP4CH_015	14.322544	-27.710306	0.2	24.38	22.69	21.1	0.35
GSGP4CH_025	14.431883	-27.549817	1.7	24.57	23.42	23.17	0.51
GSGP4CH_026	14.402968	-27.551188	1.6	20.48	19.28	18.39	0.03
GSGP4CH_029	14.416371	-27.524444	1.2	25.27	26.51	23.88	0.41
GSGP4CH_031	14.389206	-27.525201	0.4	21.82	20.28	19.21	0.08
GSGP4CH_033	14.380306	-27.552380	1.5	26.15	25.06	23.71	0.53
GSGP4CH_034	14.378663	-27.533985	0.9	20.96	20.22	19.57	0.93
GSGP4CH_036	14.372007	-27.511977	0.3	22.23	21.97	21.1	0.94
GSGP4CH_039	14.354435	-27.533600	1.1	24.02	24.29	22.58	0.46
GSGP4CH_040	14.352038	-27.533598	0.6	19.16	18.71	18.24	0.95
GSGP4CH_041	14.386473	-27.501764	0.9	24.37	22.31	20.84	0.42
GSGP4CH_043	14.437911	-27.489257	1.7	22.47	22.02	21.65	0.83
GSGP4CH_048	14.342779	-27.531282	1.6	25.92	23.85	23.42	0.42
GSGP4CH_050	14.355330	-27.508008	1.5	24.86	23.36	22.73	0.34
GSGP4CH_053	14.395581	-27.474564	0.4	18.79	18.34	17.77	0.93
GSGP4CH_058	14.321142	-27.558053	0.9	23.98	23.33	22.43	0.53
GSGP4CH_068	14.480424	-27.400231	1.9	20.83	19.73	18.79	0.04
GSGP4CH_069	14.455624	-27.390164	0.8	25.22	23.88	23.13	0.39
GSGP4CH_070	14.454167	-27.376559	1.4	23.45	21.73	20.08	0.37
GSGP4CH_071	14.505654	-27.374986	1.5	23.75	22.38	21.02	0.44
GSGP4CH_072	14.499644	-27.357176	1.4	15.83	14.77	14.04	0.91
GSGP4CH_073	14.493527	-27.385409	1.2	24.72	25.05	23.03	0.47
GSGP4CH_075	14.514680	-27.359569	1.8	19.45	18.36	17.48	0.03
GSGP4CH_076	14.480860	-27.332369	0.6	24.47	22.98	21.52	0.35
GSGP4CH_077	14.440999	-27.335585	0.8	23.63	22.6	21.55	0.71
GSGP4CH_083	14.523928	-27.834794	1.1	20.63	19.71	18.88	0.03
GSGP4CH_084	14.560893	-27.834283	1.7	21.47	19.81	17.55	0.98
GSGP4CH_085	14.426543	-27.842238	1.1	22.48	21.77	21.24	0.9
GSGP4CH_086	14.530714	-27.794584	1.1	23.63	23.04	22.26	0.71
GSGP4CH_087	14.499433	-27.792735	1.4	19.4	19.07	18.47	0.81

(continues...)

Table 3.4: WFI counterparts to Chandra sources in GSGP4 (continued).

Chandra ID	RA ^a	DEC ^a	Separation ^b	<i>g</i>	<i>r</i>	<i>i</i>	SI ^c
GSGP4CH_089	14.536883	-27.771386	1.3	22.16	21.62	20.94	0.84
GSGP4CH_090	14.619046	-27.509532	1.7	21.75	21.04	19.89	0.31
GSGP4CH_092	14.605830	-27.542745	0.5	23.97	22.97	22.45	0.46
GSGP4CH_093	14.583153	-27.482217	0.5	21.66	20.5	19.67	0.19
GSGP4CH_094	14.578471	-27.493356	0.4	22.48	21.83	21.15	0.86
GSGP4CH_095	14.575705	-27.480109	0.6	20.74	20.28	19.49	0.95
GSGP4CH_101	14.547725	-27.443313	0.5	20.17	19.96	19.51	0.94
GSGP4CH_103	14.609910	-27.410403	0.9	20	18.73	17.81	0.03
GSGP4CH_104	14.558385	-27.430544	0.5	20.54	20.33	19.8	0.85
GSGP4CH_105	14.530384	-27.453659	0.4	23.87	23.38	21.7	0.34
GSGP4CH_106	14.553446	-27.419610	1.2	26.08	23.99	22.19	0.29
GSGP4CH_108	14.503711	-27.461260	1.2	22.38	21.86	20.75	0.44
GSGP4CH_109	14.577699	-27.398860	0.6	25.44	24.39	23.21	0.37
GSGP4CH_110	14.571926	-27.393763	1.8	24.06	23.58	23.13	0.5
GSGP4CH_112	14.650649	-27.838167	0.6	22.02	21.33	20.5	0.72
GSGP4CH_113	14.647320	-27.811501	0.6	22.24	21.62	20.67	0.71
GSGP4CH_114	14.684348	-27.815560	1.3	25.01	24.32	23.21	0.56
GSGP4CH_115	14.662463	-27.787845	0.9	26.34	23.91	22.59	0.47
GSGP4CH_116	14.660509	-27.788179	1.1	24.18	23.47	22.32	0.44
GSGP4CH_117	14.716091	-27.799448	0.7	21.8	20.39	18.94	0.38
GSGP4CH_120	14.585666	-27.798879	1.9	22.64	22.19	21.65	0.39
GSGP4CH_121	14.592266	-27.761545	0.7	25.65	24.22	22.62	0.46
GSGP4CH_123	14.558595	-27.811132	1.2	24.52	23.39	22.49	0.42
GSGP4CH_125	14.640542	-27.733538	1.1	22.82	22.39	21.79	0.65
GSGP4CH_99001	14.323124	-27.438469	1.4	22.17	21.84	21.18	0.91
GSGP4CH_99008	14.437911	-27.489257	1.6	22.47	22.02	21.65	0.83
GSGP4CH_99016	14.292939	-27.831978	1.2	21.27	20.6	20.08	0.78
GSGP4CH_99018	14.477366	-27.513566	1.0	21.87	20.91	19.86	0.83
GSGP4CH_99019	14.445392	-27.593555	1.8	23.63	22.6	21.67	0.62
GSGP4CH_99020	14.429094	-27.633832	1.1	21.52	20.97	20.4	0.96
GSGP4CH_99021	14.595727	-27.671258	1.2	14.66	14.43	14.11	0.9

^a WFI positions; J2000.^b Angular separation between Chandra and WFI counterpart, in arcseconds.^c sExtractor stellerity index, with 0 meaning extended and 1 pointlike.

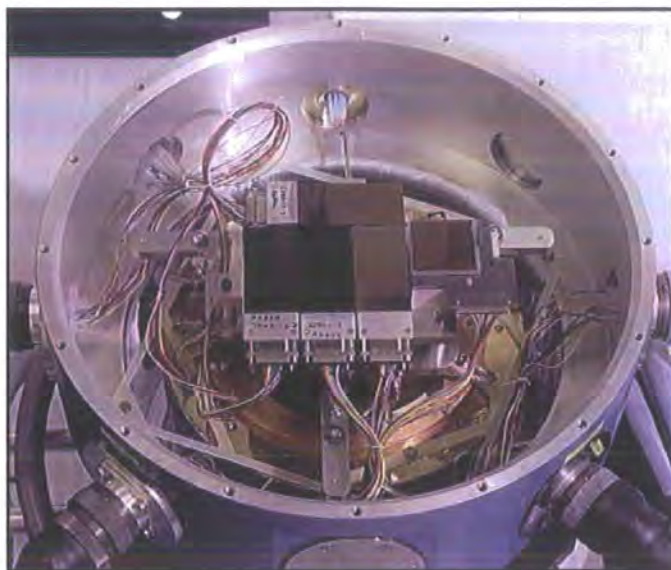


Figure 3.10: Distribution of the WFC CCDs on the focal plane.

3.2 Wide Field Camera

The Wide Field Camera (WFC) is a wide-field CCD imaging mosaic used at the prime focus of the 2.5 m Isaac Newton Telescope (INT; at the Observatorio del Roque de los Muchachos, La Palma).⁷ It comprises an autoguider and four thinned EEV 2048×4096 13.5 micron pixel CCDs (pixel scale of $0.333'' \text{ pixel}^{-1}$), each covering an area of $22.8' \times 11.4'$ on the sky for a total sky coverage of 0.29 deg^2 per exposure. Its unconventional layout can be seen in figure 3.10, which shows the WFC in the prime focus.

Almost 4 and 6 ks, split into 600 and 720 s frames, were dedicated on the nights of the 8th–9th May 2000 to observe the F864 field (centred on $\alpha = 13^h 41^m 10^s$, $\delta = 00^\circ 08' 39''$, J2000) with the Harris *R* and Sloan *i* filters, respectively (see table 3.5 on the next page). This data is complemented by WFC observations in the same field in the *B*-band by S. Croom at the AAO. Other existing imaging and photometry in this region includes the multiband data of the Sloan survey ($u > 22$, $b > 22.2$, $r > 22.2$, $i > 21.3$ and $z > 20.5$; see § 3.6.3). This, coupled with the fact that *I*-band imaging data reduction has not yet been attempted, has limited the usage of the WFC data in this thesis.

3.2.1 WFC Data and Reduction Analysis

Data reduction was undertaken only for *R*-band frames. Given that the reduction steps were the same as for AAT's WFI (except that dark current was ignored), to avoid repetition we will comment only on those aspects which are substantially

⁷<http://www.ing.iac.es>

Table 3.5: Journal of the WFC observations of the F864 field on 8th–9th May 2000.

RA ^a	DEC ^a	Band	Exposure ^b	Area ^c	FWHM ^d
13 ^h 41 ^m 10 ^s	00° 08' 39''	<i>R</i> (Harris)	3840	0.29	1.7
13 ^h 41 ^m 10 ^s	00° 08' 39''	<i>i</i> (Sloan)	6000	0.29	1.3

^aNominal pointing, B1950.
^bIntegration time, in seconds
^cCoverage, in square degrees
^dSeeing: full width at half maximum, in arcsec

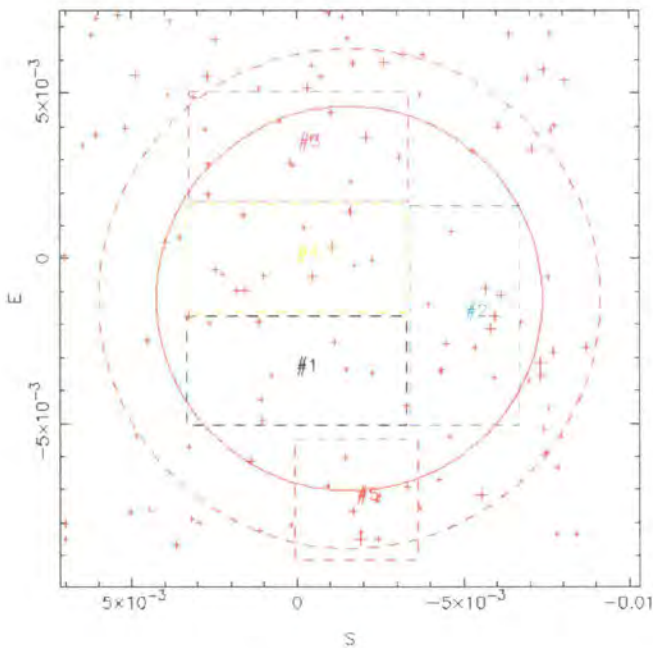


Figure 3.11: The WFC comprises four 4 k × 2 k CCDs for the science array plus a thinned 2 k × 2 k CCD for use as a dedicated frame transfer autoguider. The solid circle marks the unvignetted region while the dashed circle marks the 0.5 vignetting limit.

different or that deserve particular remark. Resources of the INT *Wide Field Survey* (WFS), publicly available at their website⁸, have been very useful.

Flat Fielding

The solid circle in figure 3.11 shows that CCD #3 suffers from important vignetting over one corner. Although the flatfielding raises the mean counts to those of the whole chip, due to the low signal, it does so at the expense of increased pixel-to-pixel variation. This area is therefore not useful for object detection or photometry and a triangular region satisfying $x + y \leq 1200.00$ was omitted from the analyses.

Defringing

A fringing pattern at the order of 0.5% arises in the flatfielded images (of about the same order of the RMS dark sky photon noise). Fringed sky-flats were constructed as described in § 3.1.1 and then compared to the `r_oct98_fringe.fits` file from the INT WFS library of fringe flats; unfortunately this was the only fringe frame available in the library for our filter. However, the pattern seemed stable over such long time interval and very good agreement was found between both fringe flats. It was then decided to employ `r_oct98_fringe.fits` for all subsequent analysis (after trimming and redimensioning it to the standards of our frames).

After optimally removing the zeroth order fringes the residual fringe pattern is negligible (less than 0.1% of sky).

3.2.2 Astrometry

As most optical systems involving refractive elements, WFC does not have a uniform plate scale over the field. The barrel distortion is severe and it can produce offsets amounting to a differential effect up to 10". A solution measured by *Starlink* staff Peter Draper and Mark Taylor in conjunction with David Gilbank was applied which produced internal astrometric calibration at the level of $\sim 0.7''$.

3.3 WHDF Imaging

To probe the evolutionary history of galaxies back to their formation epoch, Durham leads an ultradeep imaging project using ground-based telescopes. The observations are focused on a single field of very low column density ($n_H \lesssim 2.7 \cdot 10^{20} \text{ cm}^{-2}$) which is known as the *William Herschel Deep Field* (WHDF). Its location in the constellation of *Pisces* in the celestial equator makes it a feasible target from observatories in both hemispheres. It has been the subject of an extensive observing campaign from optical to infrared wavelengths, reaching depths of $U \sim 27$, $B \sim 28$, $R \sim I \sim 26$, $H \sim 22.5$ and $K \sim 20$ over 50 arcmin^2 (Metcalf et al. 2001; McCracken et al. 2000); table 3.6 on the following page provides the photometric details.

⁸<http://www.ast.cam.ac.uk>

Table 3.6: Photometric limits of the WHDF.

Band	Exposure ^a	Magnitude ^b	Area ^c	FWHM ^d	Telescope
U	34	26.8	46.4	1.35	WHT
B	28/-	28.2/27.9/26	2.8/46.8/256	1.3	WHT
R	8/-	26.3	256	1.5	WHT
I	5/-	25.6/23.8	52.2/256	1.2	WHT
Z	-	23	256	-	-
H	14	22.75	50	-	Calar Alto
K	1.0/30	20/22.75	47.2/1.8	-	UKIRT/Calar Alto

^aIntegration time, in hours
^b3 σ limit
^cCoverage, in square arcminutes
^dFull width at half maximum, in arcsec



Figure 3.12: Central 16' \times 16' *Herschel Deep Field* true colour image, formed by mapping *B*, *R* and *I* images into blue, green and red respectively. Photometry reaches $B \simeq R \simeq 26$ and $I \simeq 24$.

With photometric magnitude limits comparable to the Hubble Deep Fields, the WHDF is one of the deepest ground-based surveys. And, although much worse seeing conditions impose limits on morphological studies, it covers a five times bigger area of the sky than the two HDFs combined. Recently, it has been extended to a 16×16 arcmin² area in the bands B ($\lesssim 26$), R ($\lesssim 26$), I ($\lesssim 24$) and Z ($\lesssim 23$) to match the 75 ks Chandra ACIS-I exposure. Many counterparts have been found within a $2''$ radius from the x-ray sources. These are listed in table 3.7.

Table 3.7: Optical counterparts to Chandra sources in the WHDF.

Chandra ID	R ID ^a	RA ^b	DEC ^b	R	$B-R$	$R-I$	$R-Z$	SI ^c
WHDFCH003	07964	00:22:39.243	00:20:35.84	23.56	0.73	0.54	1.06	5
WHDFCH004	10237	00:22:38.029	00:21:38.64	23.99	1.00	0.93	1.49	5
WHDFCH005	07927	00:22:35.963	00:18:50.04	20.43	0.33	0.38	0.52	0
WHDFCH006	12165	00:22:32.584	00:23:27.84	19.31	1.65	0.76	1.13	7
WHDFCH007	07444	00:22:24.821	00:20:10.94	22.63	0.99	0.89	1.47	5
WHDFCH008	07475	00:22:22.884	00:20:13.24	24.02	0.53	0.54	-	5
WHDFCH009	06123	00:22:41.892	00:18:11.44	25.36	-	-	-	5
WHDFCH010	12178	00:22:29.053	00:23:25.14	22.33	1.32	0.94	1.56	5
WHDFCH011	09672	00:22:21.040	00:22:02.14	20.49	0.99	0.40	0.61	7
WHDFCH012	10480	00:22:49.660	00:20:41.84	24.04	-	1.18	1.92	5
WHDFCH013	08328	00:22:49.455	00:20:05.54	24.73	0.66	-	2.18	5
WHDFCH014	08222	00:22:49.414	00:20:15.94	21.29	0.84	0.21	0.48	5
WHDFCH015	10481	00:22:48.004	00:21:01.04	23.97	1.84	0.89	1.78	5
WHDFCH016	05971	00:22:45.164	00:18:22.64	20.77	0.52	0.50	0.65	2
WHDFCH017	05964	00:22:44.468	00:18:25.64	19.34	0.50	0.53	1.02	0
WHDFCH018	12895	00:22:44.458	00:23:04.04	26.53	-	-	-	5
WHDFCH019	06031	00:22:44.281	00:17:48.54	23.78	0.79	0.47	1.29	5
WHDFCH020	12403	00:22:36.142	00:24:33.84	21.43	0.79	0.70	1.07	5
WHDFCH021	12230	00:22:31.059	00:24:41.24	24.50	0.80	0.74	-	5
WHDFCH023	05089	00:22:24.109	00:17:52.74	23.60	0.40	0.29	1.19	5
WHDFCH024	05110	00:22:18.945	00:18:33.14	24.24	-	0.56	-	5
WHDFCH025	10660	00:22:51.170	00:21:47.84	18.75	2.00	0.76	1.08	7
WHDFCH026	06199	00:22:48.331	00:18:35.54	25.68	-	-	-	5
WHDFCH029	03089	00:22:30.037	00:16:14.14	22.43	1.09	0.98	1.51	5

(continues. . .)

Table 3.7: Optical counterparts to Chandra sources in the WHDF (continued).

Chandra ID	R ID ^a	RA ^b	DEC ^b	R	B-R	R-I	R-Z	SI ^c
WHDFCH030	05119	00:22:24.699	00:16:39.64	24.39	-	1.34	1.92	5
WHDFCH032	12846	00:22:47.544	00:23:54.24	25.48	-	-	-	5
WHDFCH034	03420	00:22:37.648	00:15:55.44	24.11	0.42	-	-	5
WHDFCH036	14428	00:22:31.734	00:25:38.84	21.00	0.47	0.45	0.88	2
WHDFCH037	03147	00:22:25.798	00:16:14.24	24.12	1.14	0.71	-	5
WHDFCH038	02779	00:22:23.442	00:16:02.44	20.76	0.96	0.13	0.19	2
WHDFCH039	11943	00:22:20.468	00:24:10.44	23.85	-	1.46	2.16	5
WHDFCH042	07223	00:22:13.249	00:19:53.44	23.59	-	0.99	1.20	5
WHDFCH044	10665	00:22:55.092	00:20:55.74	20.15	2.26	1.04	1.60	0
WHDFCH045	06414	00:22:51.450	00:17:24.54	25.33	-	-	-	5
WHDFCH047	14980	00:22:45.142	00:24:59.24	20.89	2.04	1.15	1.56	5
WHDFCH048	14697	00:22:41.297	00:25:33.34	22.20	1.15	0.41	0.79	5
WHDFCH049	14844	00:22:40.278	00:25:48.64	25.35	-	-	-	5
WHDFCH051	14604	00:22:33.469	00:26:03.14	25.74	-	-	-	5
WHDFCH052	03081	00:22:33.339	00:15:04.84	21.73	0.58	0.36	0.67	5
WHDFCH054	07275	00:22:12.351	00:18:48.84	24.44	-	-	-	5
WHDFCH055	07196	00:22:11.862	00:19:50.44	21.41	1.21	0.90	1.18	2
WHDFCH056	08634	00:22:55.779	00:18:54.64	24.98	-	-	-	5
WHDFCH057	10807	00:22:56.711	00:21:57.94	25.32	-	-	-	5
WHDFCH060	03073	00:22:28.453	00:15:01.94	20.50	1.76	0.81	1.14	7
WHDFCH061	02769	00:22:25.402	00:14:55.54	18.63	2.47	0.85	1.23	7
WHDFCH062	18678	00:22:58.733	00:19:48.14	25.23	-	-	-	10
WHDFCH065	13982	00:22:17.194	00:24:59.64	22.43	1.46	0.48	0.49	5
WHDFCH066	04771	00:22:11.953	00:18:17.14	21.72	1.63	0.91	1.14	5
WHDFCH067	04836	00:22:11.801	00:18:36.14	23.91	0.61	0.27	-	5
WHDFCH070	09422	00:22:10.445	00:20:51.74	22.91	-	1.11	1.50	5
WHDFCH071	06276	00:22:53.293	00:16:59.59	18.43	1.73	0.70	1.00	7
WHDFCH074	15103	00:22:44.137	00:26:20.74	24.47	-	1.43	2.29	5
WHDFCH075	14805	00:22:36.772	00:26:39.74	24.94	0.43	-	-	5
WHDFCH076	16745	00:22:32.679	00:27:02.24	24.55	0.91	-	-	5
WHDFCH080	09136	00:22:08.772	00:21:59.34	14.76	1.70	0.72	1.12	7
WHDFCH082	11255	00:23:00.826	00:20:48.64	25.80	-	-	-	5
WHDFCH083	06600	00:22:58.865	00:17:54.84	23.16	1.73	0.94	1.64	5
WHDFCH085	10925	00:22:58.481	00:22:28.74	21.78	1.25	0.54	0.56	5
WHDFCH086	13020	00:22:57.193	00:24:03.44	24.42	-	0.46	-	5
WHDFCH088	15311	00:22:51.555	00:25:25.94	23.99	-	1.36	2.18	5
WHDFCH089	04097	00:22:50.304	00:15:24.04	25.71	-	-	-	5
WHDFCH090	03630	00:22:48.795	00:15:18.74	20.03	0.63	0.22	0.31	0

(continues...)

Table 3.7: Optical counterparts to Chandra sources in the WHDF (continued).

Chandra ID	R ID ^a	RA ^b	DEC ^b	R	$B-R$	$R-I$	$R-Z$	SI ^c
WHDFCH094	17057	00:22:35.654	00:27:06.44	24.90	-	-	-	5
WHDFCH095	16698	00:22:29.883	00:27:19.64	23.56	1.14	0.61	-	5
WHDFCH097	16624	00:22:22.392	00:26:49.94	25.80	-	-	-	5
WHDFCH098	14134	00:22:15.477	00:25:45.54	26.09	-	-	-	5
WHDFCH099	11642	00:22:11.187	00:24:04.13	20.17	0.58	0.38	0.62	0
WHDFCH101	09222	00:22:06.008	00:21:15.54	24.61	0.20	-	-	5
WHDFCH102	15058	00:22:47.171	00:26:36.74	24.09	0.76	-	-	5
WHDFCH104	16930	00:22:39.373	00:27:33.94	19.70	1.39	0.46	0.82	7
WHDFCH108	02525	00:22:13.432	00:15:37.94	21.57	2.44	1.46	1.90	2
WHDFCH109	02516	00:22:09.917	00:16:28.94	18.14	0.34	0.29	0.30	0
WHDFCH110	11360	00:22:07.433	00:23:07.74	20.94	1.56	1.03	1.40	5
WHDFCH113	08779	00:23:01.247	00:19:18.01	20.95	0.40	0.07	0.34	2
WHDFCH116	17194	00:22:37.520	00:27:46.94	25.54	-	-	-	5
WHDFCH117	18463	00:22:35.536	00:13:24.64	24.65	0.72	-	-	10
WHDFCH119	02551	00:22:14.321	00:15:06.14	23.34	0.78	0.44	1.07	5
WHDFCH122	06813	00:23:02.211	00:17:50.74	25.70	-	-	-	5
WHDFCH123	06644	00:23:00.662	00:17:15.94	24.06	0.77	-	-	5
WHDFCH132	18459	00:22:29.772	00:13:25.54	25.18	-	-	-	10
WHDFCH135	18688	00:22:02.317	00:21:32.24	25.28	-	-	-	10
WHDFCH136	18826	00:23:03.603	00:22:42.34	24.48	-	-	-	10
WHDFCH137	01520	00:22:48.556	00:13:43.94	23.44	-	0.94	1.54	5
WHDFCH138	15527	00:22:59.139	00:25:27.84	21.36	0.96	0.45	-	5
WHDFCH141	01746	00:22:50.369	00:13:17.00	24.50	0.77	-	-	5
WHDFCH142	01762	00:22:53.111	00:14:09.64	24.60	0.59	-	-	5
WHDFCH150	13763	00:22:06.679	00:25:37.14	23.52	1.55	0.60	-	5
WHDFCH167	06148	00:22:47.488	00:17:11.54	25.37	-	-	-	5
WHDFCH170	01867	00:22:50.672	00:13:16.84	25.68	-	-	-	5
WHDFCH173	04722	00:22:03.724	00:17:28.59	25.94	-	-	-	5
WHDFCHN2sD_1	09916	00:22:31.872	00:21:27.02	16.07	1.35	0.68	1.00	7
WHDFCHN2sD_2	08217	00:22:47.232	00:18:58.36	20.22	1.72	0.70	1.03	7
WHDFCHN2sD_5	05452	00:22:32.110	00:18:10.44	24.91	-	-	-	5

^a Identification in the R band ($16' \times 16'$).^b Chandra positions; J2000.^c Stellerity index. 0: stellar-like; 2: probably stellar-like; 5: probably extended; 7: extended; 10: unknown.

3.4 LDSS2 Spectroscopy

In November 2001 and September 2002 we carried out spectroscopic follow-up observations of the x-ray sources in the GSGP4 and WHDF fields using LDSS2 slit-masks on the Baade 6.5 m telescope (Magellan-1 at the Observatorio de Las Campanas).⁹ The Low Dispersion Survey Spectrograph (LDSS2) is a multi-aperture mask spectrograph that can also act as an imager provided that no masks or grisms are mounted. The way it operates is by focusing the input light onto the mask which, after passing through the various apertures (slits) cut in it, enters a collimator before meeting either a filter and/or a grism. Finally, the light is then focused by the camera onto the detector with a final equivalent focal ratio of $f/2$.

Each mask covers an area on the sky of $6.5' \times 5'$ and an average field has space for about 2.5 spectra (space density of $\sim 2000 \text{ deg}^{-2}$). At typical exposure time constraints of less than two hours per mask, the sources to be observed had to be brighter than $g \simeq 23$. At this magnitude limit, the mean x-ray source density in the GSGP4 field is $\sim 300 \text{ deg}^{-2}$ and in the WHDF is $\sim 600 \text{ deg}^{-2}$, significantly lower than the optimum of $\sim 2000 \text{ deg}^{-2}$. The different amount of optical work undertaken in each field demanded a different observational strategy for each of the two fields. In both cases, though, given that our main scientific drive was to investigate the nature of the non-quasar population of the XRB, we targeted primarily non point-like optical counterparts of the x-ray sources. For field GSGP4, with not much room to manoeuvre, we specifically looked for overdensities of bright extended sources in areas about the size of a mask. We selected two regions where we fitted eighteen and ten slits in the masks (see figures 3.13 and 3.14). For the WHDF the strategy was overall different and we combined x-ray counterparts with $B:R:I$ -selected red galaxies to undertake a parallel study of the evolutionary properties of intermediate-redshift ($z \lesssim 0.5$) bulge-dominated galaxies (see chapter 5).

In total we targeted twenty x-ray sources in 2001 (all in the WHDF) and twenty-eight/sixteen in 2002 (GSGP4/WHDF). A further ninety-two $B-R > 1.6$ galaxies in the WHDF were observed as part of the evolutionary studies of early-type galaxies. We positioned the slits at the centre of the optical counterpart in the vast majority of sources where an optical counterpart was found unambiguously. However for a few x-ray objects where doubts were cast on the real optical counterpart (more than one optical counterpart within $2''$ of the x-ray source) the slits were centred on the x-ray position. We used $2''$ wide slits and the $300 \text{ lines mm}^{-1}$ grating blazed at 500 nm (*Med/Blue*), which gives a wavelength resolution of approximately 13 \AA and a wavelength range of about 500 nm of coverage. This depends on the exact position of the slit on the mask, but it is generally from ~ 400 to 900 nm . No filter to block unwanted second spectroscopic order was used.

The slit masks on GSGP4 were observed for 2.5 hr and 1 hr, broken into five sets of $\frac{1}{2}$ hr exposures and four sets of $\frac{1}{4}$ hr, respectively. Masks on the WHDF had

⁹<http://www.lco.cl>

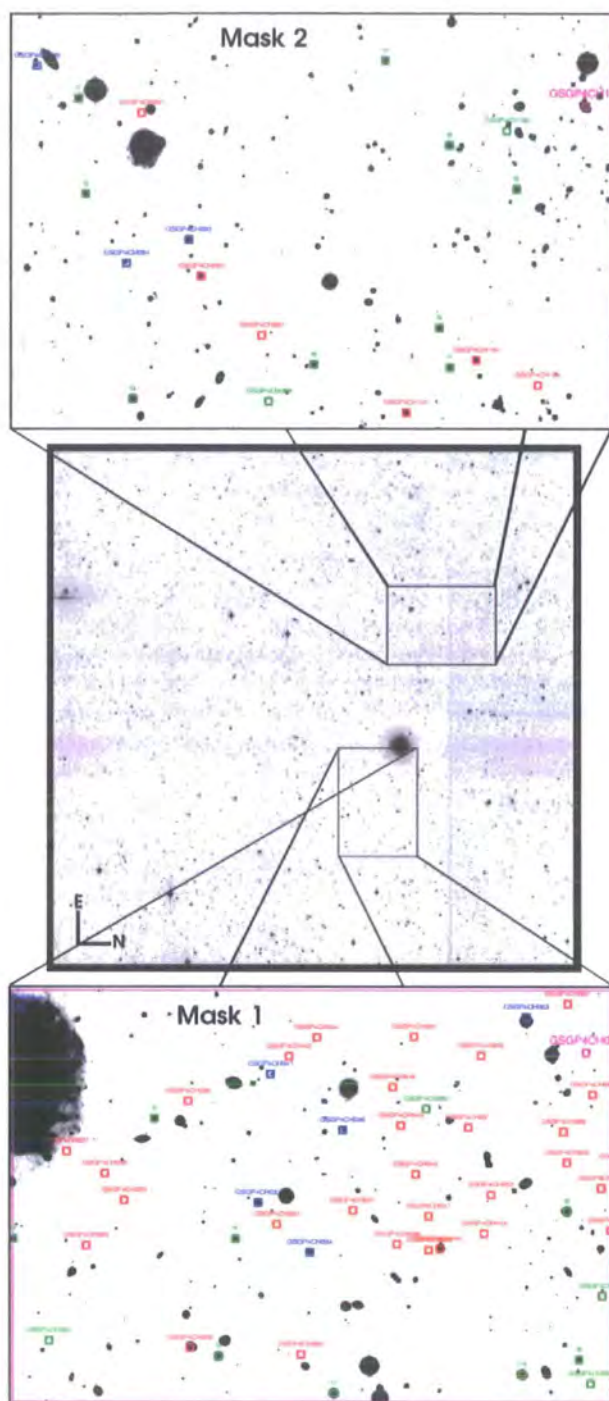


Figure 3.13: Finding chart for the two regions in field GSGP4 observed with Magellan-1/LDSS2 in September 2002. Mask 1 is centred at $\alpha = 00^h 57^m 30.32^s$, $\delta = -27^\circ 31' 05.0''$ and mask 2, at $\alpha = 00^h 58^m 20.91^s$, $\delta = -27^\circ 27' 40.0''$ (J2000).

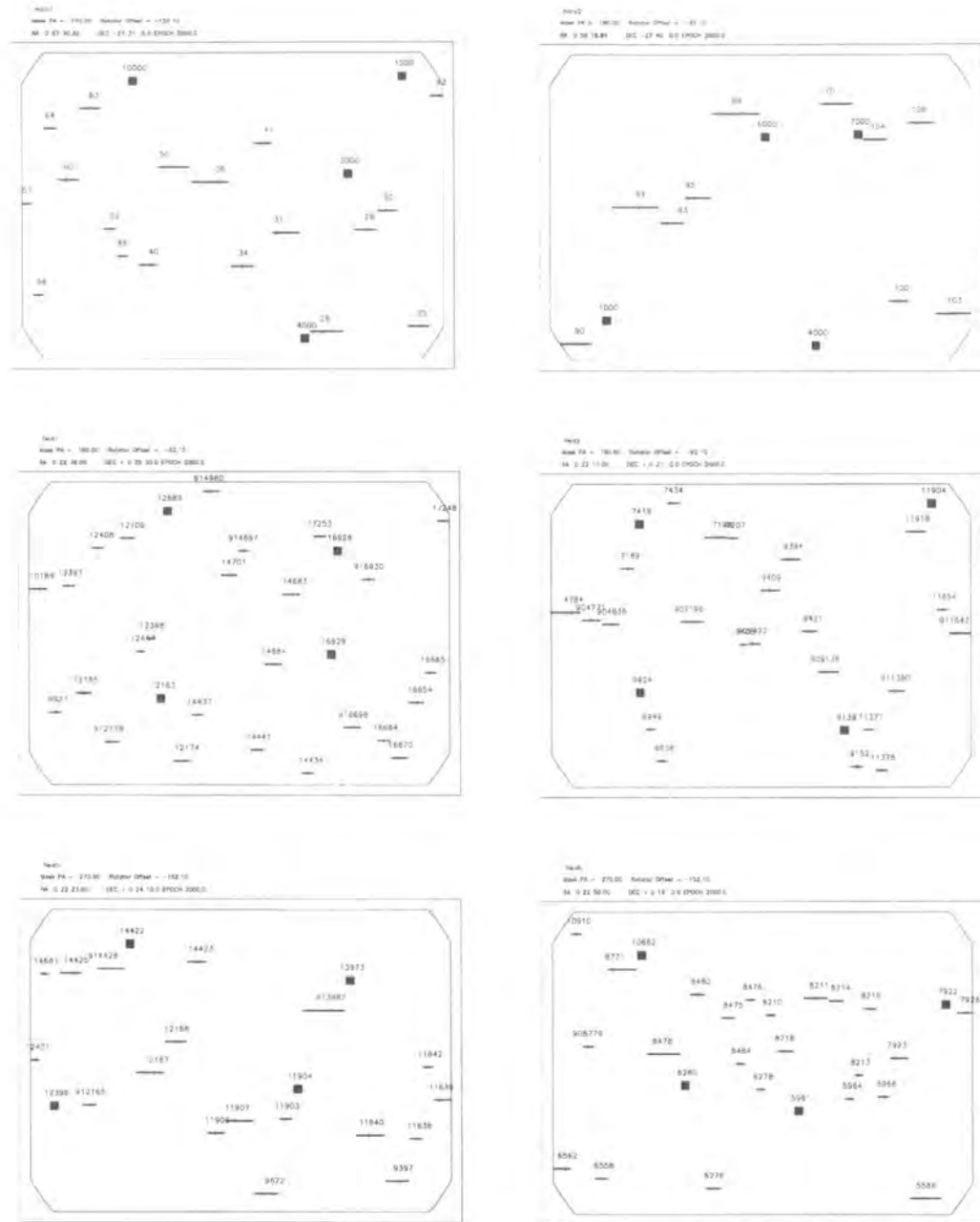


Figure 3.14: Slit masks employed in the September 2002 LDSS2 run. From left to right, top to bottom, we have the masks labelled GSGP4-1, GSGP4-2, WHDF-1, WHDF-2, WHDF-5, WHDF-6.

varying amounts of exposure time, ranging from 1 hr the least exposed to 4 hr the deepest. Conditions were photometric with seeing $\sim 0.6 - 0.8''$ FWHM. Table 3.8 on the following page gives the relevant details.

We successfully obtained redshift identifications for 45 objects of the 64 x-rays sources in our sample and for 65 of the $B - R > 1.6$ galaxies. It turned out that we obtained many spectra of x-ray counterparts which WFI and the WHT detected as very faint sources, implying large optical variability in our sample. Table 3.9 on the next page displays a break-down of the number of different types of optical counterparts found with LDSS2 spectroscopy; the reader is referred to appendix A for full details.

3.4.1 LDSS2 Data and Reduction Analysis

Spectra acquired in 2001 were reduced by P. Outram. For the 2002 data, detector signatures were reduced following the basic steps outlined in § 3.2.1. The main differences with the process described therein have to do with the different nature of data being dealt with (*i.e.*, now including projector flats; fringing is no issue in spectroscopy; *etc.*).

The data had any DC-offset removed by overscanning and zero-correcting with a master zero frame constructed from medianing 140 frames. Non-linear pixels were flagged constructing a bad pixel map, obtained by dividing 5 long-exposure (high intensity; $\sim 32 \text{ kcountss}^{-1}$) dome flats properly averaged together with IRAF task `flatcombine` into a long-flat frame, over a short-flat frame obtained from 25 short-exposure (low-intensity; $\sim 700 \text{ countss}^{-1}$) dome flats, also properly scaled and averaged together. The mask itself, in pixel-list format, was built with the routine `ccdmask` from the *nmisc* bundle ($\sigma = 8$ seemed reasonable), and it was applied to the science frames after flat fielding to interpolate over bad pixels. This step was executed immediately before combining all the science frames of the same field to produce the final reduced images, such as that shown in figure 3.16 on page 96.

Flat Fielding

The flat fielding process was slightly more involved than in the standard imaging case. Unfortunately, as comparison between twilight and dusk flats showed, the masks move slightly during telescope operation and therefore are not combinable.

It would have been ideal, then, to use sky flats taken before and after the exposure, but we do not always have enough of those to combine, so a different approach was taken. Instead of using many flats, we corrected for inaccuracies in the cutting of slits by making 1-dimensional flats. That is, we sliced every flat taken immediately after or before the science frame into single columns and then we averaged a few of those where the signal is highest. This was done in the following way: *i)* `imslice` copied individual columns from the flats taken immediately before or after the field spectra to a temporary directory. To optimise time

Table 3.8: Journal of the LDSS2 observations of the WHDF and GSGP4 fields in September 2002.

Mask	RA ^a	DEC ^a	Exposure ^b	FWHM ^c	# Slits ^d	Date ^e
GSGP4-1	00 ^h 57 ^m 30.32 ^s	−27° 31′ 05.0″	3.5	0.6	18	8 th –9 th /11 th –12 th
GSGP4-2	00 ^h 58 ^m 20.91 ^s	−27° 27′ 40.0″	1	0.6	10	12 th –13 th
WHDF-1	00 ^h 22 ^m 36.00 ^s	00° 25′ 30.0″	3	0.8	26	11 th –12 th
WHDF-2	00 ^h 22 ^m 11.00 ^s	00° 21′ 00.0″	4	0.7	23	8 th –9 th
WHDF-3 ^f	00 ^h 22 ^m 56.00 ^s	00° 23′ 25.0″	1	0.9	24	13 th –14 th
WHDF-5	00 ^h 22 ^m 23.00 ^s	00° 24′ 10.0″	1	1.1	18	9 th –10 th
WHDF-6	00 ^h 22 ^m 50.00 ^s	00° 19′ 00.0″	1	1.0	23	12 th –13 th

^aNominal pointing, J2000.
^bIntegration time, in hours
^cSeeing: full width at half maximum, in arcsec
^dNumber of slits in the mask
^eDate of the observations, of September 2002
^fCorrupted data

Run	BLAGN	NLXG	ALG	Stars
2001 (WHDF)	7	6	2	0
2002 (WHDF)	7	3	3	0
2002 (GSGP4)	8	4	4	1
Total	22	13	9	1

Table 3.9: Counterpart type break-down of Chandra sources, as obtained with LDSS2 in the WHDF and GSGP4 fields during the follow-up campaigns of 2001 and 2002. The objects have been divided amongst broad-line quasars, emission-line galaxies, absorption-line galaxies and Galactic stars.

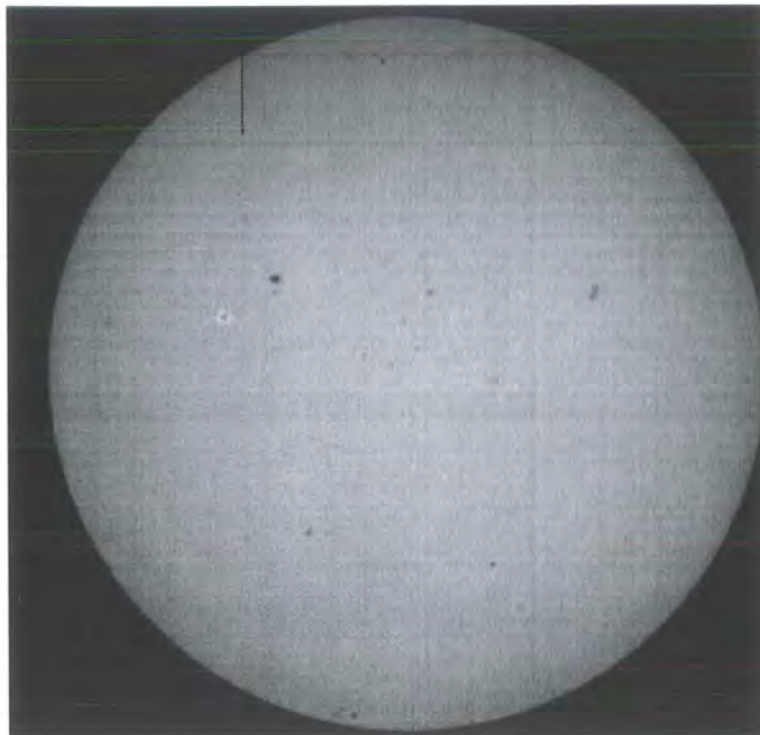


Figure 3.15: Not an abnormally active Sun, but a flatfield of the LDSS2, showing defects and many dust speckles.

and efficiency we selected only the sixty columns around the centre of the chip; these columns have the highest signal and, thus, will give the optimal results for our purposes. *ii*) We combined the sixty columns into a master 1-dimensional flat which was then *iii*) expanded again to the two-dimensional size of a normal image and used individually for every field spectra. The expansion process was done again in three substeps: first, *imstacking* the 1-d image into a 2-d image; second, we *imtransposed* so that the 2-d line becomes a 2-d column; third, we *blkrepeated* 1630 times across the *x* direction the 2-d column to have a flat of the same size as the object frames.

3.4.2 LDSS2 Extraction and Calibration Analysis

For the extraction and calibration of the slit spectra, we used throughout routines within the *noao-imred-spectred-apall* package of IRAF, which conveniently consolidates in a single task all the routines and associated parameters required for extracting spectra.

The first steps towards reducing the data were setting the parameters controlling the extraction aperture and the background windows; this was done interactively with *apall*, modifying default parameters in the aperture editor. Due to optical and

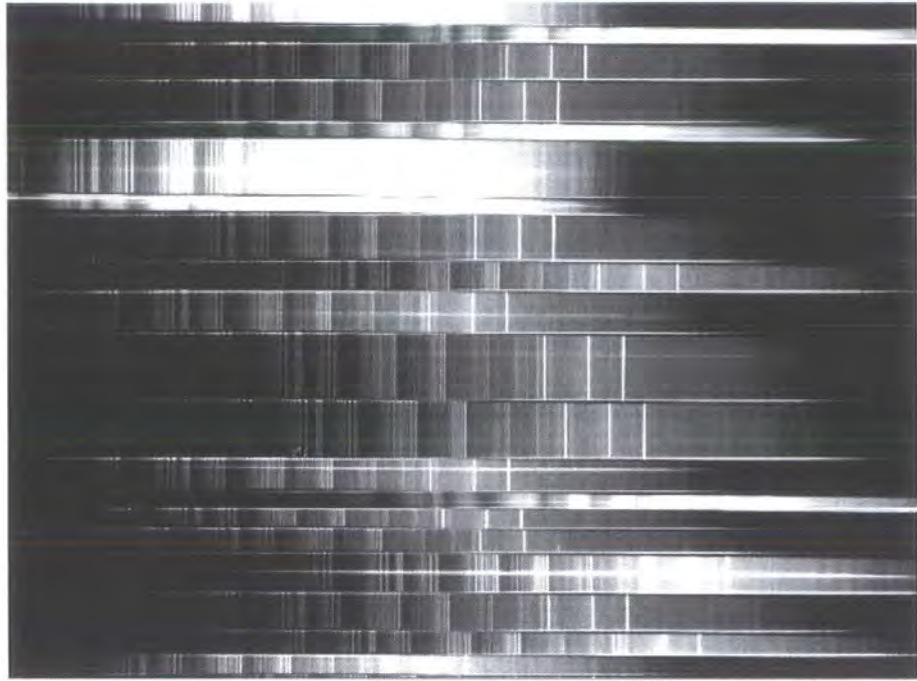


Figure 3.16: LDSS2 mask #1 on the GSGP4 field after removing the detector signature from the data. The dispersion axis goes along rows and the spatial axis, along columns. We note that the background sky spectrum is dominated by strong night-sky emission lines.

mechanical distortions and differential atmospheric refraction, the centre of the spatial profile shifts slightly with location along the dispersion axis and will not be perpendicular to the spatial axis. Therefore, we then needed to trace the centre of the profile as a function of the dispersion axis. As the final extraction step, at each point along the dispersion axis we summed the spectra within the extraction window while at the same time subtracted the background sky.

To wavelength-calibrate the spectra we extracted a 1-d spectrum from the arc-frames using identical aperture and trace parameters used for the object spectrum we wanted to fix. From these comparison spectra we determined the dispersion solution with the task `(re)identify`. The solution found was then put to the object spectra with the help of `dispcor`.

Sample spectra obtained with LDSS2 and reduced as described above are shown in figures 3.17–3.22 on pages 97–102. The complete catalogue for x-ray sources can be found in the spectro-photometric albums of appendix A.

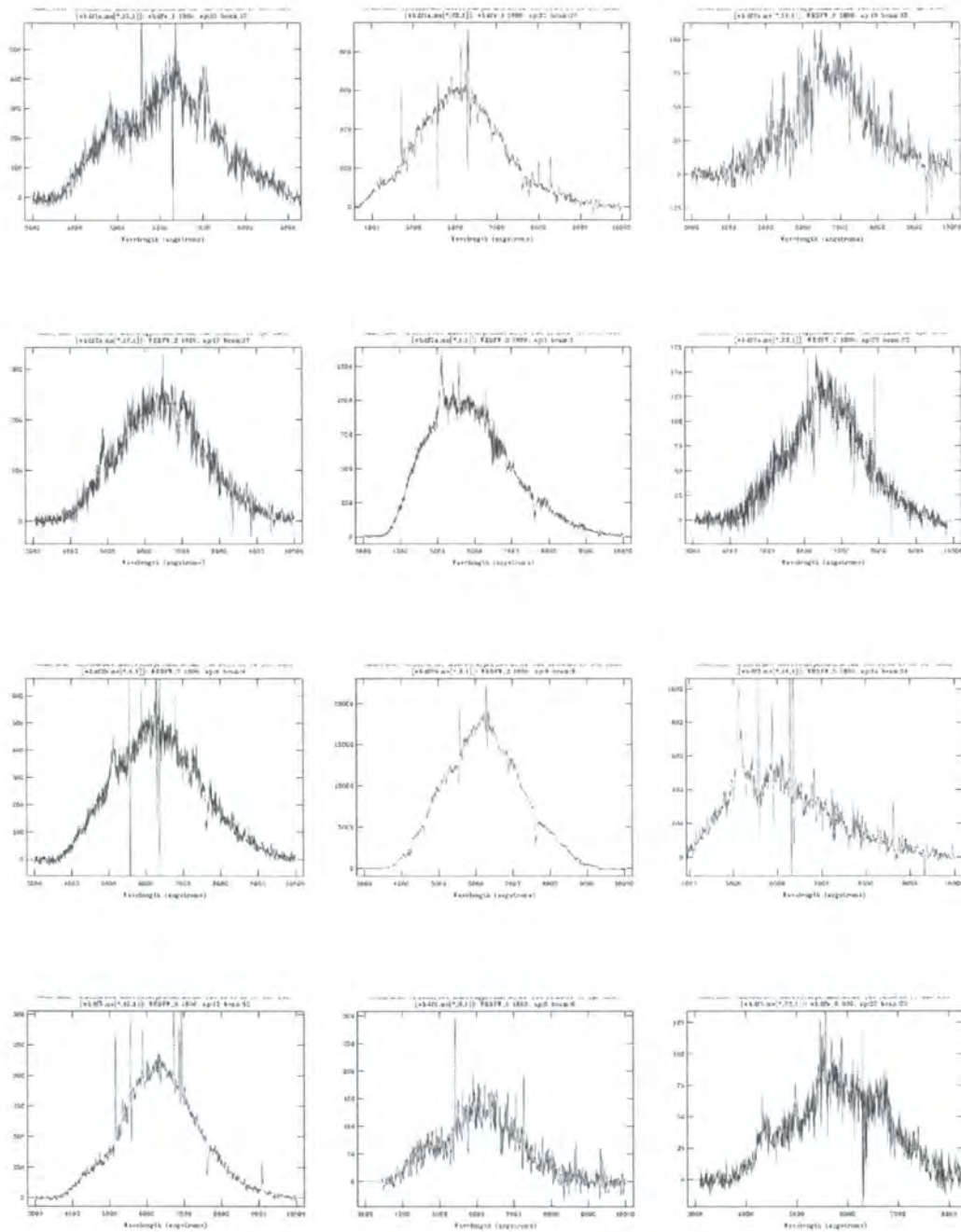


Figure 3.18: LDSS2 spectra of x-ray sources in the WHDF (masks 1, 2, 5, 6; September 2002).

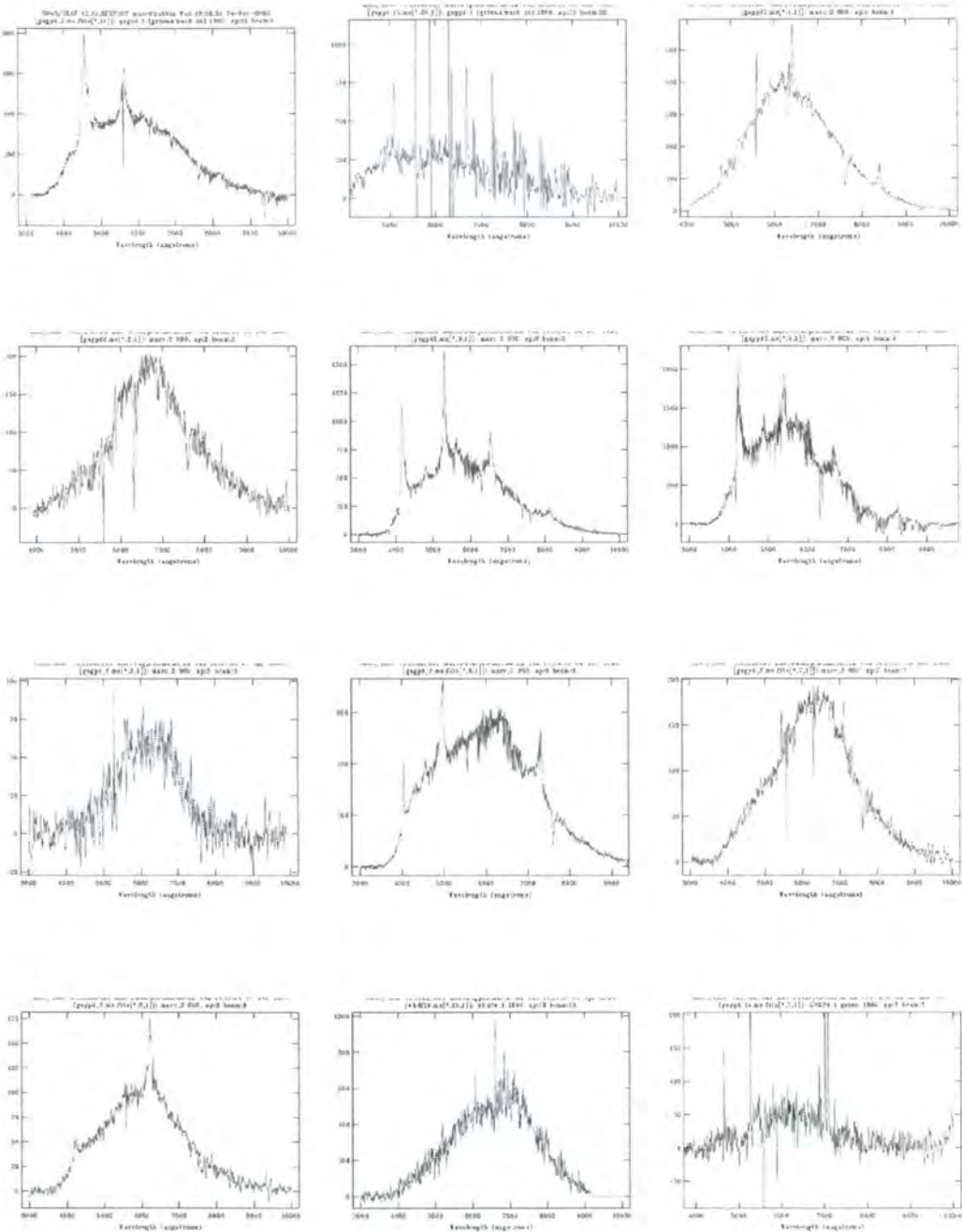


Figure 3.19: LDSS2 spectra of x-ray sources in the WHDF (mask 1) and GSGP4 (mask 2) fields (September 2002).

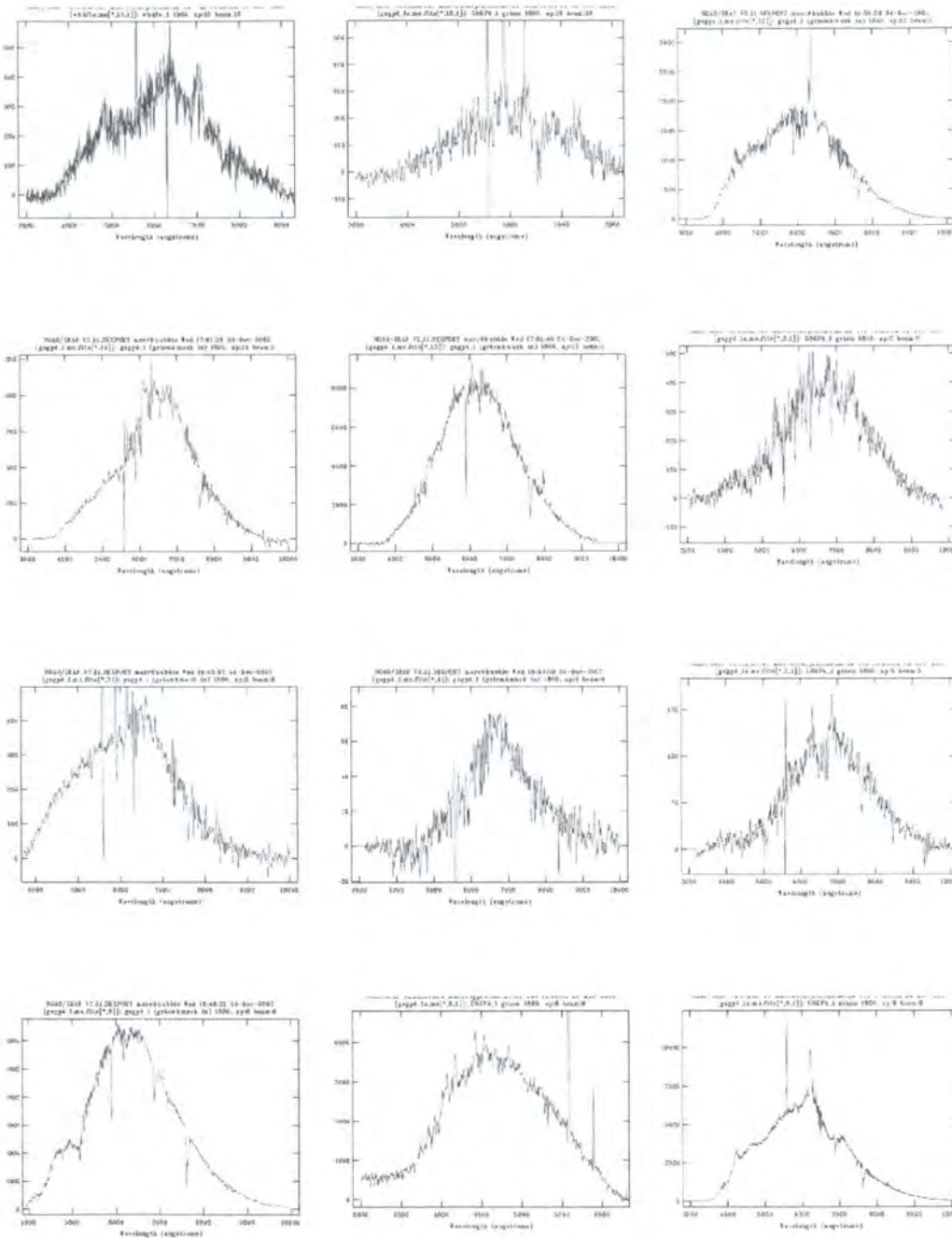


Figure 3.20: LDSS2 spectra of x-ray sources in the GSGP4 field (mask 1; September 2002).

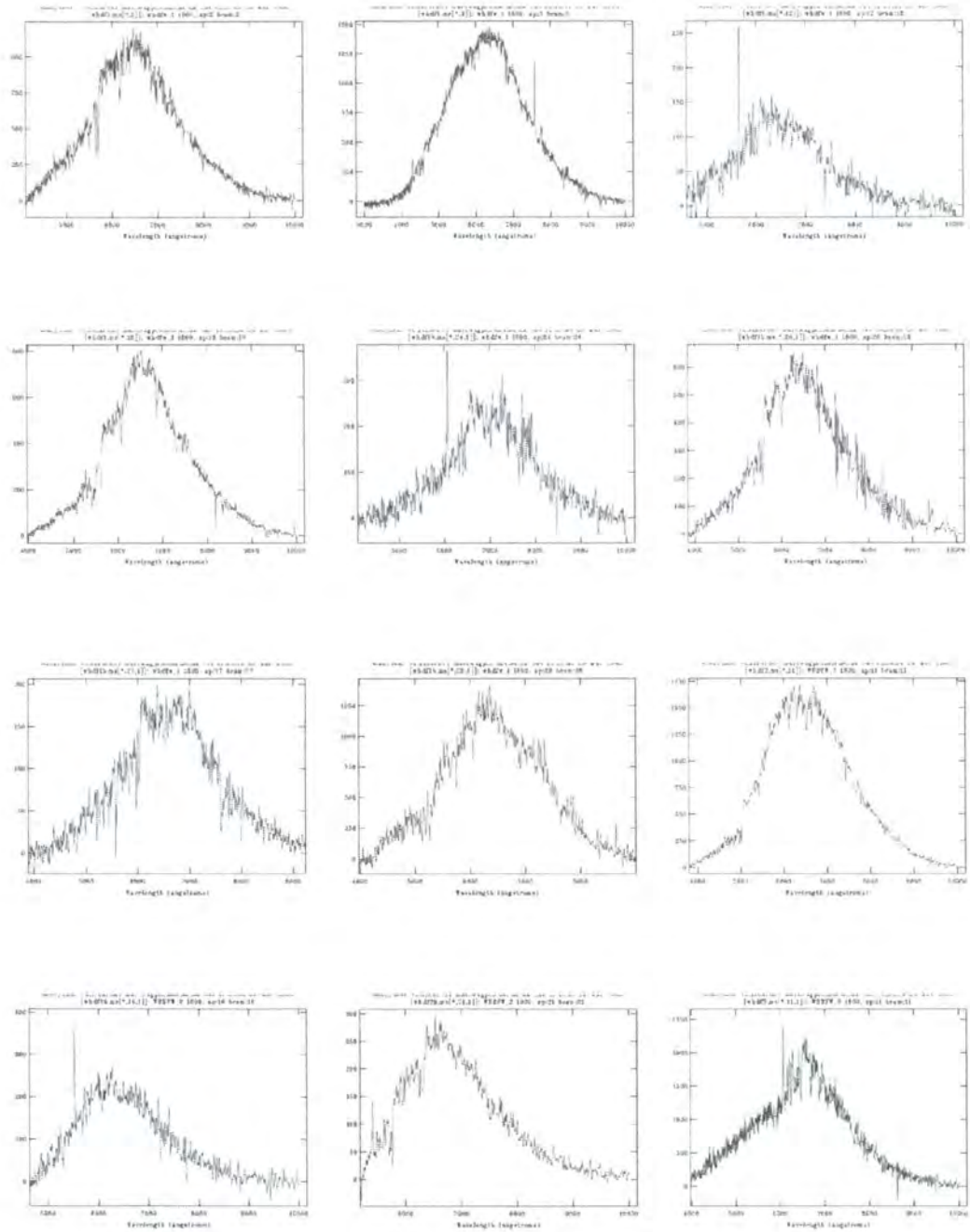


Figure 3.21: LDSS2 spectra of red-selected galaxies in the WHDF (masks 1, 2, 5; September 2002).



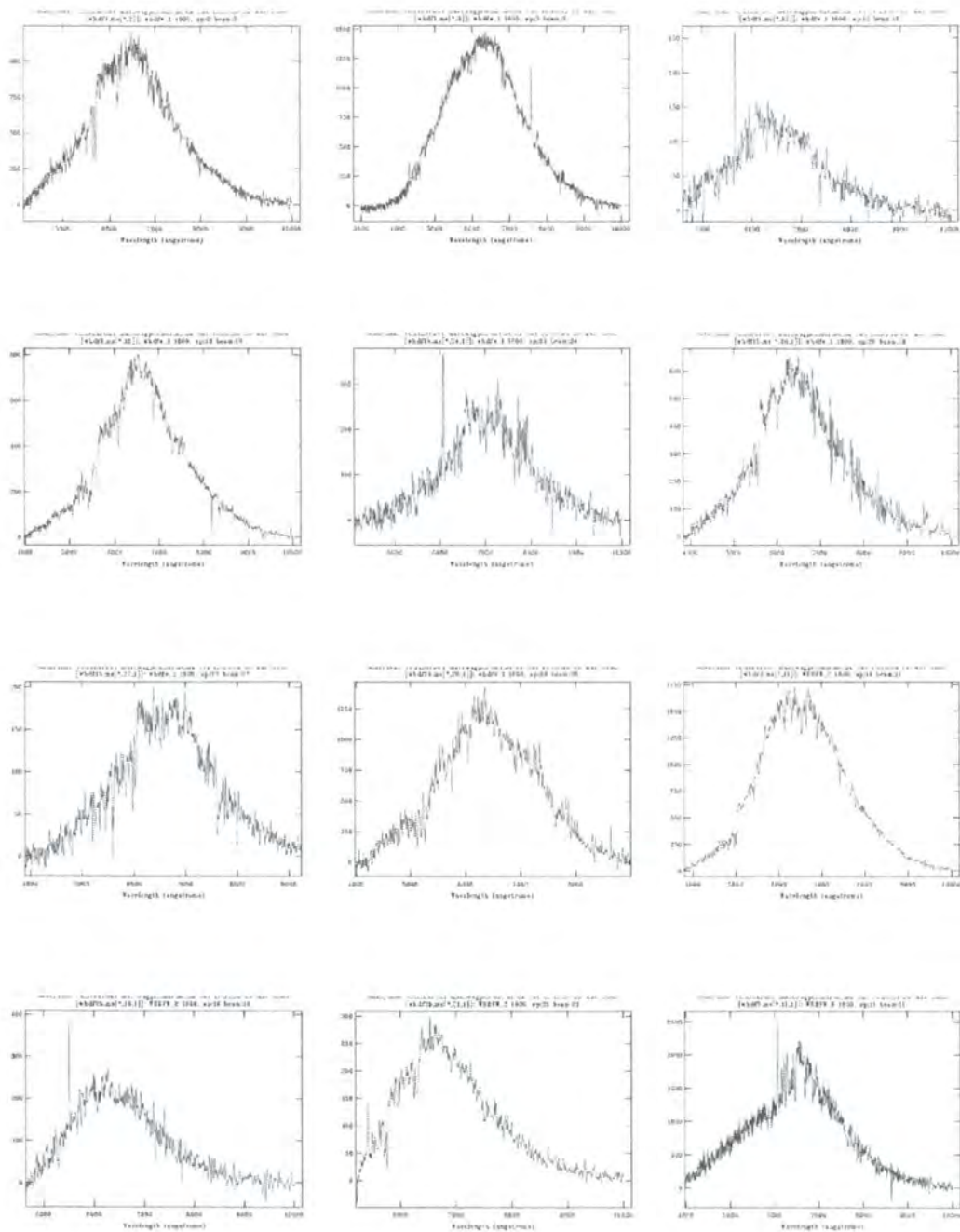


Figure 3.22: LDSS2 spectra of red-selected galaxies in the WHDF (from masks 5, 6, 1; September 2002).

Chandra ID	b_j	Aperture	Type	Redshift
<i>F864CH003</i>	21.63	57	QSO	2.34
<i>F864CH007</i>	19.73	60	Ellip.	0.254
<i>F864CH014</i>	20.63	125	QSO	1.48
<i>F864CH016</i>	21.51	131	QSO	2.22
<i>F864CH020</i>	20.56	129	QSO	2.02
<i>F864CH027</i>	18.78	36	QSO	1.09
<i>F864CH032</i>	21.26	33	Ellip.	0.326
<i>F864CH_A1</i>	17.5	49	Seyf.	0.073
<i>F864CH_A5</i>	20.22	46	Spir.	0.326
<i>F864CH_A11</i>	20.79	67	QSO	1.43
<i>F864CH_B1</i>	21.19	135	QSO	1.76
<i>F864CH_B6</i>	22.05	133	QSO	2.52
<i>F864CH_B9</i>	20.97	16	QSO	1.11
<i>F864CH_C1</i>	17.47	32	Seyf.	0.087
<i>F864CH_C3</i>	14.97	24	Star	0
<i>F864CH_C4</i>	20.09	21	QSO	2.12
<i>F864CH_C7</i>	20.29	40	QSO	1.87

Table 3.10: WYFFOS spectroscopy of Chandra objects in F864. The WYFFOS field, centred on $13^h 44^m -00^\circ 15'$ (J2000), was observed for 10800 seconds under $\sim 1.2''$ seeing conditions on 10th-11th May 2002.

3.5 WYFFOS

As a complementary program to their project to investigate the slope of the faint QSOs number counts using SDSS u, g, r, i, z selected objects, A. Myers and T. Shanks observed a sample of Chandra sources on the F864 field with the WYFFOS spectrograph on the WHT¹⁰ on 10th-11th May 2002. Myers reduced the data and found that, out of the seventeen objects with available spectra, eleven were QSOs, two elliptical galaxies, two Seyfert galaxies, one a spiral galaxy and one a Galactic star. Table 3.10 shows the identifications and redshifts.

3.6 Public Databases and Surveys

We have searched public databases to improve the number of optical counterparts to x-ray sources with known spectral type and redshift. This search has been very fruitful and has allowed gathering redshift information for eighty extra objects, mainly bright quasars.

¹⁰<http://www.ing.iac.es>

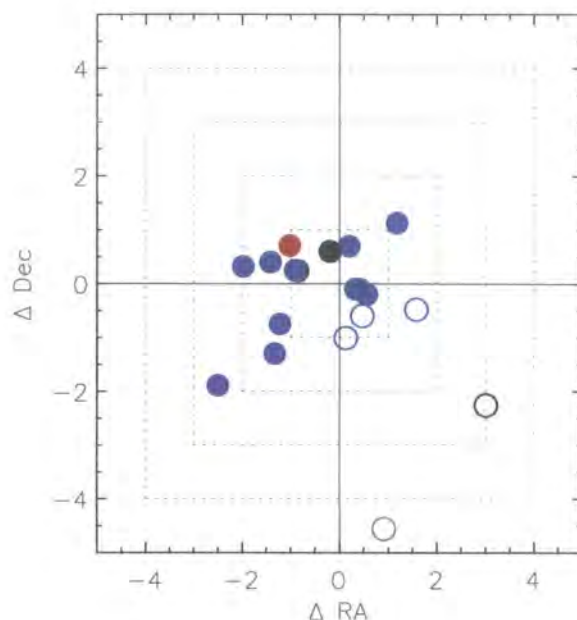


Figure 3.23: Offsets between NED and Chandra positions for the same nineteen objects from table 3.11, in arcsec units.

3.6.1 NED

The NASA/IPAC Extragalactic Database (NED)¹¹ is built around a master list of well over seven million extragalactic objects for which cross-identifications of names have been established from large compilations and from the literature. It provides bibliographic references relevant to individual objects, accurate positions and redshifts, photometry and some other basic data collected. On February 2002 we pursued batch-mode searches of counterparts to Chandra sources in the field F864. Nineteen matches (out of sixty-nine candidates) were found; details are shown in table 3.11 on the following page. Figure 3.23 is a plot of their respective offsets in relation to Chandra positions. Unfortunately, similar searches for the WHDF and GSGP4 did not yield any further identification not previously found through other channels.

¹¹NED is operated by the Jet Propulsion Laboratory, California Institute of Technology, under contract with the National Aeronautics and Space Administration. <http://nedwww.ipac.caltech.edu>

Table 3.11: NED counterparts to Chandra sources in F864.

Chandra ID	NED ID	RA ^a	DEC ^a	Separation ^b	Type	Redshift
<i>F864CH003</i>	RX J1343.4+0001	205.87178	0.02581	0.42	QSO	2.347
<i>F864CH005</i>	F864:114, 2QZ J134322.0+000009	205.84172	0.00283	0.73	QSO	1.976
<i>F864CH007</i>	ARS B134053.59+001325.1	205.86374	-0.02742	0.63	Gal	0.254
<i>F864CH016</i>	F864:158	206.09995	-0.47964	0.59	QSO	2.235
<i>F864CH027</i>	SDSS J134425.95-000056.1	206.10822	-0.01561	0.34	QSO	1.097
<i>F864CH032</i>	ARS B134147.17+001002.9	206.08673	-0.08314	1.48	Gal Sb-Sc	0.326
<i>F864CH033</i>	[CET91] 13.2.14	206.07265	-0.07828	1.24	EmLS, S0/a	-
<i>F864CH034</i>	LDSS 13.12795	206.08449	-0.09006	2.01	QSO	2.934
<i>F864CH035</i>	[CET91] 13.2.31	206.14755	-0.09222	0.89	EmLS	-
<i>F864CH_A1</i>	SDSS J134351.07+000434.8	205.96254	0.07640	0.94	QSO	0.074
<i>F864CH_A11</i>	F864:119	205.80591	-0.08377	1.63	QSO	0.667
<i>F864CH_A4</i>	F864:113	205.99889	0.01217	3.13	QSO	1.410
<i>F864CH_A5</i>	ARS B134128.28+001505.7	206.00763	0.00042	1.86	Gal (Sd-Sm)	0.245
<i>F864CH_A7</i>	F864:097	205.97237	-0.08924	1.43	QSO	1.140
<i>F864CH_A8</i>	FPG 1532	205.98221	-0.10099	4.65	-	-
<i>F864CH_A8</i>	FPG 1532	205.98221	-0.10099	3.76	Gal	-
<i>F864CH_B1</i>	F864:148	206.10216	-0.40375	1.02	QSO	1.767
<i>F864CH_C1</i>	2MASXi J1344528+00052	206.22059	0.08881	0.76	QSO	0.087
<i>F864CH_C7</i>	F864:112	206.08748	0.04070	1.65	QSO	1.884

^aX-ray positions; J2000.^bAngular separation between Chandra and NED counterpart, in arcseconds.

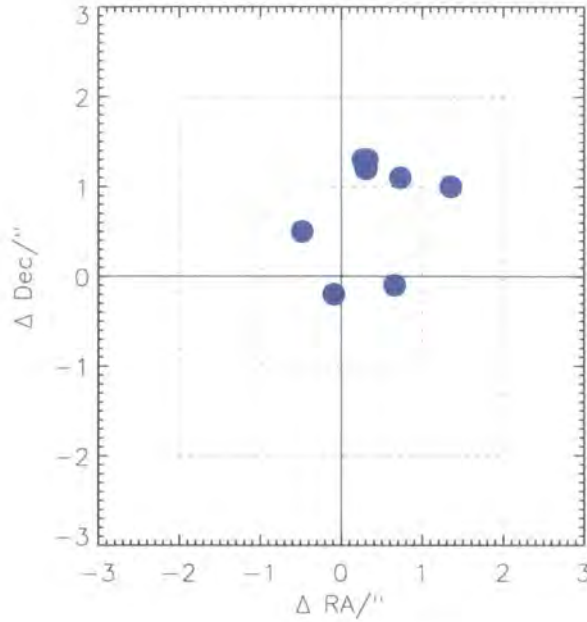


Figure 3.24: Offsets between 2QZ and Chandra positions for the objects from table 3.12 in arcsec units.

3.6.2 2dF Surveys

The 2dF Galaxy Redshift Survey (2dFGRS)¹² and the 2dF Quasar Redshift Survey (2QZ)¹³ are two integrated major spectroscopic surveys that took advantage of the capabilities of the 2dF spectrograph at the AAO to obtain, over an area of approximately fifteen hundred square degrees, spectra for $\sim 2.5 \times 10^5$, $b_j < 19.4$ magnitude, galaxies and $\sim 2.5 \times 10^4$, $b_j < 20.85$ magnitude, QSOs.

The fields were selected from the extended APM Galaxy Survey in three regions: two $75^\circ \times 5^\circ$ declination strips in the South Galactic Pole (SGP) and in an equatorial region at the North Galactic cap, and random fields scattered around the SGP strip.

GSGP4 was therefore part of the 2dF surveys. However, given the limit of $b_j = 19.45$ imposed on a survey covering such a large area, not many galaxies were found to match Chandra x-ray objects. On the other hand, ten quasars were found to be x-ray sources. This was expected on the grounds that quasars are powerful x-ray emitters and on the fainter survey limit for quasars of $B = 21$. The positional offsets between Chandra and 2QZ coordinates for these quasars are plotted in figure 3.24; a list with features such as their colours and redshifts is found in table 3.12 on the next page.

¹²<http://magnum.anu.edu.au/~TDFgg/>

¹³<http://www.2dfquasar.org>

Table 3.12: 2QZ counterparts to Chandra sources in GSGP4.

Chandra ID	2QZ ID	IAU name	RA ^a	DEC ^a	Separation ^b	b_j	$b - r$	$u - b$	Type	Redshift
GSGP4CH003	2595	J005717.9-271831	00:57:17.90	-27:18:31.4	1.24	20.28	0.63	-0.53	QSO	1.67
GSGP4CH040	2584	J005724.4-273201	00:57:24.48	-27:32:01.2	0.67	18.86	0.36	-0.8	QSO	1.22
GSGP4CH053	2589	J005734.9-272828	00:57:34.92	-27:28:28.3	0.22	18.42	0.37	-0.73	QSO	2.19
GSGP4CH082	2567	J005747.5-275412	00:57:47.51	-27:54:12.3	0.69	20.59	-0.02	-0.79	QSO	1.28
GSGP4CH083	2571	J005805.7-275005	00:58:05.74	-27:50:05.5	1.32	20.4	0.99	-0.68	QSO	0.49
GSGP4CH087	2573	J005759.8-274733	00:57:59.82	-27:47:33.6	1.68	19.29	0.64	-0.93	QSO	1.64
GSGP4CH095	2588	J005818.1-272849	00:58:18.14	-27:28:49.0	1.24	19.91	0.32	-0.73	QSO	1.61
GSGP4CH101	2591	J005811.4-272636	00:58:11.41	-27:26:36.8	1.33	20.58	0.24	-0.84	QSO	2.48
GSGP4CH104	2621	J005813.9-272550	00:58:13.98	-27:25:50.8	1.33	20.07	0.14	-0.09	QSO	2.43
GSGP4CHNS3_012	2526	J005622.5-272226	00:56:22.57	-27:22:26.5	2.53	20.15	0.03	0.01	QSO	1.13

^a2QZ positions; J2000.^bAngular separation between Chandra and 2QZ counterpart in arcseconds.

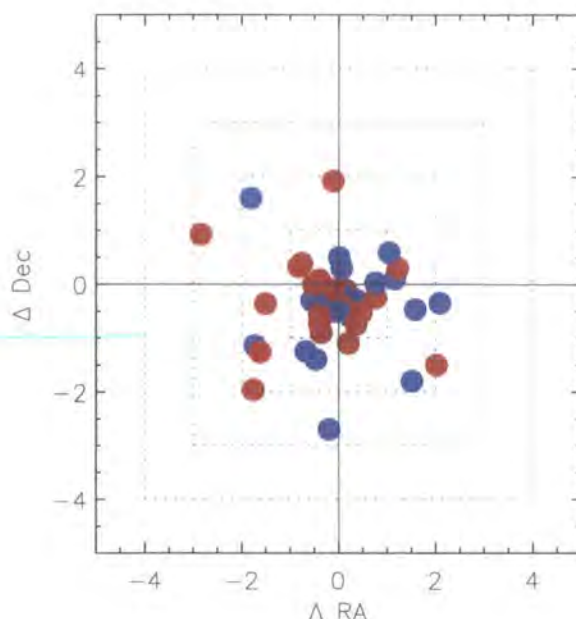


Figure 3.25: Offsets between SDSS and Chandra positions for the objects from table 3.13 in arcsec units. Fifty-one sources were found to match to better than three arcseconds.

3.6.3 Sloan Digital Sky Survey

We correlated the Early Data Release (EDR; Stoughton et al. 2002) of the Sloan Digital Sky Survey (SDSS)¹⁴ with X-ray sources to identify optical counterparts in the WHDF and F864. The SDSS will map half of the northern hemisphere, producing a detailed image of it and extensive photometric, spectroscopic and morphological information is stored for about a million galaxies and a hundred thousand quasars. This makes it the largest survey ever undertaken and a prime tool for astronomical studies.

Although both fields are covered in the SDSS, the EDR did not include any spectra for a Chandra counterpart. Given that we had already very deep imaging and photometry in the WHDF spanning a range of filters, this meant that for this field the SDSS did not bring up any new information. For field F864, on the other hand, the cross-correlation of Chandra and SDSS sources was very successful and yielded fifty-one matches (table 3.13 and figure 3.25). Through its five colours, the Sloan data provides a plethora of information for each source and, for most practical purposes in F864, we have adopted their photometry.

¹⁴<http://www.sdss.org>

Table 3.13: SDSS counterparts to Chandra sources in F864.

Chandra ID	RA ^a	DEC ^a	Separation ^b	Type	<i>u</i>	<i>g</i>	<i>r</i>	<i>i</i>	<i>z</i>	<i>b_j</i>
<i>F864CH003</i>	13:43:29.218	+00:01:32.7	0.24	Star	22.24	21.41	20.98	20.56	20.08	21.63
<i>F864CH004</i>	13:43:27.840	+00:00:08.2	0.30	Gal	22.58	20.48	18.8	18.18	17.86	20.89
<i>F864CH005</i>	13:43:22.027	+00:00:10.0	0.29	Star	20.29	20.21	20.19	19.9	19.79	20.38
<i>F864CH007</i>	13:43:27.295	-00:01:38.5	0.20	Gal	21.29	19.37	18	17.49	17.19	19.73
<i>F864CH008</i>	13:43:25.666	-00:01:23.1	0.16	Gal	22.76	23.08	22.08	21.14	20.6	23.4
<i>F864CH009</i>	13:43:32.681	-00:02:03.3	0.20	Star	20.54	20.05	20.02	19.99	19.53	20.22
<i>F864CH010</i>	13:44:13.001	-00:27:20.7	0.37	Gal	24.2	22.44	21.61	20.72	20.31	22.72
<i>F864CH013</i>	13:44:14.083	-00:29:50.1	0.30	Star	19.95	19.51	19.32	19.11	18.95	19.69
<i>F864CH014</i>	13:44:12.886	-00:30:05.5	0.40	Gal	20.75	20.45	20.3	20.05	19.79	20.63
<i>F864CH015</i>	13:44:09.257	-00:30:37.0	2.52	Gal	22.47	22.26	21.71	21.49	20.8	22.5
<i>F864CH016</i>	13:44:23.954	-00:28:46.5	0.53	Star	22.03	21.38	21.51	21.1	21	21.52
<i>F864CH017</i>	13:44:18.828	-00:30:41.9	0.64	Star	22.72	20.59	20.16	20.11	19.83	20.81
<i>F864CH019</i>	13:43:56.290	-00:25:39.6	0.48	Star	23.13	22.78	23.13	22.23	22.57	22.89
<i>F864CH020</i>	13:44:20.078	-00:31:10.6	0.51	Gal	20.87	20.43	20.55	20.33	20.14	20.57
<i>F864CH021</i>	13:43:55.553	-00:31:46.6	1.11	Gal	22.32	22.49	22.25	21.75	21.05	22.68
<i>F864CH022</i>	13:43:51.146	-00:30:49.3	0.50	Star	22.25	22.01	21.83	21.45	21.62	22.2
<i>F864CH024</i>	13:43:53.798	-00:32:37.4	2.70	Star	23.98	23.72	22.2	21.81	21.07	24.11
<i>F864CH025</i>	13:43:46.970	-00:31:15.7	2.42	Star	25.14	23.71	22.4	22.25	21.52	24.06

(continues...)

Table 3.13: SDSS counterparts to Chandra sources in F864 (continued).

Chandra ID	RA ^a	DEC ^a	Separation ^b	Type	<i>u</i>	<i>g</i>	<i>r</i>	<i>i</i>	<i>z</i>	<i>b_j</i>
<i>F864CH027</i>	13:44:25.949	-00:00:56.2	0.34	Star	18.7	18.6	18.44	18.49	18.5	18.79
<i>F864CH029</i>	13:44:25.030	+00:01:23.2	0.63	Star	21.32	21.21	21.2	20.86	20.67	21.37
<i>F864CH030</i>	13:44:38.304	-00:00:51.1	0.52	Gal	21.34	21.16	21.02	20.86	20.51	21.34
<i>F864CH032</i>	13:44:20.820	-00:04:58.9	0.40	Gal	22.62	20.91	19.64	19.11	18.7	21.26
<i>F864CH033</i>	13:44:17.439	-00:04:42.1	0.30	Star	23.38	22.66	22.65	21.94	21.42	22.82
<i>F864CH034</i>	13:44:20.354	-00:05:24.3	1.15	Star	23.53	22.25	22	21.96	21.62	22.44
<i>F864CH035</i>	13:44:35.397	-00:05:31.6	0.46	Star	23.15	23.09	22.42	22.39	21	23.35
<i>F864CH036</i>	13:44:33.574	-00:05:36.9	0.50	Star	21.59	19.04	17.54	16.02	15.2	19.42
<i>F864CH038</i>	13:44:29.203	-00:05:53.0	0.13	Gal	21.82	21.25	20.33	19.75	19.43	21.54
<i>F864CH039</i>	13:44:08.040	-00:03:08.9	0.96	Gal	22.85	22.18	21.7	21.57	21.05	22.41
<i>F864CH040</i>	13:44:24.566	-00:06:17.0	0.59	Star	20.43	20.28	20.19	20.08	19.83	20.46
<i>F864CH_A1</i>	13:43:51.065	00:04:34.7	0.89	Gal	17.73	17.3	17.01	16.59	16.55	17.51
<i>F864CH_A2</i>	13:43:44.285	00:05:08.9	1.47	Star	21.46	21.31	21.39	21.13	21.02	21.46
<i>F864CH_A3</i>	13:43:42.384	00:06:44.3	1.55	Gal	21.64	21.11	20.08	19.6	19.18	21.43
<i>F864CH_A5</i>	13:44:01.949	00:00:03.5	2.63	Gal	20.62	19.93	18.98	18.53	18.06	20.23
<i>F864CH_A6</i>	13:43:52.961	-00:04:38.4	0.85	Gal	22.4	22.1	21.12	20.42	20.03	22.4
<i>F864CH_A7</i>	13:43:53.484	-00:05:20.1	2.07	Star	20.51	20.53	20.28	20.23	20.46	20.73
<i>F864CH_A8</i>	13:43:55.630	-00:06:01.8	2.35	Star	23.39	21.21	20.38	19.93	19.76	21.5

(continues...)

Table 3.13: SDSS counterparts to Chandra sources in F864 (continued).

Chandra ID	RA ^a	DEC ^a	Separation ^b	Type	<i>u</i>	<i>g</i>	<i>r</i>	<i>i</i>	<i>z</i>	<i>b_j</i>
<i>F864CH_A9</i>	13:44:19.930	00:04:16.4	0.69	Gal	26.51	20.81	19.28	18.66	18.27	21.2
<i>F864CH_A11</i>	13:43:13.368	-00:05:01.3	0.8	Gal	21.12	20.61	20.42	19.86	19.43	20.8
<i>F864CH_B1</i>	13:44:24.545	-00:24:12.8	0.83	Gal	21.16	21.06	21.18	20.8	21.05	21.2
<i>F864CH_B3</i>	13:44:25.970	-00:25:30.5	0.82	Gal	23.36	22.54	20.8	20.27	19.75	22.96
<i>F864CH_B5</i>	13:44:46.927	-00:30:09.4	2.05	Gal	22.34	21.94	20.07	19.05	18.62	22.38
<i>F864CH_B6</i>	13:44:37.402	-00:32:37.4	0.4	Gal	24.23	21.86	21.67	21.91	21.14	22.05
<i>F864CH_B8</i>	13:44:14.472	-00:24:14.4	2.99	Gal	24.18	23.49	22.85	21.99	22.02	23.74
<i>F864CH_B9</i>	13:44:24.562	-00:13:03.1	1.43	Star	20.79	20.75	20.35	20.38	20.53	20.97
<i>F864CH_C1</i>	13:44:52.910	00:05:20.2	0.7	Gal	17.65	17.25	16.82	16.29	16.13	17.47
<i>F864CH_C2</i>	13:44:19.930	00:04:16.4	1.26	Gal	26.51	20.81	19.28	18.66	18.27	21.2
<i>F864CH_C3</i>	13:45:14.978	-00:00:47.9	1.2	Star	13.29	14.89	15.38	14.82	12.14	14.97
<i>F864CH_C4</i>	13:45:08.038	-00:05:26.7	1.92	Gal	20.45	19.91	19.71	19.57	19.07	20.1
<i>F864CH_C6</i>	13:44:55.819	-00:01:16.5	2.12	Star	21.38	20.91	20.83	20.64	20.08	21.08
<i>F864CH_C7</i>	13:44:20.890	00:02:27.0	1.65	Star	20.25	20.13	20.11	19.85	19.55	20.29
<i>F864CH_C8</i>	13:44:35.834	00:03:46.2	0.76	Star	22.15	22.44	22.27	22.06	21.79	22.62

^a SDSS positions; J2000.^b Angular separation between Chandra and SDSS counterpart in arcseconds.

3.7 Summary

This chapter has described the optical data used in the WHDF and 10×10 ks surveys. Particular emphasis has been placed on the reduction analyses of the imaging and spectroscopic data obtained with the WFI camera on the AAT and with the LDSS2 spectrograph on Magellan-1, respectively. In the photometric catalogues constructed with WFI data, we have detected optical counterparts to 67 Chandra sources in the GSGP4 field, down to magnitudes of $g = 25.3$, $r = 25.0$ and $i = 23.7$. 28 of these are a subset of the almost 200 sources targeted in 2001 and 2002 with LDSS2 to provide identifications and redshifts for Chandra sources (64 targeted in the combined WHDF and GSGP4) and for $B : R : I$ -selected elliptical and lenticular galaxies in a parallel program to study the evolutionary properties of the early-type galaxy population. Amongst the x-ray sources, several high-resolution spectra have been obtained for objects which were catalogued as very faint according to preexisting photometry and *vice versa*, implying large optical variability in our x-ray samples. Details of the data reduction of WFC/INT have also been given. Catalogues with properties of optical counterparts to Chandra sources are also constructed in a) the WHDF, from deep multiband imaging and photometry for 93 objects; in b) F864, from SDSS multiband imaging and photometry for 51 objects, from deep spectroscopy with WYFFOS for 17 objects and from publicly available spectroscopic data for 4 extra sources; and in c) GSGP4, from the 2QZ survey for 10 bright quasars.

CHAPTER IV

The Nature of the XRB

We have seen in chapter 2 that intermediately deep Chandra surveys eventually resolve the soft and hard x-ray backgrounds into discrete sources and only a negligible contribution from a diffuse hot gas such as intergalactic medium (IGM) is allowed. Also, the x-ray spectra of these sources is found to be hard enough as to solve the “spectral paradox” (§ 2.5; see also figure 4.10). Having found further evidence that explain these problems, we can now use our observations to focus on understanding the physical nature and the cosmic evolution of the sources that make the XRB and their role in models of galaxy and AGN evolution.

In section 4.1 of the present chapter we classify the x-ray sources detected serendipitously in extragalactic blank fields into separate categories and draw conclusions regarding their major x-ray emission mechanisms (star formation *vs.* AGN). In section 4.2 we address one of the most fundamental problems yet to be clarified, namely whether AGN live in old, evolved galaxies or instead in young galaxies with high levels of star formation. To answer this question we undertake a full characterisation of the galaxies that host an x-ray source. (This topic finds a natural complement in the study of the evolutionary properties of $z < 0.5$ early-type galaxies of the WHDF in colour space, in chapter 5.) We next review in section 4.3 the major strengths and weaknesses of the XRB population synthesis models, paying particular attention to type II QSOs and to the validity of the unified model for AGN at high redshifts. Finally, in section 4.4 we comment on minor contributors of the XRB: Galactic stellar contamination, extremely red objects (EROS) and ultraluminous x-ray sources (ULXs).

4.1 Source Content

Amongst the most notable x-ray emitters in the Universe capable to contributing to the XRB we find: *a)* QSOs, *b)* Seyferts, *c)* absorbed AGN,¹ *d)* low level AGN (LLAGN),

¹It is worth distinguishing between absorption of x-ray light by large column densities and obscuration of optical light by dust, for these phenomena may not be always coupled in AGN as section 4.3.2

e) Galactic stars, f) starburst galaxies, g) optically inactive galaxies, h) diffuse hot gas (clusters of galaxies, IGM, ...), etc. While the contributions at hard energies and faint fluxes from any diffuse gas or from Galactic stars are bound to be minor (§ 2.4.3, 4.4.1), a clear description of how the other classes contribute is not yet available. Of equal urgency is the research into the nature of the dominant x-ray emission mechanisms within these classes. In particular, many narrow emission-line galaxies (NELGs) are found as optical counterparts to a population of unusually x-ray luminous galaxies with hard spectra at faint fluxes (chapter 3). The origin of their x-ray photons is unclear; starburst activity and obscured AGN are the most favoured solutions, but knowing a precise answer would greatly benefit population synthesis models for the XRB and, more generally, models for the evolution of AGN.

In the present section we take a close look at the discriminants at our disposal to classify the sources and enquire about their emission mechanisms. Thus in section 4.1.1 we classify the sources according to their spatial extent and to their spectral signatures, while in section 4.1.2 we use x-ray to optical flux ratios and optical colour-colour diagrams to respectively test the relative importance of AGN/starburst emission and the relative fractions of galaxies of different Hubble type amongst x-ray-loud galaxies.

4.1.1 Source Classification

Imaging

Chandra's $\text{FWHM} = 0.5''$ spatial resolution places stringent limits on whether a source is point-like or extended. In this regard, once deconvolved with the instrument's PSF, all detections are compatible with being spatially unresolved. Hence we find no contribution from clusters of galaxies or any diffuse hot gas, although a few clusters are known to exist in our fields.² This result is expected on the basis of the small size of the fields surveyed and the negative evolution with redshift of the luminosity functions of clusters (Edge et al. 1990; meaning that most luminous clusters are most numerous at the present epoch and have been already detected with shallower and wider surveys).

We note as well that $0.5''$ roughly corresponds to 4 kpc at a redshift $z \sim 1$ and to 2 kpc at $z \sim 0.25$; it is therefore virtually impossible to distinguish any sort of extended emission in nuclear starbursts or even in low redshift optically inactive galaxies whose x-ray light would come from binaries spread across the galaxy or from interstellar hot gas with a King profile. We see, then, that Chandra imaging is not particularly useful to discriminate between classes of x-ray emitters, for most of them appear point-like.

Optical imaging is more suited to distinguish stars or QSOs (point-like) from

shows.

²In fact we only detect a minor overdensity of x-ray photons around a cluster at $\alpha = 00^h 22^m 45^s 24$, $\delta = 00^\circ 23' 26''$ (J2000), whose optical colours seem to put it at $z > 1$.

galaxies (extended). This morphological classification is very useful, particularly for sources without spectroscopy. We use it as a diagnosis on its own (as in figure 4.10) and combined with most observables (ubiquitously in this chapter).

Spectroscopy

The most direct route to identifying a source is via its spectrum. x-ray spectra are of very limited use in our samples given their faintness (typically the detectors record $\sim 10^{-3}$ counts per second per source) and multiparameter fits that would directly measure the intrinsic column densities are infeasible but for the brightest objects.^{3,4}

At present, with multi-object spectroscopic (MOS) facilities on most large telescopes, obtaining optical spectra is indeed much more productive. We have undertaken optical spectroscopic follow-up campaigns as described in chapter 3 and, together with publicly available data, have unambiguously classified 79 sources according to their lines.

Spectral Line Classification

Motivated by our spectroscopic data not having flux-calibration and by the LDSS2 instrument not having high enough spectral resolution for precise line-width measurement, as required by accurate AGN identification methods based on emission line strength ratios (e.g. Veilleux & Osterbrock 1987), we have taken a coarser approach into classifying sources. We classify the optical spectra of the extra-galactic x-ray sources into three general categories according to the following line signatures: a) broad emission lines or clear signs of any of the following emission lines, exclusive of broad-line AGN: Ne V λ 1240, Si IV, O IV λ 1400, N IV λ 1486, He II λ 1640, O III λ 1663 or N III λ 1750 (category “BLAGN”: QSOs, Sy 1 —broad-line active galactic nucleus); b) not in category BLAGN and conspicuous emission lines (category “NLXG”: Sy II, other obscured AGN, starburst —narrow emission-line x-ray galaxy); c) not in category BLAGN and marginal or no emission lines and clear absorption lines (category ALG: early-type galaxies — absorption-line galaxy).

We note that this classification, while it can unambiguously detect a broad-line AGN in a galaxy, it is incapable of differentiating between star formation and AGN since both have narrow emission-lines and are classified as NLXGs. A full treatment of this problem would require comparison of the ratio of emission intensities of various pairs of lines close together in the spectrum, as in the traditional AGN and starburst classifications based on the $\log(I_{\text{O III}}/I_{\text{H}\beta}) : \log(I_{\text{N III}}/I_{\text{H}\alpha})$ flux-ratio diagnostic diagram (e.g. Baldwin et al. 1981; Veilleux & Osterbrock 1987; Kewley et al. 2001).

³Spectral analysis of stacked sources which have been statistically grouped into meaningful categories beforehand is another possibility.

⁴As described in chapter 2, gross information about the spectra of x-ray sources can be obtained from their soft to hard band flux and hardness ratios; these are intensively used later in this chapter. Nevertheless, they are not practical for our current classification purposes.

Field	BLAGN	NLXG	ALG	Stars
WHDF	14	9	5	0
F864	11	3	2	1
GSGP4	25	4	4	1
<i>Total</i>	50	16	11	2

Table 4.1: Spectroscopic classification of sources. Summary of the number of sources in each of the types defined in the text.

Although such analysis is beyond our possibilities, in section 4.1.2 we address the issue of AGN/starburst emission under the guidance of x-ray-to-optical flux ratios.

A summary of the number of identified sources in each category is shown in table 4.1. We caution that these do not represent the true proportions of classes in the surveys for the follow-up is biased, particularly towards QSOs (many QSOs were known from previous ROSAT surveys or from the 2QZ, and many are bright which eases identification, for instance).

Luminosity Classification

A second natural advantage of spectroscopy is that it provides a redshift for the sources and hence their luminosities can be easily computed. Given that the intrinsic brightness gives direct clues on the emission mechanisms, yet another way to classify a source is according to its luminosity. Thus, AGN luminosities range from as low as $L_X = 10^{36}$ (Ho 2003) to $L_X = 10^{48}$ ergs $^{-1}$; on that scale, quasars are the luminous AGN ($L_X \geq 10^{44}$ ergs $^{-1}$, $M_B \lesssim -23$ mag). As for galaxies, typical late-types have luminosities of $10^{38} \lesssim L_{0.5-3.5 \text{ keV}} \lesssim 10^{41}$ ergs $^{-1}$ while early-type galaxies are in the range $10^{39} \lesssim L_{0.5-3.5 \text{ keV}} \lesssim 10^{42}$ ergs $^{-1}$. At the flux limits of the 10×10 ks survey, and even the WHDF, this means that we select galaxies at redshifts $z \lesssim 0.5$ (see § 2.4.1).

However, a luminosity classification would be more useful for sources without spectroscopy, for which no line classification can be used to start with. This is particularly relevant in our samples given that their optical faintness makes complete spectroscopic follow-up expensive (50% of the sources have $I \gtrsim 23.5$). The availability of multiband photometry in the WHDF and F864 fields makes the pursuit of photometric redshifts certainly desirable in order to improve the quality of our studies. Although we have been studying galactic redshift evolution in colour-colour diagrams (§ 4.1.2, 5), we have not yet attempted those. We anticipate inconsistencies due to the contamination from the light of the AGN onto the glare of the host galaxy; the available spectroscopic redshifts will provide a reliable benchmark to quantify them. Photometric redshifts remain a priority in the schedule of future work.

4.1.2 Emission Mechanisms

X-ray-to-Optical Flux Ratios

The distribution of the fluxes in the 0.5–10 keV band and in the R optical band proves a fruitful way to explore the emission mechanisms of the sources in our sample. Powerful AGN are identified in x-ray surveys by their elevated high-energy output (e.g. Elvis et al. 1994) and therefore display enhanced x-ray-to-optical flux ratios, $\log f_x/f_{\text{opt}} \gtrsim -1$. On the other hand, low-level AGN (LLAGN) and star-forming galaxies have lower flux ratios, typically $\log f_x/f_{\text{opt}} \lesssim -1$ (e.g. Maccacaro et al. 1988; Stocke et al. 1991).

Figure 4.1 shows the optical and x-ray fluxes for the two surveys, with the areas typically occupied by AGN and galaxies shaded distinctively. Morphological and spectroscopic information is provided by the following legend: a) point-like and extended sources in the optical images are plotted as skeleton stars and circles, respectively; empty triangles denote lack of reliable morphological information while optically blank counterparts to x-ray sources are marked with upward arrows; b) x-ray spectra are summarised with symbol size: bigger for hard ($\text{HR} > 0$) sources; c) optical spectral type is provided, when available, for the four classes into which we have ordered our sample: broad-line AGN (blue stars), NELGs (blue squares), absorption-line galaxies (red circles) and Galactic stars (yellow stars); empty symbols are reserved for when spectroscopic identification is ambiguous.

In the WHDF (upper panel of figure 4.1) we immediately note that, regardless of optical magnitude and despite the 3σ flux detection limit of $4 \cdot 10^{-16} \text{ erg cm}^{-2} \text{ s}^{-1}$, most x-ray sources are concentrated about fluxes $f_x \sim 10^{-14} \text{ erg cm}^{-2} \text{ s}^{-1}$. This is due to the 2–10 keV source number counts turning over at these flux regimes, in which therefore the source number counts are maximised (§ 2.4). These sources all have $\log f_x/f_{\text{opt}} \gtrsim -1$, typical of AGN. They include most of the broad-line AGN, all of the hard sources in the WHDF sample (hence we conclude that, on basis of their flux ratios, hard sources are likely powered by AGN), all of the optically blanks (hence we conclude that, on basis of their flux ratios, optically blank counterparts to x-ray sources are likely powered by AGN), $\sim 3/4$ of the narrow emission-line galaxies (both hard and soft) and $1/3$ of the absorption-line galaxies (all of which are soft, in contrast with reports from Mushotzky et al. 2000 which highlight the existence of early-type galaxies with rather hard spectra; the discrepancy might be due to cosmic variance).

In the same panel we also observe that, at very faint fluxes, $f_x \lesssim 10^{-15} \text{ erg cm}^{-2} \text{ s}^{-1}$, all sources are galaxies with very soft spectra (NLXGs and ALGs; $\text{HR} \lesssim -0.7$), occupying the parameter space region typical for non-AGN emitters. $2/3$ of all the early-types in the WHDF sample belong to this group and, moreover, all have

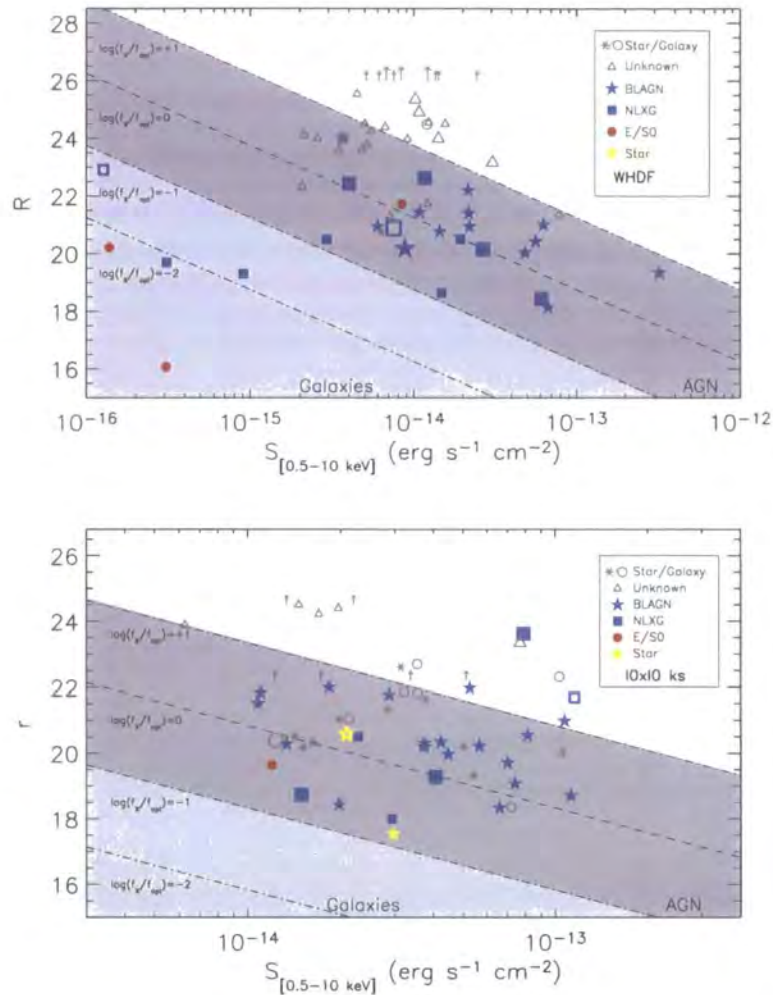


Figure 4.1: R band magnitude vs. total x-ray flux. Open circles and radial stars correspond to x-ray detections with extended and point-like optical light profiles, respectively; open triangles denote lack of morphological information and upward arrows mark lower magnitude limits of optically blank counterparts to x-ray sources. Optical spectroscopic classes are marked with different symbols (empty for ambiguous spectroscopic identifications) and the larger size denotes hard x-ray spectra. The oblique lines indicate constant x-ray-to-optical flux ratios for +1, 0, -1 and -2 while the shaded regions mark the region of the parameter space typically occupied by classic AGN (dark grey) and star-forming galaxies or LLAGN (light grey).

$\log f_x/f_{\text{opt}} \lesssim -2$, typical for ‘normal’ galaxies (galaxies without AGN or intense starbursts), in which the x-ray emission probably comes from low-mass binaries and hot interstellar gas. As for the emission-line galaxies, about $1/4$ of the total belong to this group; they have higher X-ray-to-optical flux ratios than their fellow absorption-line galaxies, more in line with high levels of star formation. This probably means that, at fluxes fainter than $f_x \sim 10^{-15} \text{ erg cm}^{-2} \text{ s}^{-1}$, we are starting to detect the x-ray-bright tail of the “normal” galaxy population reported to dominate the source number counts at ultrafaint levels ($f_x \lesssim 10^{-16} \text{ erg cm}^{-2} \text{ s}^{-1}$) in the 2 Ms Chandra Deep Field North (Hornschemeier et al. 2003).

Unfortunately we cannot make remarks of the same nature in the 10×10 ks survey due to its shallowness. However, the behaviour at bright x-ray fluxes is similar in both surveys. In particular for both it is true that bright galaxies ($f_x \gtrsim 10^{-15} \text{ erg cm}^{-2} \text{ s}^{-1}$ in the WHDF) are mostly NLXGs, either hard or soft. As in the WHDF, we detect no objects in the galaxy parameter space region, indicating that, at these levels, any on-going star formation is most likely masked out by AGN activity in the same galaxy.

Amongst the point-like population we observe a constant scaling in flux ratios and nearly all belong to the typical AGN space, at $|\log f_x/f_{\text{opt}}| \lesssim 1$. The extended population has a distribution of x-ray-to-optical flux ratios somewhat flatter, consistent with being constant. In this case, though, the dispersion of optical magnitudes per given x-ray flux is much wider than for point-like sources; this seems to suggest that, although AGN emission dominates the x-rays, the host galaxies contribute as well to the optical emission at significant levels, introducing substantial scatter in optical magnitudes.

Note that there are 9 x-ray sources without an $R \lesssim 26$ companion in the WHDF (upper panel of figure 4.1). At $z = 0.5$, $R = 26$ corresponds to $M_R = -17.5$ or, equivalently, to $L = 10^{8.92} L_{\odot}$ ($q_0 = 0.5$ and $H_0 = 50 \text{ km s}^{-1} \text{ Mpc}^{-1}$). Assuming the mass-to-luminosity ratio typical for an elliptical galaxy of $M/L = 10$ (Karttunen et al. 1994), this yields a mass for the galaxy of $\sim 10^{10} M_{\odot}$. If the Magorrian et al. (1998) relation of $M_{\bullet} \sim 3 \cdot 10^{-3} M_{\text{bulge}}$ holds at these redshifts, $R \gtrsim 26$ for the host galaxy implies a black hole mass of $M_{\bullet} \lesssim 2.5 \cdot 10^7 M_{\odot}$. If such a black hole emitted at the Eddington-limited luminosity we would detect it with a flux of $S_X \simeq 2.5 \cdot 10^{-12} \text{ erg cm}^{-2} \text{ s}^{-1}$, well above our surveys’ x-ray flux limits (which are capable of detecting a $M_{\bullet} \sim 10^4 M_{\odot}$ black hole at $z = 0.5$). Hence, with our photometric limits we can not yet test the Magorrian et al. (1998) relation at high redshifts.

Figure 4.2 on the following page shows the dependencies of the x-ray-to-optical flux ratios on the x-ray flux, the optical flux and the hardness ratio. We see that the flux ratios seem independent of x-ray flux. On the other hand, they depend strongly on the optical magnitude, with fainter sources having higher $\log f_x/f_{\text{opt}}$.

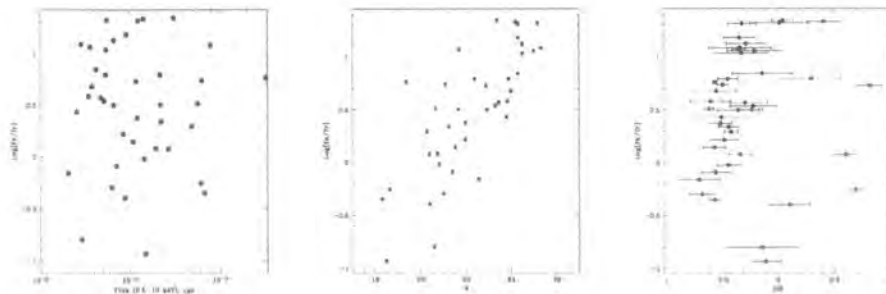


Figure 4.2: x-ray to optical flux ratios as a function of x-ray flux, R magnitude and hardness ratio for the sources in the Herschel Deep Field.

(likely due to obscuration on the assumption that the optical flux is highly dependent on nuclear light). The right-most plot shows that hard sources are optically faint and x-ray bright, as expected from a population of type II AGN at $z \lesssim 1$.

Colours

Colour indices depend on the spectral distribution of light and can therefore provide limited information about the light-emitting mechanisms of the emitter; several optical colours can then be compared to break degeneracies in separating classes of sources. In fact, this is such an effective method that it has served as the basis for several highly successful multiband photometric surveys, including the SDSS (e.g. Fukugita et al. 1996) and the COMBO-17 (e.g. Wolf et al. 2003).

We have studied a range of colour-colour diagrams for our fields, including $B-R$ vs. $R-I$, $R-I$ vs. $H-K$, $U-B$ vs. $B-R$, $I-H$ vs. $B-R$, $I-H$ vs. $R-I$, $B-R$ vs. $R-K$, etc. Figures 4.3, 4.4 and 4.5 display examples of the $B-R$ vs. $R-I$ -like colours for x-ray sources in the three surveyed fields, superposed on a surface density background built from the colours of the brightest galaxies in the corresponding field. On each plot, spectroscopic and morphological information for the sources is provided following similar conventions as in figure 4.1 on page 118. Also shown are two sets of redshift tracks based on evolutionary stellar population synthesis models of Bruzual & Charlot (2003) for early- and late-type galaxies (E/S0 and S, respectively). On these diagrams, quasars have a well-defined main locus on the blue edge (around $B-R \sim R-I \sim 0.5$ in the case of the WHDF). The bulk of x-ray galaxies is found around the region where the evolutionary tracks for very low redshift E/S0 and low redshift S coincide; moreover, the scatter in colours in these, but also in the other colour-colour diagrams, is large and therefore it seems clear that x-ray galaxies cannot be generally ascribed to a single morphological type.

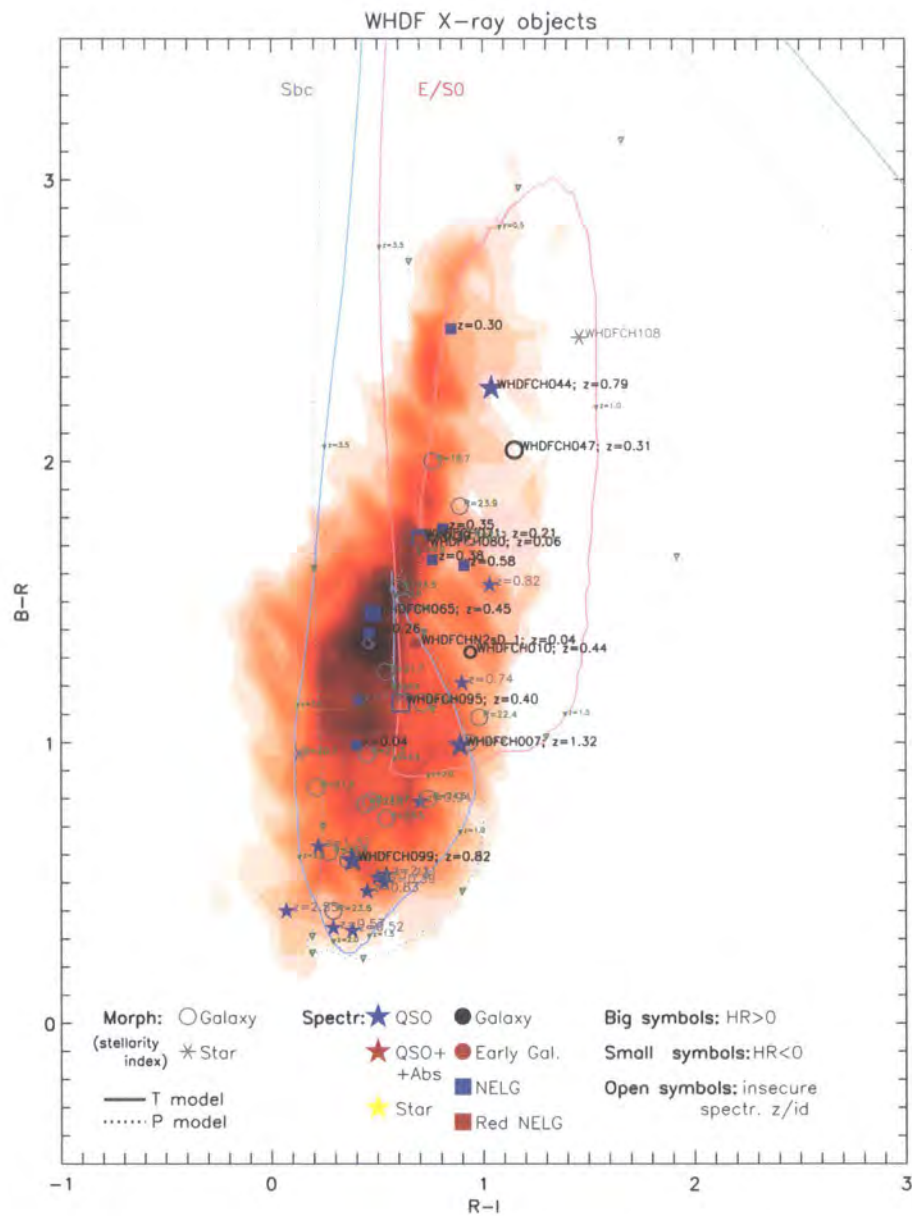


Figure 4.3: $B-R$ vs. $R-I$ for x-ray objects in the WHDF. The background density contour is made from all $R < 24$ galaxies in the field.

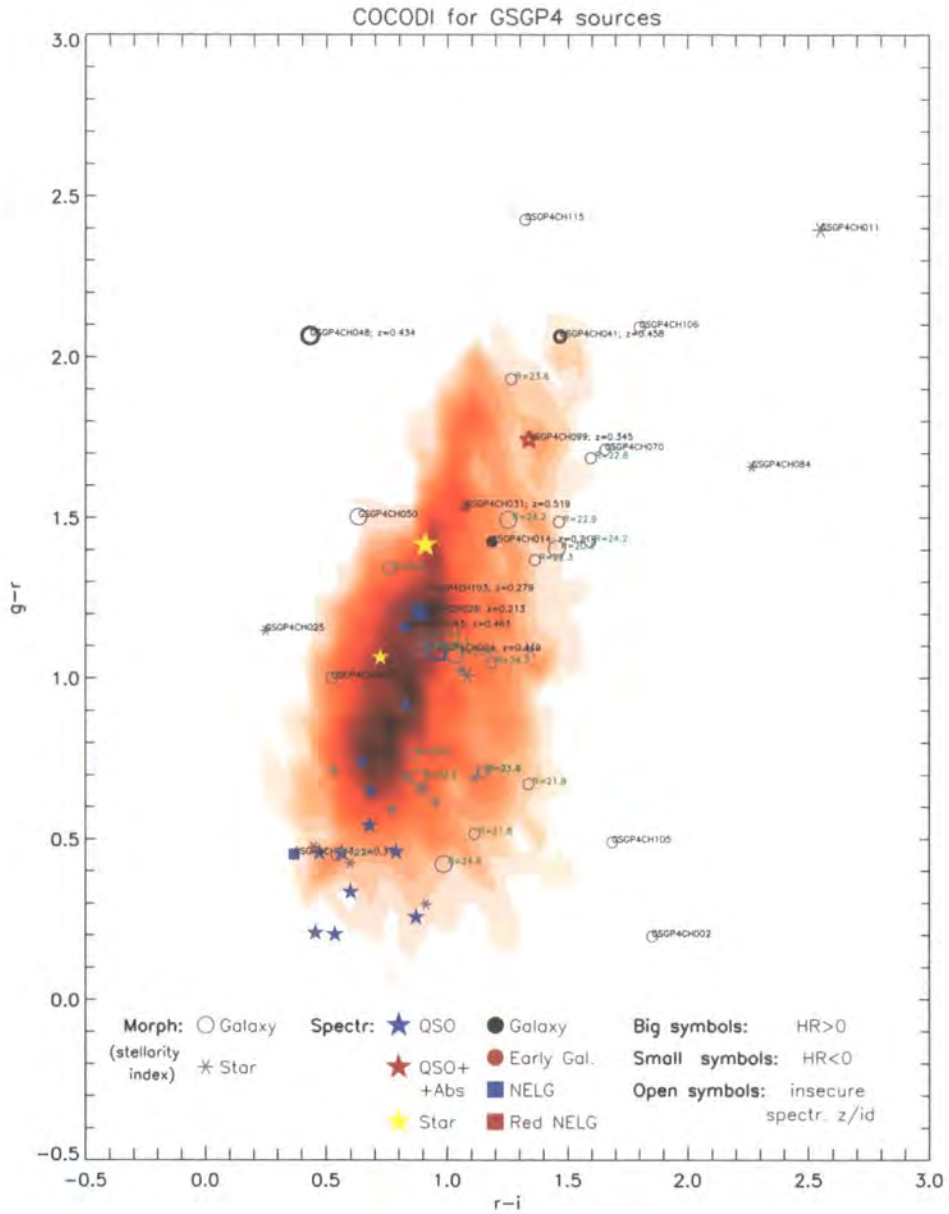


Figure 4.4: $g-r$ vs. $r-i$ for x-ray objects in GSGP4. The background density contour is made from all $r < 24$ galaxies in the field.

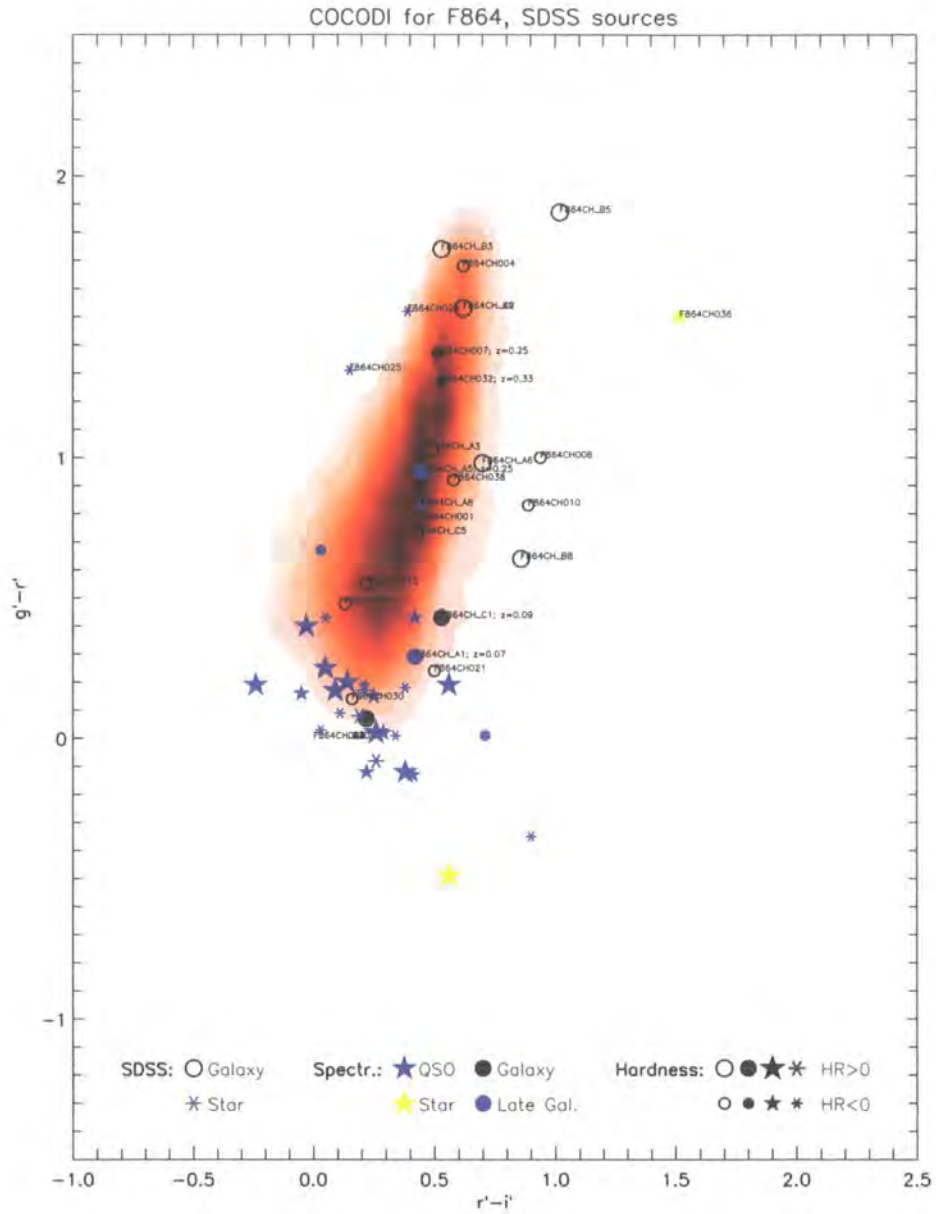


Figure 4.5: $g' - r'$ vs. $r' - i'$ for x-ray objects in F864. The background density contour is made from the 25000 brightest galaxies in g' with $g' - r' < 5.7$ of the SDSS EDR (magnitude limit of $g' = 21.65$).

In fact, if we assume that most x-ray emission in our samples is due to AGN as hinted in figure 4.1, it seems appropriate to conclude that type II AGN are hosted in a broad range of galaxies. We note as well that, according to the evolutionary tracks, many of the fainter unidentified extended objects have colours consistent with high redshift galaxies: many spirals in the WHDF ($B - R = 0.9 \pm 0.2$) and early-types in GSGP4 ($r - i \gtrsim 1.1$) and F864 ($r' - i' \gtrsim 0.5$), for instance. This also serves to show again that there are large variations in the numbers and in the populations found from one survey to another due to underlying large scale structure and Chandra's small field of view (*cf.* § 4.3.4).

4.2 AGN Host Galaxy Properties

It has been argued in section 4.1 that, regardless of the optical counterpart type, the bulk of x-ray photons detected with Chandra in deep exposures most likely have their origin in AGN emission. This conclusion is reinforced by the low number of star-forming galaxies found to be significant x-ray emitters. Indeed, out of the almost 6000 $B - R \leq 1.6$ galaxies that are actively producing stars, only a dozen are detected in the 75 ks Chandra exposure. Therefore, catalogues generated from deep x-ray surveys constitute an efficient (and least biased) method to select active nuclei. In the current section we characterise the nature of the $z \lesssim 0.7$ galactic population that host the AGN found in these catalogues.

One of the most fundamental questions to be clarified is whether AGN live in old, evolved galaxies or instead in young galaxies with high levels of star formation. Colour-colour diagrams such as figures 4.3–4.5 reveal that the bulk of x-ray galaxies is found around the region where the evolutionary tracks for very low redshift E/S0 and low redshift S coincide, although individual examples are found at positions more typical for both early- and late-type galaxies. From those plots it seems clear that x-ray galaxies cannot be generally ascribed to a single morphological type (see also chapter 5). The same conclusion is reached from pure morphological inspection of the optical images: appendix A contains multi-band thumbnail images for the counterparts of x-ray sources in the GSGP4 (page 171) and WHDF (page 180) fields and it shows that there is a wide variety of galaxy types and luminosities, from large and luminous ellipticals to beautiful spirals to red mergers with double nuclei.⁵

We now learn, from the bottom panels of figures 4.6 and 4.7, that no clear correlation exists between the colours of galaxies and their optical flux, and that the scatter in colours is reproduced at all surveyed optical magnitudes, increasing towards fainter magnitudes. In these plots we have $g - r$ and $r - i$ colours *vs.*

⁵Note, though, that most galaxies have prominent bulges and also that a very large number show signs of interactions such as double nuclei and distorted morphologies.

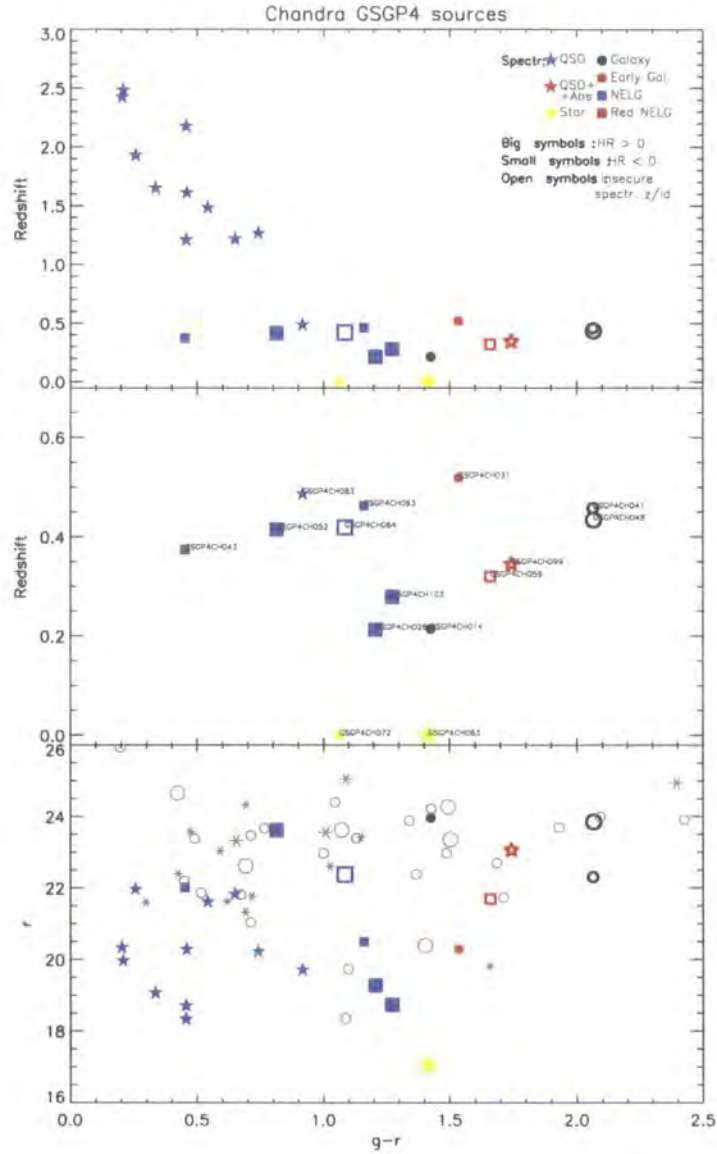


Figure 4.6: $g-r$ colours against redshift and r band magnitude for sources in the GSGP4 field (includes $S/N \gtrsim 3$ Chandra detections).

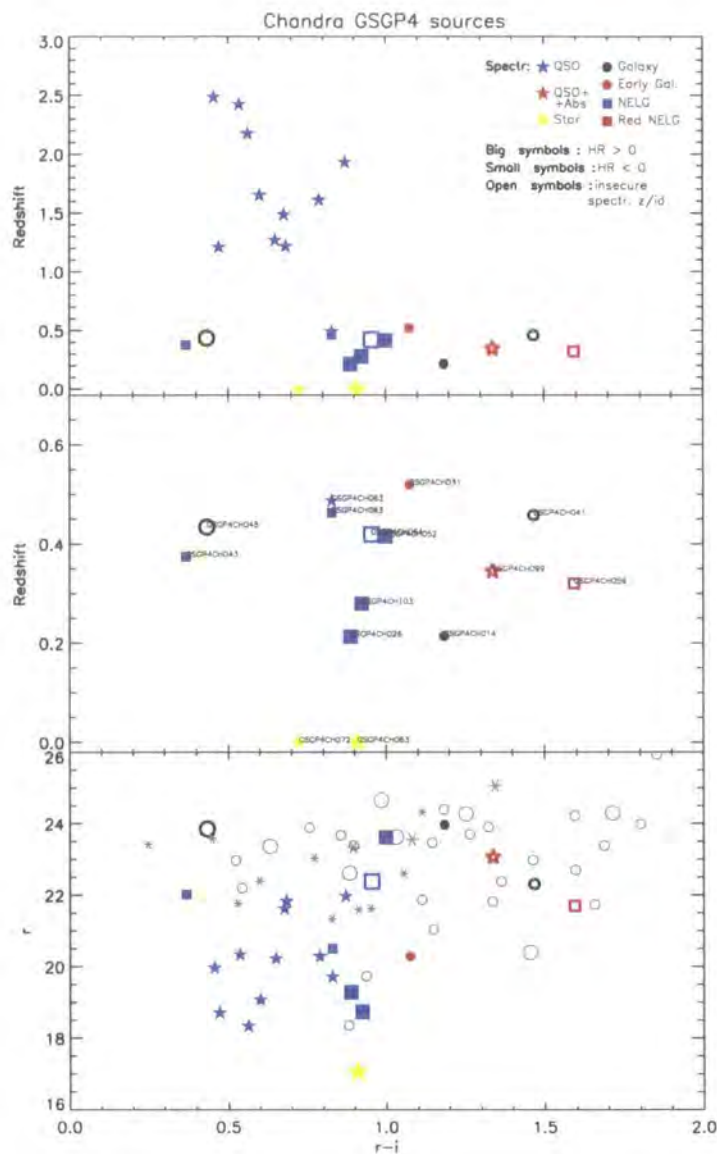


Figure 4.7: $r-i$ colours against redshift and r band magnitude for sources in the GSGP4 field.

r magnitude for the x-ray sources in the GSGP4 field (including $5/N \lesssim 3$ Chandra detections).⁶ It is seen that at bright magnitudes ($r \lesssim 21$) roughly equal fractions of early and late-type galaxies are found clustered around intermediate colours, $r-i \simeq 0.9$ and $g-r \simeq 1.3$; at fainter magnitudes galaxies span much wider colour ranges, but still they keep roughly equal proportions of galaxies with red and blue colours. The same conclusions seem to hold if we compare colours against redshifts (top and middle panel of figures 4.6 and 4.7) if we map bright magnitudes to low redshifts and faint magnitudes to high redshift. A final result derived from the bottom panels of figures 4.6 and 4.7, and also from figure 4.1, is that, in our surveys, also the hardness ratio is uncorrelated with optical flux, in disagreement with reports from other researchers who observe that the hard x-ray sources predominantly lie in the most optically bright galaxies (Barger et al. 2001).

Although the overall conclusion that type II AGN (NLXGs) are hosted in a broad range of galaxies seems unavoidable, we observe some patterns when we examine their colours against properties such as x-ray fluxes or hardness ratios. We have seen in figure 4.1 that x-ray bright sources tend to be NLXGs, whilst ALG are more common at fainter x-ray fluxes. Given that in our x-ray surveys the redshift space surveyed for both types of galaxies is the same, this suggests that typical x-ray luminosities are higher for NLXGs, as expected from an AGN/non-AGN origin of the x-ray emission from the bright NLXG/faint ALG populations, respectively. This result complements the work by Almaini et al. (1997) who found that blue and red subsamples of galaxies (dividing at $B-R=1.5$) contribute with similar amplitude to the significant cross-correlation signal between faint galaxies and unresolved XRB found in ROSAT deep fields. By acknowledging that blue galaxies are more weakly clustered, they concluded that their luminosities might have to be higher than for red galaxies, for which clustering enhances the signal. In our combined set of x-ray bright NLXGs of the WHDF and 10×10 ks surveys, we find that bright NLXGs (hosts to obscured AGN) tend to have marginally bluer colours, with the eleven brightest examples ($f_{0.5-10 \text{ keV}} \gtrsim 3 \cdot 10^{-15} \text{ erg cm}^{-2} \text{ s}^{-1}$) having a mean $\langle B-R \rangle = 1.4$. This result is, however, highly dependent on the field studied and should be confirmed with a higher sample of NLXGs. Thus, while in the GSGP4 field (which was used in the work by Almaini et al.) all x-ray bright NLXGs have notable blue colours (see, for instance, their colours in figures 4.6), in the WHDF they are significantly redder.

In figures 4.8 and 4.9 we compare the hardness ratio vs. colours (upper and middle panels) and vs. redshifts (bottom panels) of the sources in the WHDF and GSGP4 fields, respectively.⁷ Inspection of their top and middle panels shows that optically redder BLAGN span a wider range of hardness ratios and, as a result, overall they are marginally harder (more absorbed) in the x-rays. This behaviour might be clearer in the deeper WHDF, but it also occurs in the GSGP4 field if we consider

⁶Although not included for reasons of space, similar trends are observed in the equivalent plots for fields F864 and WHDF.

⁷The spectroscopic follow-up of galaxies in the F864 field is minor.

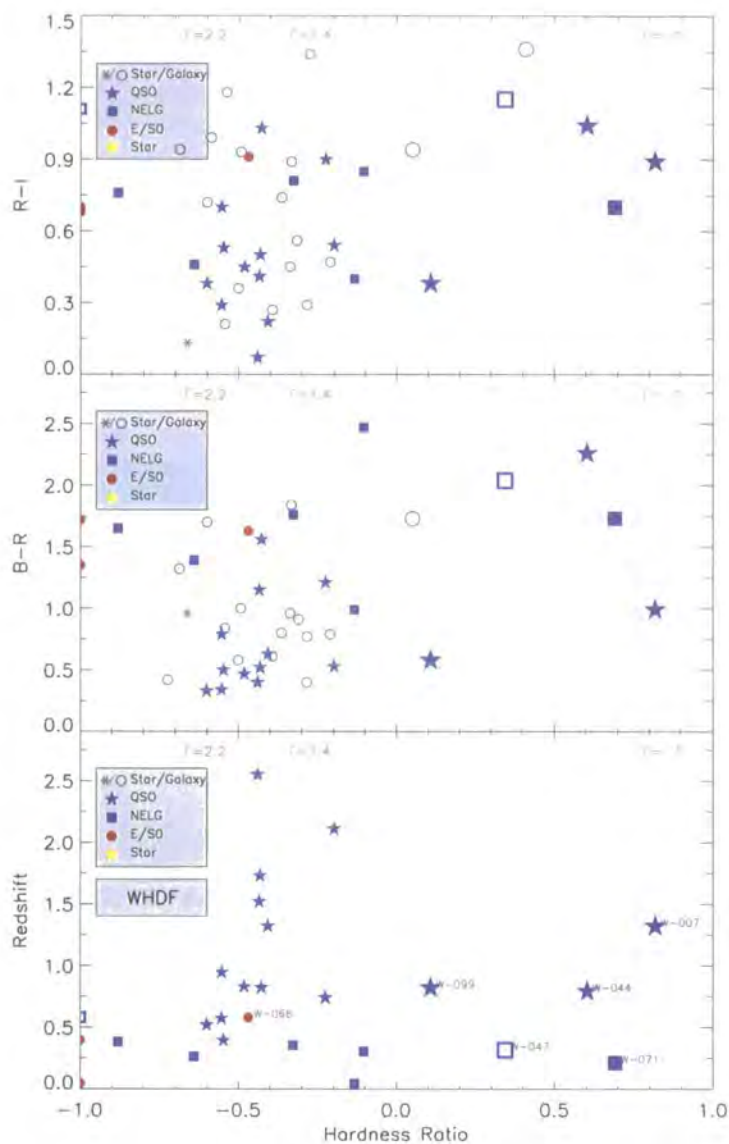


Figure 4.8: Hardness ratio against $B-R$ & $R-I$ colours and redshift for sources in the WHDF (flux limit of $\sim 1 \cdot 10^{-15} \text{ erg cm}^{-2} \text{ s}^{-1}$ in the 0.5–10 keV energy band).

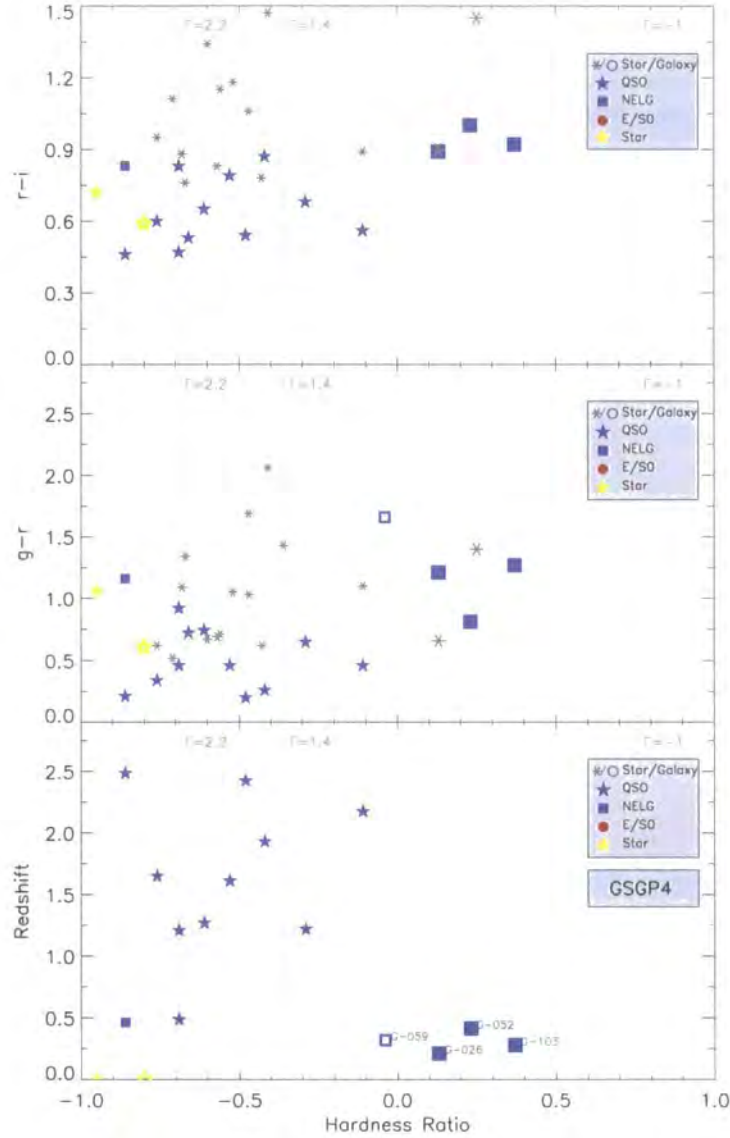


Figure 4.9: Hardness ratio against $g-r$ & $r-i$ colours and redshift for sources in the GSGP4 (flux limit $\sim 7 \cdot 10^{-15} \text{ erg cm}^{-2} \text{ s}^{-1}$ in the 0.5–10 keV band).

point-like sources as fainter QSOs. It could reflect that, amongst some QSOs, optical obscuration and x-ray absorption are related phenomena. However, this reddening is not observed amongst galaxies in general, and NLXGs in particular, as they harden. The conclusion here could be that there is a wide range of galaxy types amongst obscured AGN hosts and their varied colours averages out any possible indication that reddening is associated with absorption. Both trends, for QSOs and galaxies, are confirmed in the two surveys with all the colours available: $r - z$, $b - r$, $r - i$.

The bottom panels of figures 4.8 and 4.9 show the distribution of redshifts vs. hardness ratios. We find no clear evidence that either BLAGN or NLXGs harden with redshift. Thus, from these plots we find no hints of cosmic evolution of any of those classes, nor spectroscopically confirm the requirement from XRB population synthesis models that more absorbed sources be at high redshift (e.g. Gilli et al. 2001). This is not surprising, however, because absorbed sources at high redshifts are likely to be optically very faint and their spectroscopic follow-up, difficult. From these panels we also note that all of the bright and hard ($HR \gtrsim 0$) objects introduced in section 2.5, and which we will discuss at length in 4.3, are at redshifts $z \lesssim 1.5$. They could belong to a single population judging by their colours, where no differential trend is detected between the BLAGN and NLXGs. Rather, they appear mixed and it seems that they could be the luminous and faint examples of the same group. The lack of high redshift luminous AGN with positive hardness ratios is explained by the redshifting of hard emission into softer bands, which would render an absorbed QSO indistinguishable from an unabsorbed one.

4.2.1 Optically Blank Population

A significant fraction of Chandra sources is too faint to be detected in the optical images. In this section we characterise their known properties and argue that they do not constitute a different population but the extension at optically faint fluxes of the x-ray sources which have a spatially extended optical counterpart.

Figure 4.10 on the following page shows the source counts–flux relations for the x-ray sources in our two surveys. According to their optical morphological information, we have drawn cumulative counts separately for sources with stellar-like (blue stars) and extended (red squares) spatial distributions, for sources with unreliable stellarity index (“undetermined”; green triangles) and for undetected sources (“blanks”; black dots). At fluxes $S_{0.5-2 \text{ keV}} \gtrsim 3 \cdot 10^{-15}$ and $S_{2-10 \text{ keV}} \gtrsim 10^{-14} \text{ erg cm}^{-2} \text{ s}^{-1}$, sources from the WHDF, F864 and GSGP4 fields have been combined; at fainter fluxes, all sources belong to the WHDF. For reference, the predictions in the soft (top panel) and hard (bottom panel) bands from a XRB population synthesis model by Gunn (1999) have been included. From this figure we note two main things. First, that in both x-ray bands and at all fluxes available, the slopes

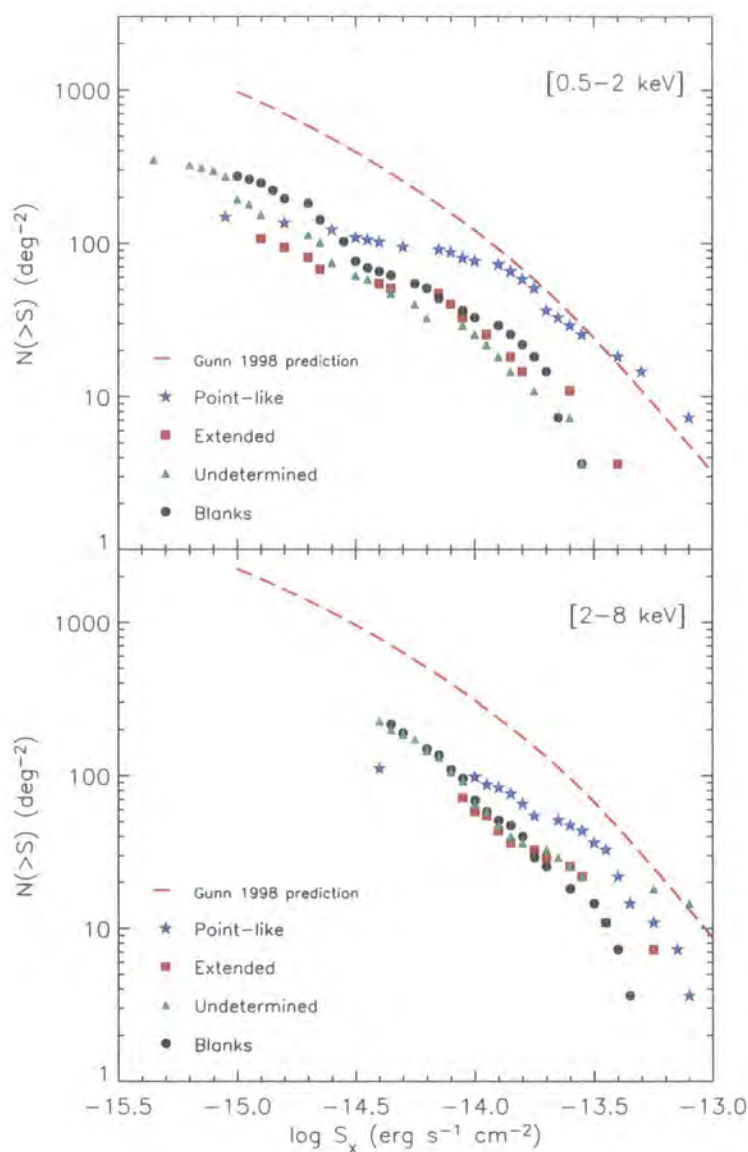


Figure 4.10: Soft (top panel) and hard (bottom panel) cumulative number counts for sources with stellar-like (blue stars) and extended (red squares) spatial distributions, for sources with unreliable stellarity index (“undetermined”; green triangles) and for undetected sources (“blanks”; black dots), according to their appearance in optical images of the WHDF, GSGP4 and F864 fields. The predictions from a XRB population synthesis model by Gunn (1999) have been included for reference.

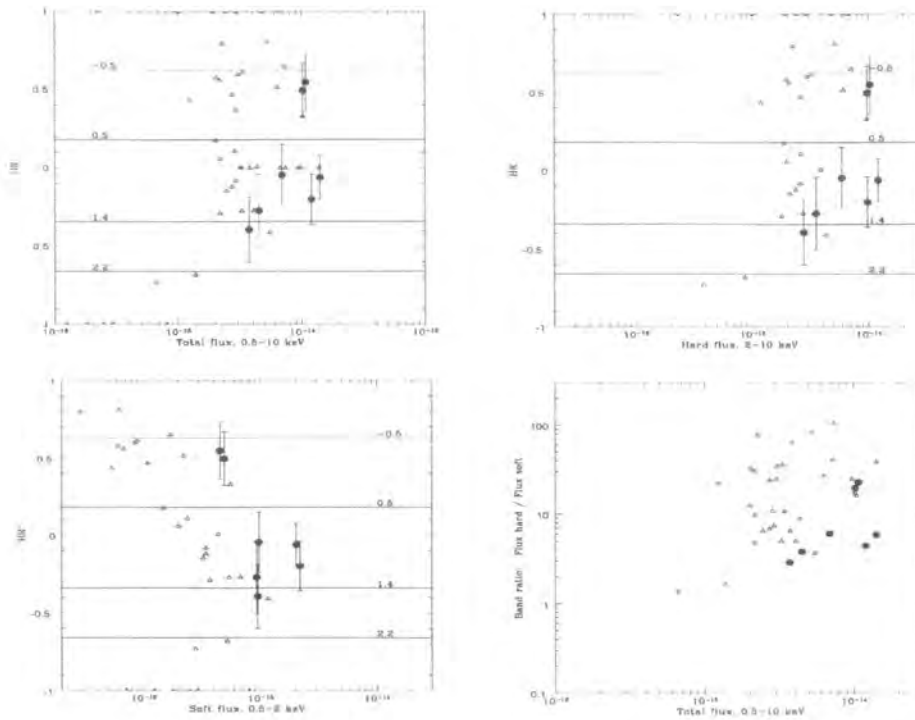


Figure 4.11: Fluxes vs. hardness and band ratios for sources without optical counterpart in the WHDF.

for extended, undetermined and optically blank objects are very similar. This suggests that they constitute, in fact, a single population where the undetermined and the blank sources are the increasingly optically faint tail of the brighter extended population. Second, we observe that the slope for these three classes is steeper than for point-like sources. Moreover, point-like sources are more numerous at bright x-ray fluxes while the other classes dominate the counts at faint fluxes. All this works into solving the so-called “spectral paradox” with a population of extended and faint hard sources different to QSOs.

Figure 4.11 shows the fluxes against hardness and band ratios for blank sources in the WHDF. It can be seen that the hard flux dominates their total flux (being, typically, 2–100 times the soft flux); this behaviour is expected from type II AGN at $z \lesssim 1$. Also, from the HR vs. total flux for all sources in our two surveys (figure 4.12) we see that sources without optical counterpart and galaxies share the same distribution. On basis of their x-ray to optical flux ratios (figure 4.1), we have concluded that optically blank counterparts to x-ray sources are too bright at \sim keV energies to be likely powered by any non-AGN mechanism. In addition, the same diagnosis served to conclude that hard sources are also likely powered

by AGN, and figure 4.11 shows that blank sources are relatively hard. Given that, by definition, blank sources are optically very faint, it is plausible that such an AGN powering their x-ray emission is obscured and lies at higher redshifts than identified galaxies.

All these arguments seem to suggest that optically faint counterparts to the x-ray sources in our surveys are mostly the high redshift counterparts to the obscured AGN identified at fluxes brighter than $S_{0.5-10 \text{ keV}} \sim 10^{-15} \text{ erg cm}^{-2} \text{ s}^{-1}$.

4.3 Population Synthesis Models

4.3.1 Obscured AGN

Over the last fifteen years several attempts to explain the XRB as a superposition of AGN spectra have been pursued in order to account for its $\Gamma \simeq 1.4$ flat spectrum above 2 keV. Thus for instance, Awaki (1991) used Ginga data to show that a proportion of 3 : 1 of Sy II to Sy I could produce all the hard XRB if the spectra of the former steepen beyond $\sim 50 \text{ keV}$. But it is the models based on the x-ray properties of unified schemes for AGN, as suggested by Setti & Woltjer (1989) and developed by Madau et al. (1994) and Comastri et al. (1995) amongst others, that have had the largest success on fitting the XRB while simultaneously accounting for the observed number counts, spectral characteristics and the relative distributions of different types of sources. These models require the presence of many absorbed sources in order to account for the flat spectrum of the hard XRB and typically predict that obscured AGN outnumber unobscured ones by a factor of 2–10.

Evidence supporting an obscured AGN origin for the XRB include results obtained from studying SMBH in the centres of nearby non-active galaxies. It is found that the observed local density in black holes, as obtained from the correlation between the mass of SMBHs and the mass of the galactic bulge (Magorrian et al. 1998), comes out to be an order of magnitude higher than predicted from the integrated QSO emission, as obtained from the mean surface brightness of the sky in optical QSOs (Soltan 1982) and a luminosity function, a bolometric correction factor and a mean accretion factor (Chokshi & Turner 1992; see also Lawrence 1999 for a review and references therein). Similar conclusions have been drawn from the relations found with the hard x-ray background and the local mass function of black holes as derived from the correlation between radio emission of galaxies and the mass of the central black hole (Franceschini et al. 1998; Fabian & Iwasawa 1999). If all the assumptions in these studies are correct (the most basic being that all the emission from quasars comes from accretion on to a massive black hole), it appears that a large population of obscured QSOs that are not observed at optical wavelengths must exist.

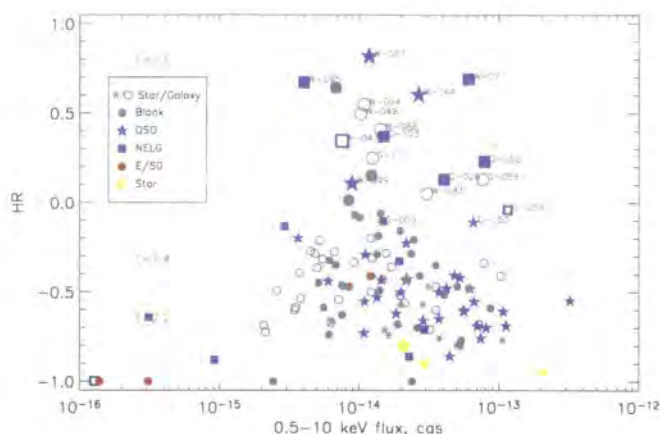


Figure 4.12: Hardness ratio with optical identification for sources in the WHDF and 10×10 ks surveys. The legend is as for figure 4.1 with the addition of grey circles for x-ray sources without optical counterpart (“blanks”). Note the hardening of, not only the extended population, but of the QSOs as well towards fainter fluxes. Also, the presence of a distinct population of bright and hard QSOs. (The labels for the hard fraction of sources denote survey id numbers.)

4.3.2 Hard QSOs

Our data agree with the XRB population synthesis models in the basic requirement that a large fraction of the XRB emission is due to obscured AGN. Until fairly recently, very few such objects were actually known, particularly at high redshift where a large fraction of the emission is known to originate. Figure 4.12 shows a plot that adds, for the most significant x-ray sources, spectro-morphological information to the hardness ratio plots of figure 2.18. Aside from QSOs, the majority of the spectroscopically identified sources are NELGs whose x-ray emission is likely due to an obscured AGN (§ 4.1.2). At x-ray fluxes around $S_{0.5-10 \text{ keV}} \sim 1 \times 10^{-14} \text{ erg cm}^{-2} \text{ s}^{-1}$ (where most of the XRB is produced) and fainter, the source counts are dominated by galaxies for which no spectroscopy is available. We have argued in section 4.2 that these galaxies mostly represent the faint tail of the obscured AGN population. If that is indeed the case, we confirm with our x-ray surveys that, at faint x-ray fluxes, the obscured population outnumbers unobscured AGN in agreement with the predictions from the models.

Unfortunately, accurate estimates of the number ratio between type II and type I AGN cannot be directly associated with the number ratio between absorbed and unabsorbed populations, which is what the models predict. Despite the fact that x-ray spectral properties of AGN are often well correlated with their optical ones (lack of optical broad lines accompanied with high column densities and *vice versa*; Nandra & Pounds 1994; Smith & Done 1996), several authors have found in the local universe that a non-negligible number of Sy I galaxies display absorption columns well in excess of $N_H > 10^{22} \text{ cm}^{-2}$ (e.g. Turner & Pounds 1989); conversely, Sy II with

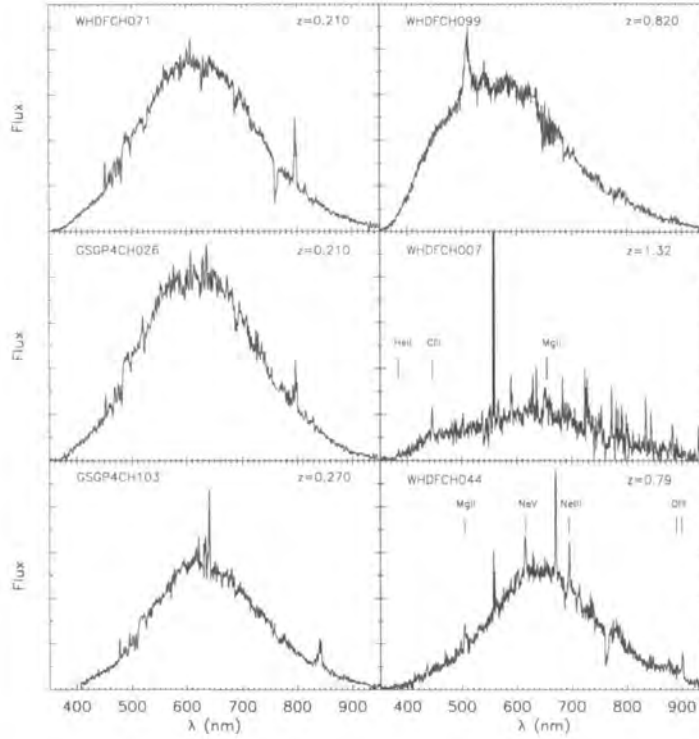


Figure 4.13: Optical spectra of the hardest BLAGN and NLXGs in our surveys.

$N_H < 10^{22} \text{ cm}^{-2}$ have been found as well (Barcons et al. 2003). At higher redshift, a few QSOs that display high columns have also been reported (e.g. Akiyama et al. 2000; Fiore et al. 1999; Pappa et al. 2001). In both the WHDF and 10×10 ks surveys we seem to find several examples of these, which can be readily identified in figure 4.12 as HR > 0 blue-starred data points.⁸ The plot shows that they constitute between $1/4$ and $1/3$ of the class of very x-ray bright and hard sources which are seen to contribute appreciably to the 2–10 keV XRB in the middle panel of figure 2.18.⁹ The spectra for some of these hard BLAGN can be seen in figure 4.13, which also includes spectra for the hardest NLXGs encountered in our surveys.

In terms of the unified schemes for AGN, the finding that also amongst distant QSOs there is a non-negligible fraction of unobscured absorbed objects, as it happens with local Seyfert 1 galaxies, adds support to the analogy between local Seyfert 1 galaxies and distant QSOs. On the other hand, if the hypothesis that their hard spectra are due to absorption is correct, their column densities should be greater than $\sim 10^{23} \text{ cm}^{-2}$ (assuming a power-law spectrum with a standard pho-

⁸We are assuming that the sources have intrinsic steep spectra (power-law with $\Gamma = 2$) hardened by moderate-to-high absorption, as opposed to intrinsic flat spectra. This has been found to be the case in the majority of objects so far surveyed and, in particular, in a study including the GSGP4 and F864 fields (Pappa et al. 2001).

⁹Incidentally, this translates in that the QSO class is found to contribute to the hard XRB a larger fraction than usually predicted by the models.

ton index of $\Gamma = 2.0$). In principle, within the framework of the simplest version of standard unification models where the molecular gas and dust which prevents the direct view of the BLR in Sy II is likely to also contain atomic gas that will absorb soft x-rays, the high column densities would yield a reddening by dust associated with this absorbing gas such that it would dim the QSOs to barely detectable limits at optical/NIR domains; even when detected, they should display narrow lines only. However this is clearly not always the case and in our survey there is a population for which large gas quantities do not imply obscuration by dust. Although scattered nuclear light might play a part (Turner et al. 1997), given the numbers and strengths of the lines, differences in dust density, composition and grain size distribution are, most likely, of major importance to account for this effect (Granato et al. 1997; Maiolino et al. 2001). Currently, the most favoured explanation is that x-ray and optical obscuration take place in two distinct media. The matter responsible for most of the x-ray absorption would not be the dusty torus but lie closer to the accretion disk, at distances comparable to the BLR radius. For the most powerful AGN it would fall inside the dust sublimation radius, where dust would be disrupted but the metal-rich gas would absorb the x-ray flux coming from the central engine. Thus, the optical spectrum would remain unaffected but large intrinsic photoelectric absorption of x-rays would occur (Weingartner & Murray 2002; Georgantopoulos et al. 2003).

4.3.3 Type II QSOs

A natural consequence of all XRB population synthesis models that account for the hard source counts at $S_{2-10 \text{ keV}} \sim 10^{-13} \text{ erg cm}^{-2} \text{ s}^{-1}$, is that highly luminous type II AGN exist (Gilli et al. 2001). Their large intrinsic absorbing columns ($N_H \gtrsim 10^{24} \text{ cm}^{-2}$) would render them as red and faint point-like sources in the optical; they would display narrow emission lines only in their spectra, high x-ray to optical flux ratios and x-ray luminosities greater than $\sim 10^{44} \text{ erg cm}^{-2} \text{ s}^{-1}$ after correcting for absorption. However, despite the fact that a few high-redshift luminous AGN with only optical narrow lines have been observed (e.g. Norman et al. 2002; Stern et al. 2002), their numbers remain substantially below the expectations; in this respect, the WHDF and $10 \times 10 \text{ ks}$ surveys are no exception, as we now see.

Spectroscopically, we have identified two high-redshift ($z > 2$) type II QSO candidates which show narrow-emission lines only in their rest-frame UV emission and which are very luminous ($L_X > 10^{44} \text{ erg s}^{-1}$):

RX J13433+0001 This point-like source ($\alpha = 13^h 43^m 29.227^s$, $\delta = +00^\circ 01' 32.9''$) was first discovered by Almaini et al. (1995) in the Deep ROSAT Survey (Shanks et al. 1991). In the optical, it shows narrow lines corresponding to Ly α and C IV $\lambda 1549$ (figure 4.14 on the next page) which give a redshift of $z = 2.35$ and, at $B = 22$, imply an absolute magnitude of $M_B = -23.7$ ($H_0 = 50 \text{ km s}^{-1}$, $q_0 = 0.5$). In the infrared, it

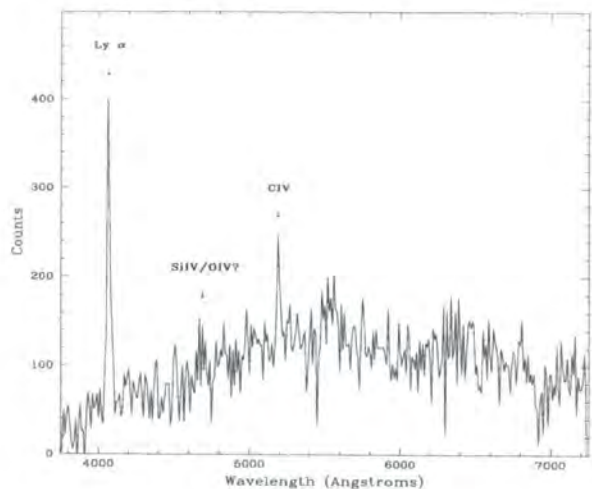


Figure 4.14: Optical spectrum of the $B = 22$ type II QSO candidate RX J13433+0001, at $z = 2.35$. The narrow Ly α and CIV λ 1549 emission lines are labelled. Obtained with the AAT/AUTOFIB instrument in March 1994.

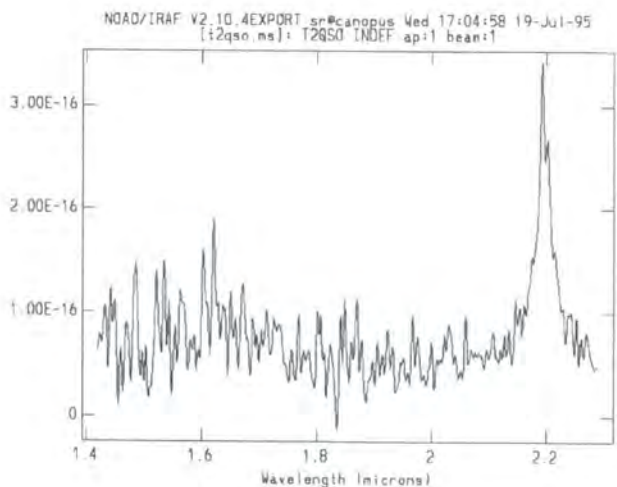


Figure 4.15: The UKIRT/CGS4 K -band spectrum of the type II QSO candidate RX J13433+0001, at $z = 2.35$. The broad H α indicates moderate obscuration. Obtained in March/May 1995.

shows broad $H\alpha$ and no $H\beta$ lines (figure 4.15). This, together with its $B - K = 5.4$ red colour, suggests that this object is a moderately obscured QSO at optical wavelengths ($A_V > 3$; Georgantopoulos et al. 1999). Closer inspection of the line ratios led Halpern et al. (1999) to reclassify this source as a narrow-line Seyfert 1 galaxy (NLS1). Although this new label does not alter the fact that RX J13433+0001 is a high-luminosity obscured AGN at high redshift, where the space density of such systems is poorly constrained and of fundamental interest to studies of the XRB, it does highlight further challenges to the simple orientation-dependent unification schemes for AGN, since NLS1 have typically steeper optical and x-ray spectra relative to normal Sy I and Sy II. The upper limit on the column density of RX J13433+0001 from the ROSAT data is $n_H \simeq 6 \cdot 10^{21} \text{ cm}^{-2}$ which is comparable to the amount inferred from the $H\alpha/H\beta$ decrement observed in the IR spectrum. However, the column implied from the combined ROSAT and ASCA data is larger, at $n_H \sim 10^{23} \text{ cm}^{-2}$. There is significant uncertainty in its hard x-ray spectral index due to normalisation differences between ROSAT and ASCA, which could be attributed to variability (Georgantopoulos et al. 1999).

In the 10×10 ks Chandra survey, RX J13433+0001 is a bright object known as F864CH003. Its flux in the soft band is $S_{0.5-2 \text{ keV}} = 5.1 \cdot 10^{-14} \text{ erg cm}^{-2} \text{ s}^{-1}$ ($L_X \sim 2 \cdot 10^{45} \text{ erg s}^{-1}$ in the same band, $H_0 = 50 \text{ km s}^{-1}$, $q_0 = 0.5$), very similar to the ROSAT flux. In the hard band, though, its flux of $S_{2-10 \text{ keV}} = 6.3 \cdot 10^{-14} \text{ erg cm}^{-2} \text{ s}^{-1}$ ($L_X \sim 3 \cdot 10^{45} \text{ erg s}^{-1}$ in the same band, $H_0 = 50 \text{ km s}^{-1}$, $q_0 = 0.5$) is significantly lower than the ASCA flux of $S_{2-10 \text{ keV}} = 2.4 \cdot 10^{-13} \text{ erg cm}^{-2} \text{ s}^{-1}$. Although the ASCA photons were gathered from a region within $1.5-2'$ from the x-ray centroid and Chandra detects three extra objects in that area (F864CH001-4), their integrated hard band flux ($S_{2-10 \text{ keV}} = 1.1 \cdot 10^{-13} \text{ erg cm}^{-2} \text{ s}^{-1}$) is still about half the ASCA flux; hence source blending does not seem to be the only cause of the differences between ROSAT and ASCA. Interestingly, the ACIS-S hardness ratio of this object ($HR = -0.61$) yields a column of $n_H \simeq 8 \cdot 10^{21} \text{ cm}^{-2}$ (assuming an absorbed power-law spectrum with photon index $\Gamma = 2.0$), again similar to the result obtained from ROSAT data. These values are typical of bright unobscured broad-lined QSOs. One way around the inconsistency between optical obscuration and lack of corresponding x-ray absorption could be that we are observing in the soft band scattered flux which does not come directly from the nucleus.

CXO WHDF J002222.9+002013 This source, at $\alpha = 00^h 22^m 22.884^s$, $\delta = +00^\circ 20' 13.2''$ (J2000) and known as WHDFCH008 in our WHDF x-ray survey, is extended and relatively faint in both optical and x-ray domains ($B = 24.5$, $R = 24$, $S_{0.5-10 \text{ keV}} = 3.6 \cdot 10^{-15} \text{ erg cm}^{-2} \text{ s}^{-1}$; figure 4.17 on the following page). It has blue $B : R : I$ colours, typical of classic, broad-lined, quasars ($B - R \simeq R - I \simeq 0.5$) but moderate absorption is suggested by its redder, $B - K = 5.0$, colour at infrared wavelengths. LDSS2 spectroscopy shows narrow-emission lines only, corresponding to Ly α , C IV $\lambda 1549$, He II $\lambda 1640$ and C III $\lambda 1909$, which yield a redshift of 2.12 (fig-

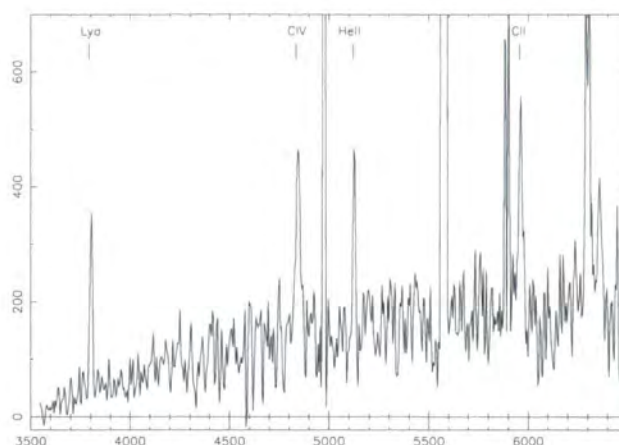


Figure 4.16: Optical spectrum of the type II QSO candidate WHDFCH008, at $z = 2.12$. The main spectral features, which consist of narrow lines of transitions usually reserved for broad-lined AGN, are labelled. Obtained with the Magellan-1 LDSS2 instrument in November 2001.

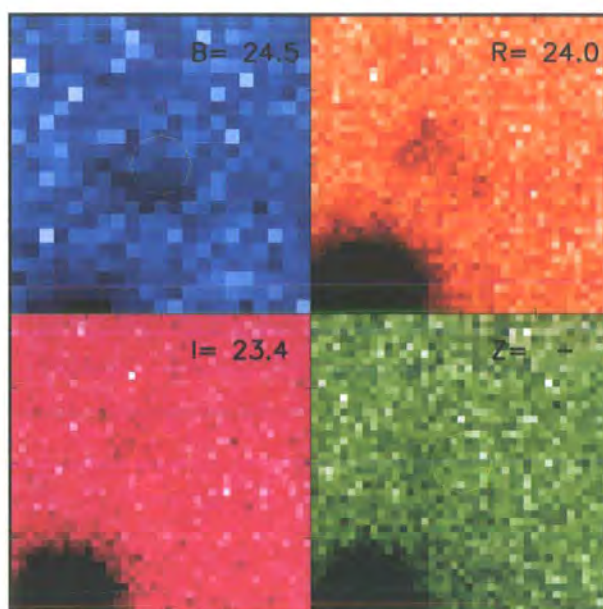


Figure 4.17: Optical images of the type II QSO candidate WHDFCH008, at $z = 2.12$. From left to right, top to bottom, the images correspond to the B , R , I and Z bands. Green circles mark Chandra positions. Each box is $10''$ wide.

ure 4.16). In contrast with RX J13433+0001, WHDFCH008 is hard at $HR = -0.19$. If this is the result of an absorbed power-law spectrum with $\Gamma = 2.0$, the columns implied are $n_H \gtrsim 10^{23} \text{ cm}^{-2}$. Then, its unabsorbed flux yields a rest-frame luminosity of $L_{0.5-10 \text{ keV}} \sim 1.6 \cdot 10^{44} \text{ erg cm s}^{-1}$.

These characteristics make of this object a prime candidate to a type II QSO. To confirm its status, IR spectroscopy that would show absence of broad Balmer lines would be desirable.

Apart from spectroscopically, we have further searched for other type II QSO candidates amongst the $\log f_x/f_{\text{opt}} \gtrsim 1$ sources and also amongst point-like sources with red colours. In the colour-colour diagrams of figures 4.3 – 4.5, seven spatially unresolved sources are found forming a red wing at colours $B - R \gtrsim 2$. Amongst them, GSGP4CH011, F864CH024 and F864CH025 have $\log f_x/f_{\text{opt}} \simeq 1$ and relatively hard spectra. These would be good candidates for type II QSOs, but unfortunately they are only marginally detected in the x-ray images. Another source, GSGP4CH099, is spectroscopically identified with a QSO, possibly embedded in an early-type galaxy, and has a soft spectrum and $\log f_x/f_{\text{opt}} \simeq 1$. Possibly the last extragalactic source within this set is WHDFCH044, one of the absorbed broad-lined QSOs discussed in the previous section. Of the remaining two sources, one is spectroscopically identified with a Galactic star (F864CH036) and the other has a soft spectrum and $\log f_x/f_{\text{opt}} \simeq -1$ which possibly places it in the same category (GSGP4CH084). Amongst the sources selected with $\log f_x/f_{\text{opt}} \gtrsim 1$ the majority are too faint in the optical images as to obtain reliable stellarity indicators and hence not many type II QSO candidates can be picked-out this way (see figure 4.1). There are no candidates in the WHDF and only F864CH003, GSGP4CH036 and GSGP4CH077 in the wider $10 \times 10 \text{ ks}$ survey. The first one is the NLS1 RX J13433+0001 and the second, a spectroscopically identified broad-lined quasar; both have blue colours in g , r and i , typical of quasars. GSGP4CH077 is a point-like source without spectroscopy; its marginally redder colours place it roughly where the evolutionary tracks for spiral galaxies at $z \sim 1$ and for ellipticals at $z \sim 2$ in our models coincide. This is not an unusual location for a classic quasar either.

Overall, only two $z > 2$ luminous highly obscured AGN with narrow lines only in their optical spectra, and just a few more candidates, are found in our surveys. This is alarming from several points of view: not only do population synthesis models of the XRB predict as much as 90% of the sources at high redshift to be type II QSOs (Gilli et al. 2001), but also the modelling of IR spectral energy distribution of AGN (Pier & Krolik 1993) and UV spectral shapes (Maiolino et al. 2001) suggest the presence of numerous type II QSOs in the Universe. In fact, the existence of a population of luminous absorbed AGN is often debated given the ubiquity of our result that narrow-lined QSOs are not commonly observed.

Nevertheless we suggest that luminous type II AGN do exist in abundance. The models require powerful AGN with large absorption columns, in analogy with

lower luminosity type II Seyfert galaxies, that will be absorption thick and hence have very flat spectra in the x-rays (“x-ray” type II QSOs). It is commonly assumed that large atomic columns associate with molecular gas and dust that render the objects optically thick and hence they should display narrow lines only (“optical” type II QSOs). But we have discussed in the previous section, and again for the NLS1 RX J13433+0001, that this assumption is often incorrect. We have also seen that most of the luminous absorbed QSOs show broad emission lines, which can be understood for instance if x-ray absorption occurred within the dust sublimation radius of the source (*cf.* § 4.3.2). Hence it comes natural to suggest that x-ray luminous absorbed AGN show broad lines more often than narrow lines only and that for this reason “optical” type II QSOs are proving so elusive.

This hypothesis offers a natural explanation to the common concern regarding the lack of luminous, high-redshift, obscured sources detected in x-ray surveys, despite the negative K -correction for absorbed x-ray sources (*e.g.* Wilman et al. 2000). In this framework, such sources would turn up as relatively x-ray bright and soft, broad-lined quasars with a high redshift, just as unabsorbed classic quasars do. Therefore, it could be tested by obtaining column density distributions from the x-ray spectra in a sample of high redshift quasars or, alternatively, from the comparison of extreme ultraviolet (EUV) and x-ray colours; uv-optical/x-ray selection techniques should not matter considerably.

Another observation that accommodates well within our hypothesis is that broad-line quasars harden at fainter x-ray fluxes, as observed in figure 4.12: it is just another manifestation that luminous and faint AGN share similar column densities, only that absorbed luminous AGN often do show broad lines. As a final note, we mention in favour that both “optical” and “x-ray” type II QSOs are closely related, that, for instance, the “optical” type II QSO of Norman et al. (2002) is the hardest source detected at $z > 2$ in their sample. Similarly, broad-lined “x-ray” type II QSO WHDFCH007, is the absolute hardest in ours (while WHDFCH044 is the fourth).

4.3.4 Redshift Distribution

Despite the many successes of the XRB population synthesis models, the advent of Chandra and XMM-Newton x-ray observatories has unveiled incongruences in those models which need to be revised. We have already addressed in the previous subsection the issue of the shortage of “optical” type II QSOs found with respect to the expectations. Another surprise has come from the redshift distributions of the AGN in deep x-ray surveys. As can be seen from the top panel of figure 4.18, the AGN (BLAGN + NLXGs) distribution in our surveys peaks at redshifts just below $z = 0.5$, which is a considerably lower redshift than what models based on ROSAT data predicted (*e.g.* $z \sim 1.3 - 1.5$, Gilli et al. 2001).

However, direct comparison between the model predictions and our data is complicated by: a) incompleteness of the optical spectroscopic identifications; b) non-

active galaxies amongst the NLXG population; and c) possible redshift distribution dominated by the presence of large scale structures. Of these three effects, the first one is likely to be the most important. In general, unidentified sources are expected to lie at a higher redshift than those already identified. On the other hand, our identifications are biased towards high redshift QSOs, since many are known from previous ROSAT observations and from the 2QZ survey. But these QSOs are generally optically bright and would have been identified preferentially during spectroscopic follow-up anyway; therefore they do not invalidate that with higher levels of completeness the AGN redshift distribution is likely to peak at higher redshifts. That said, it is highly unlikely that the peak raises to $z > 1$ given the trend observed so far and that we do not anticipate any sharp change between the optically faint galactic population and the brightest galaxies already identified (see § 4.2). As for the contamination by non-active galaxies amongst the NLXGs, we expect it to be of the order of $\lesssim 25\%$ on the basis that only $3/_{11}$ NLXGs occupy the non-AGN parameter space region in the $\log f_x/f_{\text{opt}}$ plot of figure 4.1. Excluding those from the sample does not change appreciably the AGN redshift distribution. Finally, the middle panel of figure 4.18 shows that, although some lumpiness due to large scale structure may be present in the different fields, our redshift distribution is not dominated by any of them (*cf.* the discussion on large scale structure starting on page 144).

SMBH Accretion History

Overall, we conclude from figure 4.18 that NLXGs hosting an AGN (and so probably Seyfert II galaxies) are more numerous at lower redshifts (saturating at $z \sim 0.5$, or slightly higher) than more luminous QSOs (saturating at $z \sim 1.4$). Since these peaks in the redshift distribution are expected at the end of a strong positive evolution, the natural conclusion seems to be that the two populations undergo different evolutions. One explanation to account for the observed sharp decrease of the AGN number-luminosity densities from these redshifts could stem from models where the volume emission from AGN is mostly contributed by higher luminosity objects at higher redshifts and lower luminosity sources at lower redshifts, such as that presented by Menci et al. (2004). Extrapolating the Magorrian et al. (1998) result that black hole masses positively correlate with bulge mass, given that massive AGN are typically hosted by massive galaxies, in a hierarchical clustering scenario, these models would find a natural basis if frequent galaxy merging and interactions at $z \sim 2$ provided a sustained cold gas reservoir to fuel accretion onto SMBHs while, at lower redshifts, $z < 1$, when encounters are less frequent, most gas has been converted to stars and galaxies undergo passive evolution, the major contribution to the AGN x-ray emission would come from lower luminosity sources. This late evolution of the low-luminosity AGN may be similar to that which Franceschini et al. (2002) invoke to fit the mid-infrared source counts and background (a very fast evolution up to $z = 0.8$ for the obscured AGN).

As a final remark on the top panel of figure 4.18, we note the lack of observed

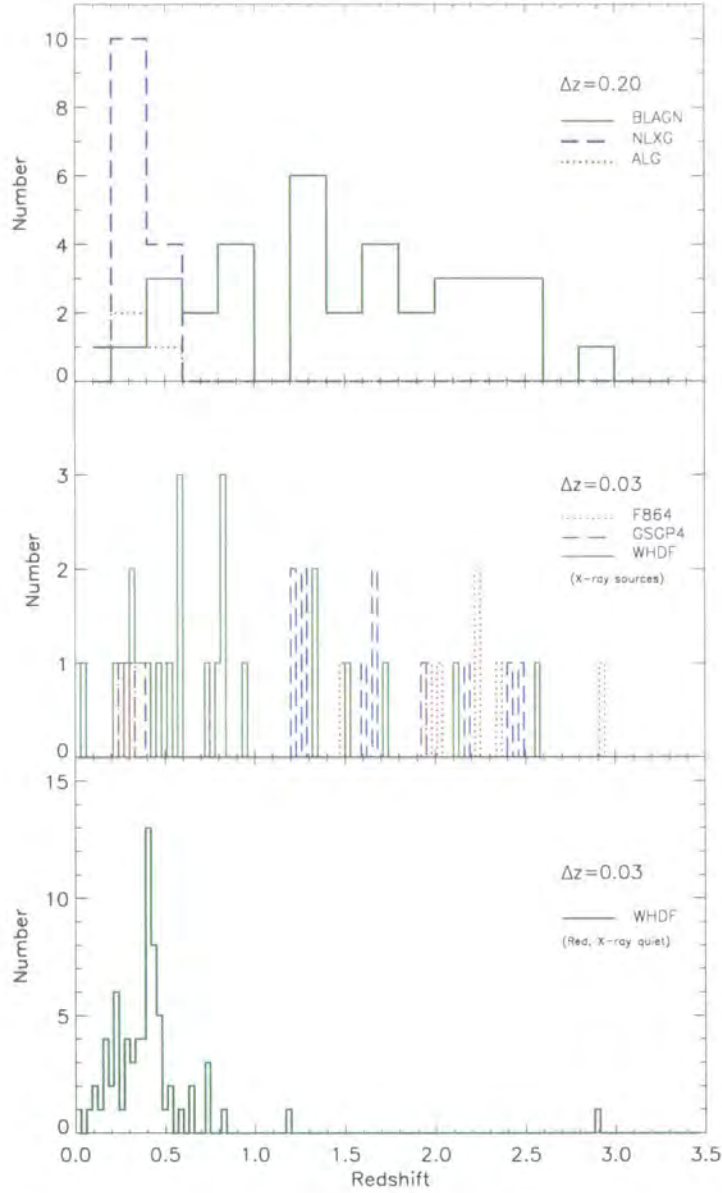


Figure 4.18: Redshift distribution of x-ray sources in the WHDF and 10×10 ks surveys. The top panel compares the distribution of the three classes of extragalactic sources identified. The middle panel shows the distribution of sources separately for the three fields (hard band flux limits of $3 \cdot 10^{-15} \text{ erg cm}^{-2} \text{ s}^{-1}$ in the WHDF and $10^{-14} \text{ erg cm}^{-2} \text{ s}^{-1}$ in the GSGP4 and F864 fields), using a narrow redshift bin interval to highlight possible spikes due to large scale structure. The bottom panel shows the redshift distribution of red, x-ray-quiet galaxies in the WHDF to compare spatial clustering between early-type galaxies and x-ray sources.

QSOs beyond $z = 3$. While the statistical quality of our high-redshift AGN is insufficient to make definitive statements on the subject, the observations hint towards a decline of the x-ray-selected QSOs at high redshift, in consonance with the space density of optically and radio selected QSOs (Schmidt et al. 1995; Shaver et al. 1996; Fan et al. 2001).

Large Scale Structure

AGN clustering has been detected and thoroughly studied at optical wavelengths (Shanks et al. 1987; Croom et al. 2001). x-ray surveys map the obscured AGN population and could be a powerful tool to study the clustering of high redshift objects. A first manifestation of large scale structure has been already encountered in the form of substantial field-to-field variation in the numbers and in the populations found in the images of the WHDF and also of the 10×10 ks survey, where the full range of cosmic variance seen in the Chandra deep fields published to date is reproduced in our set of neighbouring fields.

In figure 4.18 we take a closer look at the spatial clustering of sources in the WHDF, GSGP4 and F864 fields. The middle panel shows the redshift distribution of x-ray sources in each of the three fields. At $z > 1$ we see that at least 40% of the objects show indications of being clustered. Thus, in the GSGP4, out of 11 QSOs, 4 are between $1.3 < z < 1.4$ in two redshift spikes of width $\Delta z = 0.03$ and a further two objects form another spike at $z \simeq 1.67$; in the F864, 2 out of 7 QSOs are at $z \simeq 2.22$; and in the WHDF, 2 out of 6 are clustered at $z \simeq 1.33$. (Note that, with 7 pointings, GSGP4 has the widest surveyed area and, thus, overcomes more easily the stringent limits on the small distances probed perpendicular to the line of sight posed by Chandra's small field of view —at $z = 1$, the $16' \times 16'$ of ACIS-I correspond roughly to an area 4×4 Mpc²). Despite the low number of sources per spike, given the roughly flat distribution of QSOs between $1 \lesssim z \lesssim 3$ in the combined dataset (top panel of figure 4.18) and the small size of the redshift bins used, this result is significant and confirms that x-ray-selected QSOs are highly clustered.

At $z < 1$, redshift spikes with more than one source are seen only in the WHDF. In the bottom plot of figure 4.18 we compare this higher density regions with the redshift distribution of $B - R > 1.6$ -selected, x-ray quiet galaxies in the same field which, by virtue of their selection, should consist preferentially of $z < 0.5$ elliptical and lenticular galaxies (see chapter 5 and also figure 4.3). This comparison is motivated by the facts that over 50% of the infrared sources in the K20 survey of Cimatti et al. (2002) which are classified as early-type galaxies have been reported to lie in two x-ray structures in the Chandra Deep Field South (Gilli et al. 2003; Croom et al. 2001). Further, Brown et al. (2001) showed that the spatial cross-correlation of AGN with early-type galaxies is much stronger than with late-types; it is also well known that early-type galaxies are more likely to reside in dense environments (we have seen that high redshift luminous AGN cluster strongly). Nonetheless, there does not appear to be much correspondence between the dis-

tribution of early-type galaxies and x-ray sources in the WHDF. In particular, the most significant peak of E/S0 galaxies does not have an equivalent peak of x-ray sources.

4.4 Minor Contributors

4.4.1 Stellar Contamination

Galactic stars in our surveys are generally bright and soft x-ray emitters, have optical colours that span the whole space occupied by the galaxy population and display relatively high $\log f_x/f_{\text{opt}}$. While 27% of the Einstein Medium-Sensitivity Sky Survey (EMSSS) and about 20% of the ROSAT All Sky Survey (RASS) consist of galactic sources (Gioia et al. 1990; Motch et al. 1991; Hasinger et al. 1993), they represent only $\sim 5\%$ of the spectroscopically identified objects in our surveys. We identify two major effects that explain this drop. First is that, at the surveys flux limits ($S_{0.5-2 \text{ keV}} \simeq 4 \cdot 10^{-16}$ in the WHDF and $S_{0.5-2 \text{ keV}} \simeq 3 \cdot 10^{-15} \text{ erg cm}^{-2} \text{ s}^{-1}$ in the $10 \times 10 \text{ ks}$), we are capable of detecting bright stars ($\sim 10^{29} \text{ erg s}^{-1}$) beyond the typical scale height of the galactic disk and hence we exhaust the number of stars that can contaminate our samples. Secondly, a high fraction of stars has a rather soft spectrum; therefore, our hard-band detections might select against those. Certainly, also because we targeted intentionally high galactic latitude fields, less stellar contribution is expected. As a conclusion, we can be confident that stars do not significantly alter our conclusions when we assumed all detected sources to be of extragalactic origin (for instance during the calculation of the number-flux relationships, § 2.4 and 4.1).

4.4.2 Extremely Red Objects

Placed between local galaxies and Lyman break or submillimetre selected galaxies, extremely red objects (ERO; $R - K \gtrsim 5$; $I - K \gtrsim 4$) have optical and infrared properties consistent with passive elliptical galaxies, dusty (post-) starbursts and obscured AGN at redshifts $1 \lesssim z \lesssim 2$ (Smail et al. 1999; Pierre et al. 2001). Knowing the relative fractions of each type is important for galaxy evolution models that link the formation of elliptical galaxies with the activation of AGN. Given that the expected x-ray (and x-ray to optical) properties of obscured AGN ($L_X > 10^{42} \text{ erg cm}^{-2} \text{ s}^{-1}$ and hard spectrum) are different than those expected for dusty star-forming objects ($10^{38} < L_X < 10^{40}$ and $1.8 \lesssim \Gamma \lesssim 2.5$; e.g. Ptak et al. 1999; Ranalli et al. 2003) and for old passive galaxies (soft x-ray spectra and low $\log f_x/f_{\text{opt}}$), we can use our data in the WHDF to obtain first conclusions, at least on the relative fraction of obscured AGN amongst the ERO population.

Amongst the three-dozen EROs in the central $7' \times 7'$ WHDF ($K < 20$; McCracken et al. 2000), only one source is found to be x-ray emitter. This object, WHD-

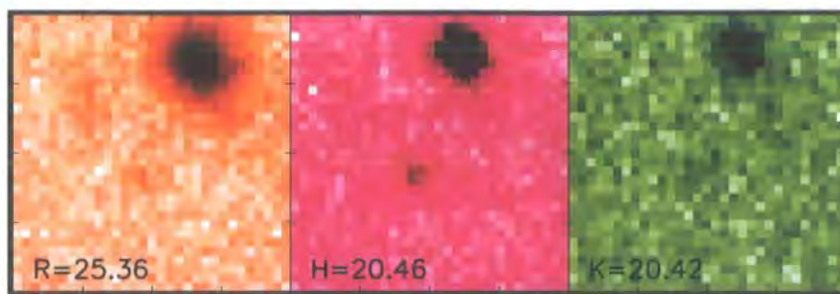


Figure 4.19: Optical images centered on the ERO WHDFCH009, also detected in the Chandra images. From left to right, the images correspond to the R , H and K bands. Each box is $15''$ wide.

FCH009 ($R = 25.2$, $B - R = 0.2$, $B - H = 4.9$, $R - K = 4.9$, $I - K = 4.0$; figure 4.19), was detected with low significance ($S/N = 2.7$) only in the hard band and shows, correspondingly, a rather hard spectrum ($HR = 0.0$) and high x-ray to optical flux ratios ($\log f_x/f_{opt} \simeq 1$), which are typical properties of obscured AGN. The object proved too faint for Magellan-1 LDSS2 spectroscopy, but its colours suggest a redshift $z \gtrsim 2$ (see evolutionary models in colour-colour diagrams in figures 4.3 and 5.4, for instance). In this field Chandra detects a total of 20 x-ray sources and hence the fraction of EROs is significantly lower than that found in other surveys (10–30%; Alexander et al. 2002; Mainieri et al. 2002; Crawford et al. 2001) but not necessarily in disagreement if such fraction depends on the limiting fluxes in both electromagnetic regimes. From this it is readily evident that obscured AGN are in minority amongst EROs and, also, that the latter are generally not powerful x-ray emitters. We conclude that the AGN fraction in the optically selected ERO sample on the WHDF is of $\sim 5\%$, thus suggesting that EROs are essentially unrelated to AGN.

In order to estimate the relative fraction of the other two types, we would need unavailable spectroscopic information which would allow the detection of absorption-line spectra for the old population and of $EW(O\text{III}]\lambda 3827) > 20$ for the dusty EROs. Spectroscopy on optical/IR EROs would also allow to group them into meaningful categories for subsequent stacking analysis of their x-ray properties.

4.4.3 Ultraluminous Compact X-ray Sources

The existence, mostly in spiral galaxies, of off-nuclear x-ray sources with high luminosities, $L_X > 10^{39} \text{ erg cm}^{-2} \text{ s}^{-1}$ (ultraluminous compact x-ray sources, ULXs), is one of the most intriguing problems in x-ray demography. Their energetic output is much higher than expected for neutron stars or low-mass black holes spherically-accreting at the Eddington limit; black holes with masses of the order $M_\bullet \sim 100 M_\odot$ are required to provide such high powers, but then serious problems are encountered when trying to model their formation mechanisms. This has led to the thought that maybe ULXs can be explained as young supernova remnants, normal X-ray binaries in which the X-ray emission is beamed towards the observer

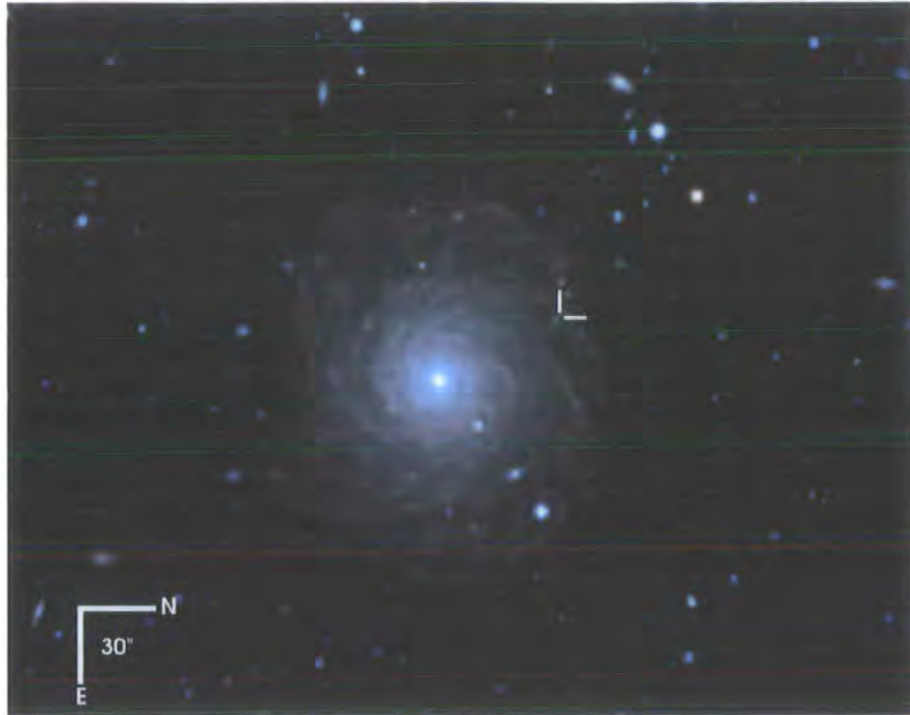


Figure 4.20: Optical image of the spiral galaxy APMUKS(BJ) B005520.08-274536.9 with the position of the ULX GSGP4CH043 marked as two perpendicular lines (at “two o’clock”; J2000 $\alpha = 00^h 57^m 45.122^s$, $\delta = -27^\circ 29' 23.0''$). The image, an inverted true-colour picture obtained from the g , r , i WFI filters, covers a field size of $5.5' \times 4.5'$; east is down and north to the right. It was acquired with the AAT on the 27th–28th December 2000 with a total integration time of 2 hours, reaching limiting depths of $g \sim 25.3$, $r \sim 25.0$, $i \sim 23.7$ magnitude in the g , r , i filters, respectively.

or, simply, as background AGN (e.g. Foschini et al. 2002; King et al. 2001; Masetti et al. 2003).

We report on the identification of the optical counterpart of a ULX in our surveys (GSGP4CH043; J2000 $\alpha = 00^h 57^m 45.122^s$, $\delta = -27^\circ 29' 23.0''$). This is a source with a soft x-ray spectrum ($HR = -0.5$; $\Gamma \simeq 1.8$) and a 0.5–10 keV flux of $5.7 \times 10^{-14} \text{ erg cm}^{-2} \text{ s}^{-1}$, apparently embedded in a region of star-forming knots in the external arms of the spiral galaxy APMUKS(BJ) B005520.08-274536.9 (figure 4.20). However, LDSS2 spectroscopy of the object (figure 4.21) reveals a narrow-emission line source at a redshift of $z = 0.368$, which implies that the ULX is a background source rather than an object associated with the nearby spiral galaxy.

The source is superposed against HII regions associated with a young stellar population in the foreground galaxy, which complicates optical identification. Our tentative WFI photometry results in magnitudes of $g = 22.5$, $r = 22.0$, $i = 21.6$ for an object distant $1.7''$ from the x-ray source. Its spectral features include strong Balmer and forbidden transition emission lines: H_β , H_γ , $[\text{O II}]\lambda 3727$ and $[\text{O III}]\lambda 5007$ (redwards of 700 nm the spectrum is very noisy and the H_α line in particular, expected

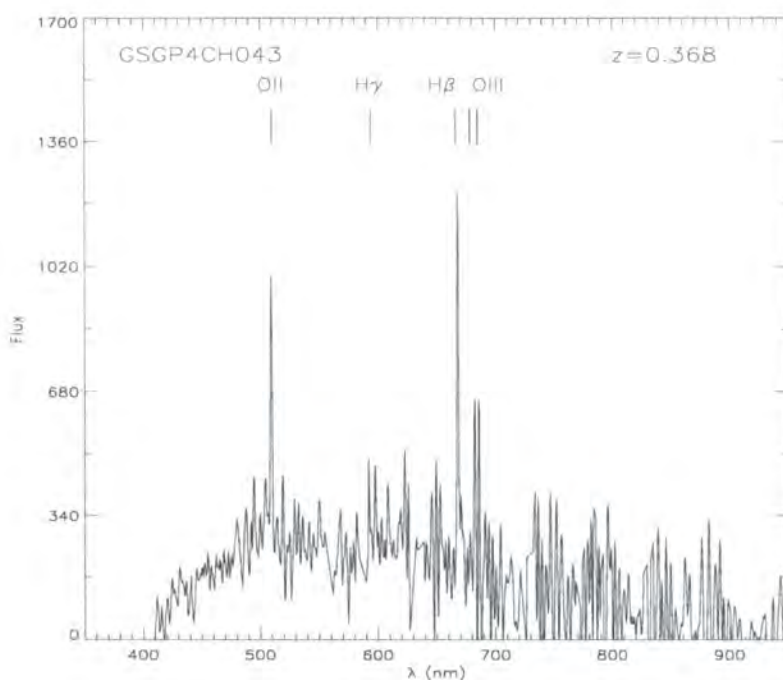


Figure 4.21: Optical spectrum of the ULX GSGP4CH043, at $z = 0.368$ in the background of nearby spiral galaxy APMUKS(BJ) B005520.08-274536.9. The main spectral features are labelled. Obtained with the Magellan-1 LDSS2 instrument in September 2002, with a total integration time of 2.5 hours.

at 898 nm, is unfortunately not properly covered). Unless confusion and starlight contamination have severely affected the redshift determination, we find that the x-ray flux in the 0.5–10 keV band implies a luminosity of $L_X \simeq 4 \cdot 10^{43} \text{ erg s}^{-1}$ (a $q_0 = 0.5$ and $H_0 = 50 \text{ km s}^{-1} \text{ Mpc}^{-1}$ cosmology has been assumed). This is typical of an average bright AGN. The source is also clearly seen in ROSAT images, although the flux is not available since it was detected blended with another source.

Recent observations of ULXs strongly argue in favour that they form a heterogeneous source class (e.g. Roberts et al. 2004). Similarly to our finding, Foschini et al. (2002) and Masetti et al. (2003) report on background sources as the optical counterparts to two ULXs (a BL Lac and a starburst nucleus, respectively). Also, in a recent study of over 80 ULXs detected with Chandra, the distribution of the basic x-ray spectral parameters for about 50% of the sources were best-fit using an absorbed power law with mean spectral index 1.67 (Swartz et al. 2003); this fit is paradigmatic of obscured AGN. Altogether these results suggest that a sizeable fraction of ULXs may be due to confusion with nuclear emission from background galaxies.

4.5 Summary

In order to quantify the contribution from different types of emitters to the XRB we have attempted different classification schemes for the x-ray sources in our surveys. From x-ray imaging analysis we have found all sources compatible with being spatially unresolved and, therefore, no evidence for any contribution from clusters of galaxies or any diffuse hot gas. While optical morphologies are very useful to distinguish point-like (QSOs and stars) from extended sources (galaxies), optical spectroscopy allows the most fruitful classification: extragalactic sources are classified into broad-line AGN (BLAGN), narrow emission-line x-ray galaxies (NLXGs) and absorption-line galaxies (ALGs) according to their ultraviolet and optical line signatures. At the current stage of the spectroscopic follow-up of Chandra sources, we have 63% of BLAGN, 20% of NLXGs, 14% of ALGs and $\sim 3\%$ of Galactic stars. These do not represent, however, the true proportions of classes in the surveys for the follow-up is biased, particularly towards QSOs (many QSOs were known from previous ROSAT surveys or from the 2QZ, for instance).

To explore the emission mechanisms of the x-ray sources, we have studied the distribution of their X-ray-to-optical flux ratios. We have noted a dichotomy between sources brighter and fainter than $f_X \sim 10^{-15} \text{ erg cm}^{-2} \text{ s}^{-1}$ in the sense that all bright sources show enhanced $\log f_X/f_{\text{opt}} > -1$, typical of AGN emission, while the faint population has $\log f_X/f_{\text{opt}} < -1$ and the dominant x-ray emission is, in that case, most likely not due to AGN. The bright population comprises the great majority of sources in the sample, including all the hard sources ($\text{HR} > 0$), all the x-ray sources without optical counterpart, most BLAGN and most NLXGs, which far outnumber ALGs. On the other hand, all the sources in the faint sample are very soft galaxies (NLXGs and ALGs in roughly equal proportions and with $\text{HR} \lesssim -0.7$) and they comprise most of the ALGs of the survey. In other words, it seems that at fluxes $f_X \lesssim 10^{-15} \text{ erg cm}^{-2} \text{ s}^{-1}$ we start to detect the x-ray-bright tail of the “normal” galaxy population with x-ray emission dominated by stellar processes, binaries and interstellar hot gas. At brighter fluxes, where the bulk of the energy of the hard XRB is emitted, most x-ray photons come from AGN, many of them possibly obscured. Indeed, from the optical identifications we have found in good correlation that hard sources have narrow emission lines in their spectra, which indicate obscuration in the standard AGN unification model and therefore they are thought to be type II AGN. Their x-ray-to-optical flux ratios support as well an AGN emission mechanism. From these and from their redshift distributions and scatter in optical and x-ray colours at all luminosities and distances, we have concluded that most narrow emission-line galaxies and optically inactive galaxies observed at bright fluxes with Chandra are low level AGN at different luminosities and/or redshifts (generally, $z < 1$). Sources with very faint optical counterpart, or even with no counterpart at all, appear to be mostly the high-redshift tail of these AGN. For the faintest galaxies, the glare of the nuclear component will be diluted by the

much stronger absorption lines of the stellar background of the bulge. These conclusions are backed by Moran et al. (2002) who perform optical spectroscopy of nearby Seyfert II galaxies simulating observations of distant Chandra sources and find that numbers of narrow emission-line galaxies in deep x-ray surveys have been underestimated; further support could be obtained from performing targeted long-slit spectroscopy to selected faint optically inactive ALG in search of emission lines.

Our data has been found in agreement with the models based on the x-ray properties of unified schemes for AGN in the basic requirement that a large fraction of the XRB is due to obscured active nuclei. At high redshift we have reported on the discovery of a new high-luminosity obscured AGN which has only narrow lines in its optical spectrum and a hard hardness ratio, *i.e.*, a candidate to a type II QSO (WHDFCH008). We have also provided support to the analyses based on ROSAT data on another such source, RXJ13433+0001. Nonetheless, the number of luminous obscured AGN at high redshifts remain significantly below the expectations from the population synthesis models of the XRB and from the modelling of IR and UV AGN SEDs. To bring agreement between the observations and the predictions we have suggested that x-ray luminous absorbed AGN show broad lines more often than not. This is based on several results, including the discovery of broad-line quasars amongst the hardest sources in the WHDF, that show that atomic columns responsible for x-ray absorption do not always associate with the molecular gas and dust that render the objects optically thick.

The redshift distribution of AGN has shown that they peak at considerably lower redshift than what models predict. NELGs hosting an AGN are more numerous at lower redshift than more luminous QSOs, which could be the result of a different evolution. We have also found that, while high- z x-ray-selected QSOs are highly clustered, at low redshift no clear correspondence is found between the positions of early-type galaxies and x-rays sources in the WHDF.

In the last section we have assessed the incidences of Galactic stellar contamination and of EROS in our samples. We have found that stars constitute only $\sim 5\%$ of the spectroscopically identified sources and therefore do not seriously affect our results based on all point-like sources being of extragalactic origin. EROS are found to be essentially unrelated to AGN. From their anecdotal presence in our catalogues we have concluded that obscured AGN are in minority amongst EROS ($\sim 5\%$) and, also, that the latter are generally not powerful x-ray emitters. We have closed this chapter reporting on the identification of the optical counterpart of the ULX GSGP4CH043. This source is apparently embedded amidst HII regions in the arms of the face-on spiral galaxy APMUKS(BJ) B005520.08-274536.9, but optical spectroscopy reveals a narrow-line emission object at $z = 0.368$, which implies that the ULX is a background source.

Evolution of Early-type Galaxies

A primary goal of galaxy evolution studies is to elucidate how the stellar content of the present universe was assembled over time and the evolution of the spheroid-dominated galaxies offers an essential discriminant between the most popular scenarios, namely monolithic galaxy formation and hierarchical galaxy formation in a cold dark matter universe (e.g. Aragon-Salamanca et al. 1998). Further, the latter scenario predicts significantly different formation histories for field or cluster early-type galaxies (Baugh et al. 1996; Kauffmann & Charlot 1998).

The study of the evolutionary properties of the early-type population also serves a second purpose which is to help clarifying which galaxy types preferentially host AGN. We have seen in chapter 4 (e.g. figures 4.3–4.5) that a very high fraction of x-ray galaxies span intermediate colours which, on basis to our models, correspond to very low-redshift elliptical ($z \lesssim 0.2$) or intermediate-redshift spiral galaxies ($z \lesssim 1$). By investigating the accuracy of the models we aim to characterize with better detail these galaxies.

5.1 Evolutionary Models

We have researched evolutionary models where galaxies form at high redshift through a monolithic collapse accompanied by a short-lived and intense burst of star formation and then followed by a passive and pure luminosity evolution (Eggen et al. 1962). These have been based on a Bruzual & Charlot (2003) globular cluster-like stellar population with an initial mass function $\Psi(M) \propto M^{-x}$, $x = 3$, convolved with a star formation history of a single starburst decaying exponentially with $e^{-t/\tau}$, e -folding time $\tau = 2.5$ Gyr, together with a $q_0 = 0.5$, $H_0 = 50 \text{ km s}^{-1} \text{ Mpc}^{-1}$ cosmology. It is found that, not only do these models reproduce the observed B -band source number counts, but also the evolutionary tracks seem to trace the distribution of galaxies on colour-colour diagrams with exactitude (figure 5.1; Metcalfe et al. 2001). To some extent, this was expected since it has been long known that early-type galaxy spectral energy distributions (SED) are regular enough as

to allow the inference of their redshift from their broad-band colour indices (e.g. Baum 1962; Koo 1985). For elliptical and lenticular galaxies at $z < 0.5$, the 400 nm break provides a sharp feature in the SED that falls on the B and R bands. Hence the break gets reflected in the $B - R$ colour, which acts as a redshift indicator, but a degenerated one because the strength of the 400 nm break varies from galaxy to galaxy. In figure 5.1 this degeneracy is broken with the $R - I$ colour which allows us to measure both redshift and SED type.¹

To investigate whether the agreement of colours with redshift is as tight as the models suggest we selected several bright galaxies spread over the $1.6 \leq B - R \leq 3$ branch and pursued spectroscopic follow-up with LDSS2 on Magellan-1 (§ 3.4); the selected sources are marked on figure 5.1. On figures 5.2 and 5.3 we plot the apparent colour indices ($B - R$ and $R - I$, respectively) against the spectroscopic redshift for these sources and compare them with the predictions from the model. We observe that the models act like an upper envelope and that many galaxies have colours much bluer than the path marked by the evolutionary tracks seems to allow. Based on the tightness of the $B : R : I$ colour-colour almost-unidimensional locus which the models reserve for elliptical galaxies, this result first came as a bit of a surprise. Moreover, our magnitude-selected galaxies should generally represent the most luminous specimens at a certain redshift ($M_R \lesssim -21$) and, given the excellent agreement found by the Sloan Digital Sky Survey team between the colours of luminous red galaxies (LRGs) and their redshifts (Eisenstein et al. 2001), also from this front we expected a colour index–redshift fit more on the tracks of the models. While the lack of sources above the envelope is due to the models being computed for brighter than L^* galaxies, and there are very few luminous galaxies redder than the old stellar populations of giant ellipticals, the large scatter obtained below the envelope instead proves that our models of simple high-redshift monolithic collapse are incorrect and need further tuning. With the simple selection criterion that galaxies be redder than $B - R \geq 1.6$ we let intrinsically bluer and distant galaxies, which can produce the observed $B - R$ red colour, into our sample. And, indeed, were just a few such cases would be expected from the models' mild evolution in the rest B luminosity density or from the increasing fraction of blue galaxies observed at intermediate redshifts (Butcher & Oemler 1984), many are observed at a range of redshifts, maybe indicating that the models should evolve faster in the rest-frame B -band; this would better account for the large number of red galaxies observed. Such contamination will be larger at higher redshifts and we do find that the fraction of galaxies with bluer colours than the models (by $\Delta(B - R) \gtrsim 0.2$ and $\Delta(R - I) \gtrsim 0.1$) increase with redshift. We note, however, that several teams that have explored independently the evolution of the E/S0 colour-magnitude relation find that there is only weak evolution in the rest B luminosity (Metcalf et al. 1996; Pozzetti et al. 1998; Bell et al. 2004) which sets limits to the

¹Note that, as can be seen in figure 4.3, high redshift spirals have the same $B - R$ and $R - I$ colours as low redshift early-type galaxies, which accidentally introduces another degeneracy.

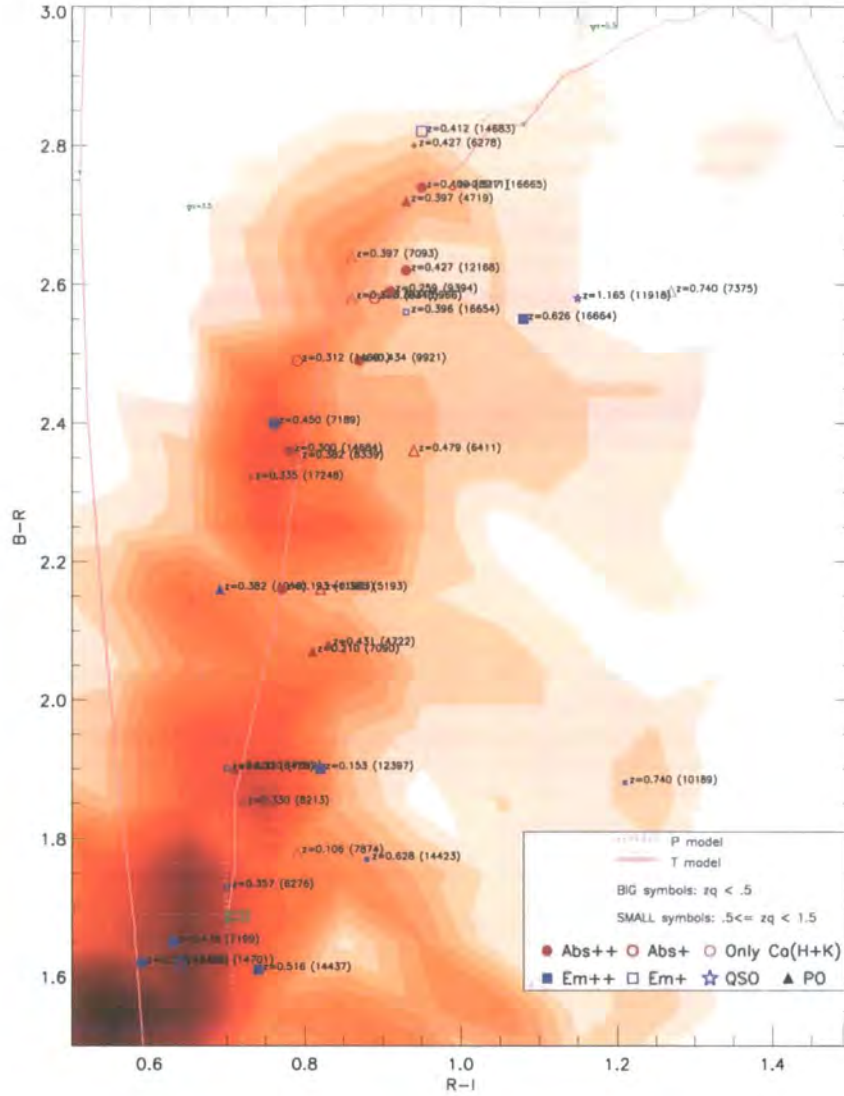


Figure 5.1: Colour-colour diagram of the red E/S0 galaxies studied. Early-type galaxies at redshifts below 0.5 are distributed in a narrow $R-I$ gap with $B-R$ colours redder than ~ 1.6 ; this region can be easily seen as the high surface density of galaxies in the background contour (constructed from all the $R < 24$ galaxies in the field). Bright sources on this colour-colour space were selected for our study; the plot shows them with a range of symbols: a) red circles indicate the presence of absorption lines in their spectra and the amount of fill denote the strengths of the lines; b) blue squares indicate narrow emission-lines in the spectra of the source and, again, filled for strong lines and shallow for weaker lines; c) blue stars denote the presence of broad lines; d) triangles are either absorption- or emission-line galaxies and, in that case, their colour serves as the discriminant. Each source is labelled with its redshift and its R -band catalogue number. In the plot there are as well two evolutionary tracks for early-type galaxies based on Bruzual & Charlot (2003) single stellar population synthesis models.

amount of blue contamination in figures 5.2 and 5.3 due to this effect.

Already since the detection of ultraviolet (UV) radiation from early-type galaxies by the Orbiting Astronomical Observatory-2 it has been noted that UV SEDs exhibit much larger scatter than their conspicuously homogeneous behaviour in the 400–2000 nm region (Code 1972; Code & Welch 1982; Pence 1976; King & Ellis 1985; Kinney et al. 1996). This most variable photometric feature, associated with low-mass helium-burning stars in extreme horizontal branch (O’Connell 1999), could cause some of the wide spread of the early-type galaxies in the colour-redshift plots.

Yet part of the blue contamination is probably due as well to later-type galaxies at intermediate redshifts sharing the same $B : R : I$ space than lower redshift bulge-dominated galaxies. The evolutionary tracks for S0–Sab galaxies are very similar and the models already indicate that a small fraction of such cases should occur. But the fact that some of the galaxies that lie well blueward of the models show narrow emission lines in their spectra and no conspicuous 400 nm break adds support to the conclusion that they are later-type galaxies and hence the models might have to be revised to allow more overlap between early and later types in this colour-colour space. Unfortunately our ground-based imaging is of insufficient resolution to obtain reliable morphological information for distant galaxies; however the Hubble Space Telescope (HST) has recently imaged the WHDF and in a few months we will have access to its data and should confirm this point. More generally, the HST images will help establish the morphology of the galaxies and could confirm that many of these are early-type galaxies but with distorted morphologies such as tidal debris or blue circumnuclear rings, as found in 5 out of 9 early-type galaxies in low-density environments recently studied by Kuntschner et al. (2002).

From the current models it seems also that a large fraction of these outsiders have excess infrared colours. This can be seen from figure 5.4 on page 157 which shows a set of colour-colour diagrams with the population subject of our study marked as filled red dots. We see in the $B - R : I - H$, $B - R : R - K$ and $R - I : I - H$ plots that the models act as blue envelopes and the sources actually fall on the red side of the infrared colour. However, this result must be taken with caution because all evolutionary tracks in figure 5.4 involve B or R magnitudes which, as we have seen, could be ill-accounted for in the models and hence the IR excesses could prove artificial. Nevertheless, we suggest that we could be dealing here with post-starburst galaxies (“E+A” or “K+A”) for which AGB stars make a significant contribution to the galaxy’s global emission. In a few cases this is corroborated by conspicuous Balmer absorption-lines and relatively weak 400 nm break, from which we infer that the burst of star formation has terminated within ~ 1 Gyr. Since the fraction of these galaxies increases with redshift ($z < 0.5$) post-starbursts could be responsible for (or at least linked to) the Butcher-Oemler effect (1984).

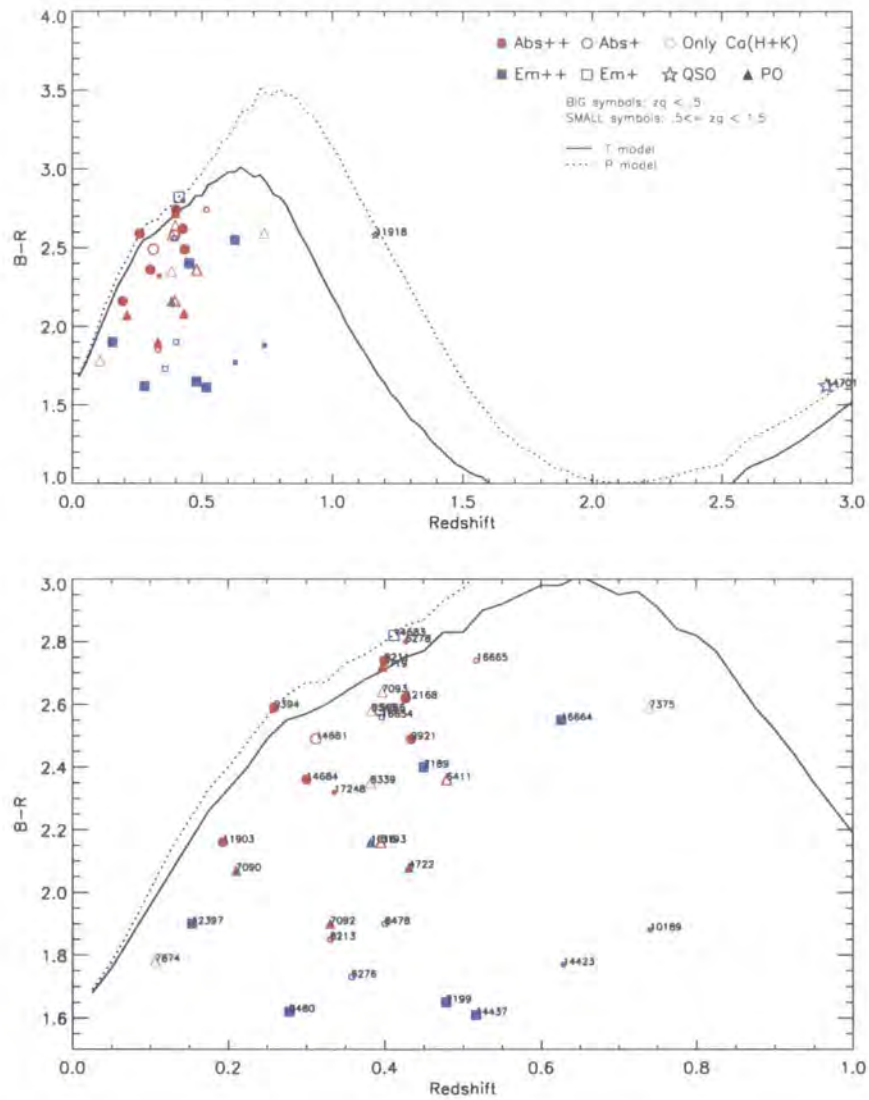


Figure 5.2: $B-R$ colour index as a function of redshift for the red field early-type galaxies in the WHDF, as selected from figure 5.1. The bottom plot is an enlarged version of the top panel, restricted to redshifts below unity. Symbols and evolutionary tracks as in figure 5.1.

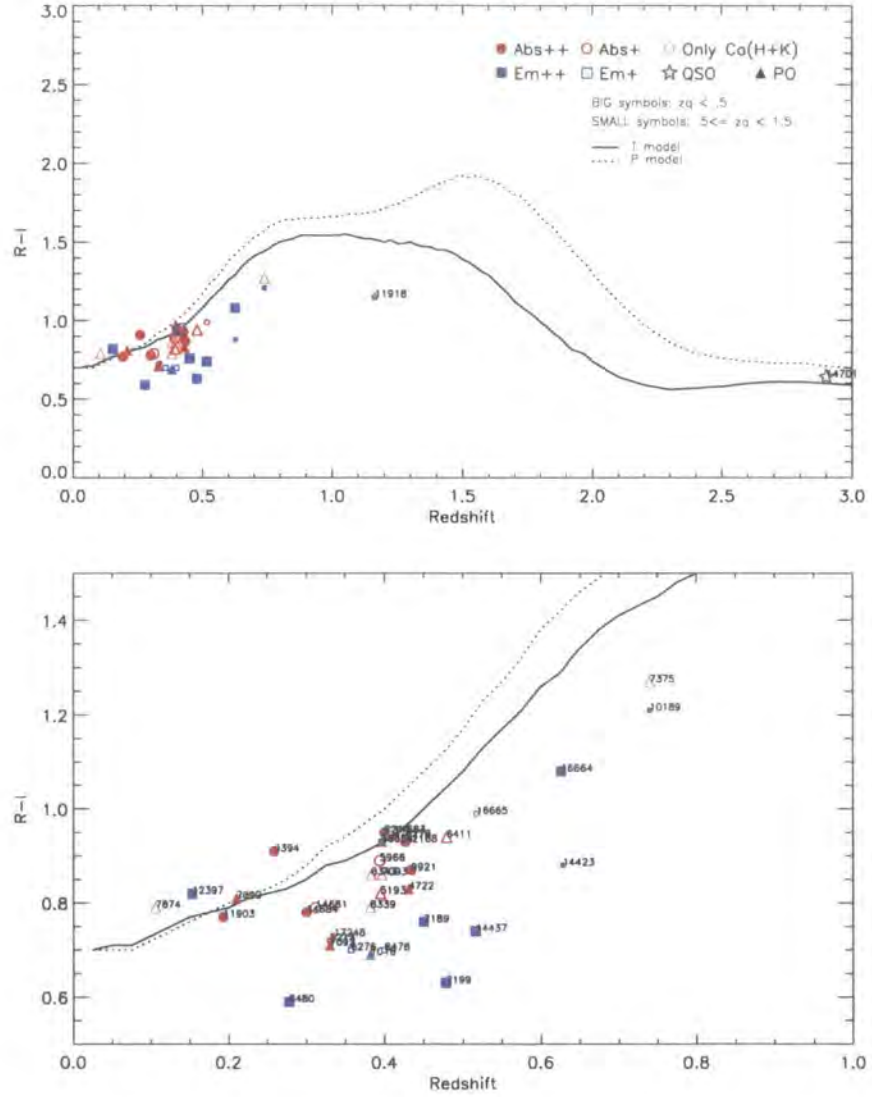


Figure 5.3: $R-I$ colour index as a function of redshift for the red field early-type galaxies in the WHDF, as selected from figure 5.1. The bottom plot is an enlarged version of the top panel, restricted to redshifts below unity. Symbols and evolutionary tracks as in figure 5.1.

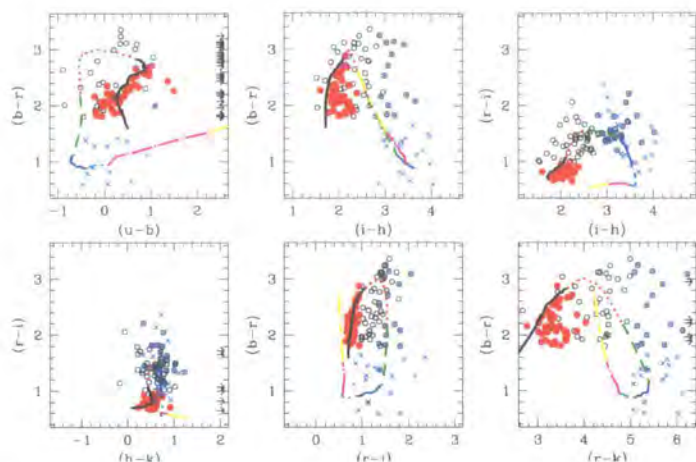


Figure 5.4: Colour-colour diagrams for field early-type galaxies in the WHDF, with studied population marked as filled red dots. Evolutionary models are overlaid.

5.2 Colour-Magnitude

Simplified forms of the Hertzsprung-Russell diagrams are plotted in the colour-magnitude diagrams of figures 5.5–5.7. It has been extensively shown that early-type galaxies obey a tightly constrained colour–absolute magnitude relation, by which the integrated colours of elliptical galaxies become progressively bluer towards fainter magnitudes (Baum 1959; de Vaucouleurs 1961; Faber 1973; Visvanathan & Sandage 1977; Bower et al. 1992a,b). This is particularly so for cluster environments where the scatter around the colour–magnitude relation is extremely small. However, field early-type galaxies have not been studied with equal thoroughness (e.g. van Dokkum et al. 2001) and hence we were interested in determining whether the homogeneity observed in clusters extends to galaxies in lower density environments. From our plots the answer is ‘no’. Figure 5.5 shows the K -corrected and passively evolved absolute R magnitude against the $B-R$ and $R-I$ rest-frame colours for the red ellipticals of the WHDF, which have been chosen along an average line of sight; the scatter is so large that it is difficult even to confirm any colour–magnitude relation at all. A similar conclusion is reached by Schade et al. (1999) and Larson et al. (1980). If the homogeneity of the colour–magnitude in clusters is indicative that the bulk of the stellar populations are old, with most of the stars having been formed before $z \sim 1$, the colour–magnitude relation of early-type galaxies in the WHDF suggests a wide range of formation times, where ongoing star formation is allowed in some galaxies almost right up to the epoch of observation. This is confirmed by the large fraction (at least $1/3$) of field ellipticals showing $[\text{O II}]\lambda 3727$ lines.

Unfortunately the lack of redshift resolution and the scatter in figures 5.6 and 5.7 make it difficult to properly study the evolution of the colour–magnitude relation and we cannot tell whether there is any evolution with look-back time.

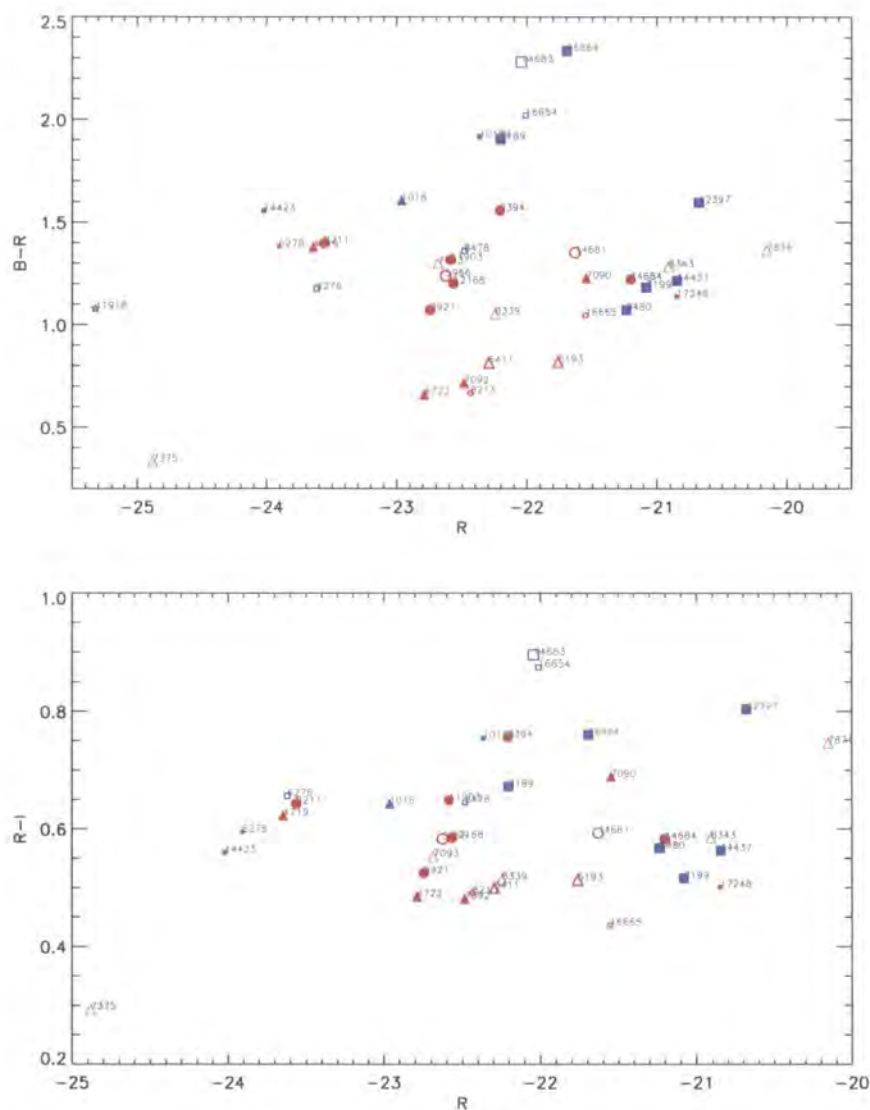


Figure 5.5: Rest-frame colour–absolute magnitude relations for the red field early-type galaxies in the WHDF. Both quantities have been K -corrected and passively evolved to $z = 0$ since not all sources are at the same distance. The symbols are the same as in previous figures.

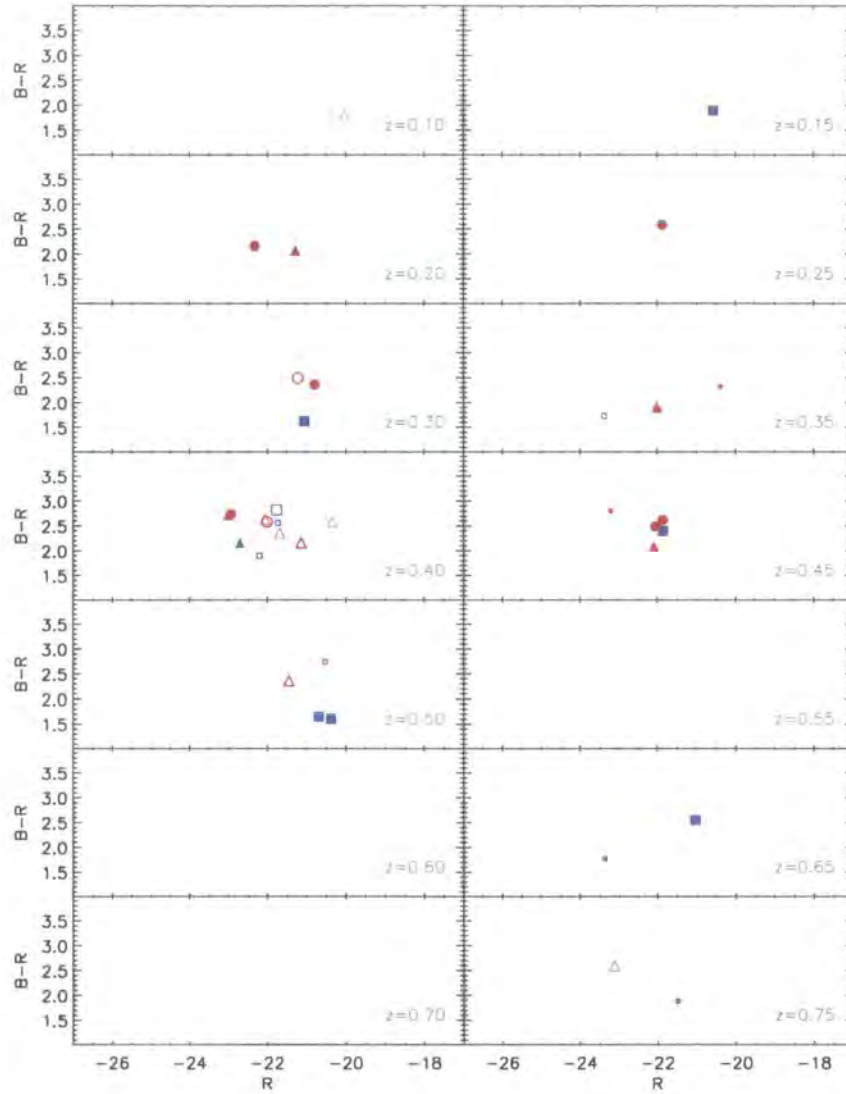


Figure 5.6: $B - R$ rest-frame colour-absolute magnitude diagrams at different redshift bins for red field early-type galaxies in the WHDF. Given that in each redshift panel objects are all at the same distance, colours and magnitudes have not been K -corrected and passively evolved to $z = 0$ so that artificial effects introduced by wrong choices of evolution do not affect the plots. The symbols are the same as in previous figures.

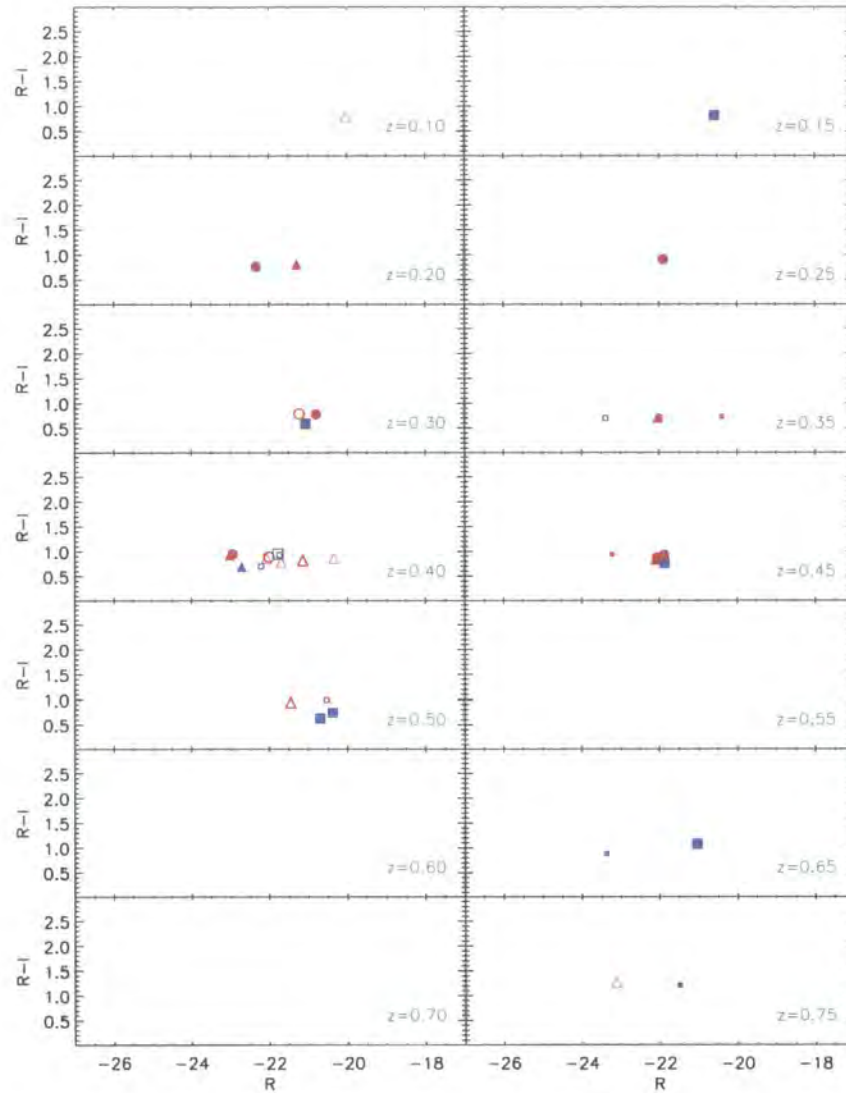


Figure 5.7: $R-I$ rest-frame colour-absolute magnitude diagrams at different redshift bins for red field early-type galaxies in the WHDF. Given that in each redshift panel objects are all at the same distance, colours and magnitudes have not been K -corrected and passively evolved to $z=0$ so that artificial effects introduced by wrong choices of evolution do not affect the plots. The symbols are the same as in previous figures.

5.3 Summary & Discussion

From a colour-selected sample of early-type galaxies in the direction of the WHDF, we find a significant fraction which show colours that are too blue to be consistent with the predictions of a simple monolithic collapse at high-redshift and passive evolution thereafter. Their large scatter in photometric observables seem to imply divergent histories and indicate that the early-type populations are more heterogeneous than implied by Baade's "population II" nomenclature (1944). In particular, significant low-redshift star formation is deduced from the large scatter in the colour-magnitude relation and from the presence of $[\text{O II}]\lambda 3727$ emission lines. We have searched for possible causes to explain these observations; in this regard, forthcoming Hubble Space Telescope images will help clarifying whether there is any contamination from later-type galaxies or if there is any connection between early-type galaxy morphologies and the observables reported. We note that our observations could accommodate well hierarchical models where early-type galaxies in low-density environments are able to incorporate stars formed at low redshifts and therefore should have younger luminosity-weighted ages than the equivalent cluster population and show a broad age distribution over the whole luminosity range (Baugh et al. 1996; Kauffmann & Charlot 1998; Cole et al. 2000).

With all this analysis, the positions of x-ray sources in colour-colour diagrams remain ambiguous. In principle, according to the models, they have generally too blue a $B - R$ colour for their redshift to be early-type galaxies. But we have seen in this chapter that this behaviour is common in many $B - R$ -selected red galaxies and that the models fail to provide a correct description of it. Moreover, in the case of x-ray galaxies, nuclear activity might as well enhance the blue emission. Hence, the proposition that many AGN in our samples are hosted by early-type galaxies at intermediate redshifts seems now more plausible than the models would initially suggest. However, we can not rule out either that they are later-type galaxies. Lenticular and Sab spiral galaxies have very similar evolutionary tracks and we have seen in § 5.1 that the data on early-type galaxies might require a larger region of overlap between early- and late-type galaxies in colour-colour diagrams. If that were the case, many x-ray galaxies could as plausibly be spirals and BRI colours would prove inadequate to disentangle the degeneracy. This confusion could even be more severe if, instead of contributing strongly to the blue emission, the AGN, many being obscured, radiated strongly in red bands. At any rate, though, this seems to suggest that, whatever the host, it is likely to possess a bulge of some sort. Inspection of the optical thumbnails of appendix A seems to confirm that this is indeed the case and few galaxies appear clearly without a bulge. However, the spatial resolution of our images is low and all conclusions in this regard, as for the study of the evolutionary properties of E/S0 galaxies, will greatly benefit from the HST images.

Summary and Conclusions

*We cannot comprehend the meaning of the Universe,
but there is something in its image
that agrees with man's imagination.*

Borges (1967)

In this thesis, two new surveys of the x-ray background (the WHDF and the 10×10 ks) have been presented. Serendipitous x-ray hard and soft sources have been identified and characterised by conducting concurrent optical and x-ray observations. The main aim of this work was to establish if x-ray luminous narrow-emission line galaxies are the sources that are the major contributors to the hard XRB along with finding an explanation for their dominant x-ray emission mechanisms.

6.1 X-ray Data

We began this work by constructing catalogues of x-ray sources from Chandra observations for each of the two surveys. In the 10×10 ks survey of fields GSGP4 and F864, 71 sources were detected with $S/N \geq 3$ down to hard band fluxes of $S_{2-10 \text{ keV}} \simeq 10^{-14} \text{ erg cm}^{-2} \text{ s}^{-1}$, over a solid angle of $\Omega \sim 0.2 \text{ deg}^2$; in the narrower and deeper WHDF, 69 sources were obtained with the same significance ($\Omega \sim 0.08 \text{ deg}^2$, $S_{2-10 \text{ keV}} \gtrsim 3 \cdot 10^{-15} \text{ erg cm}^{-2} \text{ s}^{-1}$, $S/N \geq 3$). For over 75% of the hard objects in the combined sample, a significant soft counterpart was also detected. If the hard population is representative of highly obscured AGN at low-to-intermediate redshifts ($z \lesssim 1.5$), this indicates that in type II AGN significant soft emission can still be produced. Amongst the sources detected in the soft band, only $\sim 40\%$ were found to be significant emitters in the hard band, which argues in favour of a large fraction of the XRB at soft energies resulting from unobscured AGN.

From an assessment of the basic temporal properties of the sources in our samples it was found that at most half of them seem to be constant flux-emitters over

time-scales of a decade; at time-scales of a day, acute flux changes affected 10–20% of the brightest x-ray sources in the WHDF. A more detailed statistical analysis should consider, not only the probability that an individual source outputs a non-constant flux, but also the probability that amongst a sample of M constant-flux emitters, N sources are $\geq Y\sigma$ away from the constant-flux value.

The source number counts down to fluxes of $4 \cdot 10^{-16}$ ($3 \cdot 10^{-15}$) and $3 \cdot 10^{-15}$ ($1 \cdot 10^{-14}$) $\text{erg cm}^{-2} \text{s}^{-1}$ in the soft and hard bands of the WHDF (10×10 ks) survey were derived. This revealed a spread in the normalisations of the counts of $\sim 50\%$ in the two surveys which we attributed to cosmic variance. Allowing for the necessary room for this variance, the obtained power-law fits to the $\log N$ vs. $\log S$ in the WHDF were found to be consistent with most other results in the literature; in the soft band the fit ($\log N = (-8.6 \pm 0.4) - (0.76 \pm 0.03) \log S$) is almost identical to that in the CDF-S (Giacconi et al. 2001) while, in the hard band ($\log N = (-11.8 \pm 0.5) - (1.02 \pm 0.04) \log S$), excellent agreement was obtained with the results in the SSA13 survey (Mushotzky et al. 2000). The number counts derived also compared favourably with the predictions from a population synthesis model of the XRB based on a flat distribution of columns in logarithmic space by Gunn (1999). The fit in the hard band resulted in an integrated contribution of $1.25 \times 10^{-11} \text{ erg cm}^{-2} \text{s}^{-1} \text{ deg}^2$ for fluxes $2.75 \lesssim S_{\text{(cgs)}}/10^{-15} \lesssim 100$, which means that our surveys resolve $> 70\%$ of the XRB in the same band.

The x-ray spectral properties of the sample were also described. The sources were found to harden with soft flux but not with hard flux, as expected if their flat spectra are due to absorption of soft x-ray photons. From both surveys, a population of hard bright sources with very flat spectra ($\text{HR} \sim 0.3$) was identified. Given their high fluxes, it is surprising that they remained undetected with ROSAT, although the fact that the sensitivity of x-ray detectors and their PSF depend on the spectral shape of the sources could offer an explanation.

6.2 Optical Follow-up of Chandra Sources

The details of the optical imaging and spectroscopic data reduction and calibration were presented in chapter 3. Covering most of the Chandra regions in the GSGP4 field, g -, r - and i -band imaging to depths of ~ 25.3 , 25 and 23.7 magnitudes respectively was obtained with AAT/WFI as the basis for the optical follow-up for the 10×10 ks survey. Optical counterparts for $\sim 60\%$ of the x-ray sources were thus obtained in this field. In the WHDF, deep multiband imaging down to $B \simeq 26$, $R \simeq 26.3$, $I \simeq 24$ and $Z \simeq 23$ (plus, for the privileged central area, even deeper to $B \simeq 28.2$ and with wider UV-IR spectral coverage) allowed the detection of optical counterparts for, again, $\sim 60\%$ of the Chandra sources in the field. Interestingly, optical counterparts to $\sim 70\%$ of the x-ray sources in F864 were obtained at much shallower regimes from the Sloan Digital Sky Survey. This might be understood in

conjunction with the observation, from hardness ratio vs. fluxes, that an abnormally high fraction of sources in this field are soft. Together, these two facts seem to indicate that x-ray sources in this field are mainly unobscured bright AGN, as found in previous ROSAT surveys.

Spectroscopic follow-up was conducted with Magellan-1/LDSS2 (WHDF & GSGP4) and WHT/WYFFOS (F864). In two campaigns with LDSS2 in 2001 and 2002 we targeted 64 x-ray objects, preferentially extended, and obtained reliable identifications for 45 of them. Many of these spectra correspond to sources with too faint magnitudes ($B > 23.5$), according to preexisting photometry, implying optical variability amongst our x-ray samples. During these campaigns, slit masks were optimised by targeting an additional population of 92 $B : R : I$ -selected elliptical and lenticular galaxies in a parallel program to study the evolutionary properties of the early-type galaxy population; 65 redshifts for this study were obtained. With WYFFOS, 17 identifications of x-ray sources were obtained in 2002 in F864.

Performing our own follow-up of x-ray sources proved very efficient at the identification of moderately faint sources. However, public datasets were also mined and surveys like the 2dF and SDSS were instrumental in identifying many of the brightest sources.

6.3 The Nature of the XRB

Chapter 4 covered several topics which show insight into the physical nature and the cosmic evolution of the sources that make the XRB and into their role in models of galaxy and AGN evolution. It integrated the x-ray and optical data from the preceding chapters and contains the main body of results of this thesis.

Extragalactic x-ray sources were classified into broad-line AGN (BLAGN), narrow emission-line x-ray galaxies (NLXGs) and absorption-line galaxies (ALGs) according to their ultraviolet and optical line signatures. At the current stage of the spectroscopic follow-up of Chandra sources, we have 63% of BLAGN, 20% of NLXGs, 14% of ALGs and $\sim 3\%$ of Galactic stars. These do not represent, however, the true proportions of classes in the surveys for the spectroscopic follow-up is biased towards bright sources and is still more than 50% incomplete. Nevertheless, classifying sources into these categories proved extremely useful in subsequent analyses to unveil characteristic trends of different populations.

While exploring the emission mechanisms of the x-ray sources through the distribution of their X-ray-to-optical flux ratios, a dichotomy was highlighted between sources brighter and fainter than $f_X \sim 10^{-15} \text{ erg cm}^{-2} \text{ s}^{-1}$ in the sense that all bright sources show enhanced $\log f_X/f_{\text{opt}} > -1$, typical of AGN emission, while the faint population has $\log f_X/f_{\text{opt}} < -1$ and the dominant x-ray emission is, in that case, likely not due to AGN. The bright population was seen to comprise the great majority of sources in the sample, including all the hard sources ($\text{HR} > 0$), all the

x-ray sources without optical counterpart, most BLAGN and most NLXGs. On the other hand, all the sources in the faint sample are very soft galaxies (NLXGs and ALGs in roughly equal proportions and with $HR \lesssim -0.7$) and they comprise most of the ALGs of the survey. We concluded that at fluxes $f_X \lesssim 10^{-15} \text{ erg cm}^{-2} \text{ s}^{-1}$ we might be beginning to detect the x-ray-bright tail of the “normal” galaxy population with x-ray emission dominated by stellar processes, binaries and interstellar hot gas while, at brighter fluxes, where the bulk of the energy of the hard XRB is emitted, star formation did not play a major role and we were detecting x-ray photons coming mostly from AGN. Many of those AGN, most notably the hard population, are possibly obscured on the basis that they often exhibit narrow lines in the spectra, which indicate obscuration in the standard AGN unification model and therefore they are thought to be type II AGN. From these observations and from their redshift distributions and scatter in optical and x-ray colours at all luminosities and distances, we concluded that, at fluxes $f_X \gtrsim 10^{-15} \text{ erg cm}^{-2} \text{ s}^{-1}$, not only are most narrow emission-line galaxies low level AGN, but so are the optically inactive galaxies identified and even the optically faintest sources.

Population synthesis models of the XRB were reviewed later in the chapter. As concluded from the previous section, our data were found in agreement with their basic requirement that a large fraction of the XRB is due to obscured active nuclei. The discovery of a new type II QSO candidate (WHDFCH008) at redshift $z = 2.12$ was reported. This and RX J13433+0001 are the only identified examples of luminous obscured AGN at high redshifts in our surveys. The small number remains significantly below the expectations from the models of the XRB based on the x-ray properties of unified schemes for AGN and from the modelling of IR and UV SEDs. This shortage of heavily obscured bright AGN is frequently found in deep x-ray surveys of the XRB and, to bring agreement between the observations and the predictions, we made the suggestion that x-ray luminous absorbed AGN show broad lines more often than not. This was partially based on the discovery of broad-line quasars amongst the hardest sources in the WHDF, that show that atomic columns responsible for x-ray absorption do not always associate with the molecular gas and dust that render the objects optically thick.

Another shortcoming of the models is that they predict that AGN peak at considerably higher redshifts than generally observed. Redshift distributions showed that NELGs hosting an AGN are more numerous at lower redshift than more luminous QSOs, which could be the result of a different evolution. From the redshift distribution, a second result we found is that high- z x-ray-selected QSOs are highly clustered but, at low redshift, no clear correspondence is found between the positions of early-type galaxies and x-rays sources in the WHDF.

In the last section of chapter 4, the incidences of Galactic stellar contamination and of EROS in our samples were assessed. It was found that stars constitute a negligible

fraction of our point-like sources and do not compromise our major analyses of extragalactic objects. EROS were also found to have only an anecdotal presence in our catalogues, therefore suggesting that they are essentially unrelated to AGN and also generally not powerful x-ray emitters. Finally, the identification of the optical counterpart of the ULX GSGP4CH043 was reported. This source is apparently embedded amidst HII regions in the arms of the face-on spiral galaxy APMUKS(BJ) B005520.08-274536.9, but optical spectroscopy reveals a narrow-line emission object at $z = 0.368$, which implies that the ULX is a background source.

6.4 Evolution of Early-type Galaxies

In chapter 5, the evolutionary properties of a colour-selected sample of early-type galaxies in the direction of the WHDF were investigated. Two primary goals drove this study. First, the most popular scenarios of galaxy formation, monolithic and hierarchical, make very distinct predictions on how the stellar content of the present universe was assembled over time and the evolution of the spheroid-dominated galaxies offers an essential discriminant. Secondly, it was found in chapter 4 that x-ray galaxies that host an AGN span intermediate colours which, on basis to our evolutionary models, corresponded to very low-redshift elliptical ($z \lesssim 0.2$) or intermediate-redshift spiral galaxies ($z \lesssim 1$). By testing the accuracy of the models of the evolutionary properties of the early-type population it was intended that a better characterisation of the x-ray galaxies would emerge.

The analysis yielded that the colours of the selected red galaxies are excessively blue to accommodate comfortably simple models of a monolithic collapse at high-redshift and passive evolution thereafter. No clear cause could be identified, although several were discussed: fast evolution in the rest B -band luminosity, large scatter of their UV SEDs, contamination from later-type galaxies sharing the same colour-colour space or, even, that they represent post-starburst galaxies. It was also seen that their colour-absolute magnitude relation is very loosely constrained, suggesting that there is significant low-redshift star formation in our samples. Although colour-magnitude relations for early-type galaxies in low-density environments (such as our sample, chosen along an average line-of-sight) have not been explored as thoroughly as in clusters, the existing results agree with ours (e.g. Schade et al. 1999; Larson et al. 1980). Altogether, the large scatter of photometric measurables imply divergent histories and indicate that early-type galaxies are, in fact, a rather heterogeneous population. The observations would be better understood under a hierarchical workframe, where early-type galaxies in low-density environments are able to incorporate stars formed at low redshifts (e.g. Cole et al. 2000).

After studying the evolutionary models of early-type galaxies, still no conclusive statement regarding which galaxy types do preferentially host AGN could be made

from the position of x-ray galaxies in colour-colour diagrams. According to the models, x-ray galaxies have generally too blue a $B - R$ colour for their redshift to be early-type galaxies; but chapter 5 proved that this behaviour, common amongst many $B - R$ -selected red galaxies, is ill-accounted for. In the case of x-ray galaxies, excess blue emission might as well be produced by nuclear activity. Hence, the proposition that many AGN in our samples are hosted by early-type galaxies at intermediate redshifts seemed, after all, more plausible than the models would initially suggest. On the other hand, they could as plausibly be later-type galaxies, for lenticulars and Sab spirals have very similar evolutionary tracks and, moreover, the data on E/SO's favoured a larger region of overlap between early- and late-type galaxies in colour-colour diagrams. If that were the case, BRI colours would prove inadequate to disentangle the degeneracy. This confusion could be made even more severe if the AGN, many being obscured, radiated strongly at long wavelengths. Given that our disorientation arises from the colours being intermediate between those of early- and late-type galaxies, this could be reflecting that, whatever the host, it is likely to possess a bulge of some sort. Inspection of the optical images of appendix A seems to confirm that this is indeed the case and few galaxies appear clearly without a bulge.

6.5 Future Prospects

Undoubtedly, the best news for the short term is that Chandra and XMM-Newton are performing very well and returning a wealth of quality data. Soon, the answers to the problems addressed in this thesis will be solidly established and, surely enough, other exciting matters will bother extragalactic x-ray astronomers. These are better days!

Amongst the most exciting projects for the study of the XRB in the forthcoming months are deep wide-angle surveys compiled from public archival data such as CHAMP and XMM-SSC-XID. These are able to overcome the effects of small-scale clustering due to cosmic variance introduced by the small field-of-view of modern x-ray detectors and will measure the source number counts and the x-ray luminosity function with greater accuracy.

An outstanding issue that needs to be understood is the relationship between the gas and dust found in AGN. This is important to conclusively test the predictions of obscured AGN models based on unification schemes that posit orientation and intrinsic luminosity as the two primary parameters governing the multiwavelength properties of AGN. In this regard we have proposed that luminous absorbed AGN show broad lines more often than not. This hypothesis should be tested by obtaining column density distributions from x-ray spectra of a sample of high-redshift quasars or, alternatively, from the comparison of their extreme ultraviolet and x-ray colours. Also, from our samples we have identified a type II QSO candidate and

we propose to undertake infrared spectroscopy to confirm its status.

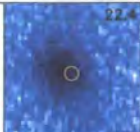
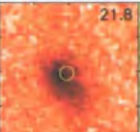
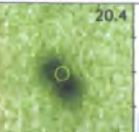
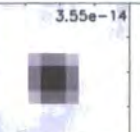
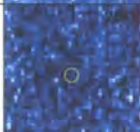
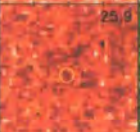
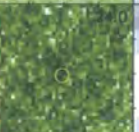
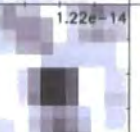
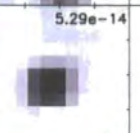
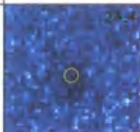
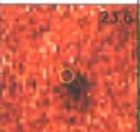

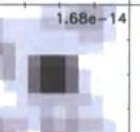

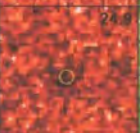



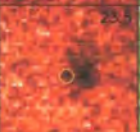

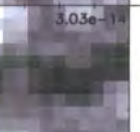




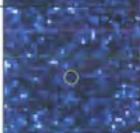


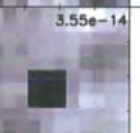
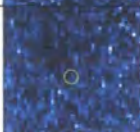
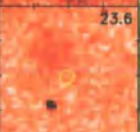


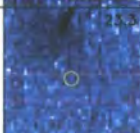
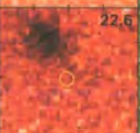


More generally, models of obscured AGN require higher levels of spectroscopic completion. Over 50% of the x-ray sources in our samples remain unidentified and an accurate determination of the relative fractions of obscured to unobscured AGN can not emerge unless sustained impulse to the spectroscopic follow-up programs is provided. We have also suggested to perform long-slit spectroscopy on selected x-ray bright absorption-line galaxies in search of emission lines that could denote an underlying hidden AGN and confirm that, at bright x-ray levels, NELGs and ALGs belong to the same population. But, to fully grasp the AGN phenomenon, it is vital that these efforts to characterise the x-ray sources in the optical are accompanied by similar undertakings at longer wavelengths, where obscured AGN models of the XRB make crucial predictions.

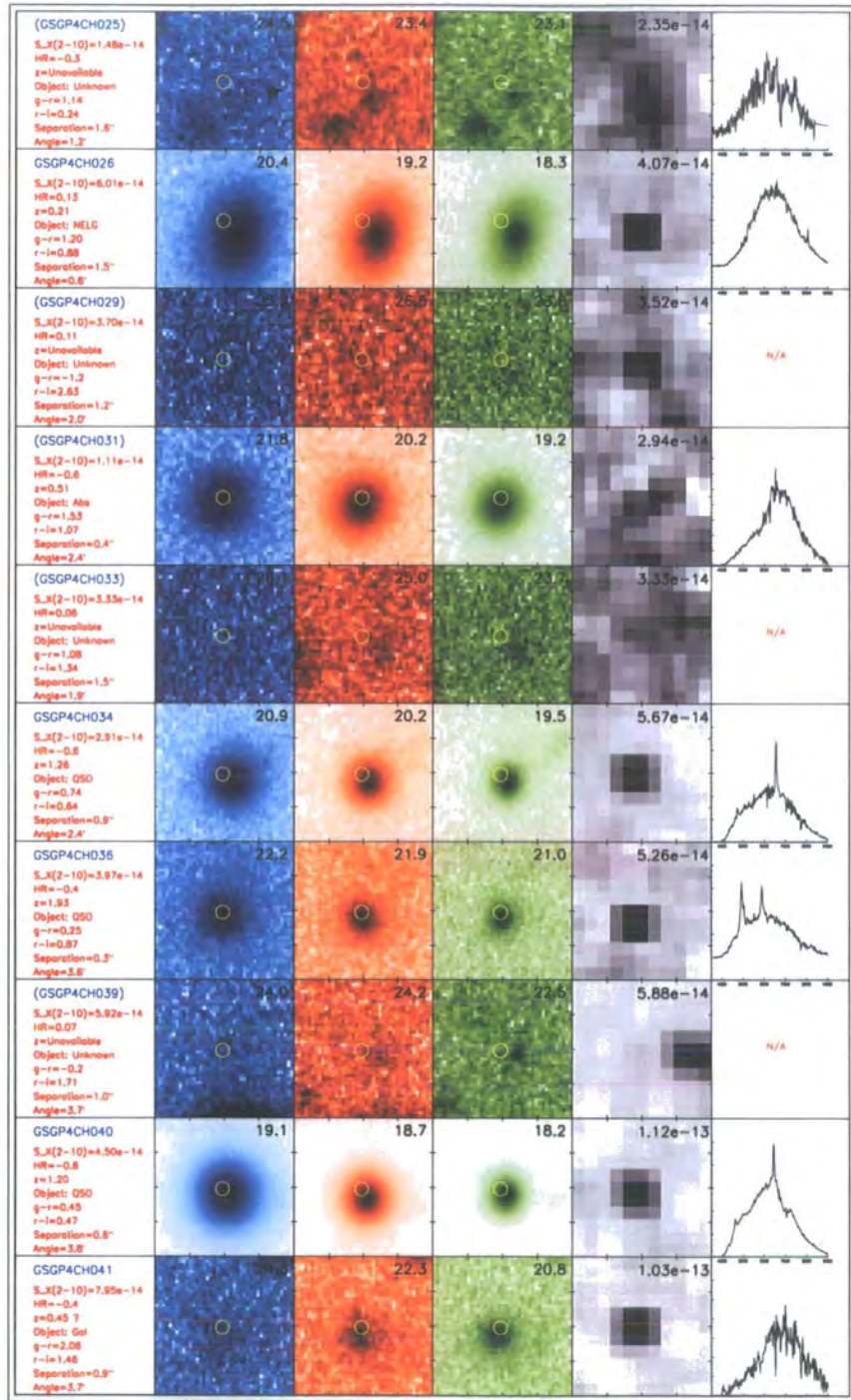
APPENDIX A

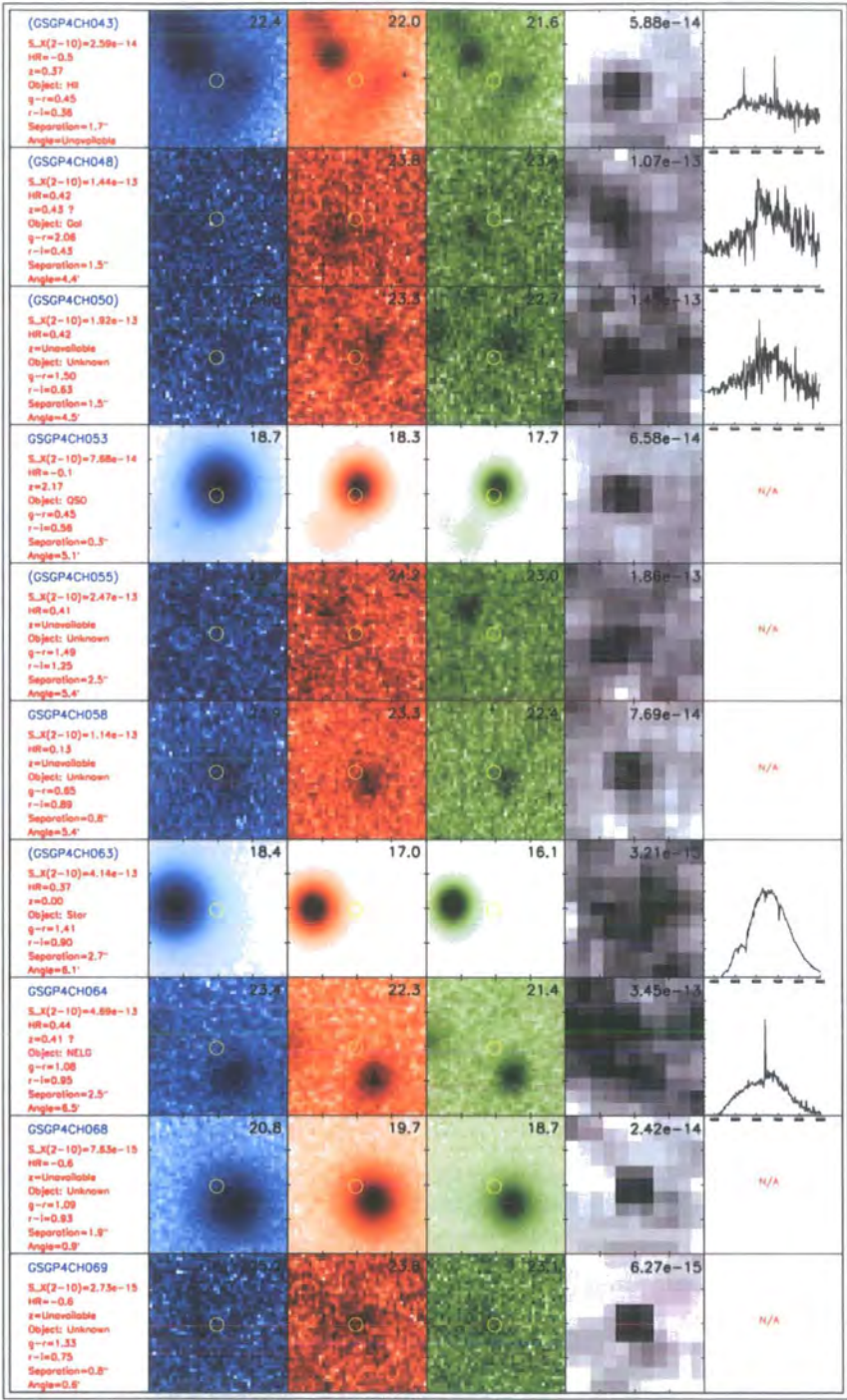
Spectro-photometric albums

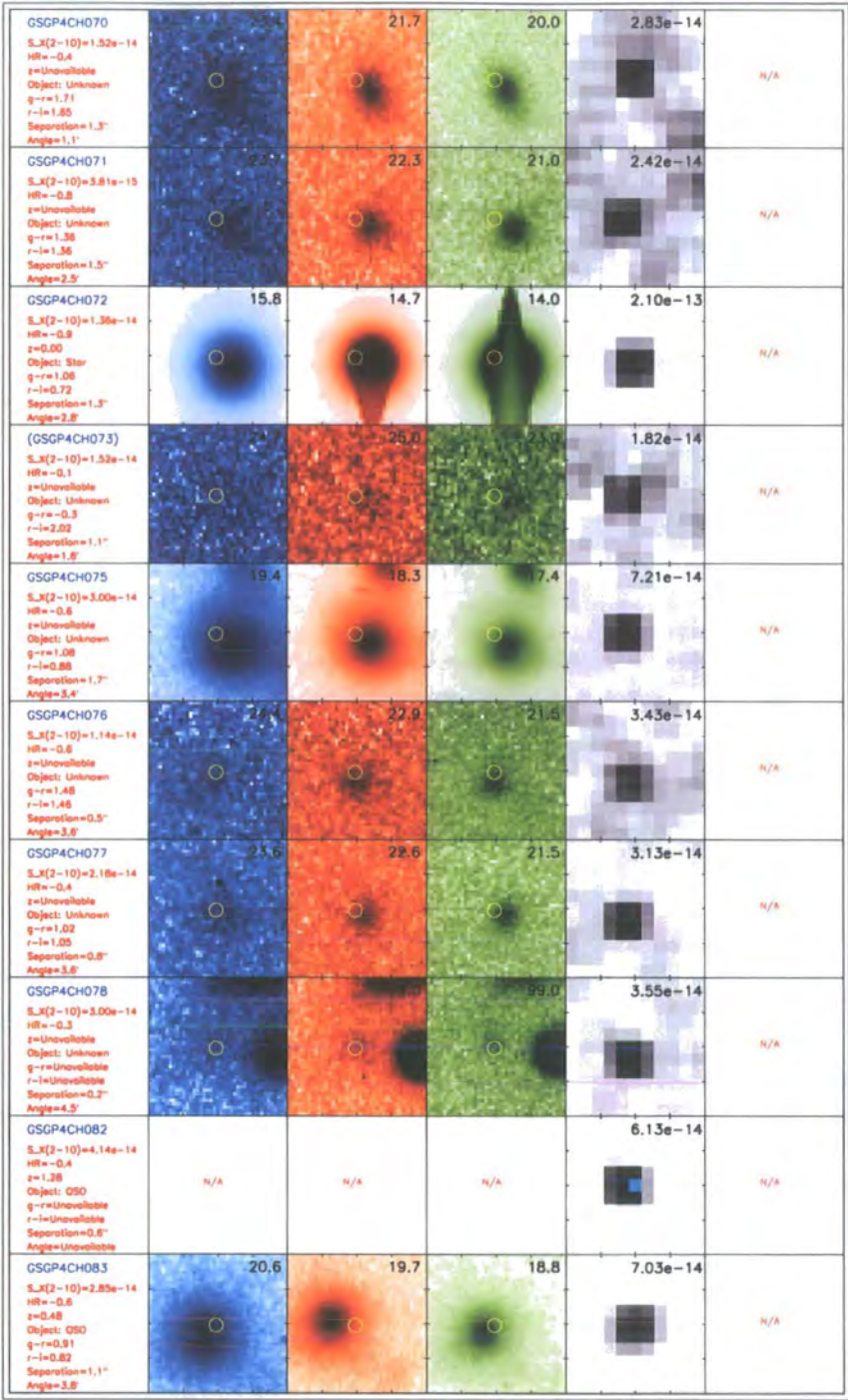
This appendix presents the spectro-photometric albums for the x-ray sources in the GSGP4 and WHDF fields. Each row of boxes corresponds to a different source. In the first box we list some characteristics of the object: x-ray flux in the hard (2–10 keV) band; hardness ratio; redshift; type of source; colour indices ($g-r$ and $r-i$ in GSGP4; $B-R$, $R-I$, $R-Z$ in WHDF); positional offset between Chandra and optical images (only in GSGP4; in WHDF they are always $< 2''$); off-axis angle of the Chandra detection with respect to the aimpoint. Whenever the name of the source is enclosed in parenthesis, the source has been detected with $S/N < 3$ in the x-ray images. The following 3 (4 in the WHDF) boxes are the optical images for the source in the g , r and i (B , R , I , Z) bands; they are labelled with the corresponding magnitude. The second-last box is the Chandra image, labelled with the flux in the 0.5–10 keV band. Finally, if available, the last box shows the optical spectrum.

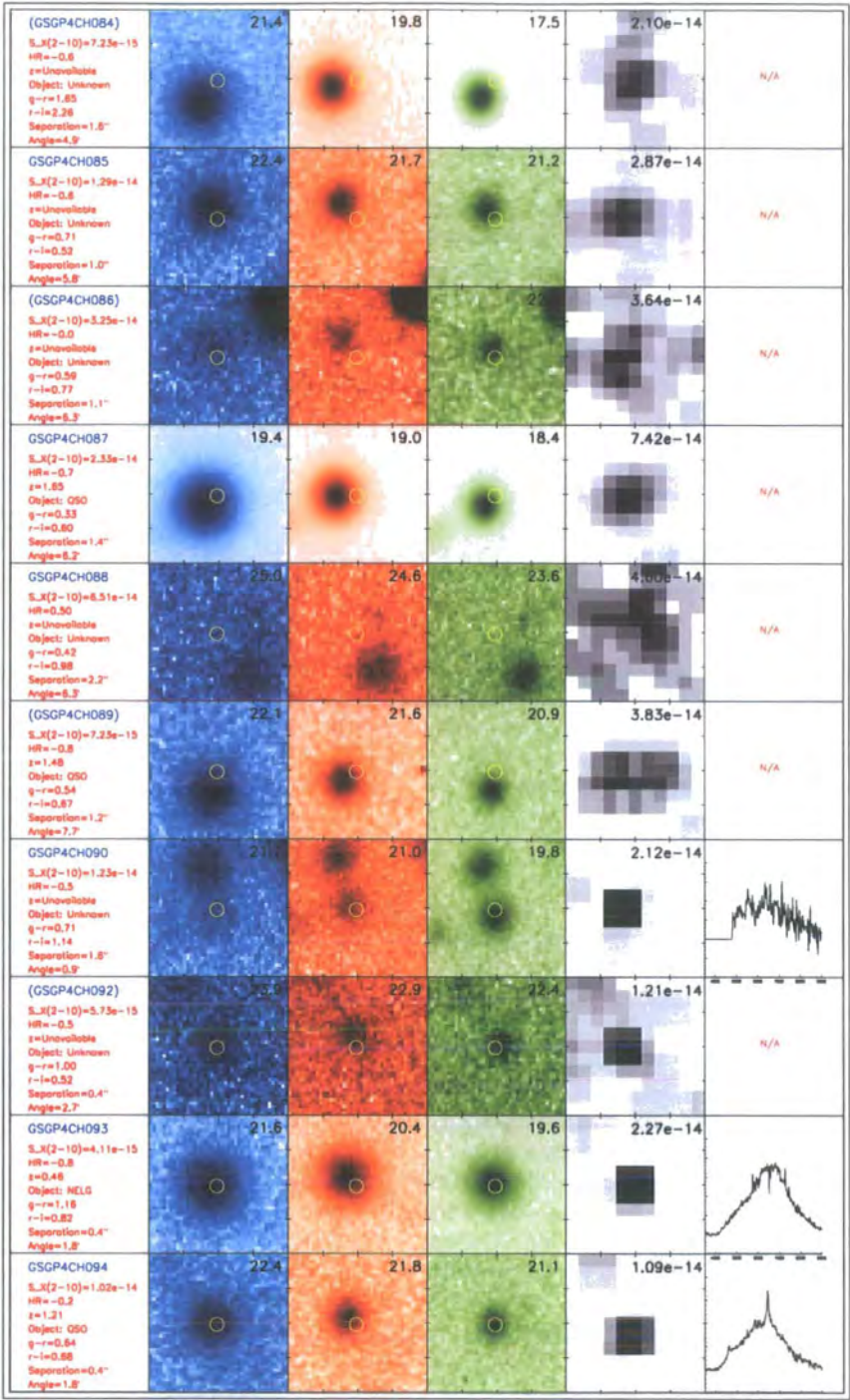
GSGP4

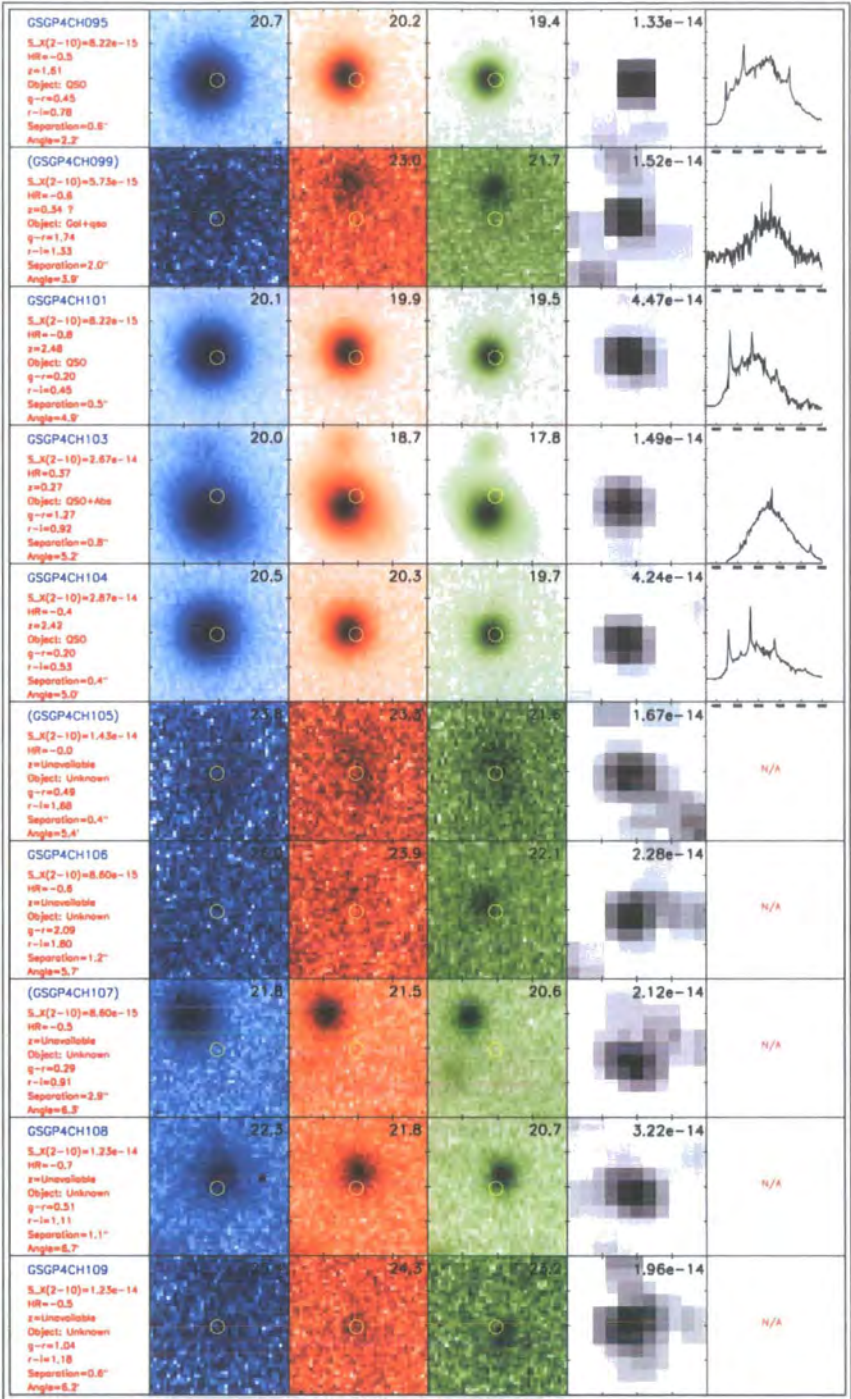
<p>GSGP4CH001</p> <p>$S_X(2-10)=1.86e-14$ $HR=-0.6$ $z=Unvaluable$ Object: Unknown $g-r=0.87$ $r-i=1.35$ Separation=$0.4''$ Angle=$0.9''$</p>					N/A
<p>(GSGP4CH002)</p> <p>$S_X(2-10)=2.88e-15$ $HR=-0.7$ $z=Unvaluable$ Object: Unknown $g-r=0.19$ $r-i=1.85$ Separation=$0.4''$ Angle=$1.8''$</p>					N/A
<p>GSGP4CH003</p> <p>$S_X(2-10)=1.44e-14$ $HR=-0.7$ $z=1.56$ Object: QSO $g-r=Unvaluable$ $r-i=Unvaluable$ Separation=$1.2''$ Angle=$Unvaluable$</p>	N/A	N/A	N/A		N/A
<p>(GSGP4CH005)</p> <p>$S_X(2-10)=1.44e-14$ $HR=-0.0$ $z=Unvaluable$ Object: Unknown $g-r=0.76$ $r-i=0.85$ Separation=$0.7''$ Angle=$4.3''$</p>					N/A
<p>(GSGP4CH011)</p> <p>$S_X(2-10)=2.29e-14$ $HR=0.00$ $z=Unvaluable$ Object: Unknown $g-r=2.39$ $r-i=2.54$ Separation=$0.3''$ Angle=$1.0''$</p>					N/A
<p>(GSGP4CH012)</p> <p>$S_X(2-10)=3.43e-14$ $HR=0.20$ $z=Unvaluable$ Object: Unknown $g-r=1.00$ $r-i=1.08$ Separation=$1.2''$ Angle=$2.0''$</p>					N/A
<p>GSGP4CH014</p> <p>$S_X(2-10)=2.29e-14$ $HR=-0.2$ $z=0.21$ Object: Gal $g-r=1.42$ $r-i=1.18$ Separation=$1.0''$ Angle=$2.0''$</p>					N/A
<p>GSGP4CH015</p> <p>$S_X(2-10)=2.46e-14$ $HR=-0.4$ $z=Unvaluable$ Object: Unknown $g-r=1.68$ $r-i=1.59$ Separation=$0.2''$ Angle=$3.0''$</p>					N/A
<p>(GSGP4CH021)</p> <p>$S_X(2-10)=4.12e-13$ $HR=0.45$ $z=Unvaluable$ Object: Unknown $g-r=1.07$ $r-i=1.03$ Separation=$2.0''$ Angle=$6.5''$</p>					N/A
<p>(GSGP4CH024)</p> <p>$S_X(2-10)=2.93e-13$ $HR=0.15$ $z=Unvaluable$ Object: Unknown $g-r=0.69$ $r-i=0.88$ Separation=$3.4''$ Angle=$6.5''$</p>					N/A

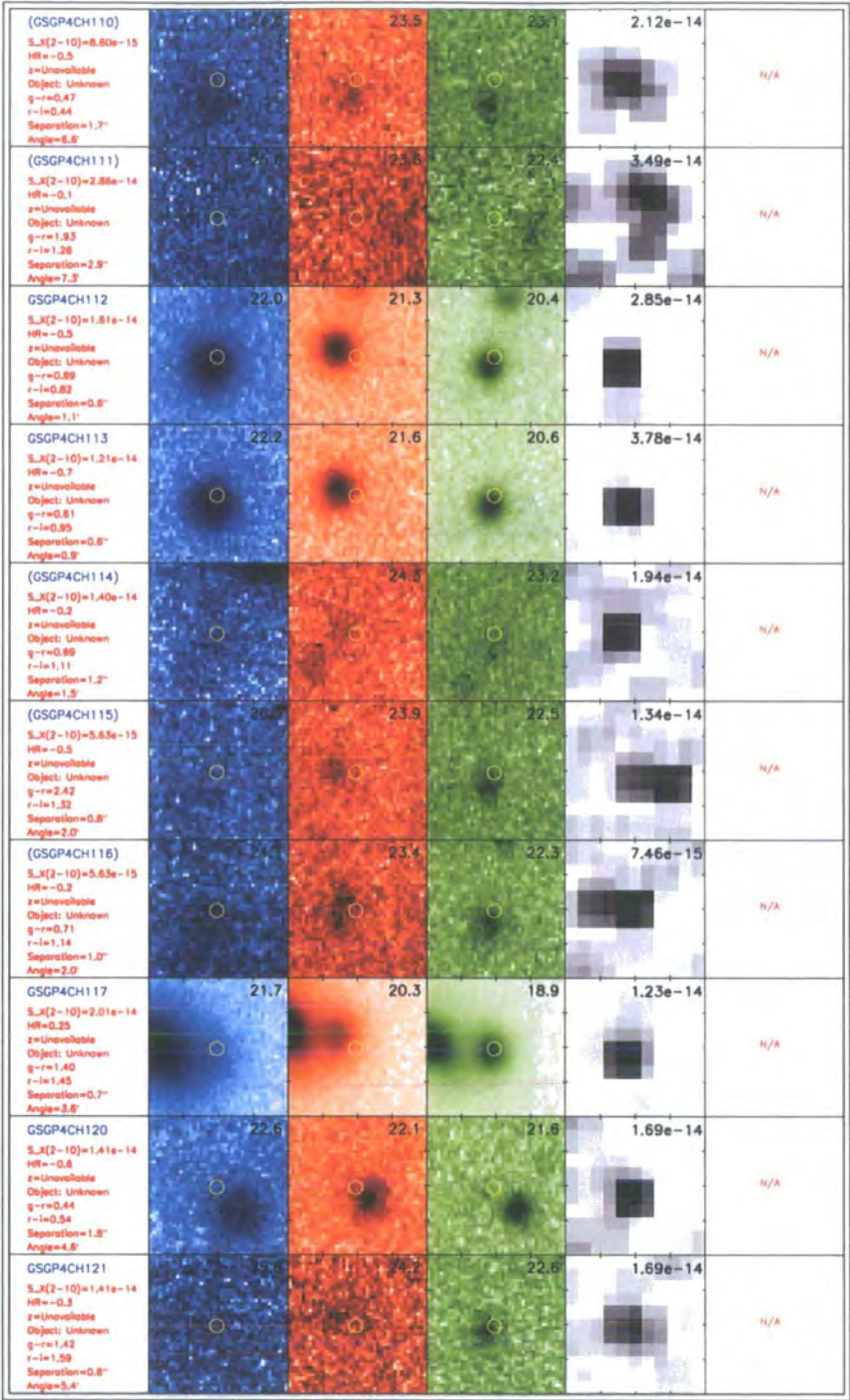


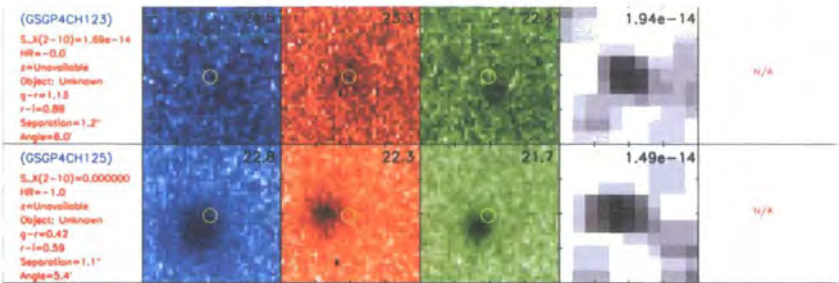




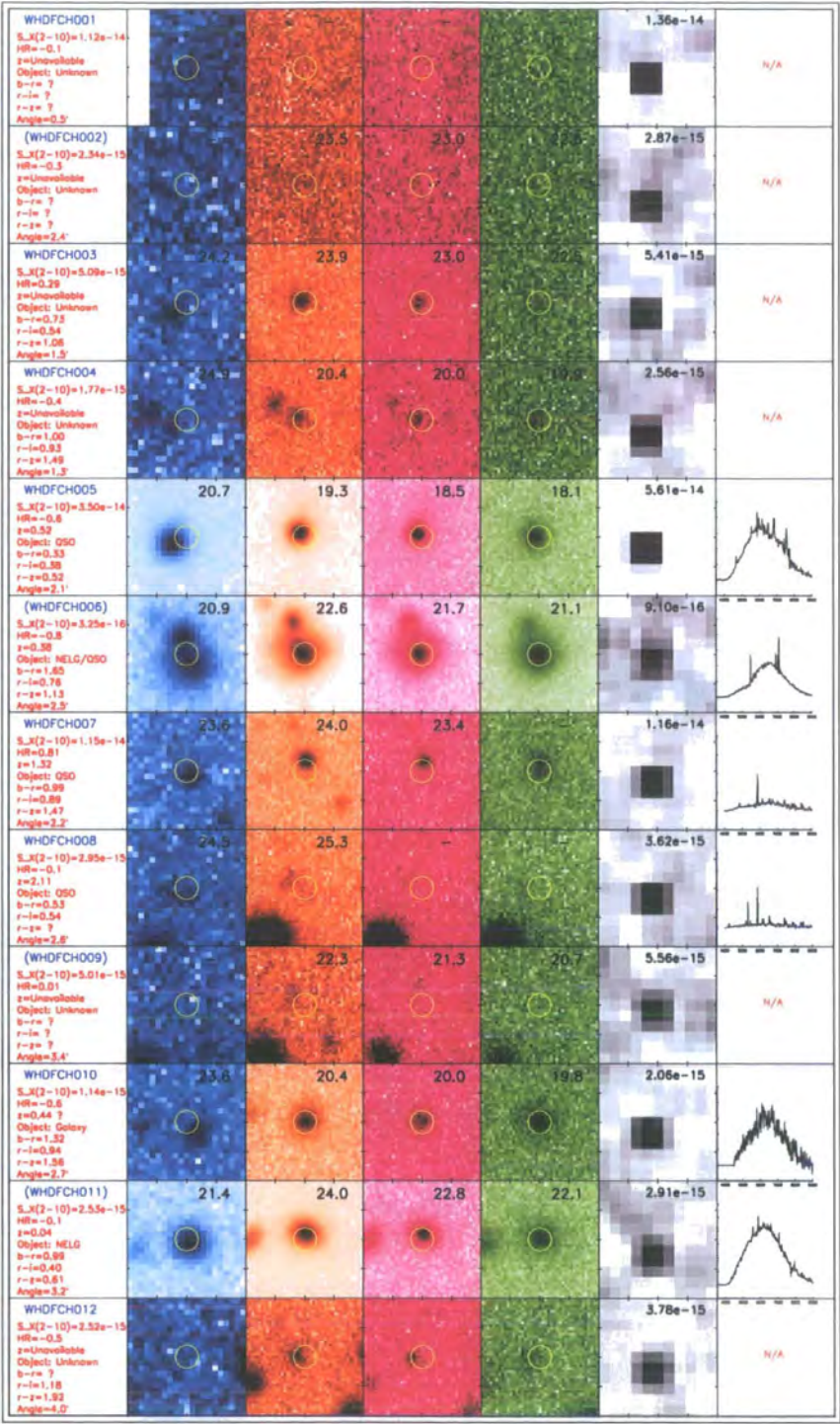


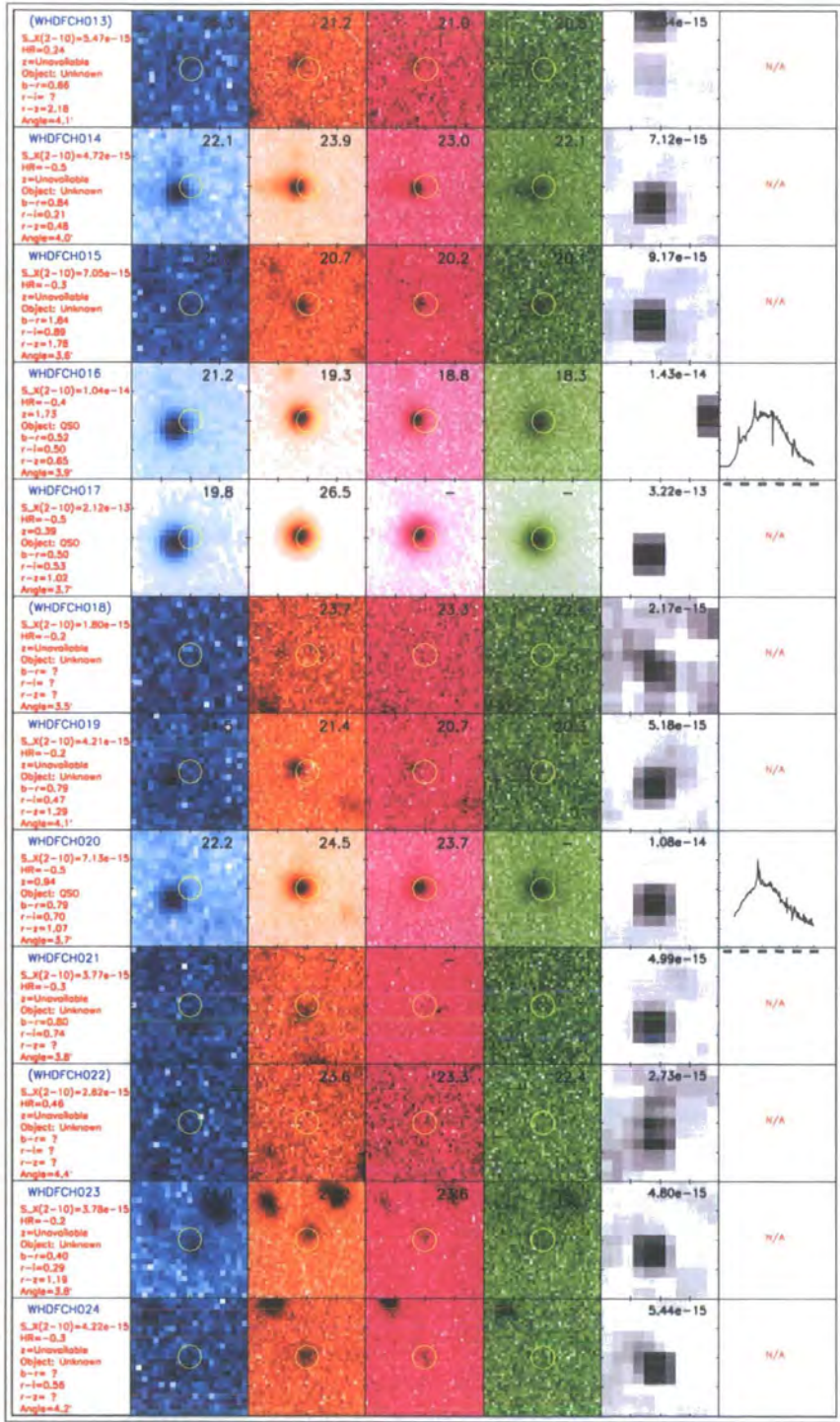




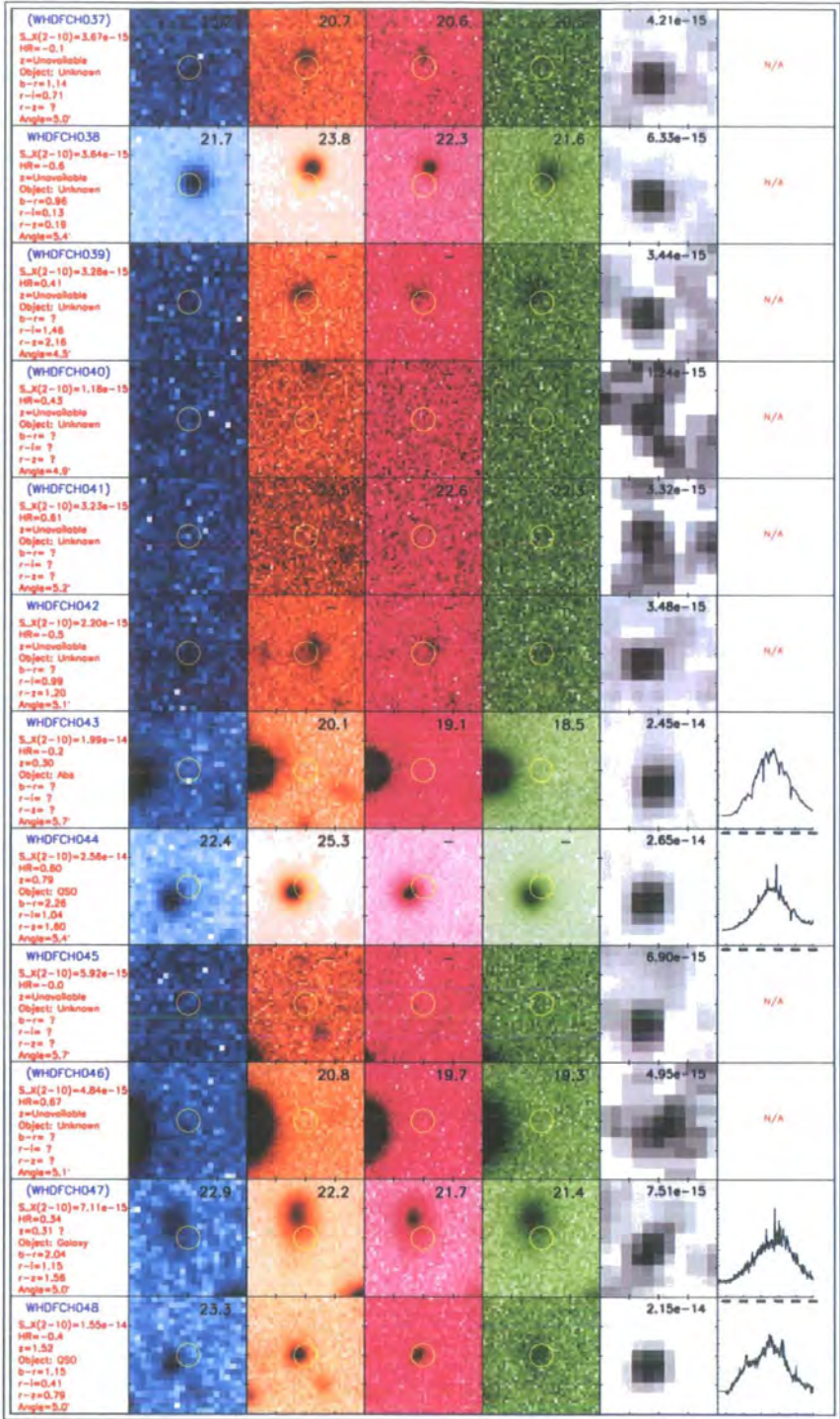


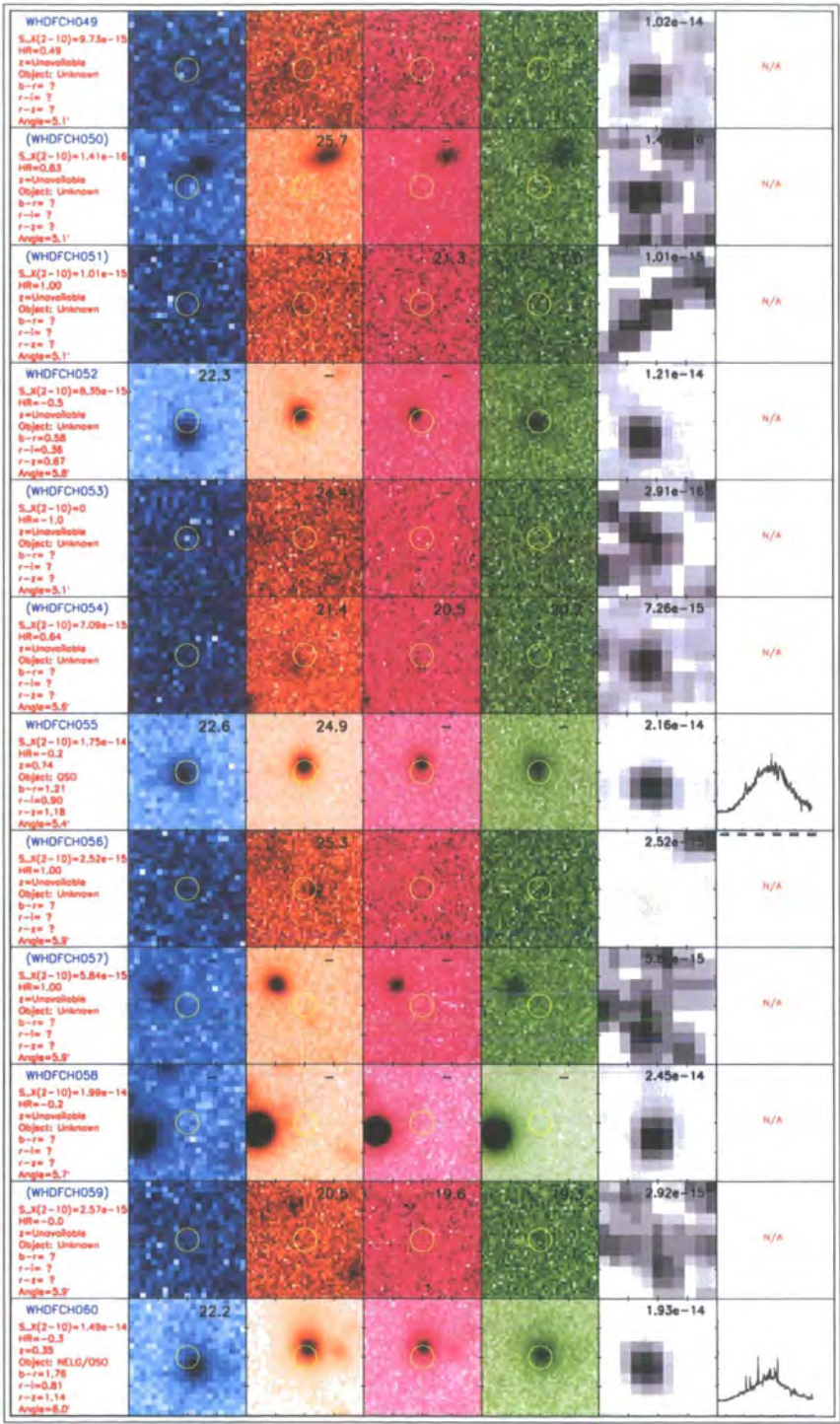
WHDF

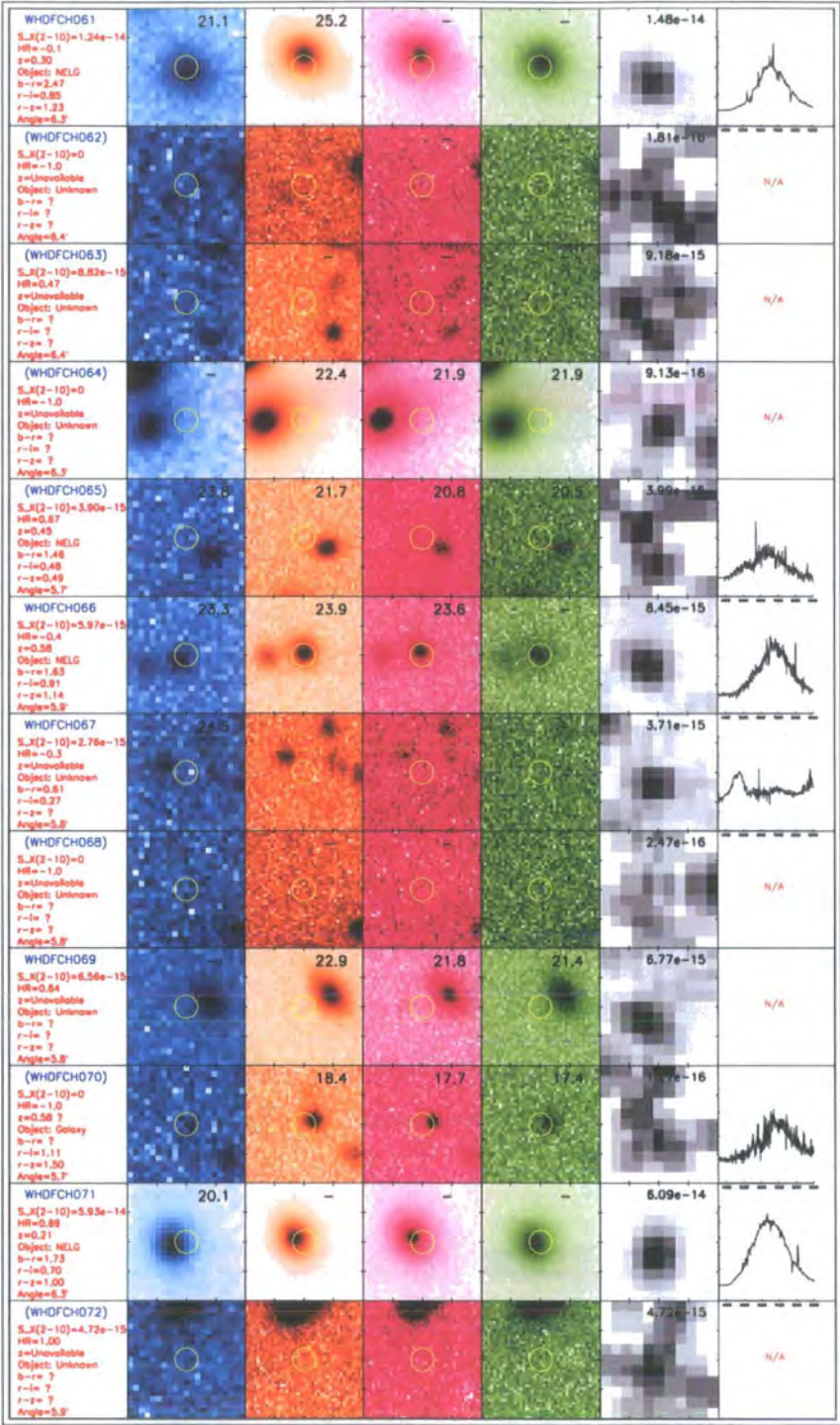


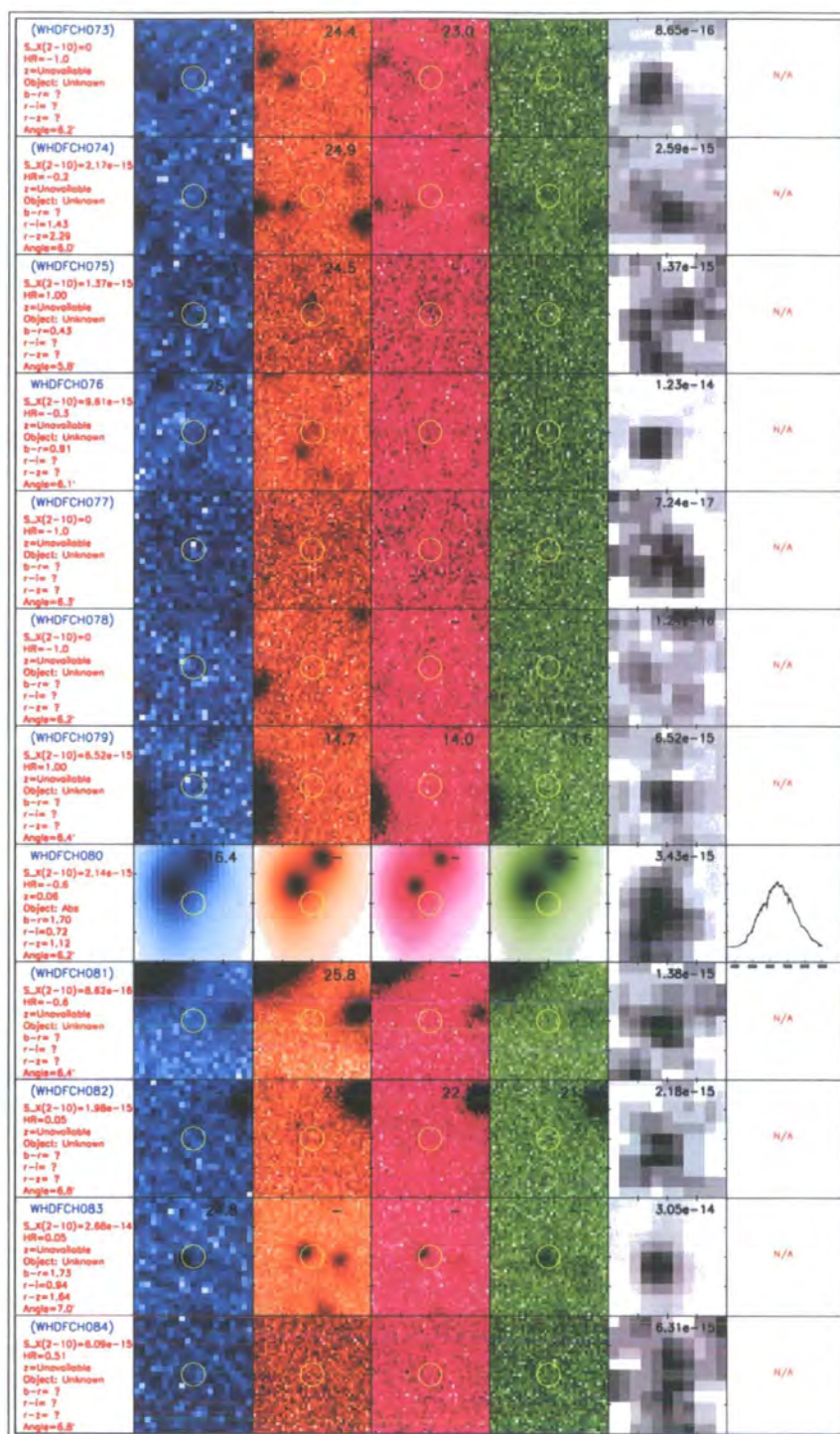


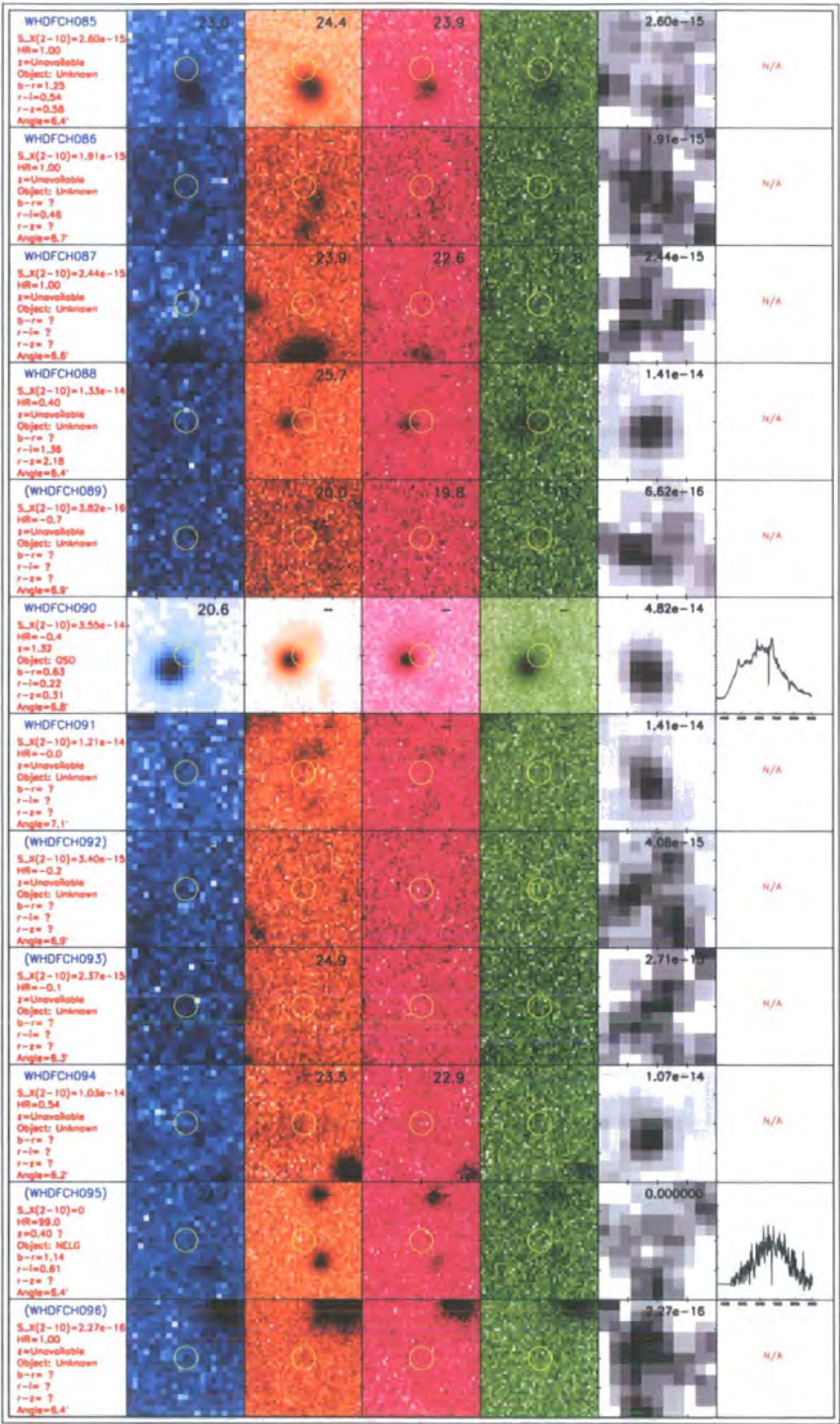




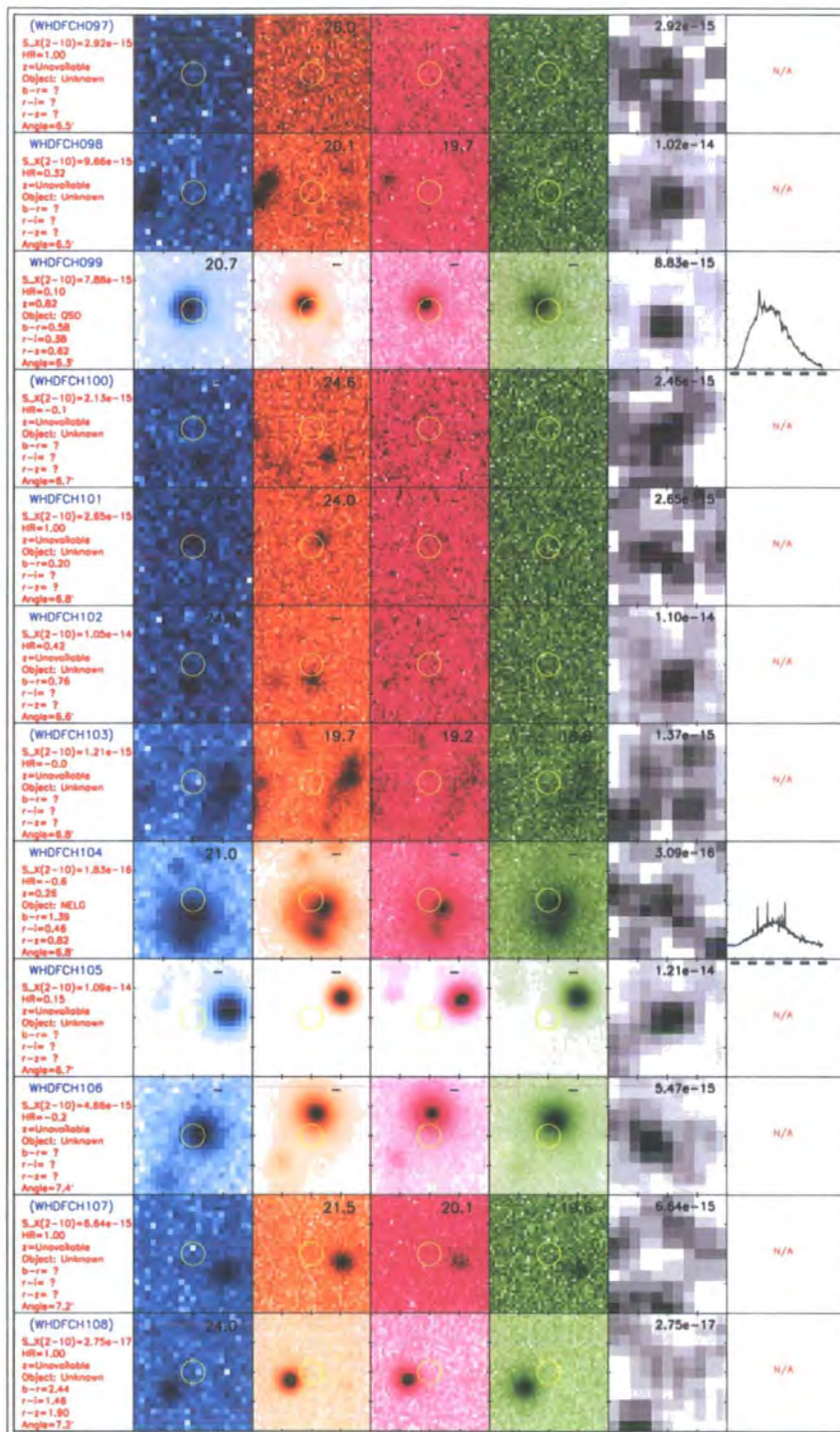


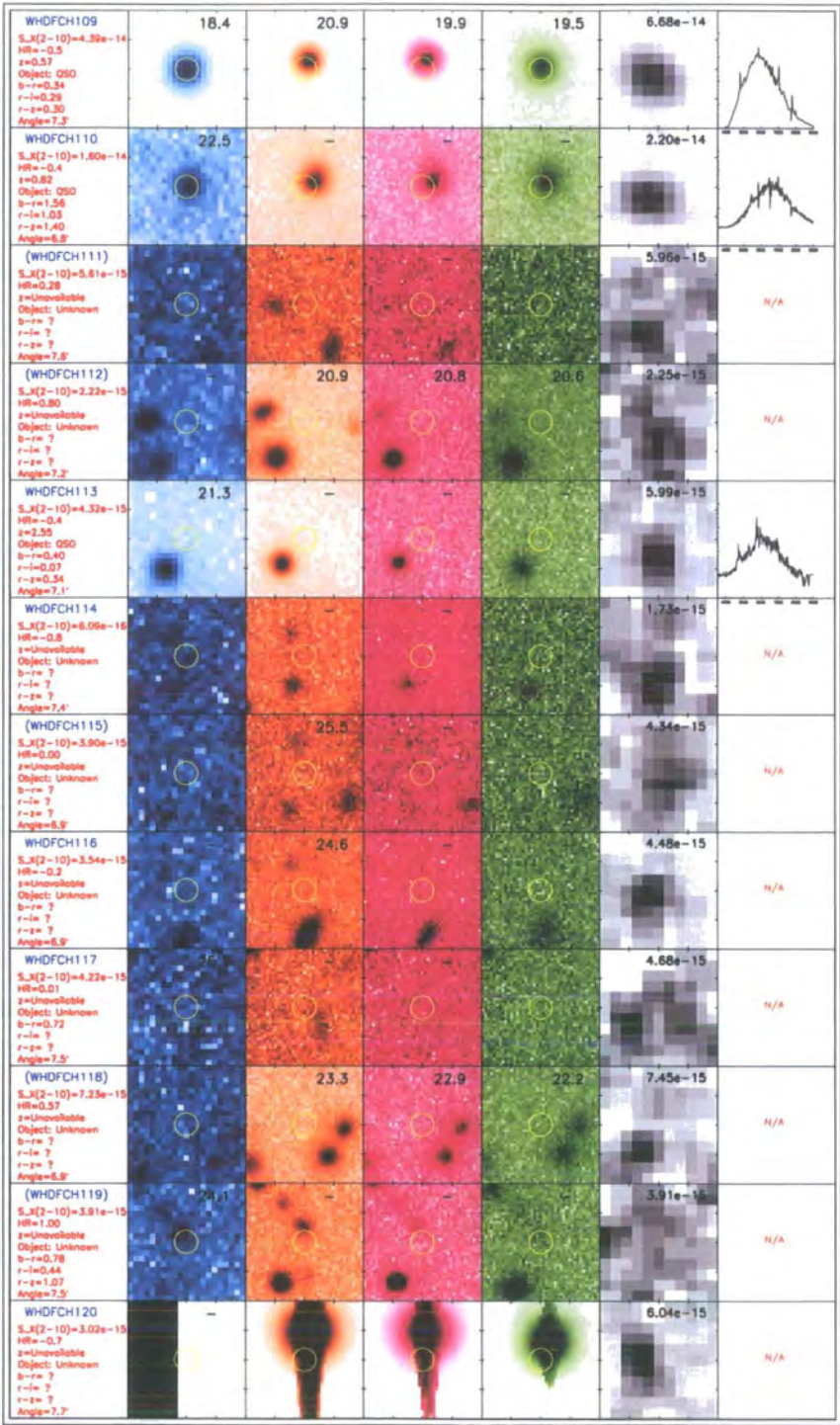

















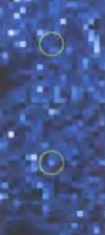










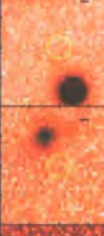




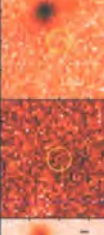



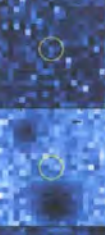
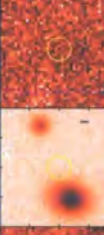



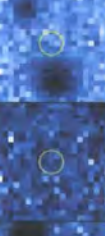



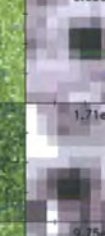

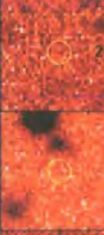



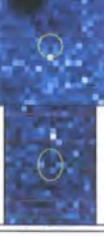




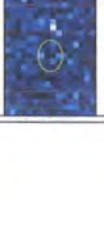






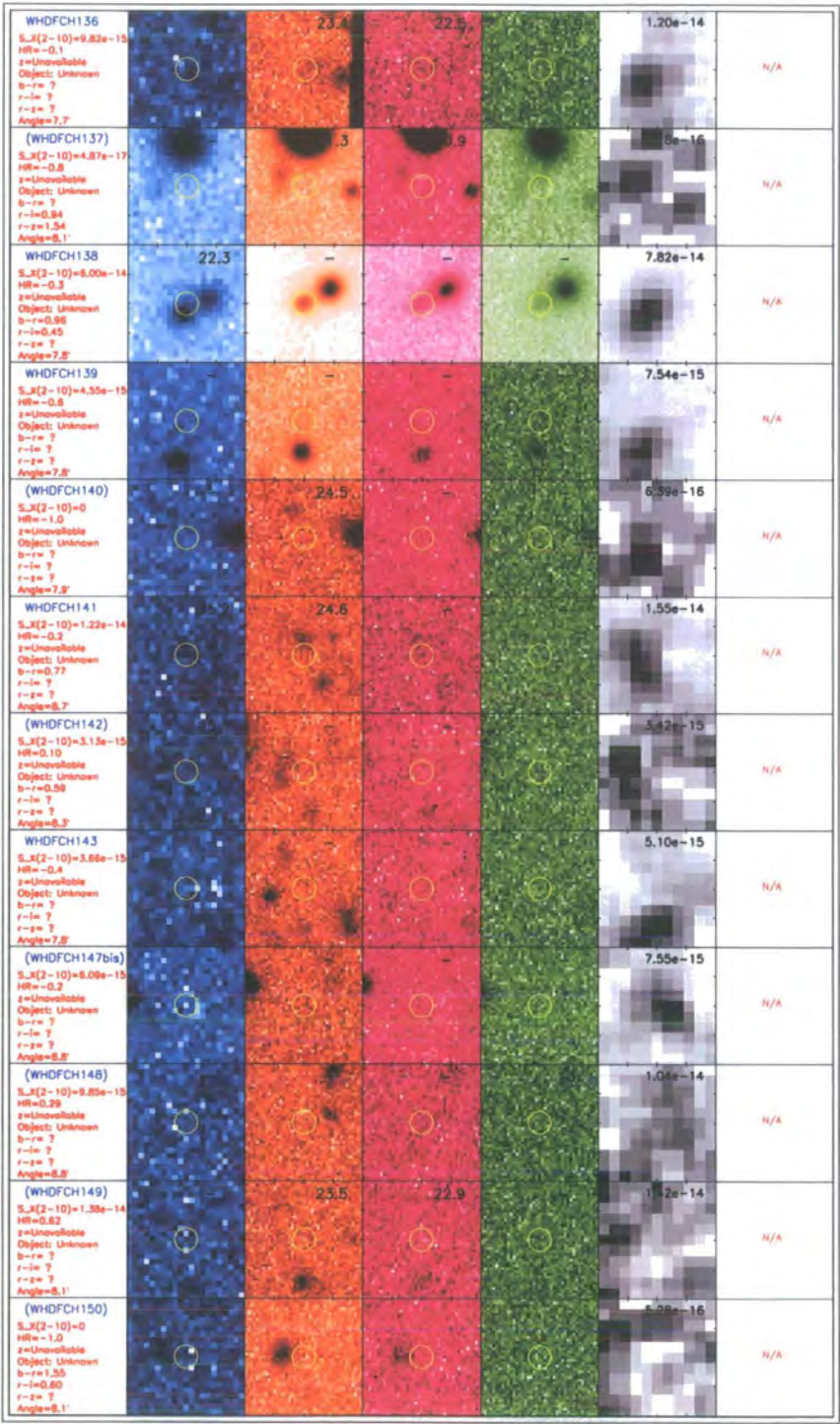


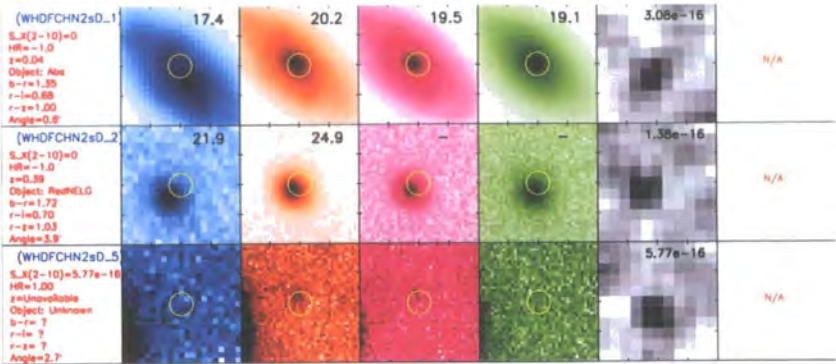
APPENDIX A. SPECTRO-PHOTOMETRIC ALBUMS





(WHDFCH121) S_x(2-10)=2.61e-15 HR=0.10 z=Unavailable Object: Unknown b-r= ? r-l= ? r-g= ? Angle=7.1'						2.85e-15 N/A
(WHDFCH122) S_x(2-10)=4.32e-15 HR=-0.4 z=Unavailable Object: Unknown b-r= ? r-l= ? r-g= ? Angle=7.8'						3.49e-15 N/A
(WHDFCH123) S_x(2-10)=3.12e-15 HR=-0.1 z=Unavailable Object: Unknown b-r=0.77 r-l= ? r-g= ? Angle=7.7'						3.56e-15 N/A
(WHDFCH124) S_x(2-10)=0 HR=-1.0 z=Unavailable Object: Unknown b-r= ? r-l= ? r-g= ? Angle=7.5'						6.02e-16 N/A
(WHDFCH125) S_x(2-10)=5.16e-15 HR=0.80 z=Unavailable Object: Unknown b-r= ? r-l= ? r-g= ? Angle=7.8'						5.22e-15 N/A
WHDFCH127 S_x(2-10)=7.28e-15 HR=0.01 z=Unavailable Object: Unknown b-r= ? r-l= ? r-g= ? Angle=7.8'						8.35e-15 N/A
(WHDFCH128) S_x(2-10)=4.90e-15 HR=-0.0 z=Unavailable Object: Unknown b-r= ? r-l= ? r-g= ? Angle=7.3'						5.56e-15 N/A
(WHDFCH129) S_x(2-10)=3.25e-15 HR=-0.1 z=Unavailable Object: Unknown b-r= ? r-l= ? r-g= ? Angle=7.3'						3.74e-15 N/A
WHDFCH130 S_x(2-10)=5.39e-15 HR=-0.3 z=Unavailable Object: Unknown b-r= ? r-l= ? r-g= ? Angle=7.8'						6.65e-15 N/A
(WHDFCH133) S_x(2-10)=0 HR=-1.0 z=Unavailable Object: Unknown b-r= ? r-l= ? r-g= ? Angle=7.5'						1.71e-16 N/A
WHDFCH134 S_x(2-10)=9.37e-15 HR=0.47 z=Unavailable Object: Unknown b-r= ? r-l= ? r-g= ? Angle=8.1'						9.75e-15 N/A
(WHDFCH135) S_x(2-10)=6.64e-15 HR=1.00 z=Unavailable Object: Unknown b-r= ? r-l= ? r-g= ? Angle=7.7'						6.64e-15 N/A





References

- Akiyama M., Ohta K., Yamada T., Kashikawa N., Yagi M., Kawasaki W., Sakano M., Tsuru T., Ueda Y., Takahashi T., Lehmann I., Hasinger G., Voges W., 2000, *ApJ*, 532, 700
- Alexander D. M., Bauer F. E., Brandt W. N., Schneider D. P., Hornschemeier A. E., Vignali C., et al., 2003, *AJ*, 126, 539
- Alexander D. M., Vignali C., Bauer F. E., Brandt W. N., Hornschemeier A. E., Garmire G. P., Schneider D. P., 2002, *AJ*, 123, 1149
- Almaini O., Boyle B. J., Griffiths R. E., Shanks T., Stewart G. C., Georgantopoulos I., 1995, *MNRAS*, 277, L31
- Almaini O., Shanks T., Boyle B. J., Griffiths R. E., Roche N., Stewart G. C., Georgantopoulos I., 1996, *MNRAS*, 282, 295
- Almaini O., Shanks T., Griffiths R. E., Boyle B. J., Roche N., Georgantopoulos I., Stewart G. C., 1997, *MNRAS*, 291, 372
- Antonucci R., 1993, *ARA&A*, 31, 473
- Antonucci R. R. J., Miller J. S., 1985, *ApJ*, 297, 621
- Aragon-Salamanca A., Baugh C. M., Kauffmann G., 1998, *MNRAS*, 297, 427
- Arnouts S., D'Odorico S., Cristiani S., Zaggia S., Fontana A., Giallongo E., 1999, *A&A*, 341, 641
- Awaki H., 1991, *ISAS Res. Note*, 473, 77
- Awaki H., Koyama K., Inoue H., Halpern J. P., 1991, *PASJ*, 43, 195
- Baade W., 1944, *ApJ*, 100, 137
- Baldwin J. A., Phillips M. M., Terlevich R., 1981, *PASP*, 93, 5
- Barber C. R., Roberts T. P., Warwick R. S., 1996, *MNRAS*, 282, 157
- Barcons X., Carrera F. J., Ceballos M. T., 2003, *MNRAS*, 339, 757
- Barcons X., Fabian A. C., Rees M. J., 1991, *Nature*, 350, 685
- Barger A. J., Cowie L. L., Mushotzky R. F., Richards E. A., 2001, *AJ*, 121, 662
- Baugh C. M., Cole S., Frenk C., 1996, *MNRAS*, 283, 1361
- Baum W. A., 1959, *PASP*, 71, 106
- Baum W. A., 1962, in *IAU Symp. 15: Problems of Extra-Galactic Research Photoelectric Magnitudes and Red-Shifts*. pp 390–+

- Bell E. F., McIntosh D. H., Barden M., Wolf C., Caldwell J. A. R., Rix H., Beckwith S. V. W., et al., 2004, *ApJ*, 600, L11
- Bertin E., Arnouts S., 1996, *A&AS*, 117, 393
- Bertin E., Dennefeld M., 1997, *A&A*, 317, 43
- Blanco P. R., Ward M. J., Wright G. S., 1990, *MNRAS*, 242, 4P
- Boella G., Butler R. C., Perola G. C., Piro L., Scarsi L., Bleeker J. A. M., 1997, *A&AS*, 122, 299
- Borges J. L., 1967, *The Book of Imaginary Beings*
- Bower R. G., Balogh M. L., 2004, in *Clusters of Galaxies: Probes of Cosmological Structure and Galaxy Evolution The Difference Between Clusters and Groups: A Journey from Cluster Cores to Their Outskirts and Beyond*. pp 326–+
- Bower R. G., Lucey J. R., Ellis R. S., 1992a, *MNRAS*, 254, 601
- Bower R. G., Lucey J. R., Ellis R. S., 1992b, *MNRAS*, 254, 589
- Boyle B. J., Fong R., Shanks T., Peterson B. A., 1990, *MNRAS*, 243, 1
- Boyle B. J., Jones L. R., Shanks T., 1991, *MNRAS*, 251, 482
- Boyle B. J., McMahon R. G., Wilkes B. J., Elvis M., 1995, *MNRAS*, 272, 462
- Boyle B. J., Shanks T., Georgantopoulos I., Stewart G. C., Griffiths R. E., 1994, *MNRAS*, 271, 639
- Brandt W. N., Alexander D. M., Hornschemeier A. E., Garmire G. P., Schneider D. P., Barger A. J., et al., 2001, *AJ*, 122, 2810
- Brandt W. N., Hornschemeier A. E., Alexander D. M., Garmire G. P., Schneider D. P., Broos P. S., Townsley L. K., Bautz M. W., Feigelson E. D., Griffiths R. E., 2001, *AJ*, in press
- Brandt W. N., Hornschemeier A. E., Schneider D. P., Garmire G. P., Chartas G., Hill G. J., et al., 2000, *AJ*, 119, 2349
- Brown M. J. I., Boyle B. J., Webster R. L., 2001, *AJ*, 122, 26
- Bruzual G., Charlot S., 2003, *MNRAS*, 344, 1000
- Burke B. E. M. R. W. H. D. C. B. M. W. D. J. P. R. G. R., Daniels P. J., 1991, *IEEE Transactions on Electron Devices*, 38, 1069
- Burnham R., 1978, *Burnham's celestial handbook. an observers guide to the universe beyond the solar system*. New York: Dover, 1978, Rev.ed.
- Butcher H., Oemler A., 1984, *ApJ*, 285, 426

- Cagnoni I., della Ceca R., Maccacaro T., 1998, *ApJ*, 493, 54
- Calderwood T., Dobrzycki A., Jessop H., Harris D. E., 2001, in ASP Conf. Ser. 238: Astronomical Data Analysis Software and Systems X The Sliding-Cell Detection Program for Chandra X-ray Data. pp 443–+
- Campana S., Moretti A., Lazzati D., Tagliaferri G., 2001, *ApJ*, 560, L19
- Chen L. W., Fabian A. C., Gendreau K. G., 1997, *MNRAS*, 285, 449
- Chokshi A., Turner E. L., 1992, *MNRAS*, 259, 421
- Cimatti A., Mignoli M., Daddi E., Pozzetti L., Fontana A., Saracco P., Poli F., Renzini A., et al., 2002, *A&A*, 392, 395
- Code A. D., ed. 1972, Scientific results from the orbiting astronomical observatory (OAO-2)
- Code A. D., Welch G. A., 1982, *ApJ*, 256, 1
- Cole S., Lacey C. G., Baugh C. M., Frenk C. S., 2000, *MNRAS*, 319, 168
- Colless M., Dalton G., Maddox S., Sutherland W., Norberg P., Cole S., Bland-Hawthorn J., Bridges T., Cannon R., Collins C., Couch W., Cross N., et al., 2001, *MNRAS*, 328, 1039
- Comastri A., Setti G., Zamorani G., Hasinger G., 1995, *A&A*, 296, 1
- Compton 1923, *Phil. Mug.*, 45, 1121
- Cowie L. L., Garmire G. P., Bautz M. W., Barger A. J., Brandt W. N., Hornschemeier A. E., 2002, *ApJ*, 566, L5
- Cowsik R., Kobetich E. J., 1972, *ApJ*, 177, 585
- Crawford C. S., Fabian A. C., Gandhi P., Wilman R. J., Johnstone R. M., 2001, *MNRAS*, 324, 427
- Croom S. M., Shanks T., Boyle B. J., Smith R. J., Miller L., Loaring N. S., Hoyle F., 2001, *MNRAS*, 325, 483
- Croom S. M., Smith R. J., Boyle B. J., Shanks T., Loaring N. S., Miller L., Lewis I. J., 2001, *MNRAS*, 322, L29
- Croom S. M., Warren S. J., Glazebrook K., 2001, *MNRAS*, 328, 150
- David L. P., Jones C., Forman W., 1992, *ApJ*, 388, 82
- de Vaucouleurs G., 1961, *ApJS*, 5, 233
- de Zotti G., Boldt E. A., Marshall F. E., Swank J. H., Szymkowiak A. E., Cavaliere A., Danese L., Franceschini A., 1982, *ApJ*, 253, 47

- della Ceca R., Braito V., Cagnoni I., Maccacaro T., 2001, *Memorie della Societa Astronomica Italiana*, 72, 841
- Dopita M., 1997, *Publications of the Astronomical Society of Australia*, 14, 230
- Dressler A., Thompson I. B., Shethman S. A., 1985, *ApJ*, 288, 481
- Eddington A. S., 1913, *MNRAS*, 73, 359
- Edelson R. A., Malkan M. A., Rieke G. H., 1987, *ApJ*, 321, 233
- Edge A. C., Stewart G. C., Fabian A. C., Arnaud K. A., 1990, *MNRAS*, 245, 559
- Eggen O. J., Lynden-Bell D., Sandage A. R., 1962, *ApJ*, 136, 748
- Eisenstein D. J., Annis J., Gunn J. E., Szalay A. S., Connolly A. J., Nichol R. C., Bahcall N. A., et al., 2001, *AJ*, 122, 2267
- Elvis M., Wilkes B. J., McDowell J. C., Green R. F., Bechtold J., Willner S. P., Oey M. S., Polomski E., Cutri R., 1994, *ApJS*, 95, 1
- Fabbiano G., Kim D.-W., Trinchieri G., 1992, *ApJS*, 80, 531
- Fabbiano G., Trinchieri G., MacDonald A., 1984, *ApJ*, 284, 65
- Faber S. M., 1973, *ApJ*, 179, 731
- Fabian A. C., Barcons X., 1992, *ARA&A*, 30, 429
- Fabian A. C., Iwasawa K., 1999, *MNRAS*, 303, L34
- Fan X., Strauss M. A., Richards G. T., Newman J. A., Becker R. H., Schneider D. P., Gunn J. E., et al., 2001, *AJ*, 121, 31
- Ferrarese L., Merritt D., 2000, *ApJ*, 539, L9
- Field G. B., Perrenod S. C., 1977, *ApJ*, 215, 717
- Fiore F., La Franca F., Giommi P., Elvis M., Matt G., Comastri A., Molendi S., Gioia I., 1999, *MNRAS*, 306, L55
- Forman W., Jones C., Cominsky L., Julien P., Murray S., Peters G., Tananbaum H., Giacconi R., 1978, *ApJS*, 38, 357
- Foschini L., di Cocco G., Ho L. C., Bassani L., Cappi M., Dadina M., Gianotti F., Malaguti G., Panessa F., Piconcelli E., Stephen J. B., Trifoglio M., 2002, in *Inflows, outflows, and reprocessing around black holes - Proceedings of the 5th Italian AGN Meeting, Como, June 11-14, 2002*. Edited by I. Cagnoni, p. 88 Search for ultraluminous X-ray sources in nearby galaxies. pp 88-+
- Foschini L., Ho L. C., Masetti N., Cappi M., Dadina M., Bassani L., Malaguti G., Palazzi E., Di Cocco G., Martini P., Ravindranath S., Stephen J. B., Trifoglio M., Gianotti F., 2002, *A&A*, 396, 787

- Franceschini A., Braitto V., Fadda D., 2002, *MNRAS*, 335, L51
- Franceschini A., Vercellone S., Fabian A. C., 1998, *MNRAS*, 297, 817
- Friedman H., Lichtman S. W., Byram E. T., 1951, *Phys. Rev.*, 83, 1025
- Fukugita M., Hogan C. J., Peebles P. J. E., 1998, *ApJ*, 503, 518
- Fukugita M., Ichikawa T., Gunn J. E., Doi M., Shimasaku K., Schneider D. P., 1996, *AJ*, 111, 1748
- Fukunaga K., 1990, *Introduction to Statistical Pattern Recognition*, 2 edn. Academic Press
- Gómez P. L., Nichol R. C., Miller C. J., Balogh M. L., Goto T., Zabludoff A. I., Romer A. K., et al., 2003, *ApJ*, 584, 210
- Garmire G., Nousek J., 1980, *BAAS*, 12, 853
- Garmire G. P., Bautz M. W., Ford P. G., Nousek J. A., Ricker G. R., 2003, in *X-Ray and Gamma-Ray Telescopes and Instruments for Astronomy*. Edited by Joachim E. Truemper, Harvey D. Tananbaum. *Proceedings of the SPIE*, Volume 4851, pp. 28–44 (2003). Advanced CCD imaging spectrometer (ACIS) instrument on the Chandra X-ray Observatory. pp 28–44
- Gendreau K. C., Mushotzky R., Fabian A. C., Holt S. S., Kii T., Serlemitsos P. J., Ogasaka Y., Tanaka Y., Bautz M. W., Fukazawa Y., et al., 1995, *PASJ*, 47, L5
- Georgakakis A., Georgantopoulos I., Vallbé M., Kolokotronis V., Basilakos S., Plionis M., Stewart G. C., Shanks T., Boyle B. J., 2004, *MNRAS*, 349, 135
- Georgantopoulos I., Almaini O., Shanks T., Stewart G. C., Griffiths R. E., Boyle B. J., Gunn K. F., 1998, *MNRAS*
- Georgantopoulos I., Almaini O., Shanks T., Stewart G. C., Griffiths R. E., Boyle B. J., Gunn K. F., 1999, *MNRAS*, 305, 125
- Georgantopoulos I., Georgakakis A., Stewart G. C., Akylas A., Boyle B. J., Shanks T., Griffiths R. E., 2003, *MNRAS*, 342, 321
- Georgantopoulos I., Stewart G. C., Blair A. J., Shanks T., Griffiths R. E., Boyle B. J., Almaini O., Roche N., 1997, *MNRAS*, 291, 203
- Georgantopoulos I., Stewart G. C., Shanks T., Griffiths R. E., Boyle B. J., 1993, *MNRAS*, 262, 619
- Georgantopoulos I., Stewart G. C., Shanks T., Griffiths R. E., Boyle B. J., 1996, *MNRAS*, 280, 276
- Giacconi R., Bechtold J., Branduardi G., et al., 1979, *ApJ*

- Giacconi R., Gursky H., Paolini F. R., Rossi B. B., 1962, *Physical Review Letters*, 9, 439
- Giacconi R., Rosati P., Tozzi P., Nonino M., Hasinger G., Norman C., Bergeron J., Borgani S., Gilli R., Gilmozzi R., Zheng W., 2001, *ApJ*, 551, 624
- Gilli R., Cimatti A., Daddi E., Hasinger G., Rosati P., Szokoly G., Tozzi P., Bergeron J., et al., 2003, *ApJ*, 592, 721
- Gilli R., Salvati M., Hasinger G., 2001, *A&A*, 366, 407
- Gioia I. M., Maccacaro T., Schild R. E., Wolter A., Stocke J. T., Morris S. L., Henry J. P., 1990, *ApJS*, 72, 567
- Giommi P., Perri M., Fiore F., 2000, *A&A*, 362, 799
- Goudfrooij P., Bohlin R. C., Walsh J. R., Baum S. A., 1998, Technical report, STIS Near-IR Fringing. II. Basics and Use of Contemporaneous Flats for Spectroscopy of Point Sources (Rev. A)
- Granato G. L., Danese L., Franceschini A., 1997, *ApJ*, 486, 147
- Griffiths R. E., Ceca R. D., Georgantopoulos I., Boyle B. J., Stewart G. C., Shanks T., Fruscione A., 1996, *MNRAS*, 281, 71
- Griffiths R. E., Murray S. S., Giacconi R., Bechtold J., Murdin P., Smith M., MacGillivray H. T., Ward M., Danziger J., Lub J., et al., 1983, *ApJ*, 269, 375
- Griffiths R. E., Padovani P., 1990, *ApJ*, 360, 483
- Gruber D. E., 1992, in *The X-ray Background The Hard X-Ray Background*. pp 44–+
- Guillén J., 1928, *Cantico ("Perfección")*. Seix Barral, Barcelona
- Gunn J. E., 1979, *Feeding the monster – Gas discs in elliptical galaxies. Active galactic nuclei*. (A79-50785 22-90) Cambridge, Cambridge University Press, 1979, p. 213–225. Research supported by the Alfred P. Sloan Foundation, pp 213–225
- Gunn K. F., 1999, PhD thesis
- Gursky H., Solinger A., Kellogg E. M., Murray S., Tananbaum H., Giacconi R., Cavaliere A., 1972, *ApJ*, 173, L99+
- Harnden F. R., Fabricant D. G., Harris D. E., Schwarz J., 1984, *SAO Special Report*, 393
- Hasinger G., 1996, *A&AS*, 120, 607

- Hasinger G., 2000, in ISO Survey of a Dusty Universe, Proceedings of a Ringberg Workshop Held at Ringberg Castle, Tegernsee, Germany, 8-12 November 1999, Edited by D. Lemke, M. Stickel, and K. Wilke, Lecture Notes in Physics, vol. 548, p.423 X-ray Surveys of the Obscured Universe. pp 423-+
- Hasinger G., Burg R., Giacconi R., Hartner G., Schmidt M., Trumper J., Zamorani G., 1993, *A&A*, 275, 1
- Hasinger G., Burg R., Giacconi R., Schmidt M., Trumper J., Zamorani G., 1998, *A&A*, 329, 482
- Hines D. C., 1991, *ApJ*, 374, L9
- Ho L. C., 2003, in ASP Conf. Ser. 290: Active Galactic Nuclei: From Central Engine to Host Galaxy The Central Engines of Low-Luminosity AGNs. pp 379-+
- Hornschemeier A. E., Bauer F. E., Alexander D. M., Brandt W. N., Sargent W. L. W., Bautz M. W., Conselice C., Garmire G. P., Schneider D. P., Wilson G., 2003, *AJ*, 126, 575
- Hornschemeier A. E., Brandt W. N., Garmire G. P., Schneider D. P., Broos P. S., Townsley L. K., et al., 2000, *ApJ*, 541, 49
- Hoyle F., 1963, *ApJ*, 137, 993
- Inoue H., Kii T., Ogasaka Y., Takahashi T., Ueda Y., 1996, in Roentgenstrahlung from the Universe ASCA Sky Surveys and the Cosmic X-Ray Background. pp 323-326
- Iwan D., Shafer R. A., Marshall F. E., Boldt E. A., Mushotzky R. F., Stottlemeyer A., 1982, *ApJ*, 260, 111
- Iwasawa K., Fabian A. C., Brandt W. N., Crawford C. S., Almaini O., 1997, *MNRAS*, 291, L17
- Jahoda K., Mushotzky R. F., Boldt E., Lahav O., 1991, *ApJ*, 378, L37
- Jarvis J. F., Tyson J. A., 1981, *AJ*, 86, 476
- Jauncey D. L., 1975, *ARA&A*, 13, 23
- Jentsch 1929, *Phys. Z.*, 30, 268
- Jerius D., Donnelly R. H., Tibbetts M. S., Edgar R. J., Gaetz T. J., Schwartz D. A., Van Speybroeck L. P., Zhao P., 2000, in Proc. SPIE Vol. 4012, p. 17-27, X-Ray Optics, Instruments, and Missions III, Joachim E. Truemper; Bernd Aschenbach; Eds. Orbital measurement and verification of the Chandra X-ray Observatory's PSF. pp 17-27
- Jones L. R., Fong R., Shanks T., Ellis R. S., Peterson B. A., 1991, *MNRAS*, 249, 481

- Karttunen H., Kröger P., Oja H., Poutanen M., Donner K. J., eds, 1994, *Fundamental Astronomy*, 2 edn. Springer Verlag
- Kauffmann G., Charlot S., 1998, *MNRAS*, 294, 705
- Kewley L. J., Heisler C. A., Dopita M. A., Lumsden S., 2001, *ApJS*, 132, 37
- Kim D.-W., Wilkes B. J., Green P. J., Cameron R. A., Drake J. J., Evans N. R., Freeman P., Gaetz T. J., et al., 2004, *ApJ*, 600, 59
- King A. R., Davies M. B., Ward M. J., Fabbiano G., Elvis M., 2001, *ApJ*, 552, L109
- King C. R., Ellis R. S., 1985, *ApJ*, 288, 456
- Kinney A. L., Calzetti D., Bohlin R. C., McQuade K., Storchi-Bergmann T., Schmitt H. R., 1996, *ApJ*, 467, 38
- Kondo H., Dotani T., Inoue H., Kii T., Mitsuda K., Tanaka Y., Ohashi T., Tawara Y., Hayashida K., Stewart G. C., 1992, in *Frontiers Science Series An Unbiased Sky Survey at High Galactic Latitude with Ginga*. pp 655–+
- Koo D. C., 1985, *AJ*, 90, 418
- Koo D. C., 1986, *ApJ*, 311, 651
- Kormendy J., Gebhardt K., 2001, in *AIP Conf. Proc. 586: 20th Texas Symposium on relativistic astrophysics Supermassive Black Holes in Galactic Nuclei (Plenary Talk)*. pp 363–+
- Kron R. G., 1980, *ApJS*, 43, 305
- Kuntschner H., Smith R. J., Colless M., Davies R. L., Kaldare R., Vazdekis A., 2002, *MNRAS*, 337, 172
- Landolt A. U., 1992, *AJ*, 104, 340
- Larson R. B., Tinsley B. M., Caldwell C. N., 1980, *ApJ*, 237, 692
- Lawrence A., 1999, *Advances in Space Research*, 23, 1167
- Lawrence A., Elvis M., 1982, *ApJ*, 256, 410
- Lilly S. J., Cowie L. L., Gardner J. P., 1991, *ApJ*, 369, 79
- Maccacaro T., Gioia I. M., Wolter A., Zamorani G., Stocke J. T., 1988, *ApJ*, 326, 680
- Mackay C. D., 1986, *ARA&A*, 24, 255
- Madau P., Ferguson H. C., Dickinson M. E., Giavalisco M., Steidel C. C., Fruchter A., 1996, *MNRAS*, 283, 1388
- Madau P., Ghisellini G., Fabian A. C., 1994, *MNRAS*, 270, L17+

- Magorrian J., Tremaine S., Richstone D., Bender R., Bower G., Dressler A., Faber S. M., Gebhardt K., Green R., Grillmair C., Kormendy J., Lauer T., 1998, *AJ*, 115, 2285
- Mainieri V., Bergeron J., Hasinger G., Lehmann I., Rosati P., Schmidt M., Szokoly G., Della Ceca R., 2002, *A&A*, 393, 425
- Maiolino R., Marconi A., Oliva E., 2001, *A&A*, 365, 37
- Maiolino R., Salvati M., Marconi A., Antonucci R. R. J., 2001, *A&A*, 375, 25
- Manners J. C., Johnson O., Almaini O., Willott C. J., Gonzalez-Solares E., Lawrence A., Mann R. G., et al., 2003, *MNRAS*, 343, 293
- Marshall F. E., Boldt E. A., Holt S. S., Miller R. B., Mushotzky R. F., Rose L. A., Rothschild R. E., Serlemitsos P. J., 1980, *ApJ*, 235, 4
- Marshall H. L., Tananbaum H., Avni Y., Zamorani G., 1983, *ApJ*, 269, 35
- Martini P., Weinberg D. H., 2001, *ApJ*, 547, 12
- Masetti N., Foschini L., Ho L. C., Dadina M., Di Cocco G., Malaguti G., Palazzi E., 2003, *A&A*, 406, L27
- Mather J. C., Cheng E. S., Eplee R. E., Isaacman R. B., Meyer S. S., Shafer R. A., Weiss R., Wright et al., 1990, *ApJ*, 354, L37
- McCammon D., Sanders W. T., 1990, *ARA&A*, 28, 657
- McCracken H. J., Metcalfe N., Shanks T., Campos A., Gardner J. P., Fong R., 2000, *MNRAS*, 311, 707
- McHardy I. M., Lawrence A., Pye J. P., Pounds K. A., 1981, *MNRAS*, 197, 893
- Menci N., Fiore F., Perola G. C., Cavaliere A., 2004, *ApJ*, 606, 58
- Metcalfe N., et al., 1995a, *MNRAS*, 274, 769
- Metcalfe N., et al., 1995b, *MNRAS*, 273, 257
- Metcalfe N., Ratcliffe A., Shanks T., Fong R., 1998, *MNRAS*, 294, 147
- Metcalfe N., Shanks T., Campos A., Fong R., Gardner J. P., 1996, *Nature*, 383, 236
- Metcalfe N., Shanks T., Campos A., McCracken H. J., Fong R., 2001, *MNRAS*, 323, 795
- Metcalfe N., Shanks T., Fong R., Jones L. R., 1991, *MNRAS*, 249, 498
- Mink D. J., 1997, in *ASP Conf. Ser. 125: Astronomical Data Analysis Software and Systems VI* WCSTools: Image World Coordinate System Utilities. pp 249–+
- Monet D. G., 1998, *Bulletin of the American Astronomical Society*, 30, 1427

- Moran E. C., Filippenko A. V., Chornock R., 2002, *ApJ*, 579, L71
- Morgan W. W., 1958, *PASP*, 70, 364
- Motch C., Belloni T., Buckley D., Gottwald M., Hasinger G., Pakull M. W., Pietsch W., Reinsch K., Remillard R. A., Schmitt J. H. M. M., Trumpler J., Zimmermann H.-U., 1991, *A&A*, 246, L24
- Mulchaey J. S., Colbert E., Wilson A. S., Mushotzky R. F., Weaver K. A., 1993, *ApJ*, 414, 144
- Mushotzky R. F., Cowie L. L., Barger A. J., Arnaud K. A., 2000, *Nature*, 404, 459
- Nandra K., Pounds K. A., 1994, *MNRAS*, 268, 405
- Neugebauer G., Green R. F., Matthews K., Schmidt M., Soifer B. T., Bennett J., 1987, *ApJS*, 63, 615
- Nikolajuk M., Papadakis I. E., Czerny B., 2004, *MNRAS*, 350, L26
- Norman C., Hasinger G., Giacconi R., Gilli R., Kewley L., Nonino M., Rosati P., Szokoly G., et al., 2002, *ApJ*, 571, 218
- O'Connell R. W., 1999, *ARA&A*, 37, 603
- Osterbrock D. E., 1989, *Astrophysics of Gaseous Nebula and Active Galactic Nuclei*. University Science Books, Mill Valley, CA
- Pappa A., Stewart G. C., Georgantopoulos I., Griffiths R. E., Boyle B. J., Shanks T., 2001, *MNRAS*, 327, 499
- Pence W., 1976, *ApJ*, 203, 39
- Peterson B. M., ed. 1997, *An introduction to active galactic nuclei*
- Phillips L. A., Ostriker J. P., Cen R., 2001, *ApJ*, 554, L9
- Piccinotti G., Mushotzky R. F., Boldt E. A., Holt S. S., Marshall F. E., Serlemitsos P. J., Shafer R. A., 1982, *ApJ*, 253, 485
- Pier E. A., Krolik J. H., 1993, *ApJ*, 418, 673
- Pierre et al., 2001, *A&A*, 372, L45
- Pozzetti L., Madau P., Zamorani G., Ferguson H. C., Bruzual A. G., 1998, *MNRAS*, 298, 1133
- Ptak A., Serlemitsos P., Yaqoob T., Mushotzky R., 1999, *ApJS*, 120, 179
- Ranalli P., Comastri A., Setti G., 2003, *A&A*, 399, 39
- Roberts T. P., Warwick R. S., Ward M. J., Goad M. R., 2004, *MNRAS*, 349, 1193

- Roche N., Shanks T., Georgantopoulos I., Stewart G. C., Boyle B. J., Griffiths R. E., 1995, *MNRAS*, 273, L15
- Romero-Colmenero E., Branduardi-Raymont G., Carrera F. J., Jones L. R., Mason K. O., McHardy I. M., Mittaz J. P. D., 1996, *MNRAS*, 282, 94
- Rowan-Robinson M., 1977, *ApJ*, 213, 635
- Schade D., Lilly S. J., Crampton D., Ellis R. S., Le Fèvre O., Hammer F., Brinchmann J., Abraham R., Colless M., Glazebrook K., Tresse L., Broadhurst T., 1999, *ApJ*, 525, 31
- Schmidt M., 1963, *Nature*, 197, 1040
- Schmidt M., 1968, *ApJ*, 151, 393
- Schmidt M., 1970, *ApJ*, 162, 371
- Schmidt M., Green R. F., 1983, *ApJ*, 269, 352
- Schmidt M., Hasinger G., Gunn J., Schneider D., Burg R., Giacconi R., Lehmann I., MacKenty J., Trumper J., Zamorani G., 1998, *A&A*, 329, 495
- Schmidt M., Schneider D. P., Gunn J. E., 1995, *AJ*, 110, 68
- Schwartz D., Gursky H., 1974, in *ASSL Vol. 43: X-ray Astronomy The Cosmic X-Ray Background*. pp 359–+
- Setti G., Woltjer L., 1989, *A&A*, 224, L21
- Seyfert C. K., 1943, *ApJ*, 97, 28
- Shafer R. A., 1983, Ph.D. Thesis
- Shanks T., Fong R., Boyle B. J., Peterson B. A., 1987, *MNRAS*, 227, 739
- Shanks T., Georgantopoulos I., Stewart G. C., Pounds K. A., Boyle B. J., Griffiths R. E., 1991, *Nat*, 353, 315
- Shanks T., Georgantopoulos I., Stewart G. C., Pounds K. A., Boyle B. J., Griffiths R. E., 1991, *Nature*, 353, 315
- Shaver P. A., Wall J. V., Kellermann K. I., Jackson C. A., Hawkins M. R. S., 1996, *Nature*, 384, 439
- Shlosman I., Begelman M. C., Frank J., 1990, *Nature*, 345, 679
- Smail I., et al., 1999, *MNRAS*, 308, 1061
- Smith D. A., Done C., 1996, *MNRAS*, 280, 355
- Soltan A., 1982, *MNRAS*, 200, 115
- Spitzer L. J., Saslaw W. C., 1966, *ApJ*, 143, 400

- Stern D., Moran E. C., Coil A. L., Connolly A., Davis M., Dawson S., Dey A., Eisenhardt P., et al., 2002, *ApJ*, 568, 71
- Stevenson P. R. F., Shanks T., Fong R., 1986, in *ASSL Vol. 122: Spectral Evolution of Galaxies New observations of galaxy number counts*. pp 439–445
- Stocke J. T., Morris S. L., Gioia I. M., Maccacaro T., Schild R., Wolter A., Fleming T. A., Henry J. P., 1991, *ApJS*, 76, 813
- Stoughton C., Lupton R. H., Bernardi M., Blanton M. R., Burles S., Castander F. J., Connolly A. J., Eisenstein D. J., Frieman J. A., Hennessy G. S., et al., 2002, *AJ*, 123, 485
- Swartz D. A., Ghosh K. K., Tennant A. F., 2003, *American Astronomical Society Meeting*, 202,
- Szalay A. S., Connolly A. J., Szokoly G. P., 1999, *AJ*, 117, 68
- Tanaka Y., Inoue H., Holt S. S., 1994, *PASJ*, 46, L37
- Truemper J., 1990, in *IAU Colloq. 115: High Resolution X-ray Spectroscopy of Cosmic Plasmas The ROSAT mission*. pp 291–294
- Turner T. J., George I. M., Nandra K., Mushotzky R. F., 1997, *ApJ*, 488, 164
- Turner T. J., Pounds K. A., 1989, *MNRAS*, 240, 833
- Ueda Y., Takahashi T., Inoue H., Tsuru T., Sakano M., Ishisaki Y., Ogasaka Y., Makishima K., Yamada T., Akiyama M., Ohta K., 1999, *ApJ*, 518, 656
- van Dokkum P. G., Franx M., Kelson D. D., Illingworth G. D., 2001, *ApJ*, 553, L39
- van Speybroeck L. P., Jerius D., Edgar R. J., Gaetz T. J., Zhao P., Reid P. B., 1997, in *Proc. SPIE Vol. 3113*, p. 89–104, *Grazing Incidence and Multilayer X-Ray Optical Systems*, Richard B. Hoover; Arthur B. Walker; Eds. Performance expectation versus reality. pp 89–104
- Vecchi A., Molendi S., Guainazzi M., Fiore F., Parmar A. N., 1999, *A&A*, 349, L73
- Veilleux S., Osterbrock D. E., 1987, *ApJS*, 63, 295
- Visvanathan N., Sandage A., 1977, *ApJ*, 216, 214
- Warwick R. S., Pye J. P., Fabian A. C., 1980, *MNRAS*, 190, 243
- Weingartner J. C., Murray N., 2002, *ApJ*, 580, 88
- Weisskopf M. C., O'dell S. L., van Speybroeck L. P., 1996, in *Proc. SPIE Vol. 2805*, p. 2–7, *Multilayer and Grazing Incidence X-Ray/EUV Optics III*, Richard B. Hoover; Arthur B. Walker; Eds. *Advanced X-Ray Astrophysics Facility (AXAF)*. pp 2–7

- Weisskopf M. C., Tananbaum H. D., Van Speybroeck L. P., O'Dell S. L., 2000, in Proc. SPIE Vol. 4012, p. 2-16, X-Ray Optics, Instruments, and Missions III, Joachim E. Truemper; Bernd Aschenbach; Eds. Chandra X-ray Observatory (CXO): overview. pp 2-16
- White N. E., Swank J. H., Holt S. S., 1983, *ApJ*, 270, 711
- Wilman R. J., Fabian A. C., Nulsen P. E. J., 2000, *MNRAS*, 319, 583
- Wolf C., Wisotzki L., Borch A., Dye S., Kleinheinrich M., Meisenheimer K., 2003, *A&A*, 408, 499
- Wolter V. H., 1952, *Ann. Phys.*, 10, 94
- Wright E. L., Mather J. C., Fixsen D. J., Kogut A., Shafer R. A., Bennett C. L., Boggess N. W., Cheng E. S., Silverberg R. F., Smoot G. F., Weiss R., 1994, *ApJ*, 420, 450
- Wu X., Hamilton T., Helfand D. J., Wang Q., 1991, *ApJ*, 379, 564
- Yang Y., Mushotzky R. F., Barger A. J., Cowie L. L., Sanders D. B., Steffen A. T., 2003, *ApJ*, 585, L85
- York D. G., Adelman J., Anderson J. E., Anderson S. F., Annis J., Bahcall N. A., Bakken J. A., Barkhouser R., Bastian S., Berman E., Boroski W. N., Bracker S., et al., 2000, *AJ*, 120, 1579
- Zamorani G., Henry J. P., Maccacaro T., Tananbaum H., Soltan A., Avni Y., Liebert J., Stocke J., Strittmatter P. A., Weymann R. J., Smith M. G., Condon J. J., 1981, *ApJ*, 245, 357



*Queda curvo el firmamento,
compacto azul, sobre el día.
Es el redondeamiento
del esplendor; melodía.
Todo es cúpula. Reposa,
central sin querer, la rosa,
y un sol en cenit sujeta.
Y tanto se da el presente,
que el pie caminante siente
la integridad del planeta.*

Guillén (1928)

